PREPARATION AND CHARACTERIZATION OF CYANIDE-BRIDGED MOLECULAR CLUSTERS AND EXTENDED NETWORKS USING THE BUILDING-BLOCK APPROACH

A Dissertation

by

FERDI KARADAS

Submitted to the Office of Graduate Studies of
Texas A&M University
in partial fulfillment of the requirements for the degree of

DOCTOR OF PHILOSOPHY

December 2009

Major Subject: Chemistry

PREPARATION AND CHARACTERIZATION OF CYANIDE-BRIDGED MOLECULAR CLUSTERS AND EXTENDED NETWORKS USING THE BUILDING-BLOCK APPROACH

A Dissertation

by

FERDI KARADAŞ

Submitted to the Office of Graduate Studies of
Texas A&M University
in partial fulfillment of the requirements for the degree of

DOCTOR OF PHILOSOPHY

Approved by:

Chair of Committee,	Kim R. Dunbar
Committee Members,	Timothy R. Hughbanks
	Hongcai Zhou
	Donald G. Naugle
Head of Department,	David H. Russell

December 2009

Major Subject: Chemistry

ABSTRACT

Preparation and Characterization of Cyanide-Bridged Molecular Clusters and Extended Networks Using the Building-Block Approach. (December 2009)

Ferdi Karadaş, B.S., Middle East Technical University; M.S., Bilkent University
Chair of Advisory Committee: Dr. Kim R. Dunbar

The cyanide ligand has frequently been used to prepare clusters with novel magnetic properties due to its ability to provide an efficient pathway for superexchange between metal centers that are bound in an end-to-end fashion. One of the common synthetic approaches in this chemistry is to design suitable cyanide containing precursors and then to react such building blocks with metal complexes consisting of accessible sites. The triphos ligand (triphos: 1,1,1-tris(diphenylphosphinomethyl)ethane) has been employed in this vein to prepare metal complexes, one of which is a five coordinate paramagnetic complex ($S = 1/2$) with a square pyramidal metal center, $[Co^{II}(triphos)(CN)_2]$. A family of molecular squares, $[\{M^{II}Cl_2\}_2\{Co^{II}(triphos)(CN)_2\}_2]$ (M= Mn (**2**), Fe (**3**), Co (**4**), Ni (**5**), and Zn (**6**)), has been synthesized by the reaction of $Co^{II}(triphos)(CN)_2$ and MCl_2 (M= Mn, Co, Ni, Zn) or $Fe_4Cl_8(THF)_6$ in CH_2Cl_2/EtOH mixture. A series of cyanide-bridged trinuclear complexes, $\{[Co(triphos)(CN)_2]_2[M(MeOH)_4]\}(ClO_4)_2$ (M = Mn (**7**), Fe (**8**), Co (**9**), and Ni (**10**)) and tetranuclear complexes, $\{[Co(triphos)(CN)_2]_2[M(MeOH)_4]_2\}(ClO_4)_4$ (**[Co_2M_2]** M = Mn (**11**) and Ni (**12**)) have been synthesized in a similar fashion by the reaction of $Co^{II}(triphos)(CN)_2$ and $M(ClO_4)_2 \cdot 6H_2O$ (M= Mn, Fe, Co, Ni) in methanol. The trinuclear compounds (**7-9**),

and tetranuclear complexes (**2-6**, **11**, **12**), are characterized by antiferromagnetic coupling between metal centers while magnetic behavior of **10** indicates the presence of ferromagnetic interactions between the paramagnetic metal centers. Interactions between magnetic orbitals of Co(II) and M(II) ions were also investigated by means of the density functional theoretical (DFT) calculations.

Another triphos containing building block, $[(\text{triphos})\text{Re}(\text{CN})_3]^-$ anion (**13**), has been employed to prepare derivatives of a cubic SMM cluster with four octahedral Re(II) ions and four tetrahedral Mn(II) sites bridging through cyanide ligand. The reactions of Re(II) precursor with MnI_2 and solvated Mn(II) ions resulting in derivatives of Re_4Mn_4 cube with different ligands attached to the Mn center other than the chloride atom were reported. Our efforts on linking these cubes using organo cyanide ligands such as dicyanamide (dca^-) and 7,7,8,8–tetracyanoquinodimethane (TCNQ^-) to form extended networks were also discussed.

To her;

Yaşam kadar gerçek
Yaşamak gibi sahte
Öyle çok şey var ki
Yaralayan insanı
Bir yürek çarpıntısı
Onu her gördüğünde
Öyle çok şey var ki bak
Sana dair..

ACKNOWLEDGEMENTS

First I would like to thank my advisor, Kim R. Dunbar, for her guidance and patience. Her curiosity regarding any scientific matter that eventually led to a broad background in chemistry is the quality that I admire most about her and that she tried to instill in me all these years. For this reason, she encouraged me to go to several conferences and meetings, some of which were out of country. I will also carry her passion and scientific discipline, which had and -I am sure- will have a great impact on my academic career.

I would also like to thank the other members of my dissertation committee, Professors Timothy R. Hughbanks, Donald G. Naugle, and Hongcai Zhou for reading this work and for their helpful comments. My master's thesis advisor, Prof. Sefik Suzer, at Bilkent University and my undergraduate advisor, Prof. Meral Kizilyalli, merit acknowledgment for allowing me to work in their labs and to take my first baby steps in the scientific world.

Much of this dissertation research is directly inspired by the works of others in the Dunbar group. I thank Dr. Eric J. Schelter for his help in learning the basic experimental techniques for air-free chemistry and in helping me to adapt the lab in the first year. I am also glad that he left a great capping ligand (triphos) behind which I used almost in every part of my work. My next guide in the lab was Dr. Mikhail Shatruk, who not only was a perfect mentor with his unique enthusiasm, but also a great friend. He participated in a lot of projects in those four years and I never heard him complaining about any of his work since he always liked what he was doing. He literally believed in each of his reactions and I believe that was the secret of his success. He helped me during almost every part of my research with his helpful discussions and knowledge.

Next on the list is Carolina O. Avendaǹo. Where do I start? Shall I start from the countless number of personal plans we made together or her deep obsession with organizing my work area? Whenever she starts a new experiment she has to clean everything and somehow that everything also includes my bench and desk. She gained this unnatural right by being a true friend. We explored the rhenium chemistry together, and I am sure exploring new things will continue throughout the rest of our lives. I also thank Matthew G. Hilfiger for his friendship. I always enjoyed his coffee and admired his ability to stay calm.

My thanks also go to J. Dafhne Aguirre and Alfredo Angeles Boza for their friendship in and outside the lab. Dafhne, it was always a good feeling to have someone next to you going through the same steps of the doctoral degree program and sharing those feelings without having to express them. I thank the whole Dunbar Group. I thank Dr. Andrey Prosvirin for his help in magnetism and magnetic measurements, Dr. John Bacsa for his discussions on crystallography. I also thank Dr. José Ramón Galán-Mascarós, Dr. Helen Chifotides, Dr. Akira Ota, Dr. Xinyi Wang and the visiting professor, Hanhua Zhao, for their discussions. I also thank Kristen Funck, Edward Funck, Ian Giles, Nazario Lopez, Heather Southerland, Sarah Lane, Zhongyue Zhang, and Codi Anne Sanders for their support.

I thank all of my soccer mates who made this city bearable. I also thank Dr. Cafer T. Yavuz and Dr. Mert Atilhan for their help in shaping my future career.

My last and biggest thanks are for my eternal friend and wife, Yağmur Karadaş; the one who kept me on this path with her endless support. She has given me her curiosity to learn and actually taught me that real life is hidden in the small details. She is key to my metamorphosis since I am not who I was before I met her, but I am now much closer to who I wanted to be for all those years. All those things we shared in the past are the clear indications to the fact that we, together, will make it to the point we want to go and the place where we want to be.

LIST OF COMPOUNDS

(1) Co(triphos)$(CN)_2$

(2) $\{[Co(triphos)(CN)_2]_2[MnCl_2]_2\}\bullet 3CH_2Cl_2$

(3) $\{[Co(triphos)(CN)_2]_2[FeCl_2]_2\}\bullet 3CH_2Cl_2$

(4) $\{[Co(triphos)(CN)_2]_2[CoCl_2]_2\}\bullet 3CH_2Cl_2$

(5) $\{[Co(triphos)(CN)_2]_2[NiCl_2]_2\}\bullet 4CH_2Cl_2$

(6) $\{[Co(triphos)(CN)_2]_2[ZnCl_2]_2\}\bullet 4CH_2Cl_2$

(7) $\{[Co(triphos)(CN)_2]_2[Mn(MeOH)_4]\}(BF_4)_2$

(8) $\{[Co(triphos)(CN)_2]_2[Fe(MeOH)_4]\}(BF_4)_2$

(9) $\{[Co(triphos)(CN)_2]_2[Co(MeOH)_4]\}(BF_4)_2$

(10) $\{[Co(triphos)(CN)_2]_2[Ni(MeOH)_4]\}(BF_4)_2$

(11) $\{[Co(triphos)(CN)_2]_2[Mn(MeOH)_4]_2\}(BF_4)_4$

(12) $\{[Co(triphos)(CN)_2]_2[Ni(MeOH)_4]_2\}(BF_4)_4$

(13) $[Et_4N][Re(triphos)(CN)_3]$

(14) $\{[Re(triphos)(CN)_3]_4[MnI]_4\}$

(15) $\{[Re(triphos)(CN)_3]_4[Mn(CH_3CN)]_4\}(ClO_4)_4$

(16) $\{[Re(triphos)(CN)_3]_4[Mn(ClO_4)]_3[Mn(CH_3OH)(CH_3O)]\}$

(17) $\{[Re(triphos)(CN)_3]_4[Mn(N(CN)_2)]_4\}$

(18) $\{[Re(triphos)(CN)_3]_4[(Mn(C_{12}H_4N_4))_3(Mn(C_{12}H_5N_4)(CH_3O))]\}$

TABLE OF CONTENTS

Page

CHAPTER Page

LIST OF FIGURES

FIGURE Page

FIGURE Page

FIGURE Page

FIGURE Page

FIGURE Page

FIGURE Page

LIST OF TABLES

CHAPTER I

INTRODUCTION TO MOLECULAR MAGNETISM AND HIGH SPIN METAL CYANIDE CLUSTERS

MOLECULAR MAGNETISM

The fact that nanosized magnets can exhibit not only classic magnet behavior but also other interesting magnetic phenomena due to quantum size effects has received much attention from various science disciplines.[1-7] This interest initiated a new field in magnetism, namely molecular magnetism, which focuses on the understanding of the design, preparation, and detailed spectroscopic and magnetic analyses of magnets based on paramagnetic molecules. While molecular magnets hold great promise for technological applications, they are also important because they could serve as simple models for understanding basic magnetic concepts such as exchange interaction and anisotropy.[8-14] The investigation of the origin of anomalous magnetic behavior in $Cu_2(O_2CCH_3)_4L_2$ (L = solvent) system by Bleaney and Bowers[15] in 1952 can be considered as a milestone in this chemistry, since this complex was the first one to be a simple model for applying the basic concepts of magnetism to a small molecule. The concept of superexchange interactions through ligands was born out of these and related studies. While most copper complexes had straightforward magnetism for an S=1/2 spin

---

This dissertation follows the style and format of the *Journal of the American Chemical Society*.

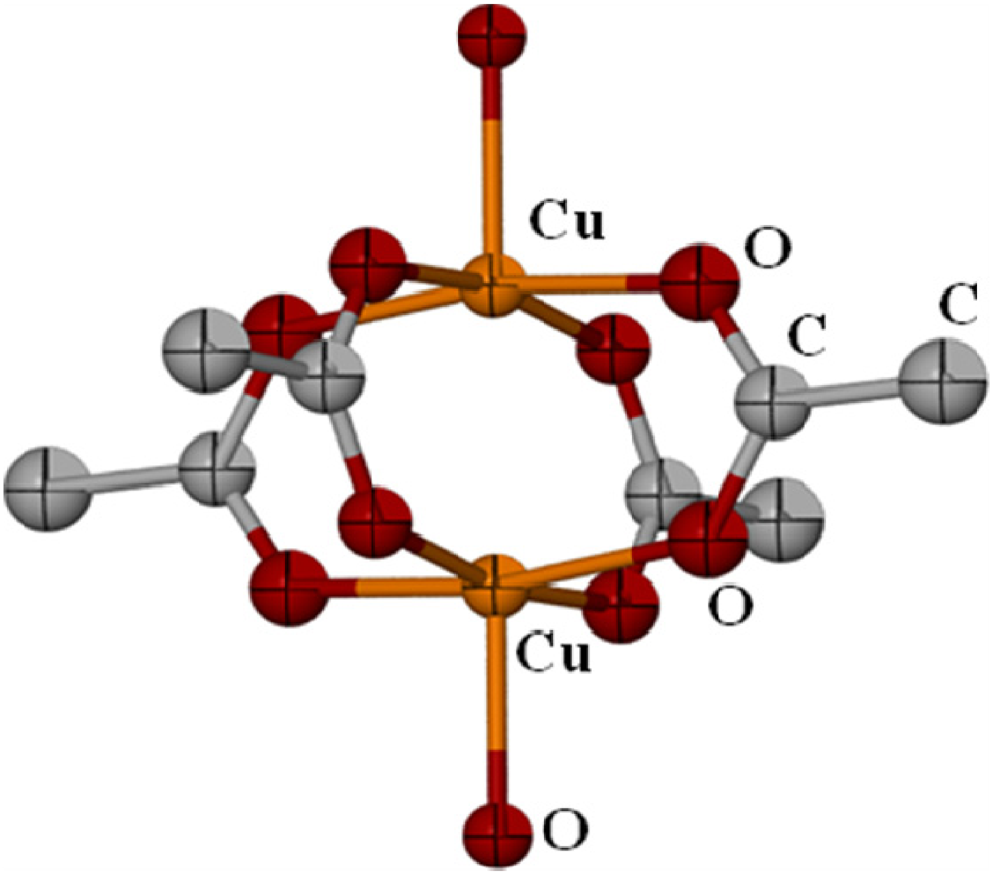

Figure 1. The structure of $[Cu(O_2CCH_3)_2(H_2O)]_2$ (Hydrogen atoms were omitted for the sake of clarity).[15]

system, magnetic studies performed on the dinuclear paddlewheel copper complex indicated the presence of magnetic interactions between Cu(II) ions.[16] The EPR studies later performed on the molecule also supported the presence of an antiferromagnetic interaction between the Cu(II) centers,[17] which raised another important question: how does the interaction occur. The crystal structure of $[Cu(O_2CCH_3)_2(H_2O)]_2$, later refined by Van Niekerk and Schoening,[18] revealed that the two copper ions, separated by 2.616 Å, are connected through four acetate bridging groups as shown in Figure 1. There are two possible pathways for the interaction of spin centers, namely the direct exchange interaction through a Cu-Cu interaction or indirect interactions through the bridging acetate groups. In order to address this issue, several derivatives of the copper acetate compound were prepared by substituting the acetate groups with CX_3COO^- ligands (X= Cl, Br, D and etc.) as well as the water ligand with other solvent ligands such as D_2O and p-toluidine.[19-23] Magnetic and crystallographic studies performed on such derivatives indicated that the Cu-Cu distance doesn't play a significant role on the strength of the interaction, which led to the conclusion that the indirect coupling scenario is essential for the magnetic coupling of the di-copper complexes. In fact, when two paramagnetic ions are separated from each other with a diamagnetic bridging ligand, a pathway through the bridging ligand could provide magnetic communication between the spins of the two metal ions. This type of indirect interaction through a bridging group is called *superexchange*, resulting in a weaker magnetic coupling than that in direct exchange.[24,25] Superexchange coupling, represented as the parameter J, results in the splitting of energy

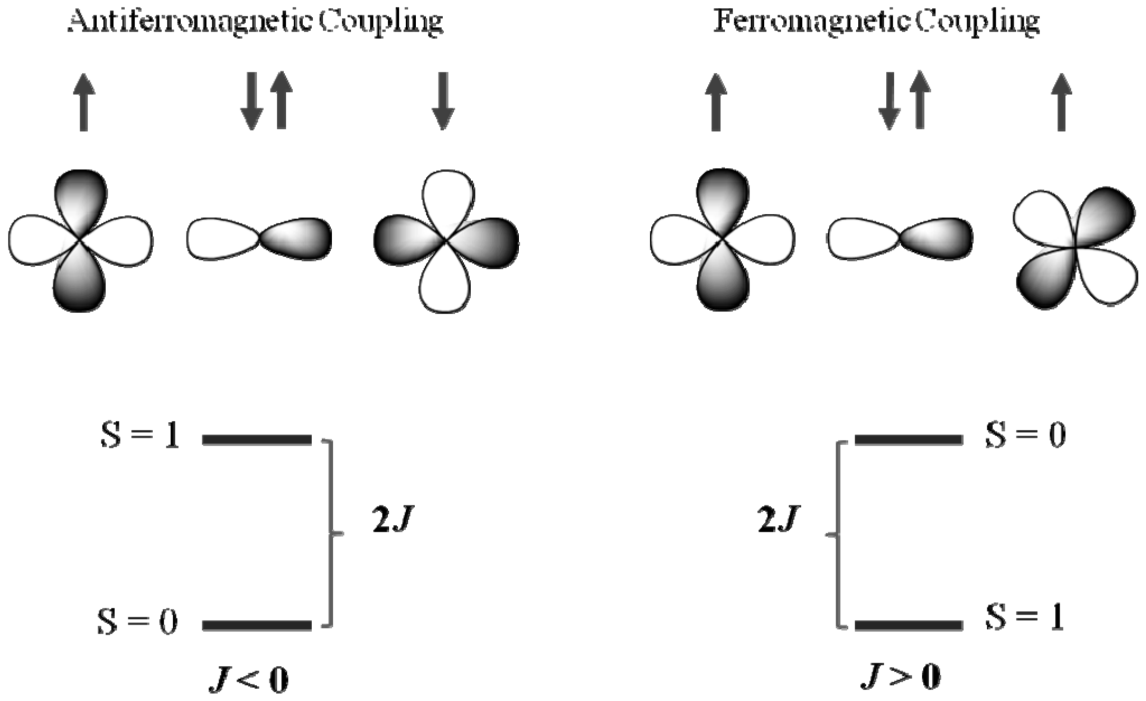

Figure 2. Interactions of orthogonal orbitals through diamagnetic bridging ligands result in antiferromagnetic coupling ($J < 0$) while those of non-orthogonal orbitals result in ferromagnetic coupling ($J > 0$).

levels with different spin values. For the Cu(II) dimer, the energy levels are arranged as shown in Figure 2, where the S = 1 state is the excited state which is 2J higher than the ground state (S = 0). Bleaney and Bowers predicted the energy gap between these spin levels successfully by fitting the temperature dependent magnetic behavior of the sample with the Van Vleck equation, which is known as Bleaney-Bowers equation when the system is that of two S = ½ spin centers coupling through a bridging ligand.[15]

The weak magnetic coupling due to superexchange leads to low-lying excited states of different spins as stated above, which may be populated at even thermally accessible energies (<1000 cm^{-1}).[26,27] The resulting ground state will be either the low spin or the high spin state, depending on whether the type of the superexchange is antiferromagnetic or ferromagnetic, respectively.

After the Cu story unfolded there was much activity on similar Cu(II) dimers[28-31] as well as other dinuclear metal complexes,[32,33] which helped in the understanding of the magnetic behavior of molecule based magnets. The success on such simple systems encouraged the magnetism community to design and characterize more complicated spin clusters. The first example of a bona fide molecular magnet that exhibits magnetic ordering was reported by Wickman *et al.*[34] The iron(III) (d^5) dithiocarbamate complex, bis-(N, N-diethyldithiocarbamato) iron(III) (Figure 3a), exhibits an intermediate spin value of 3/2 rather than one of the more common low-spin (S= 1/2) or high-spin (S= 5/2) values. Detailed magnetic measurements confirmed the presence of ferromagnetic ordering and an easy axis of magnetization (T_c= 2.5 K). Three years later, in 1970, Martin *et al.*, reported magnetization and magnetic susceptibility studies on a

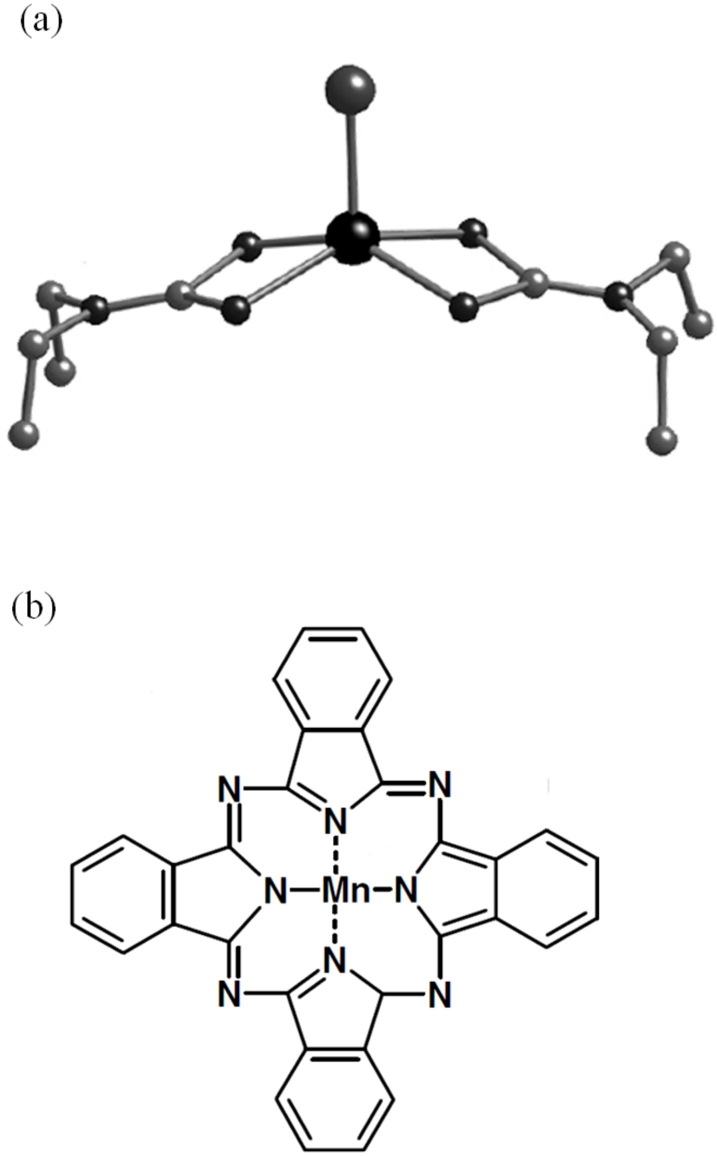

Figure 3. a) The molecular magnet, bis-(N, N-diethyldithiocarbamato) iron(III), exhibits ferromagnetic ordering (Tc = 2.5 K).[34] b) Manganese(II) phthalocyanine displays ferromagnetic interactions.[35]

manganese(II)phthalocyanine compound (Figure 3b), a planar molecule that forms parallel stacks in the crystal structure leading to ferromagnetic interactions between the manganese ions of adjacent molecules.[35] Later Kahn and coworkers reported the first example of a molecular ferrimagnet based on the Cu(II)-Mn(II) combination.[36-38] Miller and Epstein prepared one of the first examples of a molecular ferrimagnet containing an organocyanide building block, specifically tetracyanoethylene ($TCNE^-$) (Figure 4),[39] while Girolami and Verdaguer *et al.*, independently discovered that the Prussian blue derivatives order above room temperature (Figure 5).[40,41] These discoveries led to the realization of materials with ordering temperatures well above room temperatures, resulting in a rapidly growing interest in making higher dimensionality frameworks. Nevertheless, such extended networks have some disadvantages in that they are not only difficult to crystallize but are also structurally ill-defined. The structure can have random disorders in the 3D network, which brings uncertainty to the correlation of the physical properties with the structural data. For this reason, the study of lower dimensionality materials and discrete clusters grew in significance not only for understanding the magnetic exchange behavior, but also for their interesting magnetic properties in their own right, one of which is single molecule magnetism.

SINGLE MOLECULE MAGNETISM

One of the remarkable properties of magnetic materials is that they are composed of small regions called magnetic domains, in which all the spins have the same magnetic orientation. The domains form in order to minimize the total energy of the system. These

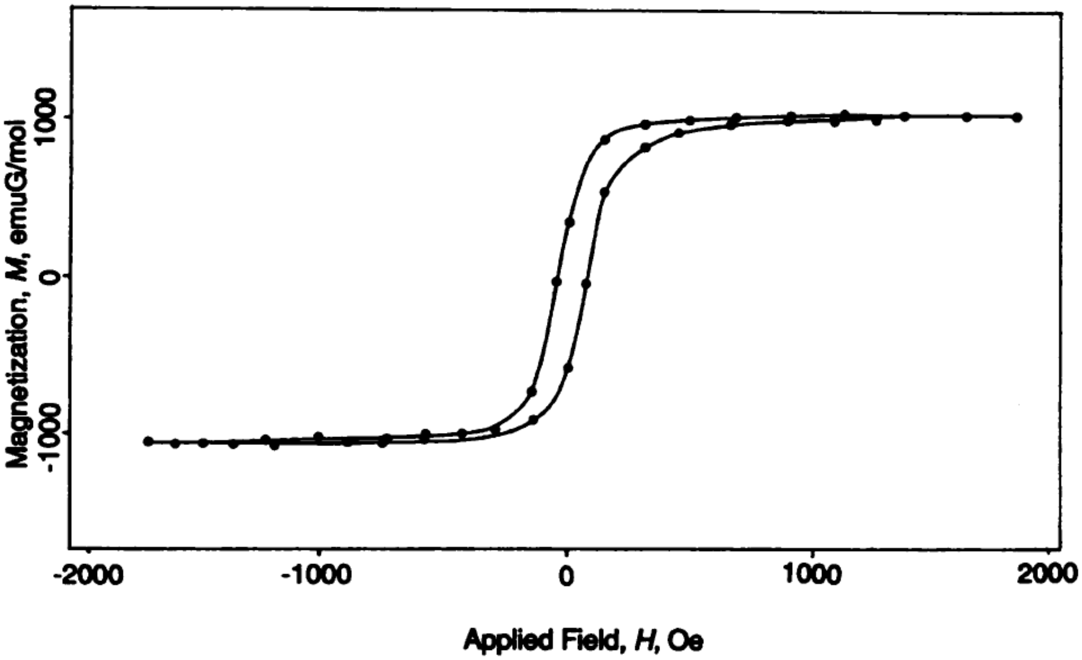

Figure 4. Hysteresis of $V(TCNE)_x(CH_2Cl_2)_y$ (x ~ 2, y ~ 1/2) at room temperature.[39]

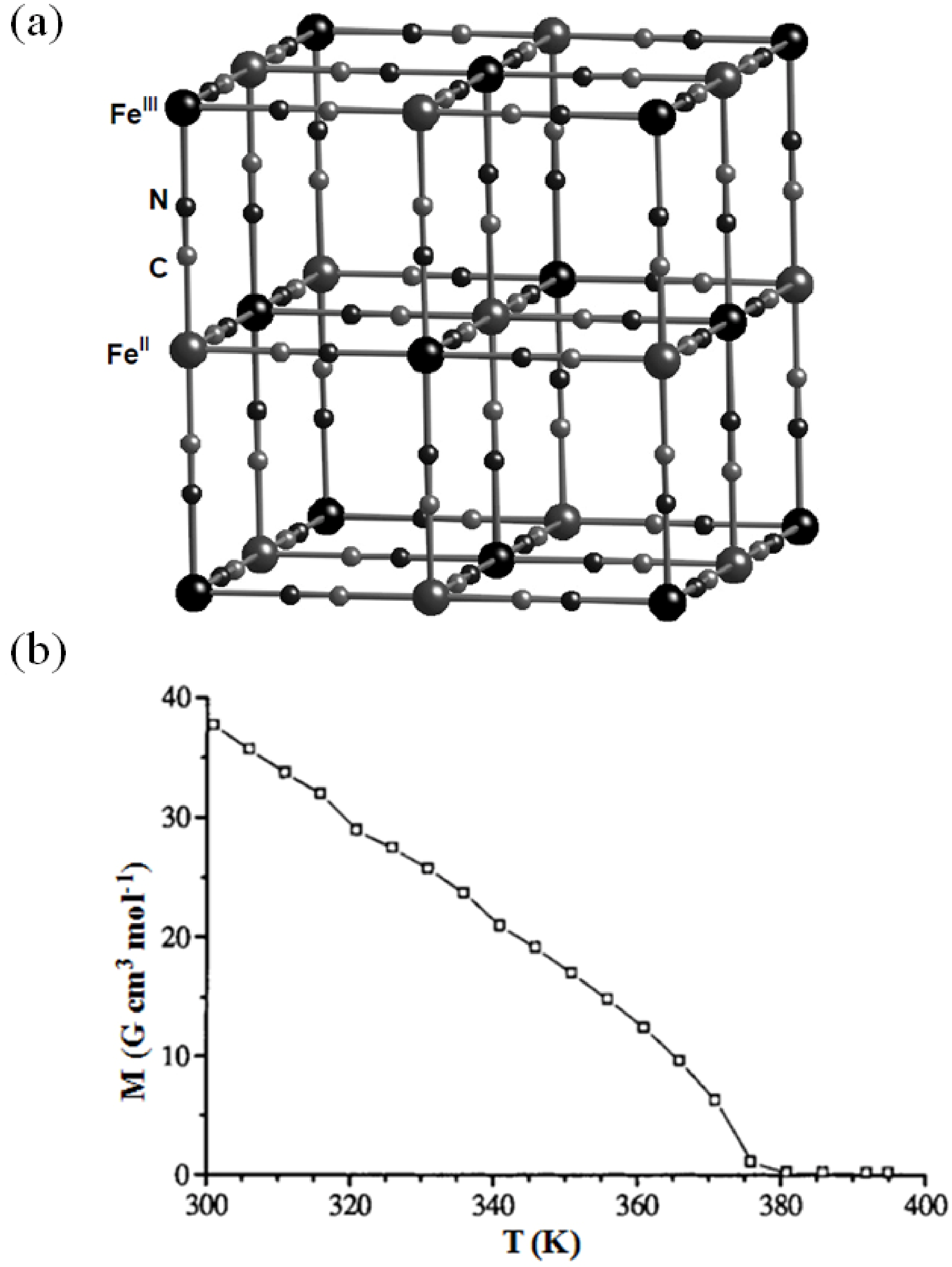

Figure 5. a) A fragment of the extended crystal structure of Prussian Blue. b) Temperature dependence of the zero-field cooled magnetization of $\mathrm{KV^{II}[Cr^{III}(CN)_6]\bullet 2H_2O\bullet 0.1KOTf}$ at an applied field of 50 G.[40]

domains are separated by interfaces, domain walls, in which the direction of magnetization changes from that in one domain to that in the other domain typically by 90° or 180°. The size of domain walls, with a finite width (on the order of 100 nm but very much dependent on the material), are governed by two opposing factors, exchange and magnetocrystalline energy. When a field is applied to the sample, the domain walls begin to collapse or “dissolve” and domains merge. Once the applied field is strong enough to saturate the sample, the domain with the spins aligned in the same direction of the field begins to dominate the structure, and the result is a single domain.

Another way to achieve a single domain situation is to prepare materials having particle sizes smaller than the critical size such that the particle can no longer form domain walls. These single domain particles can also exhibit bistable magnetic behavior leading to hysteresis. While the origin of the hysteretic behavior of bulk magnetic materials is a multidomain property, it is the presence of an energy barrier between the up and down spins for nanomagnets. The energy required to switch between these two stable spin ground states, ‘up’ and ’down’ orientations is referred to as the *energy barrier* (ΔE) for inversion of their magnetization and depends on the anisotropy and the volume of the particle. The energy barrier decreases as the particle size decreases; hence hysteresis vanishes below a critical size limit since thermal energy (k_bT) overcomes the energy barrier resulting in the equal population of the spin states. At this size regime, the particle exhibits *fast relaxation* between its opposite spin orientations, a regime that is known as *superparamagnetism*. It could be assumed that the whole system behaves like having one large spin which fluctuates continuously between its spin states. Note that the temperature is another parameter since thermal energy increases with an increase in the thermal energy. The temperature at which the energy barrier is equal to the thermal energy is called the blocking temperature (T_b).

Single domain and superparamagnetic behavior is only observed as the size of a bulk magnet is decreased namely in particular. Therefore, the discovery that an isolated high-spin molecule could exhibit phenomena similar to these attracted both chemists and physicists due to its possible application in high-capacity information storage devices.[42]

The $[Mn_{12}O_{12}(O_2CCH_3)_{16}(H_2O)_4]$ (Mn12-acetate) molecule, first prepared and structurally characterized by Lis in 1980,[43] consists of a ring of eight Mn(III) ions surrorunding a $[Mn^{IV}_4O_4]$ cubane core to form a disk shaped cluster (Figure 6). The molecule received little attention up until the time its magnetic properties were investigated by Christou and Gatteschi *et al.*, in 1993.[44,45] These authors reported the temperature dependence of the magnetic susceptibility indicating ferrimagnetic behavior wherein all eight Mn(III) spins are antiferromagnetically coupled to the four Mn(IV) spins to give an $S = 10$ high spin ground state (Figure 7a). Studies also showed the presence of an appreciable axial magnetic anisotropy ($D < 0$) where origin is the Jahn-Teller distortion of Mn(III) ions combined with the anisotropic shape of the cluster, resulting in an energy barrier for magnetic reversal similar to the one in superparamagnetic particles. Magnetic hysteresis was observed in the 2 – 2.8 K range ($H_c = 1.5$ T at 2.1 K) (Figure 7b), resulting from a much longer relaxation time and a higher thermal barrier compared to a superparamagnet with small degree of anisotropy and rather than from the motion of magnetic domain walls as in a bulk ferromagnet.

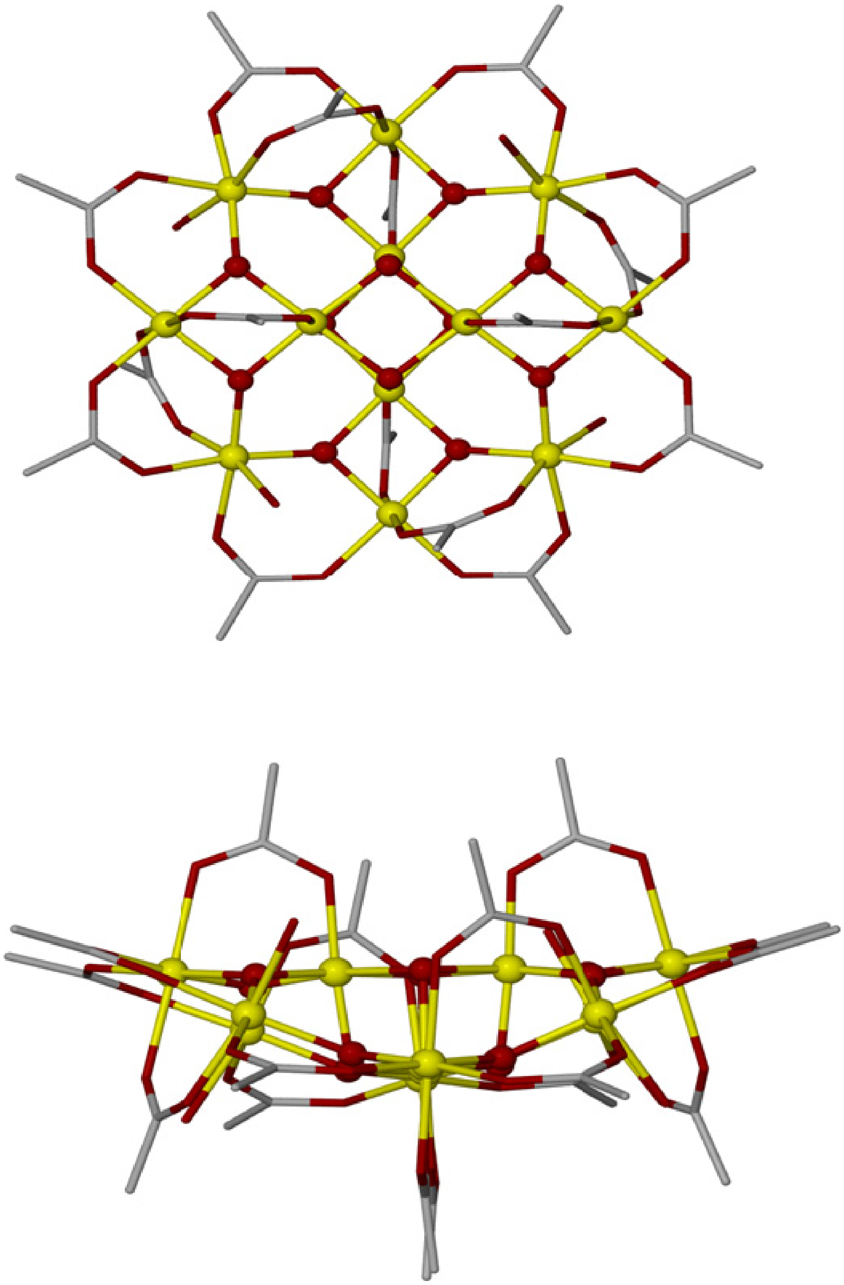

Figure 6. Top and side views of $[Mn_{12}O_{12}(O_2CCH_3)_{16}(H_2O)_4]$ (Mn_{12} acetate).[44,45] Gray atoms correspond to Mn while black ones correspond to oxygen atoms. (H atoms have been omitted for the sake of clarity.)

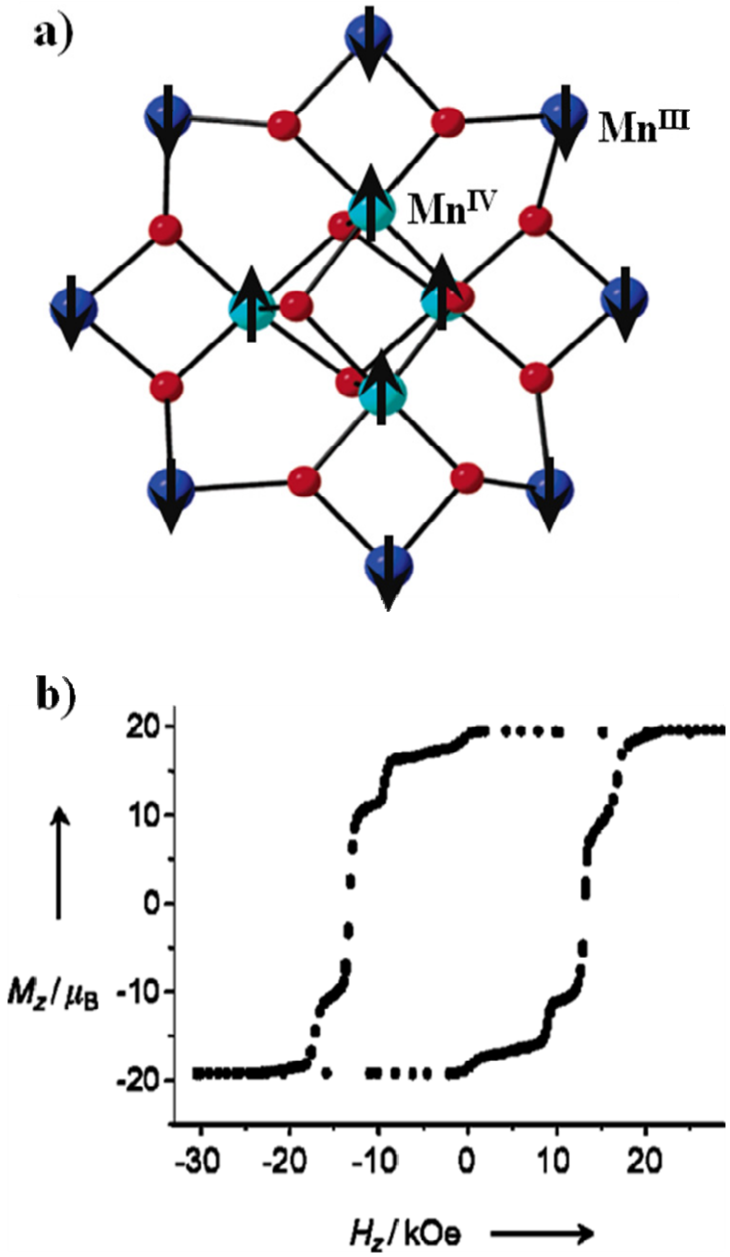

Figure 7. a) General spin scheme of the Mn12-acetate molecule illustrating the ferrimagnetic behavior wherein Mn(III) spins are down and Mn(IV) spins are up resulting in S = 10 high-spin ground state. b) Hysteresis of the molecule below T = 3 K.[45]

Since the magnetic behavior is molecular in origin, the term, single-molecule magnet (SMM), was coined for such molecules suggesting that the individual molecules that behave as tiny magnets.[46] In other words, the Mn_{12} acetate molecule exhibits a slow relaxation between its ‘up’ and ‘down’ spin states along an easy axis as a response to the applied field below a certain temperature, the so-called *blocking temperature* (T_b). For a single-molecule magnet (SMM), the energy barrier between opposite spin states is described as denoted in Figure 8;

$$\Delta E = |D| \times S^2 \text{ for integer spin,}$$

$$\Delta E = |D| \times (S^2 - 1/4) \text{ for half-integer spin system}$$

where S is the spin and D is the axial anisotropy of the cluster. The barrier for Mn_{12} acetate is calculated approximately as 62 cm^{-1}, which leads to a magnetic relaxation half-life of two months at 2 K.[47,48] Evidence supporting the possibility of storing information in a small molecule has been garnered through magnetization measurements at low temperatures. As opposed to hysteresis loops of usual bulk magnets, steps in the hysteresis curve are clearly observed, which correspond to the tunneling of the magnetization as the energy levels $\pm m_s$ on either side of the potential energy barrier achieve the same energy and come into resonance as fixed values are changed.

In a strong magnetic field, the degeneracy of the separate sets of states is removed and one spin manifold dominates. Such a spin oriented system could have potential applications as data storage media where each cluster would represent a single bit of information. To realize this technology, an increase in the total spin of the molecule or the anisotropy, thus in the energy barrier, is of crucial importance to

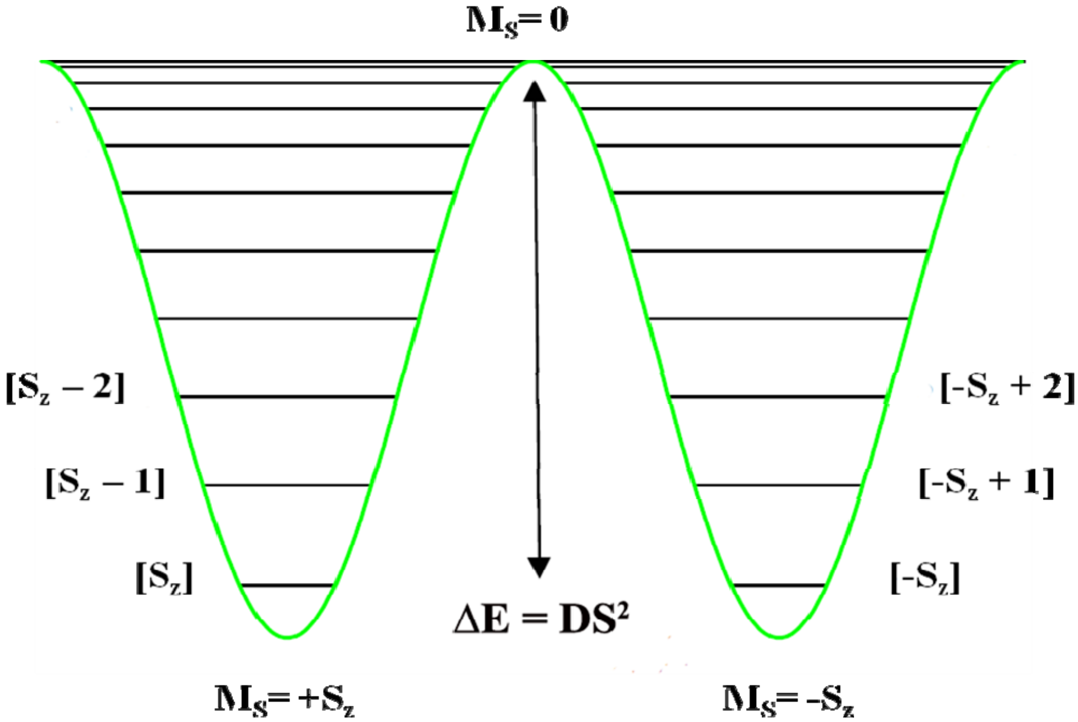

Figure 8. Energy levels for a spin state, S, with easy axis of magnetization. The +M levels are located on the left well while the –M ones are located on the right one.

improve the blocking temperature and the duration of storage. Compounds with high-spin ground states have been designed and being investigated explicitly for this purpose.[49,50] Since the total anisotropy of a cluster is the combined result of individual single ion anisotropy of the metal centers in the molecule and shape anisotropy of the cluster, different strategies have been used to obtain molecules with appreciable D values, too. One logical step is to increase the anisotropy of the individual ions. Paramagnetic metal ions, particularly those of the 4d and 5d transition series have been the primary focus due to the fact that they are subject to spin orbit coupling effects, which is a different approach to increasing anisotropy than increasing the $|-D|$ value. Successful implementation of such strategy is exemplified by the magnetic properties observed for the heptanuclear $K\{[(Me_3tacn)Mo^{III}(CN)_3]_6Mn^{II}\}(ClO_4)_3$[51] complex (Figure 9a) and the octanuclear $\{[Re^{II}(triphos)(CN)_3]_4[Mn^{II}Cl]_4\}$[52] cluster (Figure 9b), both of which are SMMs. Other examples of SMMs containing Re(IV),[53] W(V),[54-56] and Mo(III),[56] and Mo(V) [51,56] ions have also been reported.

Another common approach to prepare single molecule magnets is the modification of available SMMs in a controlled fashion resulting in compounds with higher $|-D|$ values of the same spin value. This method led to the successful preparation of Mn_{12} acetate derivatives with essentially the same $[Mn_{12}(\mu_3\text{-}O)_{12}]$ core, but with different peripheral ligands.[57-65] Small structural modifications in these complexes yielded remarkable changes in the physical and magnetic properties of these clusters such as solubility, redox and quantum tunneling properties. For example, Christou *et al.*, have observed different magnetic properties in two Mn_{12} acetate isomers that

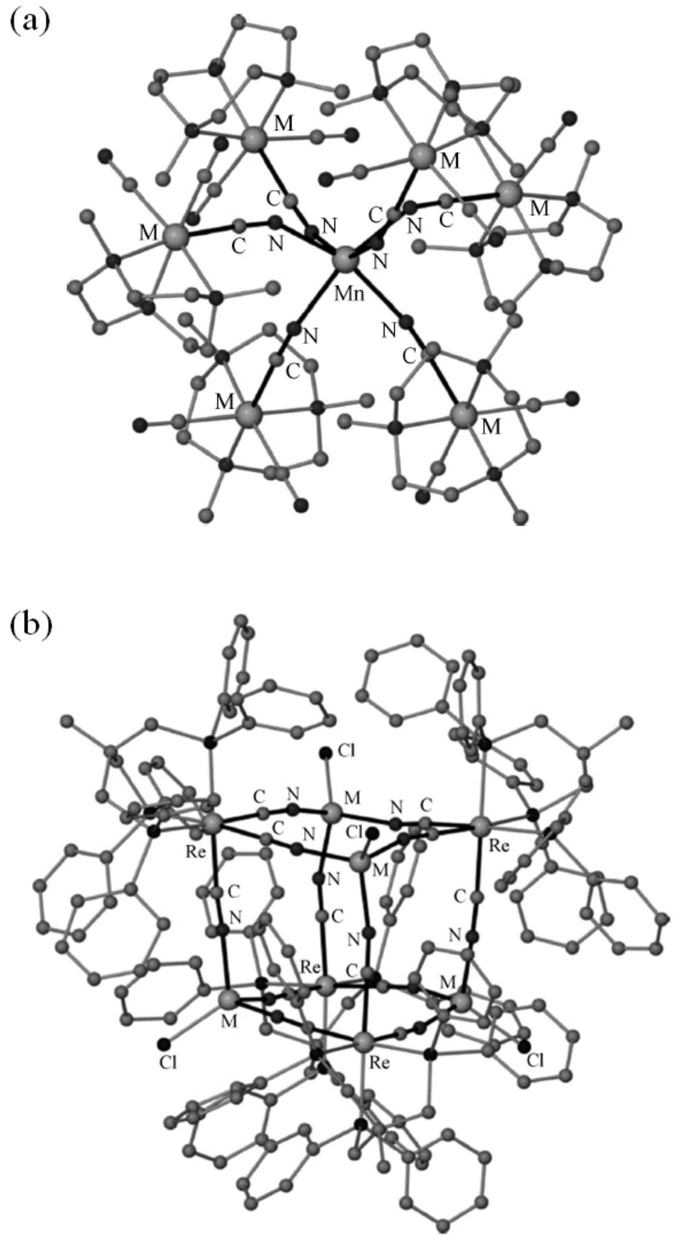

Figure 9. Molecular structures of the a) $\{[(Me_3tacn)Mo^{III}(CN)_3]_6Mn^{II}\}$ cation[51] and b) $\{[Re^{II}(triphos)(CN)_3]_4[Mn^{II}Cl]_4\}$ cluster[52].

crystallize in the same space group and differ only in the identity of one solvent molecule of crystallization at one position. The energy barrier (U*eff*) of the $[Mn_{12}O_{12}(O_2CCH_2Bu^t)_{16}(H_2O)_4]•CH_2Cl_2•CH_3NO_2$ cluster is 62 K while that of the isomorphous cluster, $[Mn_{12}O_{12}(O_2CCH_2Bu^t)_{16}(H_2O)_4]•CH_2Cl_2•CH_3CN$, is reported as 42 K.[66]

Although most of the SMMs reported to date are based on metal oxide clusters, enormous structural variability limits synthetic control over geometric and magnetic properties. Developing alternative cluster systems with promising bridging ligands for controlling S and D, or developing L•S schemes (spin-orbit coupling) for anisotropy, therefore, presents a worthwhile challenge.

CYANIDE AS A BRIDGING LIGAND

An important bridging group in the field of molecular magnetism is the cyanide ion, which has been widely used as a linker to prepare magnetic molecules and materials. The cyanide linkage provides a short (~5.0 Å), efficient pathway for superexchange between metal ions and the symmetry of the overlap pattern with metal ions in the M–C≡N–M’ unit dictates the sign of the exchange interaction.[67,68] In fact the use of cyanide in chemistry goes back to the 18th century when the German artist Diesbach accidentally discovered the mixed-valent iron cyanide material $Fe^{III}_4[Fe^{II}(CN)_6]_3•14H_2O$, which later became known as *Prussian blue*. The compound was structurally characterized by Ludi *et al.*, many years ago and was found to consist of a 3D network of Fe(II) and Fe(III) ions connected to each other through the cyanide linker in a face centered cubic arrangement with one fourth defects, could simply be prepared by reacting $K_4Fe^{II}(CN)_6$ with $Fe^{III}Cl_3$ in aqueous solution.[69,70] The compound exhibits usual paramagnetic behavior and magnetic ordering at a relatively high temperature, 5.6 K, due to electronic delocalization. This finding led to the preparation of various bimetallic '*Prussian Blue*' derivatives, which exhibit spontaneous magnetization at high temperatures (~376 K).[40]

Theoretical studies and systematic work on Prussian Blue analogues lent further insight into the superexchange behavior that dominates, namely the fact that unpaired spins in adjacent metal orbitals in the M–C≡N–M' unit and that the same symmetry (t_{2g}-t_{2g} or e_g-e_g) couples antiferromagnetically through cyanide, while those in orthogonal orbitals (t_{2g}-e_g) couple ferromagnetically for octahedral metal ions. This phenomenon is merely illustrated by analyzing the overlap of the molecular orbitals of cyanide with those of the metal ions. Figure 10 shows molecular orbitals of the cyanide ligand, in which the 1π and 5σ are HOMO while LUMO is a π type ($2\pi^*$) orbital. Magnetic orbitals of the metal center interact with cyanide orbitals of the same symmetry. t_{2g} type orbitals of both metal centers interact with either the 1π or $2\pi^*$ orbital and e_g type orbitals overlap with the 5σ orbital resulting in an antiferromagnetic coupling in both cases since they overlap with cyanide orbitals of same symmetry (Figure 11). Conversely, the e_g-t_{2g} pair results in ferromagnetic coupling due to the overlap of these orbitals with cyanide orbitals of different symmetry. The situation is corroborated by the observation of antiferromagnetic coupling for Prussian blue analogues with t_{2g}-t_{2g} electronic configurations such as $KV^{II}[Cr^{III}(CN)_6]\cdot 2H_2O$[40] ($t_{2g}^3$-$t_{2g}^3/t_{2g}^2$),

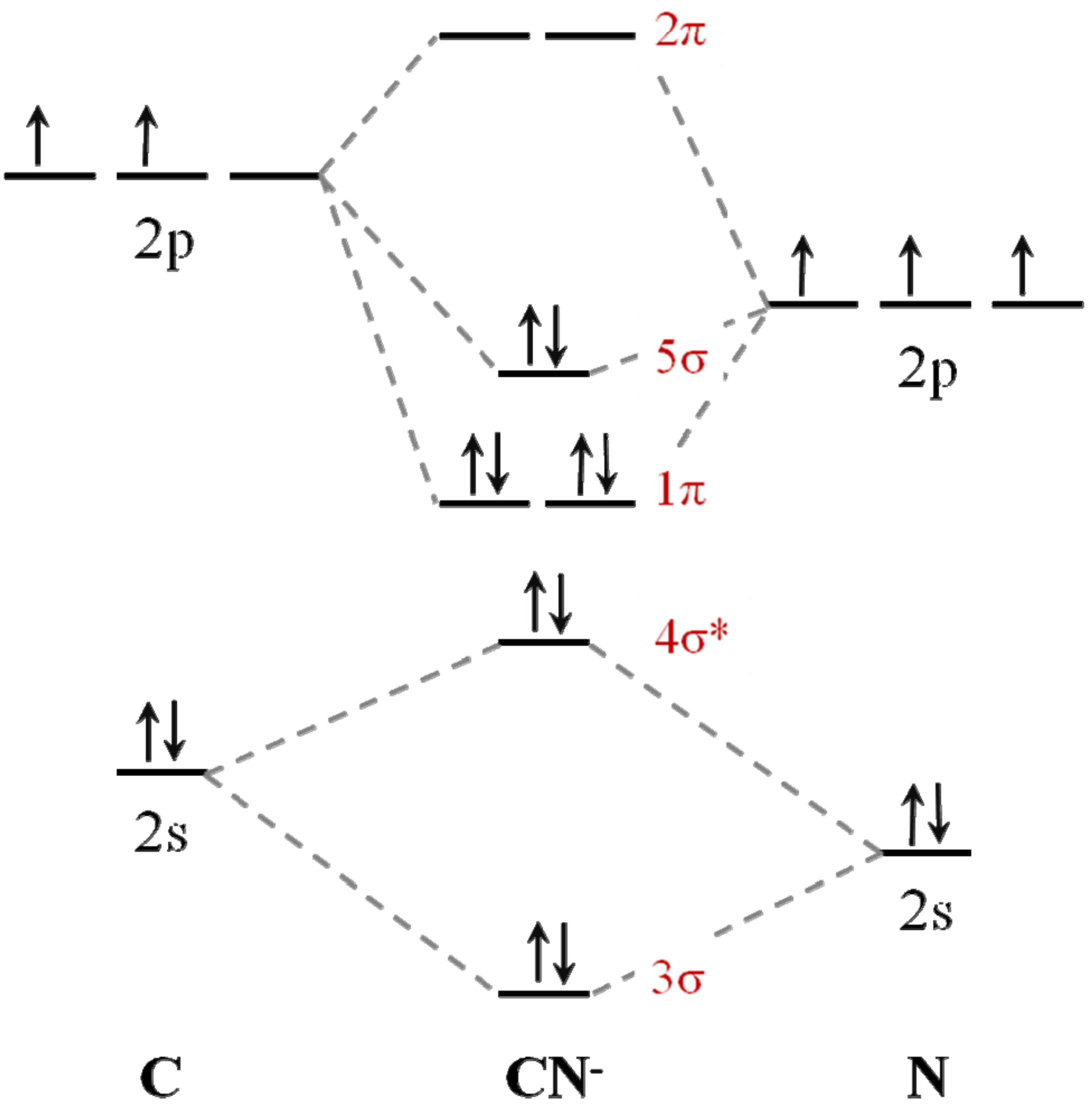

Figure 10. Molecular orbital diagram of the CN^- molecule.

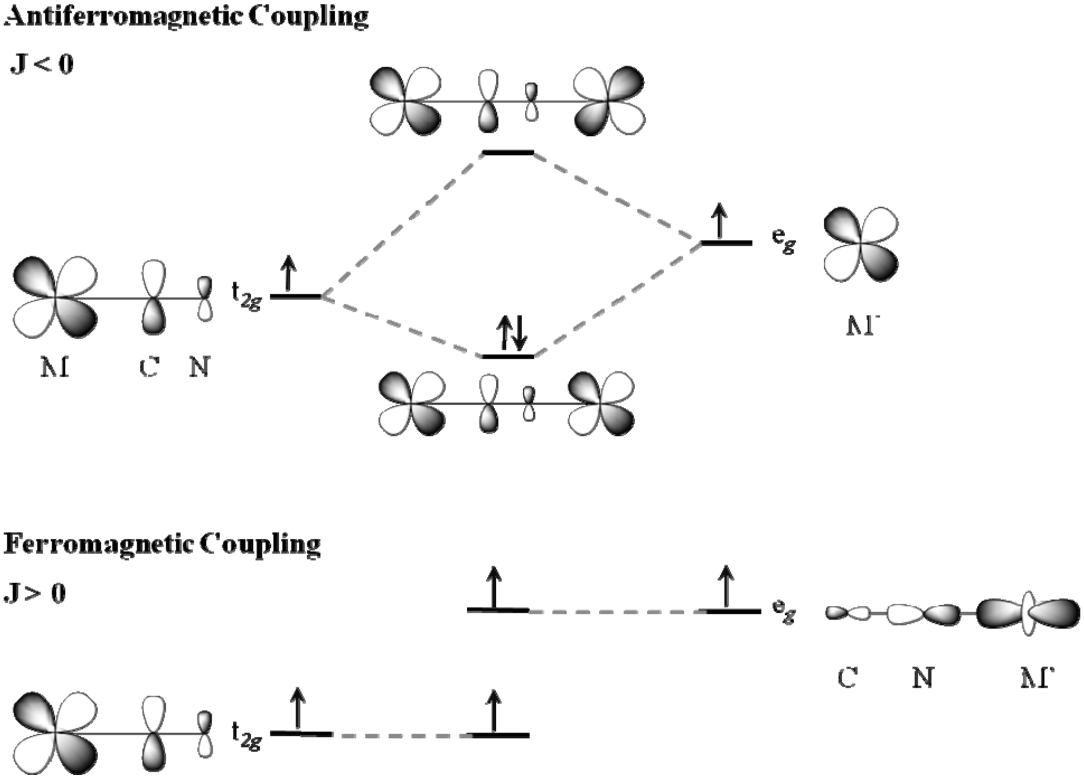

Figure 11. Diagram depicting the orbital interactions of metal ions with the bridging cyanide ligand. Top: Metal orbitals of same symmetry interact with same type of cyanide orbitals resulting in ferromagnetic coupling. Bottom: Metal orbitals of orthogonal symmetry interact with different types of cyanide orbitals resulting in antiferromagnetic coupling.

$V^{III}[Mn^{III}(CN)_6]$[71] (t_{2g}^4-t_{2g}^2), and $Cr^{III}[Mn^{III}(CN)_6]$[71] (t_{2g}^4-t_{2g}^3). On the contrary, ferromagnetic coupling was observed for analogues possessing t_{2g}-e_g electronic configurations such as $Ni^{II}_3[Fe^{III}(CN)_6]_2$[72] ($t_{2g}^5$-$e_g^2$), $Ni^{II}_3[Mn^{III}(CN)_6]\bullet 12H_2O$[73] ($t_{2g}^4$-$e_g^2$), and $Ni^{II}_3[Cr^{III}(CN)_6]_2\bullet 9H_2O$[73,74] ($t_{2g}^3$-$e_g^2$). It is also well known that antiferromagnetic interactions through cyanide π^* orbitals are typically much stronger than ferromagnetic interactions resulting in an antiferromagnetic coupling in the presence of any competitive situation as in the case of $Mn[Mn(CN)_6]$[75] (t_{2g}^4-$t_{2g}^3e_g^1$), $Co_3[Fe(CN)_6]_2$[72] (t_{2g}^5-$t_{2g}^5e_g^2$), and $Fe_4[Fe(CN)_6]_3\bullet xH_2O$[70] ($t_{2g}^5$-$t_{2g}^4e_g^2$).

In addition to cyanide clusters with octahedral metal ions, the quest for introducing metal ions with other geometries into magnetic clusters is one of the main themes in this field since orientation of magnetic orbitals is a critical factor for defining magnetic coupling.[76-78] A series of dinuclear Cu(II) complexes demonstrate this point clearly wherein Cu(II) centers with trigonal bipyramidal geometries are connected through the cyanide ligand.[79] The cluster $[Cu^{II}_2(bpy)_4(CN)](PF_6)_3$ has been found to have weak antiferromagnetic coupling ($J = -9.4\ cm^{-1}$) whereas the complex $[Cu^{II}_2(tren)_2(CN)](PF_6)_3$ exhibits stronger antiferromagnetic coupling ($J = -88\ cm^{-1}$), the main difference being attributed to the orientation of interacting orbitals with respect to each other as supported by theoretical studies (Figure 12). Several other studies performed on cyanide bridged clusters have shown that the nature as well as the magnitude of exchange coupling can be successfully correlated to the overlap of the orbitals on the metal ion and the cyanide ligand. Although the M–C≡N–M' unit is nearly linear in most cases, bending has been observed with M–C–N and C–N–M' angles far

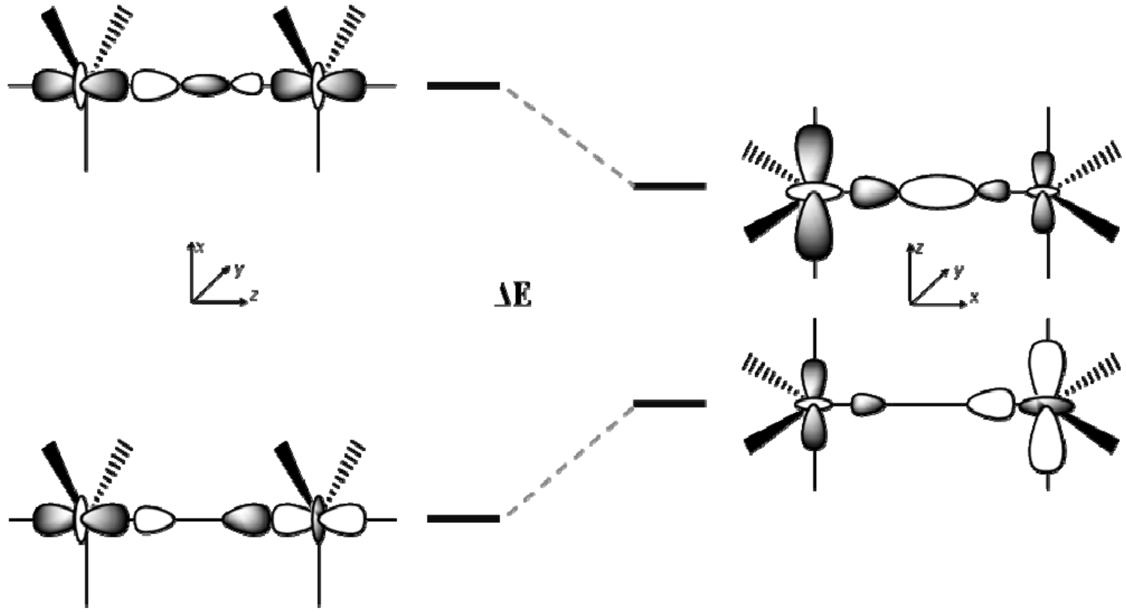

Figure 12. Diagram depicting the molecular orbitals of $[Cu^{II}_2(tren)_2(CN)](PF_6)_3$ (left side) and $[Cu^{II}_2(bpy)_4(CN)](PF_6)_3$ (right side) as a result of the interaction of d_{z^2} orbitals of Cu(II) ions with the s orbital of the CN^- bridge.[79]

from 180°. Compounds containing metal ions with different geometries and non-linear M–C≡N–M' units prompt the need for engaging in experimental work correlated with theoretical studies in order to understand their magnetic behavior, since the interaction of magnetic orbitals with cyanide orbitals do not necessarily follow the general scheme as explained in the previous section.

The major goal of the project described in this dissertation is to design and perform deliberate syntheses of families of cyanide bridged clusters in order to reveal the superexchange interactions through the cyanide ligand connected to metal ions with different geometries other than octahedral metal ions. Chapter II describes the use of an unusual five-coordinate mononuclear precursor, $Co^{II}(triphos)(CN)_2$, to prepare families of cyanide bridged complexes. Chapter III focuses on the correlation of theoretical studies with the magnetic properties of cyanide complexes, prepared by using the aforementioned building-block. Further work involves the preparation of derivatives of a cyanide bridged SMM, based on a cube. The goal is to use these pseudo-cubic clusters for further chemistry with the purpose of preparing extended materials incorporating SMMs, the results of which will be presented in Chapter IV.

CHAPTER II

PREPARATION AND CHARACTERIZATION OF A FAMILY OF CYANIDE-BRIDGED MOLECULAR SQUARES*

INTRODUCTION

Polynuclear metal complexes are widely studied due to their fascinating catalytic, photophysical, electronic, and magnetic properties.[80] Of these, molecular squares represent one of the simplest types of molecular architectures. Because of their structural simplicity, the physical properties of molecular squares can often be interpreted, provided that one is armed with a basic knowledge of the behavior of the parent mononuclear building blocks. Research in our group and in other laboratories has focused on the chemistry of magnetic molecular squares that form readily under thermodynamic control with a careful choice of ML_n precursors.[81-102] One category of molecular square or grid molecule makes use of nitrogen heterocyclic ligands as the linker groups. For example, the bptz ligand (bptz = 3,6-bis(2-pyridyl)-1,2,4,5-tetrazine) gives rise to molecular squares and pentagons when octahedral metal ions are used as building blocks.[103-105]

Another important bridging group in the chemistry of molecular squares is the

---

* Portions of this chapter were taken from Karadas, F.; Schelter, E. J.; Shatruk, M.; Prosvirin, A. V.; Bacsa, J.; Smirnow, D.; Ozarowski, A.; Krzystek, J.; Telser, J.; Dunbar, K. R. *Inorg. Chem.* **2008**, *47*, 2074-2082 with the permission of the American Chemical Society. *Copyright 2008 American Chemical Society.*

cyanide ion, which has been widely used as a linker to prepare magnetic molecules and materials since the cyanide linkage provides a short, (~5.0 Å), efficient pathway for superexchange between metal ions.[67] Metal-cyanide squares composed of paramagnetic ions can yield molecules with high spin ground states, which hold potential for the development of new molecules that exhibit interesting magnetic properties such as single molecule magnetism.

One reason for the interesting magnetic properties of molecular squares is the fact that all four metal ions of a molecular square reside approximately in the same plane which reduces the cancellation of the local magnetic anisotropies of the metal ions and results in higher global anisotropy of the cluster (Figure 13). In addition to the geometry of the entire cluster and of the linking group, another important parameter defining the magnetic behavior of the cluster is the coordination geometry at each metal center. Therefore, control and variation of coordination environment around the metal centers represents an interesting avenue to explore. Provided that there are capping ligands present that exert a dominant influence on the geometry at the metal center, it has been possible to realize a number of different clusters based on a convergent building block approach. The first reported tetranuclear cyanide bridged cluster, to our knowledge, is $[Cp_2Ti^{III}(CN)]_4$ square (Figure 13a), which was prepared by Schinnerling *et al.*, with cyclopentadienyl (Cp) capping ligands.[89] The cyclopentadienyl ligand was also used by other groups to yield Cp-capped molecular squares based on Rh_4[86] (Figure 13b) and Fe_2Cu_2[82] units (Figure 13c). Complexes of bpy (2,2'-bipyridine) and phen (1,10-

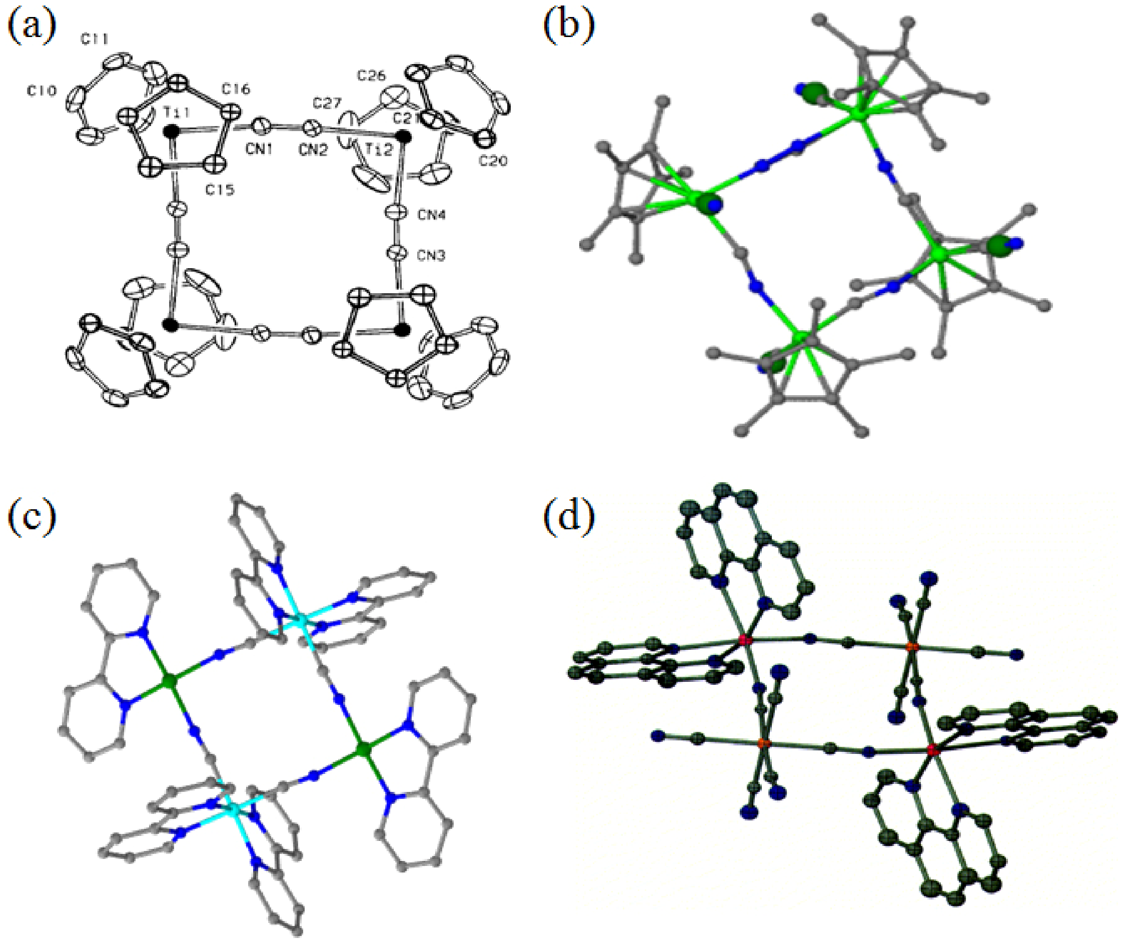

Figure 13. Structures of some of the previously reported cyanide-bridged molecular squares, a) $[Cp_2Ti^{III}(CN)]_4$,[89] b) $[Cp^*Rh(CN)_3]_2[Cp^*RhCl]_2$,[86] c) $[Fe_2Cu_2(\mu\text{-}CN)_4(bpy)_6]^{+4}$,[82] and d) $\{[Zn(phen)_2]_2[Fe(CN)_6]_2\}^{-2}$.[81]

phenanthroline) have also been used by our group[81] and by Vahrenkamp[90] and Oshio *et al.*[82,83,88]

The triphos ligand (triphos: 1,1,1-tris(diphenylphosphinomethyl)ethane) has been employed in our laboratory to prepare a family of cubic clusters based on the $[Re(triphos)(CN)_3]^-$ building block.[52,101,106] Given this success, we searched for convenient triphos containing metal-cyanide compounds that could be used to prepare a series of magnetic molecular squares. A perusal of the literature revealed that there exists a five coordinate paramagnetic complex (S = ½) with a square pyramidal metal center, $[Co^{II}(triphos)(CN)_2]$, synthesized by Rupp *et al.*,[107,108] with a C-Co-C bond angle approximately 90°. Combination of this convergent precursor with divergent metal dichlorides led to a series of cyanide-linked molecular squares.[109,110] Herein, the synthesis and characterization of a homologous series of molecular squares based on the distorted square pyramidal Co(II) complex and tetrahedral 3d metal ions will be presented.

EXPERIMENTAL

Materials

Unless otherwise stated, all experiments were performed using standard anaerobic, Schlenk techniques. $Fe_4Cl_8(THF)_6$[111] was prepared according to the published procedures. The anhydrous starting materials $MnCl_2$, $CoCl_2$, $NiCl_2$, $ZnCl_2$ were purchased from Aldrich and used as received.

Syntheses

Co(triphos)(CN)$_2$ (1). Synthesis of the title compound was reported previously.[108] A slightly different procedure was adopted in this project. Co(ClO$_4$)$_2$•6H$_2$O (0.730 g, 2 mmol) and triphos (1.248 g, 2 mmol) were dissolved in 30 mL of acetonitrile in a schlenk flask to give a green solution. The solution was allowed to stir for 2 hours. NaCN (0.196 g, 4 mmol) dissolved in H$_2$O/MeOH (1:1, 20 mL) was added dropwise to give a red solution. The solution was dried under vacuum, the residue dissolved in CH$_2$Cl$_2$ and filtered to remove NaClO$_4$. The solution was dried under vacuum to obtain a red-brown powder. Yield = 1.2 g (80%). Single crystals were grown over a three days period in a closed thin tube by slow diffusion of ether into a CH$_2$Cl$_2$ solution of Co(triphos)(CN)$_2$. Elemental analysis calc'd for Co(triphos)(CN)$_2$, CoC$_{43}$H$_{39}$N$_2$P$_3$: C 70.19, H 5.35, N 3.81; found: C 70.08, H 5.52, N 3.62. IR(Nujol), ν(C≡N), cm^{-1}: 2096, 2101.

{[Co(triphos)(CN)$_2$]$_2$[MnCl$_2$]$_2$} (2)•3CH$_2$Cl$_2$. A red solution of Co(triphos)(CN)$_2$ (100 mg, 0.136 mmol) in 30 mL of dichloromethane was slowly layered with a solution of MnCl$_2$ (34 mg, 0.270 mmol) in 30 mL of ethanol. The mixture was left to stand undisturbed for 3 – 4 days. Dark red crystals of **2** that formed after 3 days were collected by filtration and washed with copious amounts of ethanol. Yield = 42 mg (40%). Elemental analysis calc'd for **2,** Co$_2$Mn$_2$C$_{86}$H$_{78}$N$_4$Cl$_4$: C 63.37, H 3.36, N 3.44, Cl 8.70; found: C 62.52, H 3.64, N 3.20, Cl 8.27. IR(Nujol), ν(C≡N), cm^{-1}: 2119(s), 2101(w).

{[Co(triphos)(CN)$_2$]$_2$[FeCl$_2$]$_2$} (3)•3CH$_2$Cl$_2$. A red solution of Co(triphos)(CN)$_2$ (200 mg, 0.272 mmol) in 30 mL of dichloromethane was slowly layered with a solution of

$Fe_4Cl_8(THF)_6$ (130 mg, 0.139 mmol) in 30 mL of ethanol under N_2. The mixture was left to stand undisturbed for 2 – 3 days. Blue-red crystals of **3** that formed over the course of 3 days were collected by filtration and washed with copious amounts of ethanol. Yield = 38 mg (36%). Elemental analysis calcd. for **3**, $Co_2Fe_2C_{86}H_{78}N_4Cl_4$: C 63.30, H 4.82, N 3.43, Cl 8.69; found: C 62.82, H 4.62, N 3.28, Cl 8.33. IR (Nujol), cm^{-1}: 2120(s), 2101(w).

$\{[Co(triphos)(CN)_2]_2[CoCl_2]_2\}$ (4)•3CH_2Cl_2. A red solution of $Co(triphos)(CN)_2$ (100 mg, 0.136 mmol) in 30 mL of dichloromethane was slowly layered with a solution of $CoCl_2$ (34 mg, 0.270 mmol) in 30 mL of ethanol. The mixture was left to stand undisturbed for 3 – 4 days. Dark green crystals of **4** that formed after 3 days were collected by filtration and washed with copious amounts of ethanol. Yield = 65 mg (62%). Elemental analysis calc'd for **4**, $Co_4C_{86}H_{78}N_4Cl_4$: C 63.06, H 4.80, N 3.42, Cl 8.66; found: C 62.81, H 4.53, N 3.24, Cl 8.20. IR (Nujol), cm^{-1}: 2132(s), 2101(w).

$\{[Co(triphos)(CN)_2]_2[NiCl_2]_2\}$ (5)•4CH_2Cl_2. A red solution of $Co(triphos)(CN)_2$ (100 mg, 0.136 mmol) in 30 mL of dichloromethane was slowly layered with a solution of $NiCl_2$ (34 mg, 0.270 mmol) in 30 mL of ethanol. The mixture was left to stand undisturbed for 3 – 4 days. Dark green crystals of **5** that formed after 3 days were collected by filtration and washed with copious amounts of ethanol. Yield = 54 mg (52%). Elemental analysis calc'd for **5**, $Co_2Ni_2C_{86}H_{78}N_4Cl_4$: C 63.10, H 4.80, N 3.42, Cl 8.66; found: C 62.77, H 4.60, N 3.06, Cl 8.12. IR (Nujol), cm^{-1}: 2133(s), 2102(w).

$\{[Co(triphos)(CN)_2]_2[ZnCl_2]_2\}$ (6)•4CH_2Cl_2. A red solution of $Co(triphos)(CN)_2$ (100 mg, 0.136 mmol) in 30 mL of dichloromethane was slowly layered with a solution of

$ZnCl_2$ (34 mg, 0.270 mmol) in 30 mL of ethanol. The mixture was left to stand undisturbed for 3 – 4 days. Red-brown crystals of **6** that formed after 3 days were collected by filtration and washed with copious amounts of ethanol. Yield = 59 mg (56%). Elemental analysis calc'd for **6**, $Co_2Zn_2C_{86}H_{78}N_4Cl_4$: C 62.57, H 4.76, N 3.39, Cl 8.59; found: C 62.28, H 4.68, N 3.19, Cl 8.31. IR (Nujol), cm^{-1}: 2140(s), 2104(w).

Single Crystal X-ray Diffraction Studies

Single crystals of compounds **2-6** were grown over a one week period in a sealed 3 mm diameter thin tube by slow diffusion of an EtOH solution of $M^{II}Cl_2$ into a CH_2Cl_2 solution of Co(triphos)$(CN)_2$. The crystals were suspended in polybutene oil and mounted on a cryoloop and placed in a cold N_2 stream. The data were measured at 110(2) K on a Siemens SMART CCD diffractometer with graphite monochromated Mo-K_α (λ_α = 0.71073 Å) radiation. Intensity data were collected with 0.3° ω-scans at a detector distance of 5 cm, and integrated with Bruker SAINT[112] software package. The intensities were corrected for beam inhomogeneity, crystal absorption with the program SADABS.[113] Symmetry related and redundant reflections were averaged with the program XPREP. Solution and refinement of the crystal structures was carried out using the SHELX[114] suite of programs and X-SEED.[115] The option SQUEEZE in PLATON[116] was used to eliminate the contribution of the electron density in the solvent region from the intensity data. The use of SQUEEZE produced better refinement results and the solvent-free model was employed for the final refinement. Systematic absences indicated that the crystals belong to the space group *P*21/*n* (No. 14). The final refinement was performed with anisotropic thermal parameters for all non-hydrogen atoms. A summary of pertinent information relating to unit cell parameters, data collection, and refinements are provided in Tables 1-3.

High-frequency and High-field EPR (HFEPR)

All of the molecular square complexes (**2-6**) were investigated by HFEPR methods using either the Mm and sub-mm Wave Facility,[117] or the EMR Facility[118] at NHMFL. The former experimental setup employs tunable frequencies in the 150 – 700 GHz range generated by backward wave oscillators, and the resistive “Keck” magnet enabling 0 – 25 T field sweeps. The latter spectrometer is based on a 17 T superconducting magnet and uses a 13 ± 1 GHz base frequency source (Virginia Diodes Inc., Charlottesville, VA) followed by an amplifier and a series of frequency multipliers, thus providing EPR spectra at intermediate frequencies, e.g., V-band (48 – 56 GHz), as well as at high frequencies. Detection was effected with an InSb hot-electron bolometer (QMC Ltd., Cardiff, UK). Modulation for detection purposes was provided alternatively by chopping the sub-THz wave beam (“optical modulation”) or by modulating the magnetic field. A Stanford Research Systems SR830 lock-in amplifier converted the modulated signal to DC voltage. Typically, 30 – 50 mg of polycrystalline sample was used in either experiment. Additional X-band measurements were performed on compound **6** using a commercial Bruker E680X spectrometer.

Table 1. Crystallographic data and structural refinement parameters for **(2)**•$3CH_2Cl_2$ and **(3)**•$3CH_2Cl_2$.

	(2)•$3CH_2Cl_2$	**(3)**•$3CH_2Cl_2$
Formula	$Co_2Mn_2C_{86}H_{78}P_6N_4Cl_4$	$Co_2Fe_2C_{86}H_{78}P_6N_4Cl_4$
Space group	$P2_1/n$ (No. 14)	$P2_1/n$ (No. 14)
Unit cell	a = 14.079(3) Å	a = 13.998(3) Å
	b = 16.444(4) Å	b = 16.412(4) Å
	c = 19.995(5) Å	c = 19.929(5) Å
	β = 90.129(4) °	β = 90.166(7) °
Unit cell volume, V	4629(8) Å^3	4578.2(19) Å^3
Z	2	2
Density, ρ_{calc}	1.480 g/cm^3	1.436 g/cm^3
Abs. coeff., μ	1.116 mm^{-1}	1.109 mm^{-1}
Crystal color and habit	dark-red plate	Blue plate
Crystal size	0.30×0.30×0.03 mm	0.39×0.27×0.21 mm
Temperature	110(2) K	110(2) K
Radiation, λ	Mo-Kα, 0.71073 Å	Mo-Kα, 0.71073 Å
Min. and max. θ	2.48 to 27.48°	1.02 to 27.48°
Reflections collected	45463	21456
	[R_{int} = 0.1465][a]	[R_{int} = 0.0688]
Independent reflections	10446	9596
Data/parameters/restraints	10446 / 502 / 12	9596 / 565 / 70
R [$F_o > 4\sigma(F_o)$]	R_1 = 0.0697[b]	R_1 = 0.0721
	wR_2 = 0.1566[c]	wR_2 = 0.1778

[a] $R_{int} = \Sigma|F_o^2 - F_o^2(\mathrm{mean})| / \Sigma[F_o^2]$

[b] $R_1 = \Sigma||F_o| - |F_c|| / \Sigma|F_o|$

[c] $wR_2 = \{\Sigma[w(F_o^2 - F_c^2)^2] / \Sigma[w(F_o^2)^2]\}^{1/2}$, $w = 1 / [\sigma^2(F_o^2) + (aP)^2 + bP]$, $P = [2F_c^2 + \mathrm{Max}(F_o^2,0)]/3$. For **2**, a = 0.0688, b = 0; for **3**, a = 0.0835, b = 0.

Table 2. Crystallographic data and structural refinement parameters for **(4)**•$3CH_2Cl_2$ and **(5)**•$4CH_2Cl_2$.

	(4)•$3CH_2Cl_2$	**(5)**•$4CH_2Cl_2$
Formula	$Co_4C_{86}H_{78}P_6N_4Cl_4$	$Co_2Ni_2C_{86}H_{78}P_6N_4Cl_4$
Space group	$P2_1/n$ (No. 14)	$P2_1/n$ (No. 14)
Unit cell	a = 14.193(5) Å	a = 14.085(3) Å
	b = 16.481(6) Å	b = 16.365(3) Å
	c = 19.750(7) Å	c = 19.875(4) Å
	β = 90.366(7) °	β = 90.10(3) °
Unit cell volume, V	4620(3) $Å^3$	4581.5(16) $Å^3$
Z	2	2
Density, ρ_{calc}	1.489 g/cm^3	1.254 g/cm^3
Abs. coeff., μ	1.204 mm^{-1}	1.024 mm^{-1}
Crystal color and habit	Green-blue plate	Blue plate
Crystal size	0.32×0.22×0.19 mm	0.34×0.32×0.26 mm
Temperature	100(2) K	110(2) K
Radiation, λ	Mo-Kα, 0.71073 Å	Mo-Kα, 0.71073 Å
Min. and max. θ	2.06 to 28.41°	2.17 to 27.62°
Reflections collected	38562 [R_{int} = 0.0656][a]	27965 [R_{int} = 0.0654]
Independent reflections	10853	10853
Data/parameters/restraints	10853 / 563 / 8	9799 / 496 / 12
R [$F_o > 4\sigma(F_o)$]	R_1 = 0.0653[b]	R_1 = 0.0554
	wR_2 = 0.1502[c]	wR_2 = 0.1368

[a] $R_{int} = \Sigma \left| F_o^2 - F_o^2(\text{mean}) \right| / \Sigma[F_o^2]$

[b] $R_1 = \Sigma \left\| F_o \right| - \left| F_c \right\| / \Sigma \left| F_o \right|$

[c] $wR_2 = \{\Sigma[w(F_o^2 - F_c^2)^2] / \Sigma[w(F_o^2)^2]\}^{1/2}$, $w = 1 / [\sigma^2(F_o^2) + (aP)^2 + bP]$, $P = [2F_c^2 + \text{Max}(F_o^2,0)]/3$. For **4**, a = 0.0617, b = 4.2708; for **5**, a = 0.0684, b = 0.

Table 3. Crystallographic data and structural refinement parameters for **(6)**•4CH_2Cl_2.

	(6)•4CH_2Cl_2
Formula	$Co_2Zn_2C_{86}H_{78}P_6N_4Cl_4$
Space group	$P2_1/n$ (No. 14)
Unit cell	a = 13.930(2) Å
	b = 49.141(8) Å
	c = 19.890(3) Å
	β = 90.004(3) °
Unit cell volume, V	13616(4) $Å^3$
Z	6
Density, ρ_{calc}	1.276 g/cm^3
Abs. coeff., μ	1.147 mm^{-1}
Crystal color and habit	Brown plate
Crystal size	0.27×0.18×0.11 mm
Temperature	100(2) K
Radiation, λ	Mo-Kα, 0.71073 Å
Min. and max. θ	1.10 to 28.35°
Reflections collected	139897 [R_{int} = 0.1004][a]
Independent reflections	10853
Data/parameters/restraints	33158 / 1408 / 0
R [$F_o > 4\sigma(F_o)$]	R_1 = 0.1015[b]
	wR_2 = 0.2592[c]

[a] $R_{int} = \Sigma \left| F_o^2 - F_o^2(\text{mean}) \right| / \Sigma[F_o^2]$

[b] $R_1 = \Sigma \left\| F_o \right| - \left| F_c \right\| / \Sigma \left| F_o \right|$

[c] $wR_2 = \{\Sigma[w(F_o^2 - F_c^2)^2] / \Sigma[w(F_o^2)^2]\}^{1/2}$, $w = 1 / [\sigma^2(F_o^2) + (aP)^2 + bP]$, $P = [2F_c^2 + \text{Max}(F_o^2,0)]/3$ where a = 0.1206, b = 17.3388.

RESULTS AND DISCUSSION

Syntheses

The Co(II) center exhibits a square pyramidal geometry which is typical for most phosphine complexes of Co(II), including those with chelating and monodentate phosphine ligands.[119] The presence of a capping triphos ligand and two cyanide ligands positioned at a C–Co–C angle of ~87° renders this compound a convenient precursor for the assembly of molecular squares (Figure 14). The C–Co–C angle is smaller than C–Co–C angles in a homoleptic square pyramidal anion $[Co(CN)_5]^{3-}$ (88.6 – 99.6°).[120] This decrease is attributed to the steric effect of the bulky triphos ligand in the $Co(triphos)(CN)_2$ complex.

A claret solution of $Co(triphos)(CN)_2$ in dichloromethane was reacted with solutions of MCl_2 (M= Mn, Co, Ni, and Zn) or $Fe_4Cl_8(THF)_6$ in ethanol to form the title compounds. In the case of compound **3**, $Fe_4Cl_8(THF)_6$ was used instead of $FeCl_2$, since the THF solvate is a purer form of ferrous chloride and thus is an excellent source of Fe(II) for substitution chemistry. The compounds are stable both in solution and solid phase, except for **3**, which is air sensitive. The complexes are nearly insoluble in common solvents such as CH_2Cl_2, MeOH, hexane and MeCN. They are soluble only in DMF and slightly soluble in propylene carbonate.

Single Crystal X-ray Structures

Single crystals of the products were prepared by slow diffusion of an EtOH solution of MCl_2 into a CH_2Cl_2 solution of $Co(triphos)(CN)_2$. The molecular squares are

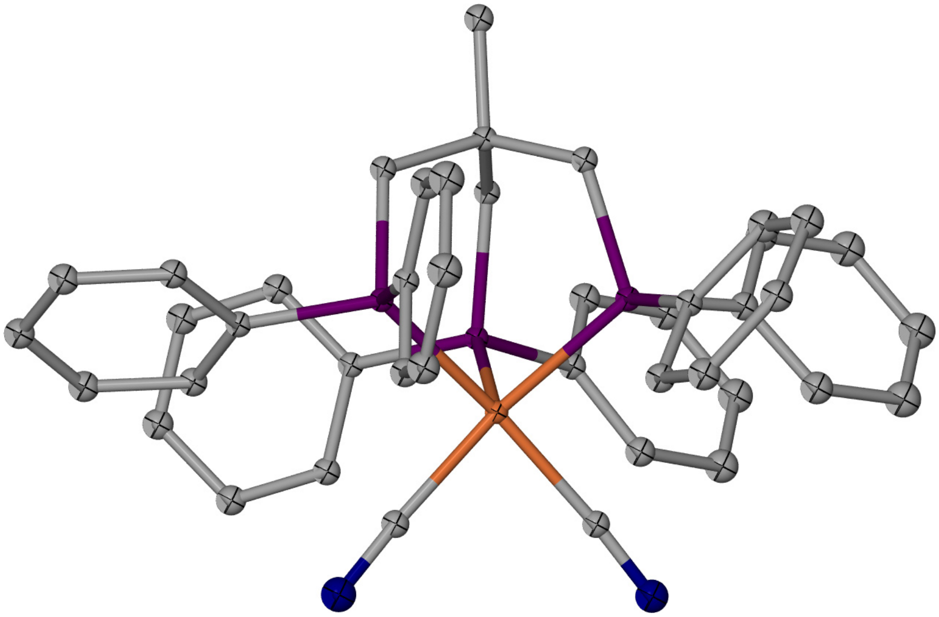

Figure 14. Structure of Co(triphos)(CN)$_2$ (**1**). Thermal ellipsoids are projected at the 50% probability level.

composed of alternating Co(triphos)$(CN)_2$ and MCl_2 units (Figure 15). The molecule crystallizes on an inversion center, so that the asymmetric unit is composed of one half of the square. The Co(II) sites remain pentacoordinate, with only slight changes to the metal-ligand coordination sphere as compared to the starting material. The C–Co–C angle is similar in all of the structures (~85^{o}, Table 4-8). The coordination geometry around the M(II) sites is distorted tetrahedral and consists of two N atoms of the cyanide groups and two Cl^{-} ions. The distorted tetrahedral environment of the M(II) sites is primarily related to the steric demand of the triphos ligand. The N–M–N angles vary between $101.5(2)^{o}$ and $105.2(1)^{o}$. The combination of square pyramidal and tetrahedral metal centers results in a more distorted molecular square as compared to those based on octahedrally coordinated metal ions. For example, the previously reported $Fe^{III}Ni^{II}$ square, $[Tp^{*}Fe^{III}(CN)_3Ni^{II}(DMF)_4]_2[OTf]_2$[91] exhibits $C–Fe^{III}–C$ and $N–Ni^{II}–N$ angles of $86.8(2)^{o}$ and $92.3(1)^{o}$, respectively and the $Fe^{II}Co^{II}$ square, $[Fe^{II}Co^{II}(\mu\text{-}CN)(bpy)_8](PF_6)_4$[82] has $C–Fe^{II}–C$ and $N–Co^{II}–N$ angles equal to $91.9(1)^{o}$ and $91.2(2)^{o}$, respectively. Bond distances and angles for compounds **2-6** are provided in Tables 4-8.

Space-filling diagrams of the squares clearly indicate that the chloride atoms attached to M(II) are still readily accessible for further substitution reactions with cyanide precursors, although the bulk of triphos ligand distorts the structure (Figure 16).

In all of the square complexes (**2-6**), the crystal structures indicate that there are no obvious pathways for intermolecular magnetic communication among metal centers as there is neither H-bonding nor any apparent strong dipolar interaction since the

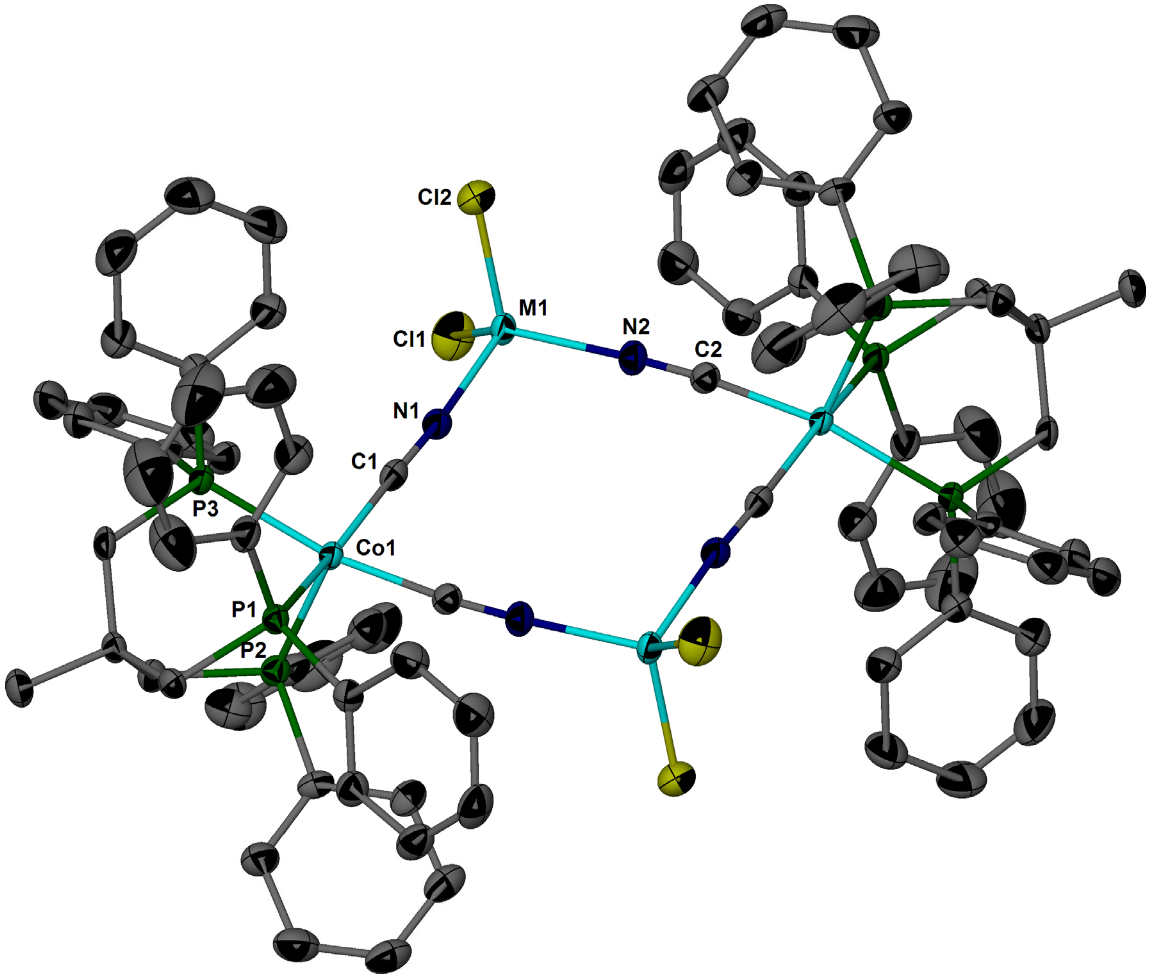

Figure 15. Structure of compounds **2–6** (H atoms are omitted for the sake of clarity).

shortest intermolecular M···M distance in e.g., **4** is a Co···Co distance of 7.950 Å (Figure 17).

Infrared Spectroscopy

Infrared spectroscopy performed on polycrystalline samples of the products reveals two $\nu_{C\equiv N}$ stretches, located at 2119(s) and 2101 cm^{-1} in compound **2**, 2120(s) and 2101(w) cm^{-1} in **3**, 2132(s) and 2101(w) cm^{-1} in **4**, 2133(s) and 2100(w) cm^{-1} in **5**, and 2140(s) and 2104(w) cm^{-1} in **6**. There is a positive shift of 23, 24, 36, 37, and 44 cm^{-1}, respectively, as compared to the starting material, for which the $\nu_{C\equiv N}$ stretches are located at 2096(s) and 2101(w) cm^{-1}. A shift to higher frequencies is a clear indication of the formation of a bridging cyanide mode.[107] Most of the reported molecular squares exhibit similar $\nu_{C\equiv N}$ modes, with either one or two bands depending on the symmetry of the molecule. For example, the Fe^{II}Cu^{I} square, $[CpFe(CO)(\mu\text{-}CN)_2Cu(PMePh_2)_2]_2$[8] exhibits two $\nu_{C\equiv N}$ stretches, located at 2110 and 2095 cm^{-1}.

Magnetic Studies

DC magnetic susceptibility measurements for the molecular square compounds and the mononuclear building block Co(triphos)(CN)$_2$ were performed on freshly prepared crushed polycrystalline samples in the temperature range of 2 – 300 K at an applied magnetic field of 1 kOe.

Table 4. Selected bond distances (Å) and angles (^{o}) for compound **2**.

Atoms	Distance (Å)	Atoms	Angle(^{o})
Co1 – C1	1.875(5)	C1 – Co1 – C2	84.87(17)
Co1 – C2	1.894(5)	C1 – Co1 – P1	160.52(15)
Co1 – P1	2.215(2)	C2 – Co1 – P1	89.41(14)
Co1 – P2	2.2875(19)	C1 – Co1 – P3	91.65(13)
Co1 – P3	2.239(2)	C2 – Co1 – P3	167.75(15)
M1 – N1	2.083(5)	P1 – Co1 – P3	90.02(5)
M1 – N2	2.077(4)	C1 – Co1 – P2	107.77(16)
M1 – Cl1	2.308(2)	C2 – Co1 – P2	101.76(16)
M1 – Cl2	2.336(2)	P1 – Co1 – P2	91.62(8)
		P3 – Co1 – P2	90.48(7)
		N2 – M1 – N1	103.16(14)
		N2 – M1 – Cl1	116.22(12)
		N1 – M1 – Cl1	104.72(12)
		N2 – M1 – Cl2	107.52(14)
		N1 – M1 – Cl2	106.49(13)
		Cl1 – M1 – Cl2	117.29(6)
		C1 – N1 – M1	172.6(4)
		N1 – C1 – Co1	176.0(4)
		C2 – N2 – M1	173.2(4)
		N2 – C2 – Co1	175.4(4)

Table 5. Selected bond distances (Å) and angles (^{o}) for compound **3**.

Atoms	**Distance (Å)**	**Atoms**	**Angle(^{o})**
Co1 – C1	1.894(5)	C1 – Co1 – C2	85.18(19)
Co1 – C2	1.894(5)	C1 – Co1 – P1	161.24(17)
Co1 – P1	2.2281(15)	C2 – Co1 – P1	89.48(14)
Co1 – P2	2.2436(16)	C1 – Co1 – P3	91.46(15)
Co1 – P3	2.2855(17)	C2 – Co1 – P3	168.00(17)
M1 – N1	2.028(4)	P1 – Co1 – P3	90.07(6)
M1 – N2	2.029(4)	C1 – Co1 – P2	107.73(17)
M1 – Cl1	2.2597(18)	C2 – Co1 – P2	101.97(16)
M1 – Cl2	2.2691(18)	P1 – Co1 – P2	90.96(6)
		P3 – Co1 – P2	90.03(6)
		N2 – M1 – N1	101.49(16)
		N2 – M1 – Cl1	115.07(13)
		N1 – M1 – Cl1	104.56(14)
		N2 – M1 – Cl2	107.02(13)
		N1 – M1 – Cl2	107.13(14)
		Cl1 – M1 – Cl2	119.70(6)
		C1 – N1 – M1	173.5(5)
		N1 – C1 – Co1	173.8(5)
		C2 – N2 – M1	173.9(4)
		N2 – C2 – Co1	175.8(4)

Table 6. Selected bond distances (Å) and angles (^{o}) for compound **4**.

Atoms	**Distance (Å)**	**Atoms**	**Angle(^{o})**
Co1 – C1	1.887(4)	C1 – Co1 – C2	84.98(15)
Co1 – C2	1.886(4)	C1 – Co1 – P1	160.89(12)
Co1 – P1	2.2173(13)	C2 – Co1 – P1	89.56(12)
Co1 – P2	2.2955(12)	C1 – Co1 – P3	91.81(11)
Co1 – P3	2.2368(12)	C2 – Co1 – P3	167.94(12)
M1 – N1	1.983(3)	P1 – Co1 – P3	89.74(4)
M1 – N2	1.989(4)	C1 – Co1 – P2	107.82(12)
M1 – Cl1	2.2346(14)	C2 – Co1 – P2	102.11(12)
M1 – Cl2	2.2569(13)	P1 – Co1 – P2	91.23(5)
		P3 – Co1 – P2	89.95(4)
		N2 – M1 – N1	105.15(13)
		N2 – M1 – Cl1	115.51(10)
		N1 – M1 – Cl1	106.21(10)
		N2 – M1 – Cl2	107.13(10)
		N1 – M1 – Cl2	106.39(10)
		Cl1 – M1 – Cl2	115.58(5)
		C1 – N1 – M1	175.3(3)
		N1 – C1 – Co1	173.0(3)
		C2 – N2 – M1	173.0(3)
		N2 – C2 – Co1	175.2(4)

Table 7. Selected bond distances (Å) and angles (^{o}) for compound **5**.

Atoms	**Distance (Å)**	**Atoms**	**Angle(^{o})**
Co1 – C1	1.883(4)	C1 – Co1 – C2	84.47(14)
Co1 – C2	1.885(4)	C1 – Co1 – P1	157.88(12)
Co1 – P1	2.3156(13)	C2 – Co1 – P1	89.44(11)
Co1 – P2	2.2424(11)	C1 – Co1 – P3	91.47(10)
Co1 – P3	2.2115(11)	C2 – Co1 – P3	166.96(13)
M1 – N1	1.981(3)	P1 – Co1 – P3	89.72(4)
M1 – N2	1.992(3)	C1 – Co1 – P2	110.26(12)
M1 – Cl1	2.2343(13)	C2 – Co1 – P2	102.91(12)
M1 – Cl2	2.2407(14)	P1 – Co1 – P2	91.83(4)
		P3 – Co1 – P2	90.12(4)
		N2 – M1 – N1	104.39(12)
		N2 – M1 – Cl1	115.24(10)
		N1 – M1 – Cl1	105.41(10)
		N2 – M1 – Cl2	107.36(10)
		N1 – M1 – Cl2	107.28(10)
		Cl1 – M1 – Cl2	116.24(5)
		C1 – N1 – M1	175.2(3)
		N1 – C1 – Co1	174.6(3)
		C2 – N2 – M1	173.8(3)
		N2 – C2 – Co1	175.7(3)

Table 8. Selected bond distances (Å) and angles (°) for compound **6**.

Atoms	Distance (Å)	Atoms	Angle(°)
Co1 – C1	1.887(4)	C1 – Co1 – C2	84.98(15)
Co1 – C2	1.886(4)	C1 – Co1 – P1	160.89(12)
Co1 – P1	2.2173(13)	C2 – Co1 – P1	89.56(12)
Co1 – P2	2.2955(12)	C1 – Co1 – P3	91.81(11)
Co1 – P3	2.2368(12)	C2 – Co1 – P3	167.94(12)
M1 – N1	1.983(3)	P1 – Co1 – P3	89.74(4)
M1 – N2	1.989(4)	C1 – Co1 – P2	107.82(12)
M1 – Cl1	2.2346(14)	C2 – Co1 – P2	102.11(12)
M1 – Cl2	2.2569(13)	P1 – Co1 – P2	91.23(5)
		P3 – Co1 – P2	89.95(4)
		N2 – M1 – N1	105.15(13)
		N2 – M1 – Cl1	115.51(10)
		N1 – M1 – Cl1	106.21(10)
		N2 – M1 – Cl2	107.13(10)
		N1 – M1 – Cl2	106.39(10)
		Cl1 – M1 – Cl2	115.58(5)
		C1 – N1 – M1	175.3(3)
		N1 – C1 – Co1	173.0(3)
		C2 – N2 – M1	173.0(3)
		N2 – C2 – Co1	175.2(4)

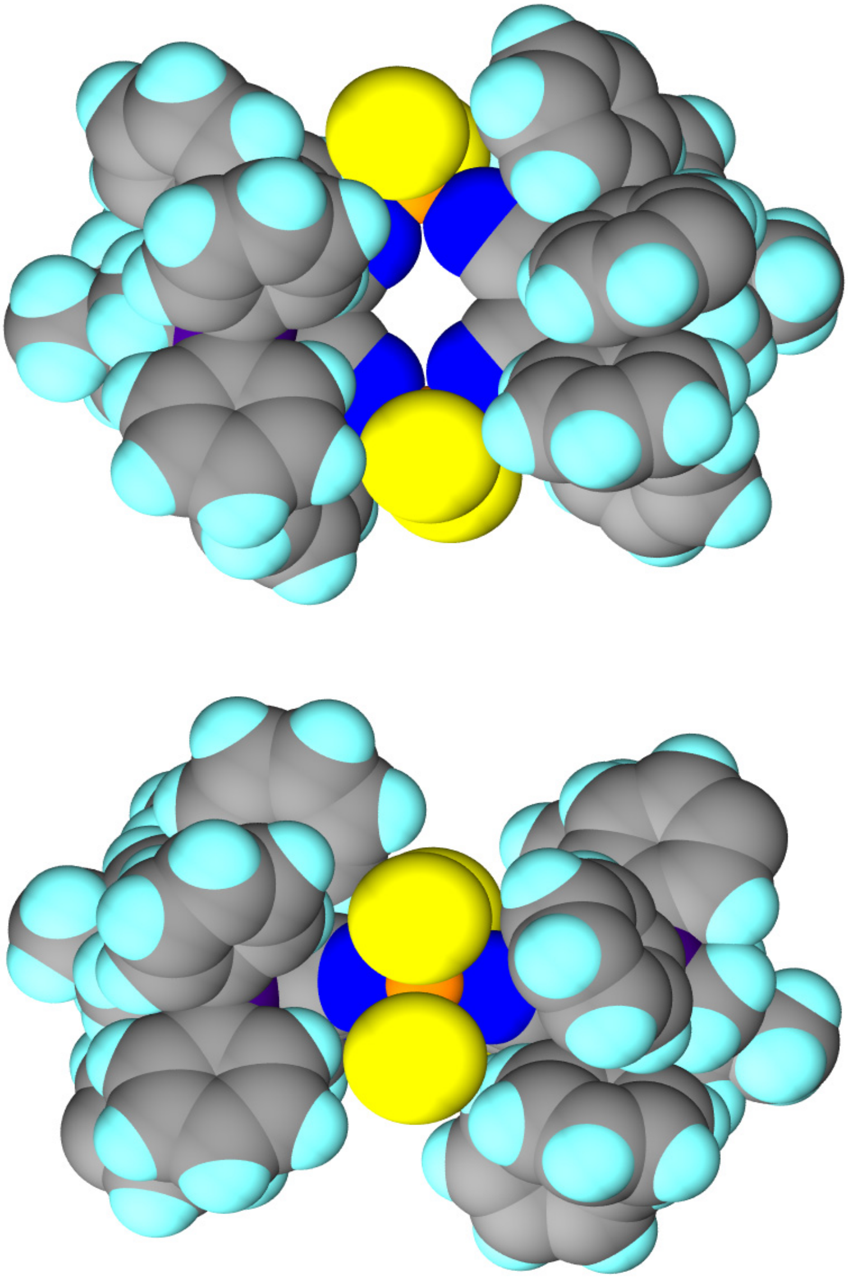

Figure 16. Space-filling diagrams of compound **2** depicted from the top and the side.

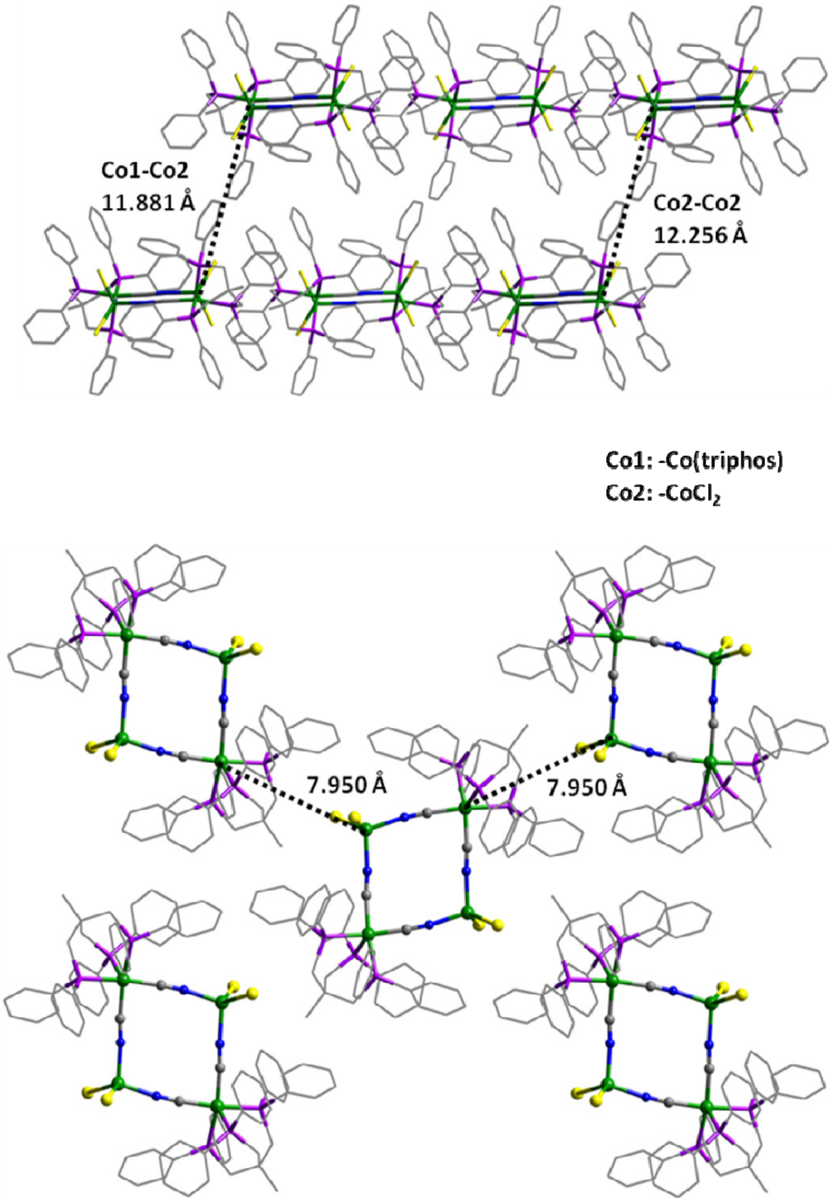

Figure 17. Packing diagrams for compound **4**. The intermolecular Co···Co distances are labeled in both figures. The top figure lists the Co···Co distances between the layers while the bottom figure indicates the distances within the layer.

Co(triphos)(CN)$_2$ (1). For the mononuclear starting material (**1**), the value of χT at 300 K is 0.41 emu·mol^{-1}·K and remains constant over the entire temperature range, typical of a simple paramagnet with an $S = 1/2$ spin ground state and $g = 2.12$[108] (Figure 18). This is comparable to the magnetic properties of other square-pyramidal Co(II) phosphine complexes such as Co(PPh$_2$Et)$_3$(CN)$_2$, Co(PPh$_2$Me)$_3$(CN)$_2$, Co(dpe)$_2$(CN)$_2$, and Co(HPPh$_2$)$_3$(CN)$_2$.[119]

{[Co(triphos)(CN)$_2$]$_2$[ZnCl$_2$]$_2$} (6)•3CH$_2$Cl$_2$. For the square compounds, the compound **6** will be considered first, in which the M(II) ions are diamagnetic Zn(II) ions, which results in a simple paramagnet composed of two mononuclear Co(triphos)(CN)$_2$ units per cluster. The value of χT at 300 K is 1.05 emu·mol^{-1}·K and remains constant over the whole temperature interval for this cluster. A plot of χT *vs.* T obeys the Curie law. Field dependent magnetization data are fit to a Brillouin function for two isolated centers with $S = 1/2$ (Figure 19). The calculated values are listed in Table 9. The data indicate an absence of magnetic interaction between the two low-spin Co(II) ions in the molecular square, which allows to make the assumption that the magnetic interaction between the two Co(II) centers in the diagonally opposite corners of the square can be neglected. This assumption will be used when treating magnetic data for the other square compounds in this work. Magnetic measurements on the other compounds, in which all four metal ions are paramagnetic, give evidence of strong magnetic interactions between adjacent ions.

Table 9. Magnetic parameters for compounds **2-6.**

Comp.	M(II)	$g_{M(II)}$	J (cm^{-1}	Spin ground state, S_{total}	D (cm^{-1})^{b}	D (cm^{-1}) (HFEPR)	E (cm^{-1}) (HFEPR)
2	Mn	2.02	–10	4	–0.24	–0.22[c]	–0.009[c]
3	Fe	2.12	–9	3	–2.98	[d]	[d]
4	Co	2.40 [e]	–8.0	2	–2.74	[d]	[d]
5	Ni	2.8 [f]	–6	1	–6	[d]	[d]
6[g]	Zn	0	~ 0	2 × (S = 1/2)	0	0	0

[a] The –2J formalism is employed.

[b] Determined by fitting of DC susceptibility and field-dependent magnetization data, except for **5**, where only magnetization fits were successful.

[c] Determined by fits of single-frequency HFEPR spectra.

[d] HFEPR results for **3**, **4**, and **5** complexes were inconclusive. Studies of **3** were further complicated by its being very air-sensitive.

[e] This g value is reasonable for tetrahedral Co(II). For example, g = 2.248 for Co(II) in ZnS(β);g = 2.23 for $[Co(NCS)_4]^{2-}$, and g = 2.48 for $[CoBr_4]^{2-}$.[124]

[f] This g value is unusually high and is likely related to the fact that fits for this compound were problematic, as described in the text.

[g] The compound **6** exhibited magnetic behavior of two isolated S = 1/2 systems. Low- and intermediate-frequency EPR (9.4 and 52.8 GHz, respectively) was used in this case.

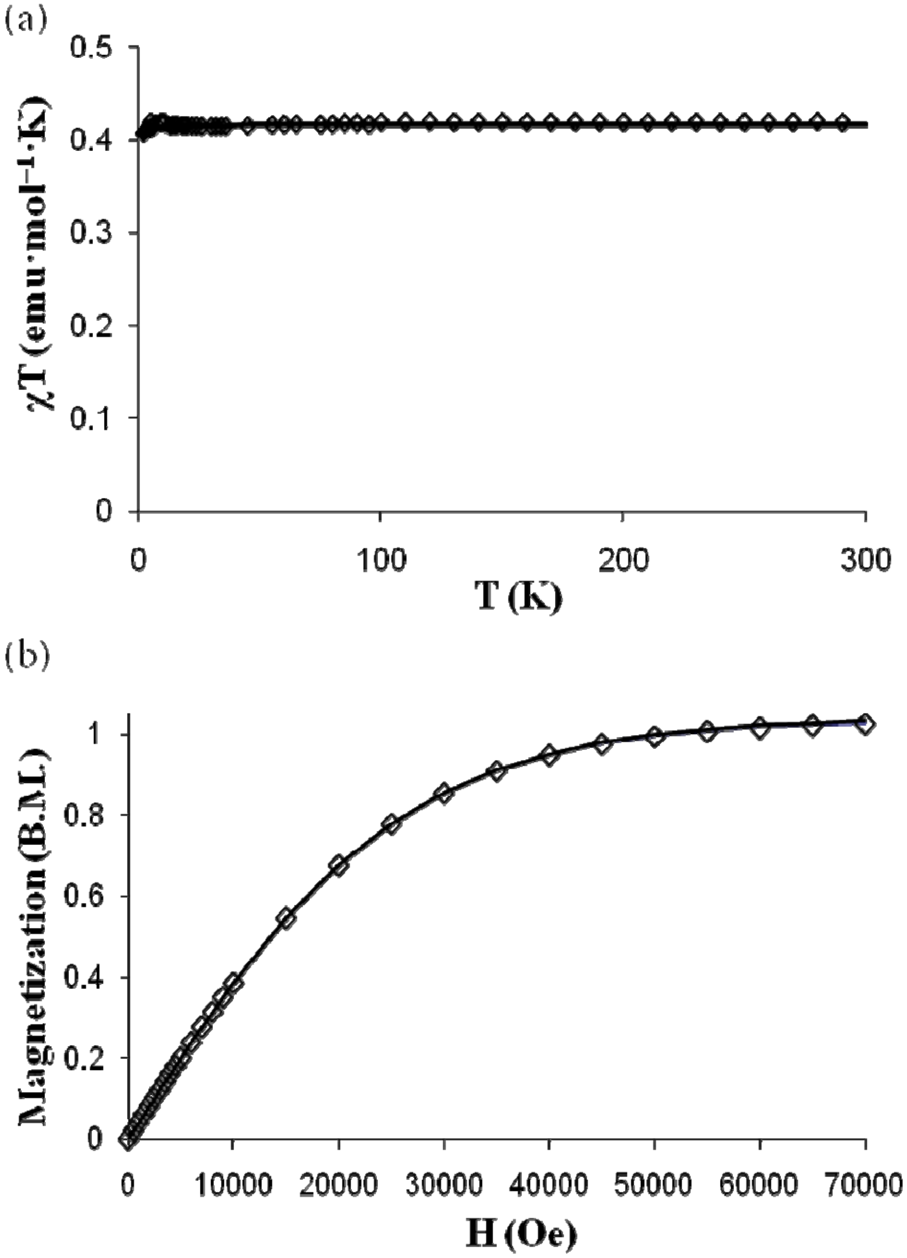

Figure 18. a) Temperature dependence of the χT product for compound **1**. b) Magnetization measurement performed at 1.8 K.

{[Co(triphos)(CN)$_2$]$_2$[MnCl$_2$]$_2$} (2)•3CH$_2$Cl$_2$. In the case of compound **2**, the DC susceptibility studies revealed a value of $\chi T = 8.7$ emu·mol^{-1}·K at 300 K, which is considerably lower than the spin-only value of 9.5 emu·mol^{-1}·K expected for two Co(triphos)(CN)$_2$ units ($S = 1/2$, $\chi T = 0.41$) and two Mn(II) ions ($S = 5/2$) in the absence of magnetic coupling (Figure 20a). The value of χT decreases upon cooling until $T \sim 65$ K, below which χT abruptly increases to reach a maximum of 9.96 emu·mol^{-1}·K at 6 K. The decrease of χT between 300 and 65 K indicates the presence of antiferromagnetic (AF) interactions between the two $S = 1/2$ Co(II) and the two $S = 5/2$ Mn(II) ions. The observed maximum for the $\chi_m T$ product at 6 K is indicative of the stabilization of an $S = 4$ ground state, whereas the decrease at lower temperatures (6 – 2 K) is attributed to zero field splitting (zfs) effects. An examination of the ground spin state for **2** was carried out by performing the magnetization measurements at different temperatures in order to determine the zfs parameters more accurately. The data were fit using the program ANISOFIT,[121] where the best fit was obtained by applying the following Hamiltonian with the parameters $S_{total} = 4$, $g = 1.95$, $D = -0.24$ cm^{-1} (where D is the axial zfs parameter) (Figure 21).

$$\mathrm{H} = g\mu_B H_z S_z + D[S_z^2 - (1/3)S(S+1)] \qquad (1)$$

Field dependent magnetization measured at 1.8 K in the field range of 0 – 70 kOe approaches a value of 7.86 μ_B, which is also in good agreement with the expected ground state spin value from AF coupling; $S_{total} = |S_{Mn1} - S_{Co1} + S_{Mn2} - S_{Co2}| = 4$ (8 μ_B)

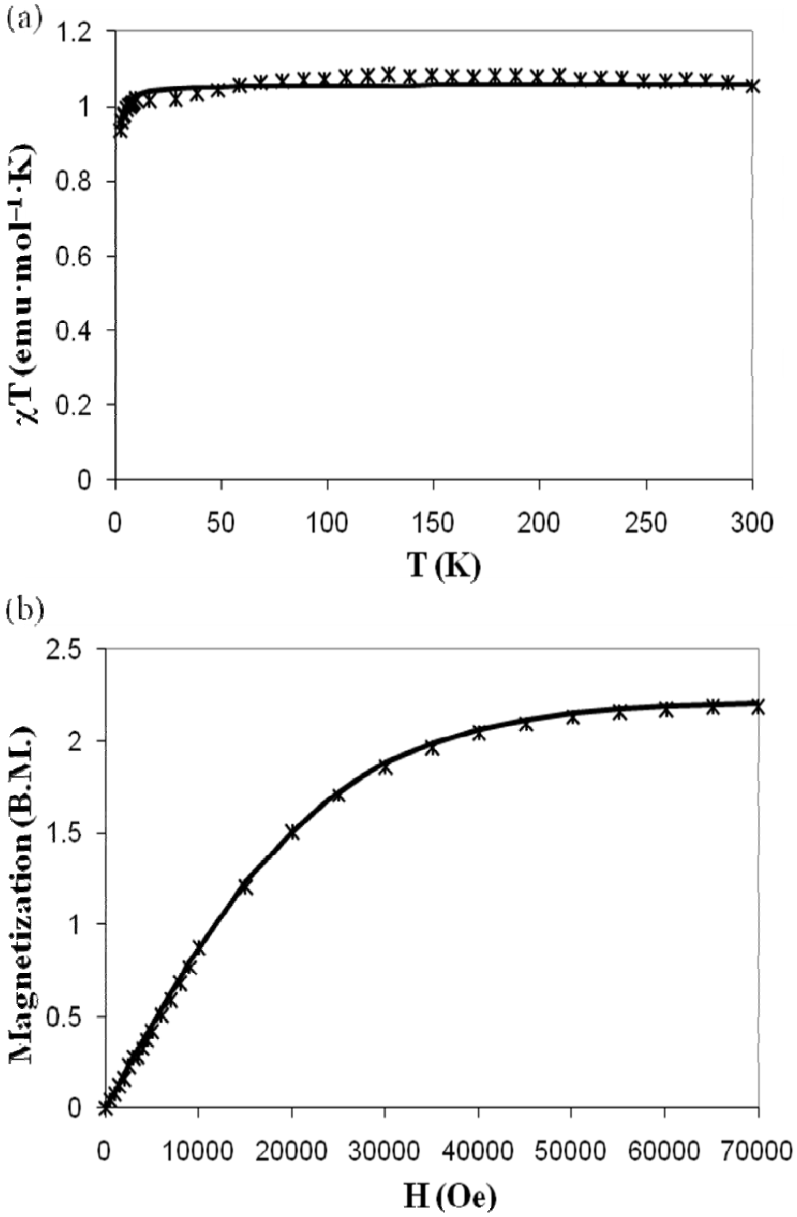

Figure 19. a) Temperature dependence of the χT product for **6**. b) Magnetization measurement performed at 1.8 K. The solid lines correspond to the simulation fit according to Brillouin function for two isolated spin centers.

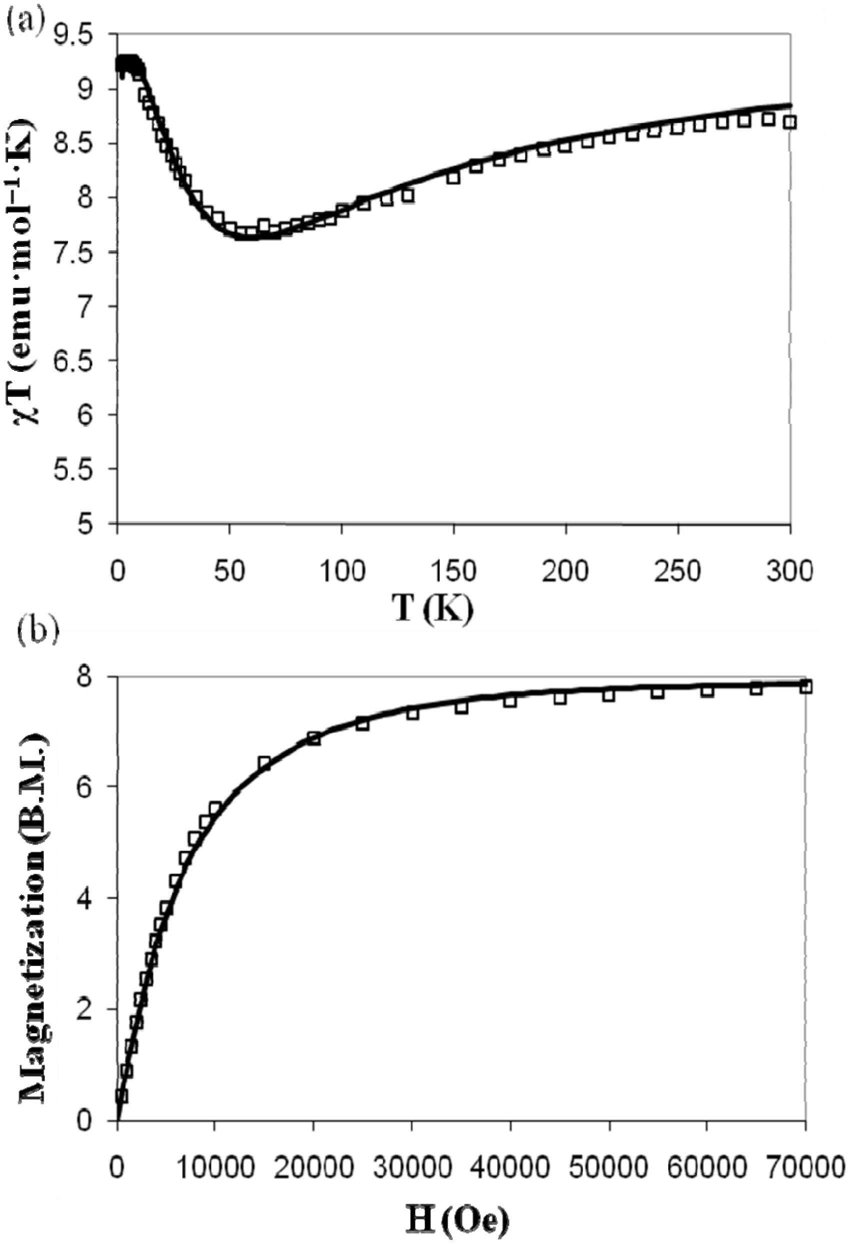

Figure 20. a) Temperature dependence of the χT product for **2**. The solid line corresponds to the simulation by Magpack program according to Eq. 2 (see text). b) Magnetization measurement performed at 1.8 K. The solid line corresponds to the simulation by Magpack program according to Eq. 1 (see text).

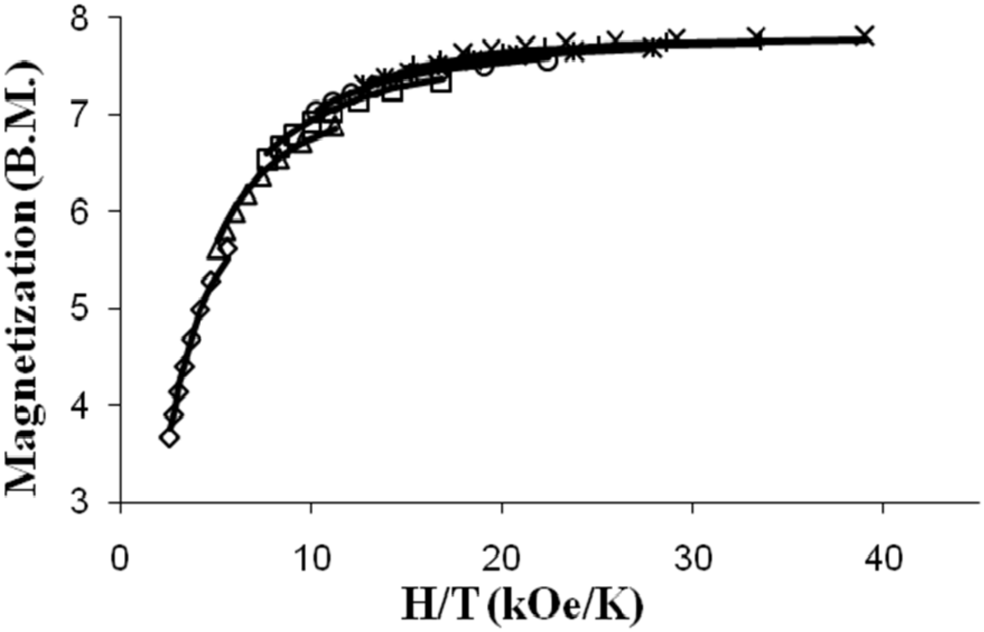

Figure 21. Plot of M vs H/T for compound **2** in the 1–7 T field range from 1.8 to 3.9 K. The solid lines represent the best fit to the parameters $S = 4$, $g = 1.95$, $D = -0.24$ cm^{-1}.

(Figure 20b). An acceptable model for the magnetization of **2** was achieved using MAGPACK,[122,123] by applying the above Hamiltonian for the low temperature behavior using the same values for the magnetic parameters obtained from the DC susceptibility measurement. Simulations of the χT versus T data using MAGPACK also allowed for estimations of g(Mn) and exchange parameter J. A spin-Hamiltonian was constructed in the limit of an isotropic Zeeman interaction, which contains only one J value, taking advantage of the molecular symmetry (Eq. 2).

$$H = 2\mu_B H_z\cdot(g_{Co}\cdot S_{z,Co} + g_M\cdot S_{z,M}) - 2J\cdot(S_{Co1} + S_{Co2})\cdot(S_{M1} + S_{M2}) + 2D\cdot[S^2_{z,M} - (1/3)S\cdot(S + 1)] \quad (2)$$

All the terms given in Eq. 2 have their usual meanings, and index M refers to Mn(II) in this case. The calculated values are listed in Table 9. Each low-spin Co(II) center is assigned the parameters S = 1/2 and g = 2.12 based on magnetometry measurements.

$\{[Co(triphos)(CN)_2]_2[FeCl_2]_2\}$ (3)•$3CH_2Cl_2$. The value of χT at 300 K is 7.3 emu·mol^{-1}·K and decreases upon cooling for compound **3**, which indicates the presence of an antiferromagnetic interaction between the Co(II) and Fe(II) ions. Below 30 K, the value increases to reach a maximum of 5.5 emu·mol^{-1}·K at 9 K and then decreases at lower temperatures. Field dependent magnetization data and simulation using Eq. 1 are shown in Figure 22b. Plots of the χT *vs.* T and simulation using Eq. 2 are depicted in Figure 22a. An examination of the ground state for **3** by ANISOFIT yielded the parameters:

$S_{\text{total}} = 3$, $g = 2.04$, $D = -2.98\ \text{cm}^{-1}$ (Figure 23).The calculated values are listed in Table 9. The total cluster spin value, $S_{total} = 3$ for **3** arises in the same way as that found for compound **2**. The spins of the Co(II) ions are antiferromagnetically coupled to those of the M(II) ions: $S_{\text{total}} = |S_{\text{Fe1}} - S_{\text{Co1}} + S_{\text{Fe2}} - S_{\text{Co2}}|$.

$\{[Co(triphos)(CN)_2]_2[CoCl_2]_2\}$ (4)•$3CH_2Cl_2$. For the compound **4**, the value of χT at 300 K is 6.8 emu·mol^{-1}·K and decreases upon cooling, an indication of antiferromagnetic coupling between the low spin and high spin Co(II) ions. Below 20 K, the χT value increases to reach a maximum of 5.2 emu·mol^{-1}·K, which indicates the stabilization of $S_{\text{total}} = 2$ ground state, and finally decreases below 7 K. Field dependent magnetization data and simulation using Eq. 1 are shown in Figure 24b. Plots of the χT *vs.* T and simulation using Eq. 2 are shown in Figure 24a. An examination of the ground state by ANISOFIT yielded the parameters: $S_{total} = 2$, $g = 2.37$, $D = -2.74\ \text{cm}^{-1}$ (Figure 25). The calculated values are listed in Table 9.

The complex **4**, as measured by AC susceptibility in its mother liquor, shows no indication of relaxation phenomena. The complex that has been thoroughly dried in air, however, exhibits a weak, frequency-dependent out-of-phase signal. The dried compound also exhibits a narrow hysteresis loop at 1.8 K, with a coercivity of ~300 Oe and remnant magnetization of 0.1 μ_B, These results indicate that decomposition of some or all of the sample occurs during the drying process.

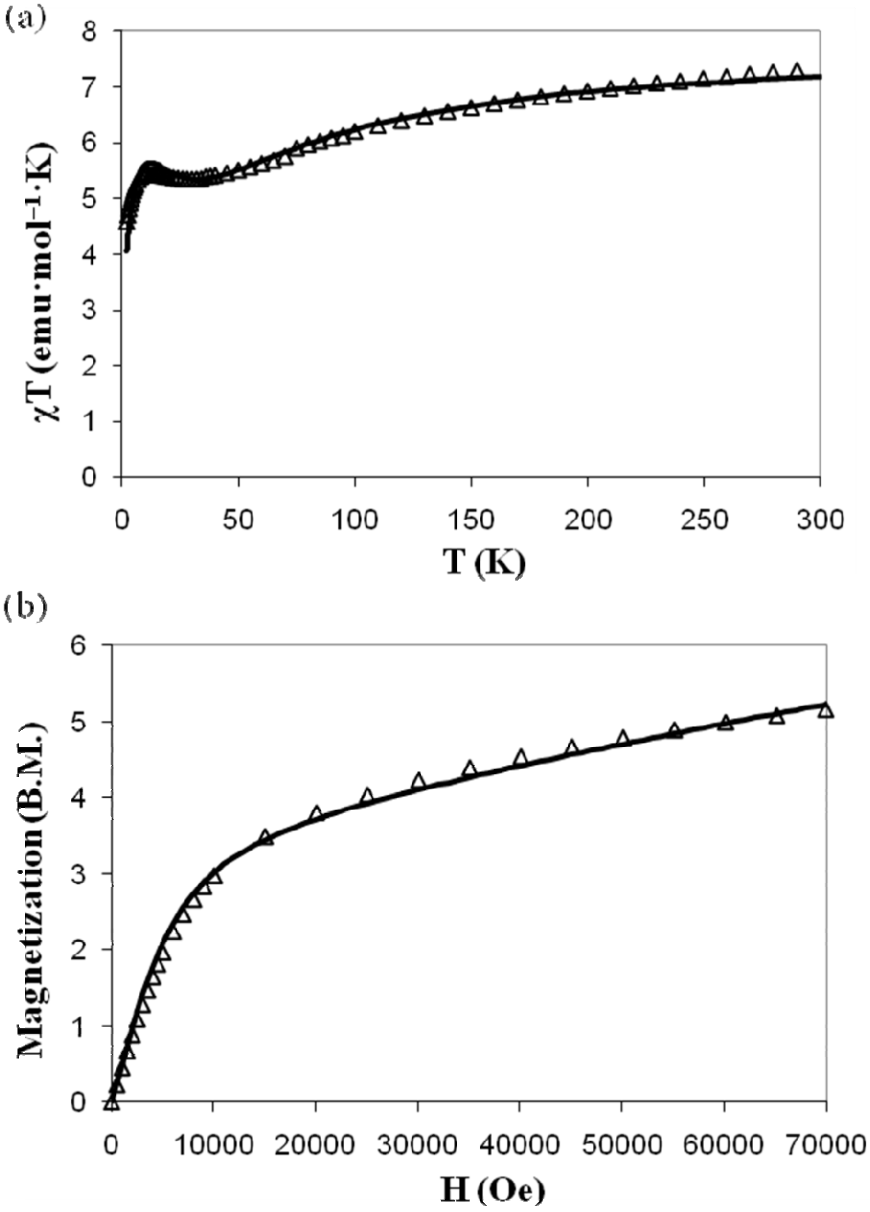

Figure 22. a) Temperature dependence of the χT product for **3**. The solid line corresponds to the simulation by Magpack program according to Eq. 2 (see text). b) Magnetization measurement performed at 1.8 K. The solid line corresponds to the simulation by Magpack program according to Eq. 1 (see text).

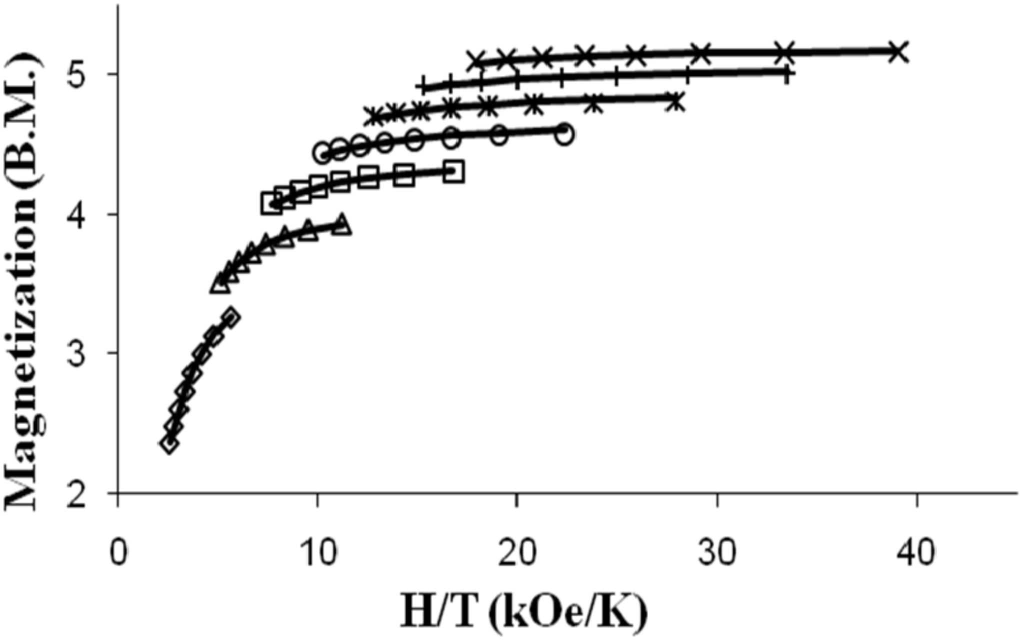

Figure 23. Plot of M *vs* H/T for compound **3** in the 1–7 T field range from 1.8 to 3.9 K. The solid lines represent the best fit to the parameters $S = 3$, $g = 2.04$, $D = -2.98$ cm^{-1}.

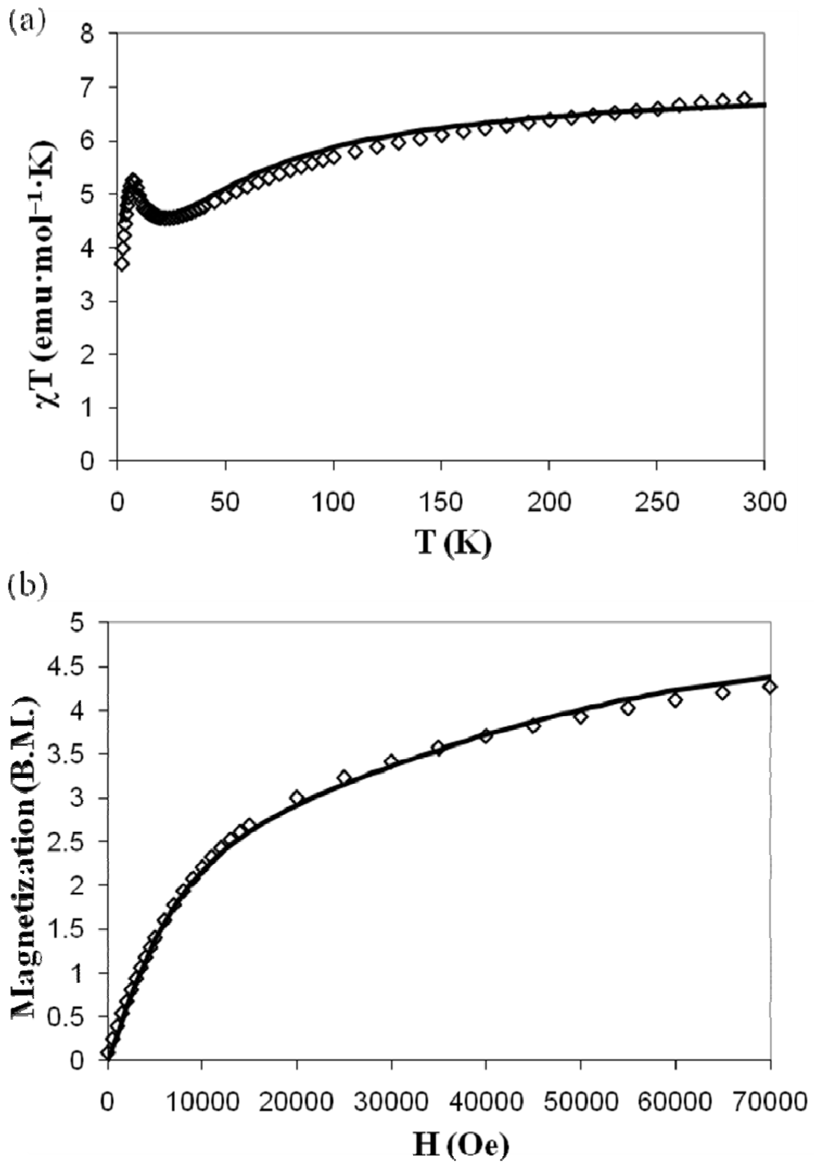

Figure 24. a) Temperature dependence of the χT product for **4**. The solid line corresponds to the simulation by Magpack program according to Eq. 2 (see text). b) Magnetization measurement performed at 1.8 K. The solid line corresponds to the simulation by Magpack program according to Eq. 1 (see text).

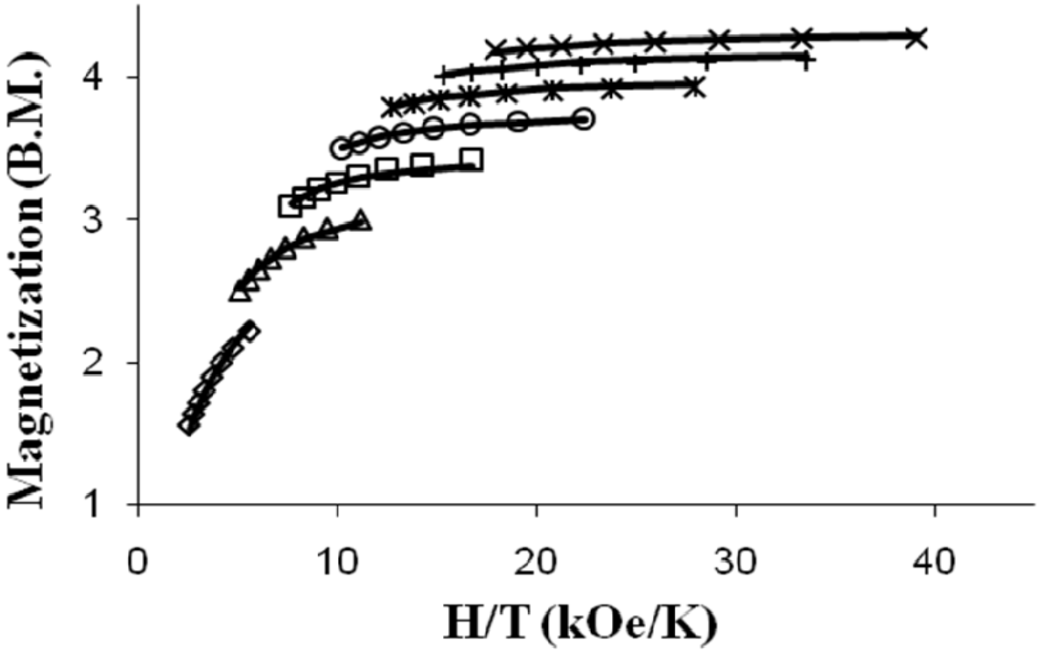

Figure 25. Plot of M *vs* H/T for compound **4** in the 1–7 T field range from 1.8 to 3.9 K. The solid lines represent the best fit to the parameters $S = 2$, $g = 2.37$, $D = –2.74\ \text{cm}^{-1}$.

{[Co(triphos)(CN)$_2$]$_2$[NiCl$_2$]$_2$} (5)•3CH$_2$Cl$_2$. The value of χT at 300 K is 4.8 emu·mol^{-1}·K for compound **5** and continuously decreases upon cooling, which indicates the presence of an antiferromagnetic interaction between the Co(II) and Ni(II) ions (Figure 26a). The best fit to 1.8 K field dependent magnetization data was obtained with MAGPACK using parameters S = 1, g = 2.57, D = –6 cm^{-1} (Figure 26b), although the quality of the fit is not very good. Analysis of the ground state for **5** by ANISOFIT failed to give satisfactory results (Figure 27).The reason for the poor fit could be the presence of low-lying excited states, which arise due to zfs and spin-orbit coupling effects. Plots of the χT *vs.* T and the simulation using Eq. 2 are shown in Figure 26a. The calculated values are listed in Table 9. A g-value of approximately 2.8 for the Ni(II) ion is obtained when the data are fit assuming antiferromagnetic coupling between the Co(II) and Ni(II) centers. This g-value is rather high for a tetrahedral Ni(II) ion ($g \approx 2.2$ is typical),[17] which also can be explained by the presence of low-lying excited states, which leads to the higher effective g-value.

EPR Studies

Co(triphos)(CN)$_2$ (1). The X- and V-band EPR spectra of the mononuclear complex Co(triphos)(CN)$_2$ **(1)** were measured as a reference and the spectra are shown in Figure 28. The EPR spectra of **1** at 4.2 K (V-band) could be simulated using the following spin Hamiltonian parameters; S = ½, g_x = 2.148, g_y = 2.106, g_z = 2.054.

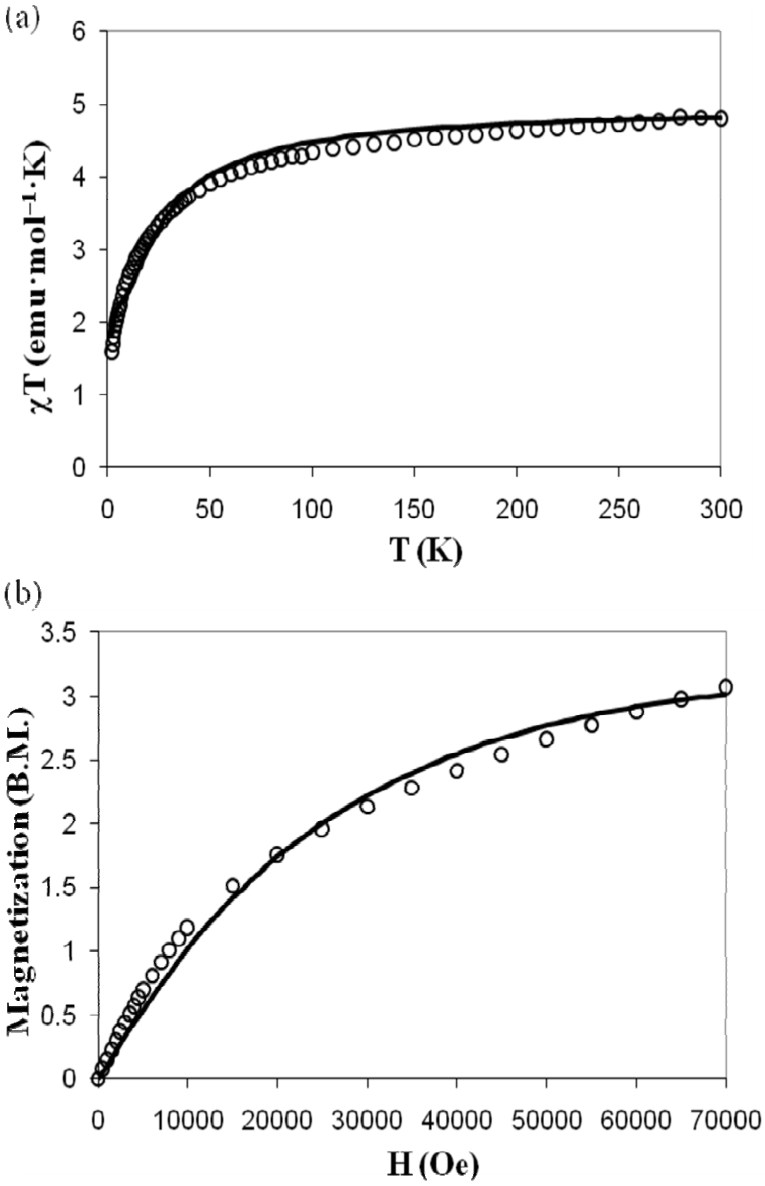

Figure 26. a) Temperature dependence of the χT product for **5**. The solid line corresponds to the simulation by Magpack program according to Eq. 2 (see text). b) Magnetization measurement performed at 1.8 K. The solid line corresponds to the simulation by Magpack program according to Eq. 1 (see text).

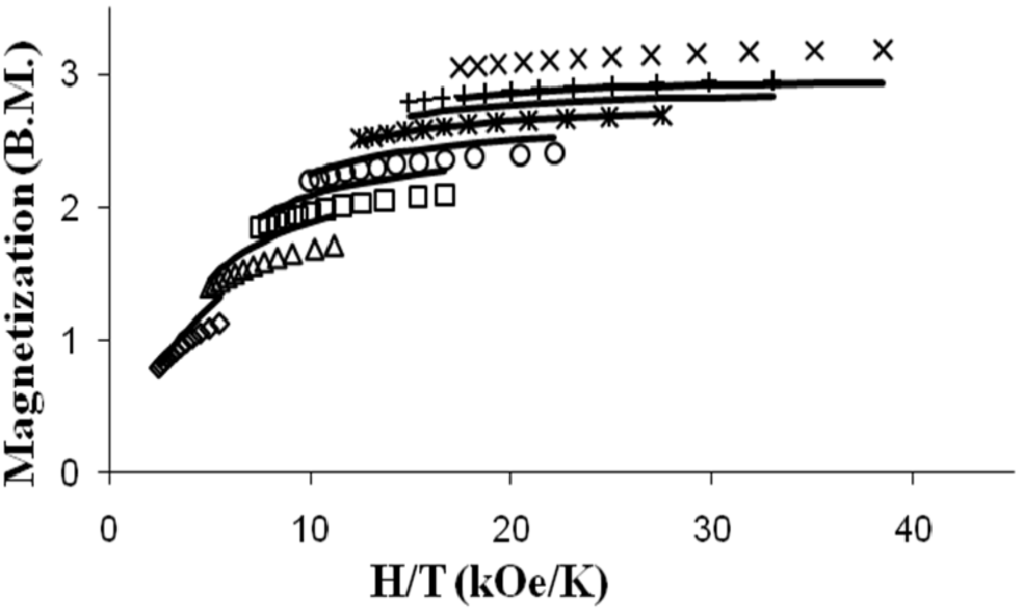

Figure 27. Plot of M *vs* H/T for compound **5** in the 1–7 T field range from 1.8 to 3.9 K. The solid lines represent the best fit to the parameters $S = 1$, $g = 2.57$, $D = -6$ cm^{-1}.

{[Co(triphos)(CN)$_2$]$_2$[ZnCl$_2$]$_2$} (6)•4CH$_2$Cl$_2$. Low-temperature EPR spectra of **6** are depicted in Figure 29, recorded at conventional, X-band (9.4 GHz), and intermediate-frequency, V-band (52.8 GHz) conditions. While the X-band spectrum consists of a single unresolved line, V-band EPR offers a vastly increased spectral resolution. The V-band spectrum can be adequately simulated assuming a powder distribution of crystallites and using $S = 1/2$, $g_x = 2.15$, $g_y = 2.12$, $g_z = 2.01$. The average g value is 2.10, which agrees well with magnetic measurements that gave an isotropic $g = 2.10$. These g matrix values are characteristic for mononuclear low-spin Co(II) complexes, confirming the lack of significant magnetic exchange between the Co(II) moieties in the complex.

{[Co(triphos)(CN)$_2$]$_2$[MCl$_2$]$_2$} (2-6). The other molecular square complexes, containing exclusively paramagnetic single ions and exhibiting net integer spin ground states, were investigated by HFEPR at low temperatures (generally 5 K, and in some cases up to 40 K). Of these, only the complex **2** gave informative results. A possible reason for this will be given below.

An exemplary spectrum for **2** recorded at 310 GHz and 40 K is shown in Figure 30 together with its simulation assuming a powder distribution of crystallites in the sample. The spectrum was analyzed and simulated using the standard spin Hamiltonian, which is given in Eq. 3, which is the same as in Eq. 1 but includes the transverse anisotropy parameter E of the cluster:[125]

$$\mathrm{H} = g\mu_B H_z S_z + D[S_z^2 - (1/3)S(S+1)] + E[S_x^2 - S_y^2]. \tag{3}$$

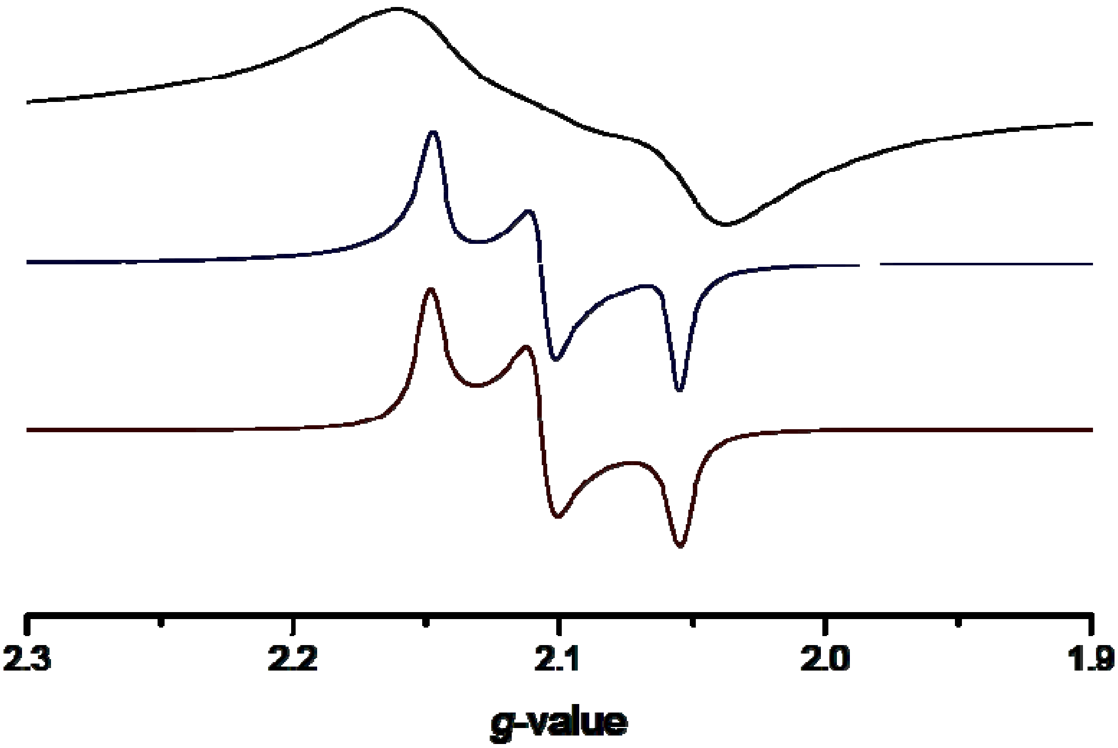

Figure 28. X-band (9.65 GHz, top trace) and V-band (50.0 GHz, middle trace) EPR spectra of Co(triphos)(CN)$_2$ at 10 K (X-band) or 4.2 K (V-band) normalized with respect to the *g*-value. The bottom trace is a powder simulation of the V-band spectrum using the following spin Hamiltonian parameters: $S = ½$, $g_x = 2.148$, $g_y = 2.106$, $g_z = 2.054$.

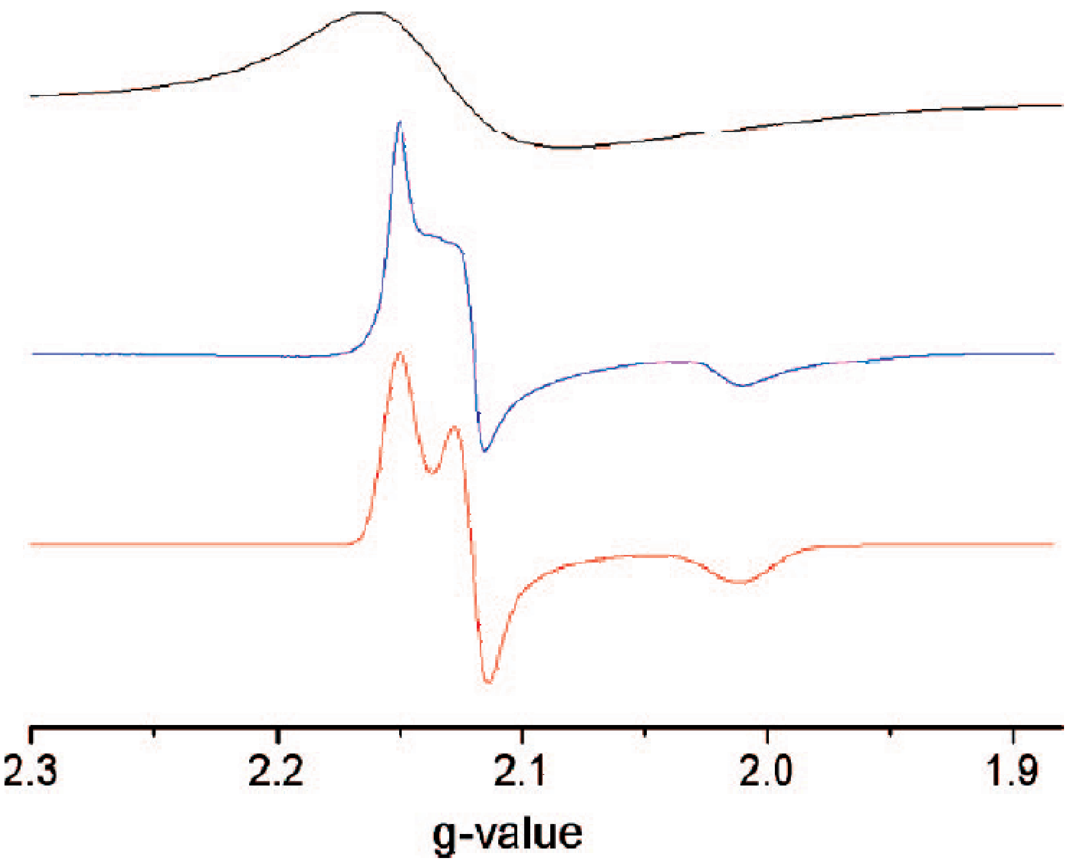

Figure 29. X-band (9.40 GHz, top trace) and V-band (52.8 GHz, middle trace) EPR spectra of **6** at 4.2 K normalized with respect to the *g*-value. The bottom trace is a powder simulation of the V-band spectrum using the following spin Hamiltonian parameters: $S = 1/2$, $g_x = 2.15$, $g_y = 2.12$, $g_z = 2.01$.

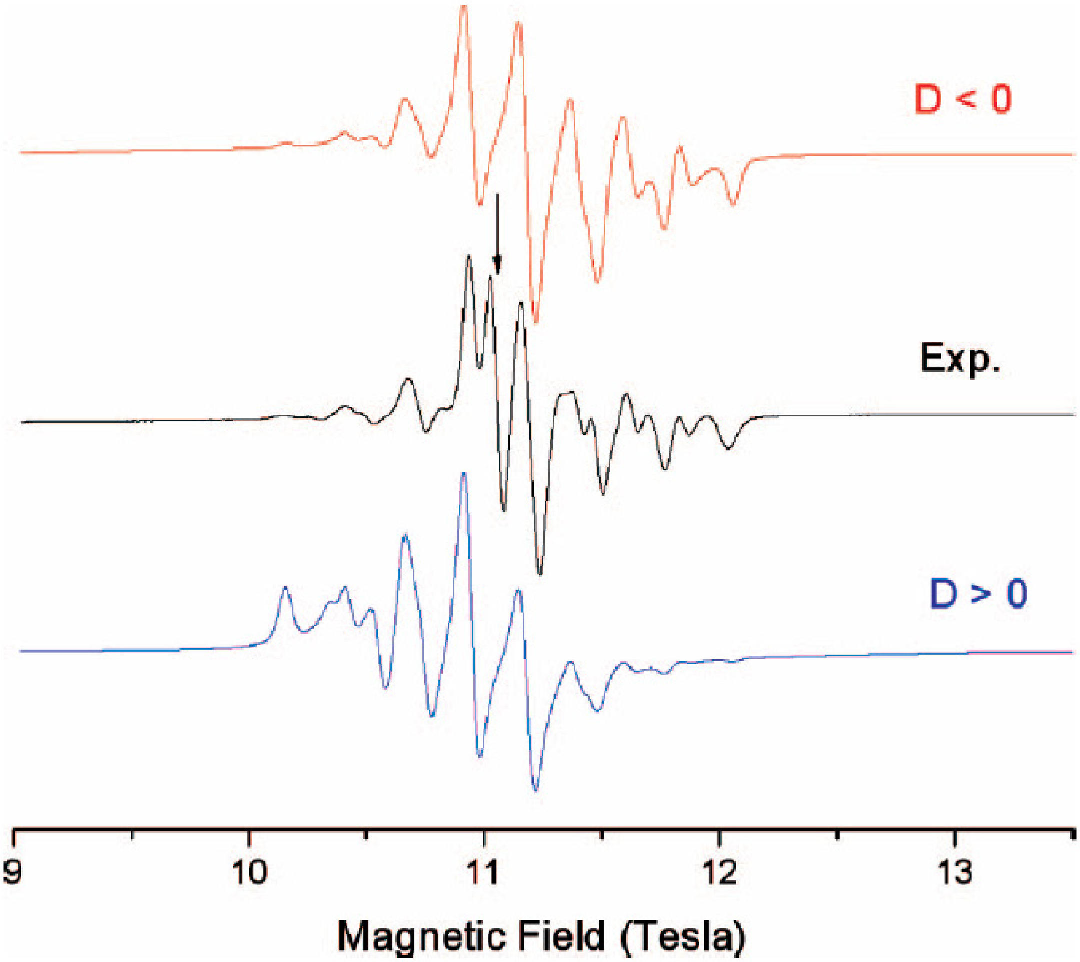

Figure 30. Representative HFEPR spectrum of **2** at 309.6 GHz and 40 K. Middle trace: experiment. Top trace: simulation using parameters: $S = 4$, $D = -0.22$ cm^{-1}, $E = -0.009$ cm^{-1}, $g_{\perp} = 1.995$, $g_{\|} = 2.000$. Bottom trace: simulation using positive zfs parameters of the same magnitude. The experimental spectrum contains an extra resonance at g = 2.00 possibly originating from free (i.e. uncoupled to other metal ions) Mn(II), indicated by the arrow, which is not reproduced in the simulation.

The simulation unequivocally confirmed the $S_{\text{total}} = 4$ ground state of the complex, and determined its spin Hamiltonian parameters. The obtained value of the zfs parameter $D = –0.22\ \text{cm}^{-1}$ (the negative sign being established through simulations, see Figure 30) is within 10% of the D value obtained from magnetometry. Magnetormetry is generally insensitive to E, in contrast to HFEPR, a magnetic resonance technique.[126] Thus, a small rhombicity of the zfs tensor was also found by HFEPR: $|E| = 0.009\ \text{cm}^{-1}$, since the agreement between experiment and simulation was much worse if E was assumed to be zero. The g-matrix values are very close to 2.00, with $g_{\perp} = 1.995$ and $g_{||} = 2.000$.

The complexes **4** and **5** gave no HFEPR signals over the entire magnetic field range, despite use of multiple frequencies. The complex **3** is very air sensitive and the sample handling/loading procedures for HFEPR inevitably led to formation of a modest amount (qualitatively, based on other studies) of an unknown decomposition product with $S = 1/2$, which was easily seen by HFEPR, but no signals were attributable to the $S_{\text{total}} = 3$ ground state found by magnetometry measurements.

EPR simulations using the spin Hamiltonian parameters obtained by magnetometry for **3-5** indicate that a wealth of HFEPR signals should in principle be observed for these integer spin complexes at the microwave frequencies available to us. The question then arises as to why no such signals were observed, although the complex **2** was fully amenable to study by HFEPR.

A qualitative reason for this difference is attributed to the nature of the M single ions in complexes **2-6**. For **2**, the single ion has an orbitally spherically symmetric, half-integer spin electronic ground state ($^6A_1$ in T_d) and generally smaller zfs and longer electron spin relaxation times, so that conventional EPR spectra are readily observed for Mn(II).[127] However, for the other M single ions, there are significant orbital contributions to the ground state, resulting in larger zfs and faster electronic relaxation times. For both Fe(II) and Ni(II), the electronic ground states are orbitally degenerate and with integer spin, in T_d symmetry respectively, ^5E and $^3T_1$, and both are fraught with severe difficulties in observation of conventional EPR spectra For Co(II), the ground state is orbitally non-degenerate and with half-integer spin, $^4A_2$ in T_d, but zfs can be quite significant for Co(II) and observation of conventional EPR can be problematic.[128]

These effects that are manifest in EPR relaxation of the Fe(II), Ni(II), and Co(II) single ions are likely carried over into the molecular square complexes, where there is the added complication that magnetic exchange interactions lead to complicated "ladders" of spin states, providing further, efficient relaxation pathways. For example, a calculation of energy levels for a four spin system with $S_1 = S_3 = 1/2$ with $g = 2.10$ (i.e., Co(triphos)) and with $S_2 = S_4 = 1$ with $g = 2.20$ and $D = -10$ cm^{-1} (reasonable for Ni(II)) and $J_{12} = J_{34} = -10$ cm^{-1} (all other $J_{ij} = 0$) gives 36 spin states in six levels (either four- or eight-fold degenerate in zero field) each separated from the next highest levels by ~ 3 – 5 cm^{-1}. Such a system is not conducive to long electronic spin relaxation times. We thus suspect that for molecular square complexes **3**, **5**, and even **4**, electronic spin relaxation is so fast that the EPR transitions that nominally would be observable are broadened beyond detection.

CONCLUSIONS

This work represents the first time that a paramagnetic metal center with a square pyramidal geometry has been introduced into a molecular square motif. The successful building block for assembly of these molecular squares is Co(triphos)$(CN)_2$, which contains a low-spin (S = 1/2) Co(II) ion in a square-pyramidal environment. Five complexes of general formula $\{[Co(triphos)(CN)_2]_2[MCl_2]_2\}$, (M = Mn, Fe, Co, Ni, Zn; **2-6**) were prepared by reaction of Co(triphos)$(CN)_2$ with the corresponding MCl_2 compound (or $Fe_4Cl_8(THF)_6$). These complexes can be described as molecular squares in which the square-pyramidal Co(II) ions are linked by tetrahedral M(II) ions. Magnetic and EPR measurements of **1** (S_{Zn} = 0) support the conclusion that there is no magnetic interaction between the low-spin Co(II) ions. However, in the case of paramagnetic M(II) centers, there is significant antiferromagnetic coupling between the Co(II) and M(II) ions. This interaction generally follows the spin-coupling model: $S_{total} = |S_{M1} - S_{Co1} + S_{M2} - S_{Co2}| = |2S_M - 1|$. Thus, for **2**, S_{total} = 4; for **3**, S_{total} = 3; for **4**, S_{total} = 2; for **5**, S_{total} = 1.

An important outcome of this study is that the building-block approach yields a family of cyanide clusters with a predicted geometry. This observation is promising for the area of molecular magnetism because, in addition to single-ion anisotropy, cluster geometry can be seen to be a major factor that produces anisotropy by shape. A square geometry is one of the most desirable shapes to increase shape anisotropy because of its planarity. By taking advantage of this geometry, we have achieved the preparation of high spin clusters with appreciable D-values as determined by magnetometry, and, in the case of **2**, by HFEPR measurements. Moreover, these molecular square compounds have negative *D*-values, which increase the interest in this family of compounds, since a negative *D*-value is a prerequisite for single molecule and single chain magnetism. In considering the applications for these compounds, it is important to note that the clusters **2-6** could be used to prepare larger assemblies and extended clusters. Despite the presence of the bulky triphos ligands, space-filling diagrams of the squares (Figure 16) clearly show that the chloride ligands of the tetrahedral M(II) ions should be able to be substituted for bridging ligands that can link the squares into higher nuclearity molecule-based architectures.

CHAPTER III

EXPERIMENTAL AND COMPUTATIONAL INVESTIGATION OF MAGNETIC COUPLING THROUGH THE CYANIDE LIGAND IN RELATED FAMILIES OF TRINUCLEAR AND TETRANUCLEAR CYANIDE-BRIDGED CLUSTERS

INTRODUCTION

The cyanide ligand has frequently been used to prepare clusters with novel magnetic properties due to its ability to provide an efficient pathway for superexchange between metal centers that are bound in an end-to-end fashion.[67,68] The ongoing research to prepare such clusters, which has been combined with theoretical studies to investigate the coupling pathway provided by the bridging ligand, has provided important insight to the understanding of the nature of fascinating photophysical, electronic and magnetic properties demonstrated by these compounds.[41,79,129-133] The mixing of unpaired spins is mediated by the cyanide ligand, and it is a well established fact that unpaired electrons in adjacent orbitals of octahedrally coordinated metal centers couple antiferromagnetically if the orbital mixing is symmetry-allowed (t_{2g}-t_{2g} or e_g-e_g) and ferromagnetically if the orbitals are orthogonal to each other (t_{2g}-e_g).[134-140] This principle has been verified by numerous experimental observations for discrete cyanide-bridged clusters with octahedral metal centers but not much has been done for other geometries.[68] A change of coordination geometry will affect the orientation of magnetic orbitals and, consequently, the nature of magnetic superexchange.[76-78] An excellent example is offered by a series of dinuclear cyanide-bridged Cu(II) complexes, in which Cu(II) centers adopt a trigonal bipyramidal coordination geometry. The magnetic coupling constants for these clusters are drastically different, ranging from –9.4 to –88 cm^{-1}. This difference has been explained by a change in orientations of the d_{z^2} magnetic orbitals, a conclusion supported by theoretical studies.[79]

One of the common synthetic approaches in this area of magnetochemistry is to design suitable cyanide containing precursors and then to react such building blocks with metal complexes consisting of accessible sites. The nature of the resulting compound is governed mainly by the geometry of the reactants and the neutrality of the product. The typical clusters have all their cyanide ligands involved in bridging interactions with no labile ligands; examples are $\{[(bpy)_2Fe^{II}(CN)_2]_2[Co^{II}(bpy)_2]_2\}(PF_6)_4$ reported by Oshio *et al.*,[82] and $\{[(tacn)Co^{III}(CN)_3]_4[Cr^{III}(tacn)]_4\}OTf_{12}$ by Long and co-workers.[141] There are also clusters with a combination of dangling cyanide and/or labile ligands that are accessible for further chemistry such as $\{[Re^{II}(triphos)(CN)_3]_4[Mn^{II}Cl]_4\}$ by Dunbar *et al.*,[52] $\{[(bpy)Cr^{III}(CN)_4]_2[Mn^{II}(H_2O)_4]\}$ by Julve *et al.*,[142] $\{[(Tp)Fe^{III}(CN)_3]_2[Mn^{II}(MeOH)_4]\}$ by Gao *et al.*,[143] and $\{[(bpy)W^{V}(CN)_6]_2[Co^{II}(dmso)_4]\}$ by Hong and co-workers.[54] Another possible strategy is to prepare charged discrete clusters with reactive sites that are more soluble in polar solvents so that systematic preparation of higher nuclearity clusters can be undertaken.

In one study in this dissertation, the molecule $Co^{II}(triphos)(CN)_2$,[107,108] a pentacoordinate metal complex with one unpaired spin, was reacted with chloride salts of 3d metal ions to prepare molecular squares of general formula; $\{[Co^{II}(triphos)(CN)_2]$

$[MCl_2]\}$ (M= Mn, Fe, Co, Ni, Zn).[109,110] Magnetic studies revealed that antiferromagnetic coupling occurs between the square pyramidal low spin Co(II) center (S = 1/2) and the tetrahedral metal center for this family of cyanide bridged clusters. Herein, we report the preparation and characterization of a new family of trinuclear and tetranuclear cyanide bridged clusters from reactions of the pentacoordiante Co(II) building block with solvated salts of 3d metal ions. Computational studies performed on these clusters will also be presented.

EXPERIMENTAL

Materials

The precursors $Mn(ClO_4)_2{\cdot}6H_2O$, $Fe(ClO_4)_2{\cdot}6H_2O$, $Co(BF_4)_2{\cdot}6H_2O$, $Ni(ClO_4)_2{\cdot}6H_2O$, triphos, and anhydrous $CoCl_2$ were purchased from Aldrich and used as received. The starting materials $Co(triphos)(CN)_2$[108], $[Mn(CH_3CN)_4](BF_4)_2$,[144] and $[Ni(CH_3CN)_6](BF_4)_2$[144] were prepared according to reported procedures. All solvents were dried by standard methods.

Syntheses

$\{[Co(triphos)(CN)_2]_2[Mn(MeOH)_4]\}(BF_4)_2$, (7). A colorless solution of $[Mn(CH_3CN)_4](BF_4)_2$ (54 mg, 0.138 mmol) in 15 mL of methanol was slowly added to a claret solution of $Co(triphos)(CN)_2$ (202 mg, 0.277 mmol) in 20 mL of methanol under N_2. The mixture was left to stand undisturbed for 3 – 4 days. Dark red crystals of **(7)**$\cdot 2H_2O$ that formed were filtered and washed with 10 mL of methanol/ether (1:1 v/v) and then a copious amount of diethyl ether. Yield = 40%. Elemental analysis Calcd. for

7, $Co_2MnC_{90}H_{94}N_4P_6O_4B_2F_8$: C 59.10, H 5.18, N 3.07, O 3.50; found: C 58.98, H 5.32, N 3.12, O 3.65. IR(Nujol), ν(C≡N), cm^{-1}: 2121(s), 2094(s).

Compounds **8-10** were obtained by using the same procedure and the corresponding metal salt. The yields were 28%, 32%, and 46%, respectively. Elemental analysis Calcd. for **8**, $Co_3C_{90}H_{94}N_4P_6O_4B_2F_8$: C 59.07, H 5.18, N 3.06, O 3.50; found: C 58.49, H 5.24, N 3.02, O 3.82; elemental analysis Calcd. for **9**, $Co_3C_{90}H_{94}N_4P_6O_4B_2F_8$: C 58.21, H 5.11, N 3.02, O 10.34, Cl 3.77; found: C 57.88, H 5.23, N 2.94, O 10.98, Cl 3.69; elemental analysis calcd. for **10**, $Co_3C_{90}H_{94}N_4P_6O_4B_2F_8$: C 58.24, H 5.11, N 3.02, O 10.35, Cl 3.77; found: C 57.73, H 5.28, N 2.92, O 10.68, Cl 3.62. IR (Nujol), cm^{-1} for **8**: 2131(s), 2094(s); for **9**: 2134(s), 2094(s); for **10**: 2138(s), 2094(s). The single crystals of **8**·$3H_2O$, **9**·CH_3OH and **10**·$2CH_3OH$ were obtained in the same way as described for **7**·$2H_2O$.

{[Co(triphos)(CN)$_2$]$_2$[Mn(MeOH)$_4$]$_2$}(BF$_4$)$_4$ (11). A claret solution of Co(triphos)$(CN)_2$ (202 mg, 0.277 mmol) in 20 mL of methanol was added dropwise to a colorless solution of $[Mn(CH_3CN)_4](BF_4)_2$ (108 mg, 0.277 mmol) in 15 mL of methanol under N_2 at –42°C. The mixture was left to stand without stirring for 1 day. Dark red crystals of **(11)**·$4CH_3OH$ that formed were filtered and washed with 12 mL of methanol/ether (1:2 v/v) and then a copious amount of diethyl ether. Yield = 22%. Elemental analysis Calcd. for **11**, $Co_2Mn_2C_{94}H_{110}N_4P_6O_8B_4F_{16}$: C 51.64, H 5.08, N 2.56, O 5.86; found: C 51.44, H 5.16, N 2.48, O 6.09. IR(Nujol), ν(C≡N), cm^{-1}: 2132(s), 2106(w).

{[Co(triphos)(CN)$_2$]$_2$[Ni(MeOH)$_4$]$_2$}(BF$_4$)$_4$, (12). This compound was prepared in an analogous fashion to that described above for **11**. Yield = 28%. Elemental analysis Calcd. for **12**, $Co_2Ni_2C_{94}H_{110}N_4P_6O_8B_4F_{16}$: C 51.50, H 5.06, N 2.56, O 5.84; found: C 51.22, H 5.09, N 2.59, O 6.16. IR(Nujol), ν(C≡N), cm^{-1}: 2148(s), 2106(w).

Single Crystal X-ray Diffraction Studies

In a typical experiment, a crystal selected for study was suspended in polybutene oil (Aldrich) and mounted on a cryoloop which was placed in an N_2 cold stream. Single crystal X-ray data for all the compounds were collected on a Bruker APEX diffractometer at 110 K. The data sets were recorded as three *ω*-scans of 606 frames each, at 0.3° stepwidth, and integrated with the Bruker SAINT[112] software package. For each compound, the data set was indexed in a monoclinic unit cell and systematic absences indicated the space group to be $P2_1/n$ for **7-10** and C2/*c* for **11-12**. The absorption correction (SADABS[113]) was based on fitting a function to the empirical transmission surface as sampled by multiple equivalent measurements. Solution and refinement of the crystal structures was carried out using the SHELX suite of programs and X-SEED,[115] a graphical interface. Structural solution by direct methods resolved the positions of all metal atoms and most of the lighter atoms. The remaining non-hydrogen atoms were located by alternating cycles of least squares refinements and difference Fourier maps. The final refinement has been carried out with anisotropic thermal parameters for all non-hydrogen atoms. A summary of pertinent information relating to unit cell parameters, data collection, and refinements is given in Tables 10-12. Selected

Table 10. Crystallographic data and structural refinement parameters for **(7)**•$2H_2O$ and **(8)**•$3H_2O$.

	(7)•$2H_2O$	**(8)**•$3H_2O$
Formula	$Co_2MnC_{90}H_{90}P_6N_4O_{10}B_2F_8$	$Co_2FeC_{90}H_{98}P_6N_4O_8B_2F_8$
Space group	$P2_1/n$ (No. 14)	$P2_1/n$ (No. 14)
Unit cell	a = 11.207(5) Å	a = 11.172(16) Å
	b = 18.536(12) Å	b = 18.530(17) Å
	c = 21.678(13) Å	c = 21.70(3) Å
	β = 96.37(2) °	β = 96.90(2) °
Unit cell volume, V	4475(4) $Å^3$	4461(10) $Å^3$
Z	2	2
Density, ρ_{calc}	1.425 g/cm^3	1.412 g/cm^3
Abs. coeff., μ	0.689 mm^{-1}	0.710 mm^{-1}
Crystal color and habit	Dark-red block	Dark-red plate
Crystal size	0.21×0.18×0.17 mm	0.22×0.16×0.13 mm
Temperature	110(2) K	110(2) K
Radiation, λ	Mo-Kα, 0.71073 Å	Mo-Kα, 0.71073 Å
Min. and max. θ	1.45 to 28.27°	1.45 to 28.65°
Reflections collected	37198	36086
Independent reflections	10733	10521
Data/parameters/restraints	10733 / 320 / 0	10521 / 320 / 0
R [$F_o > 4\sigma(F_o)$]	R_1 = 0.0551	R_1 = 0.0832
	wR_2 = 0.1503	wR_2 = 0.2036

[a] $R_{int} = \Sigma|F_o^2 - F_o^2(\text{mean})| / \Sigma[F_o^2]$

[b] $R_1 = \Sigma||F_o| - |F_c|| / \Sigma|F_o|$

[c] $wR_2 = \{\Sigma[w(F_o^2 - F_c^2)^2] / \Sigma[w(F_o^2)^2]\}^{1/2}$, $w = 1 / [\sigma^2(F_o^2) + (aP)^2 + bP]$, $P = [2F_c^2 + \text{Max}(F_o^2,0)]/3$. For **7**, a = 0.0617, b = 4.2708; for **8**, a = 0.0684, b = 0.

Table 11. Crystallographic data and structural refinement parameters for **(9)**•1CH_3OH and **(10)**•1CH_3OH.

	(9)• 1CH_3OH	**(10)**•1CH_3OH
Formula	$Co_3C_{92}H_{100}P_6N_4O_{14}Cl_2$	$Co_2NiC_{92}H_{102}P_6N_4Cl_2O_{14}$
Space group	$P2_1/n$ (No. 14)	$P2_1/n$ (No. 14)
Unit cell	a = 11.2090(10) Å	a = 11.402(3) Å
	b = 18.5531(17) Å	b = 19.250(5) Å
	c = 21.6941(19) Å	c = 20.784(5) Å
	β = 96.454(4) °	β = 99.759(10) °
Unit cell volume, V	4482.9(7) $Å^3$	4496(2) $Å^3$
Z	2	2
Density, ρ_{calc}	1.422 g/cm^3	1.419 g/cm^3
Abs. coeff., μ	0.733 mm^{-1}	0.803 mm^{-1}
Crystal color and habit	Blue plate	Green-blue plate
Crystal size	0.12×0.11×0.08 mm	0.19×0.17×0.12 mm
Temperature	108(2) K	110(2) K
Radiation, λ	Mo-Kα, 0.71073 Å	Mo-Kα, 0.71073 Å
Min. and max. θ	3.14 to 39.25°	1.91 to 28.30°
Reflections collected	8267	39800
Independent reflections	2329	10936
Data/parameters/restraints	2329 / 421 / 0	10936 /320 / 0
R $[F_o > 4\sigma(F_o)]$	R_1 = 0.0629	R_1 = 0.0553
	wR_2 = 0.2260	wR_2 = 0.1305

[a] $R_{int} = \Sigma|F_o^2 - F_o^2(\text{mean})| / \Sigma[F_o^2]$

[b] $R_1 = \Sigma||F_o| - |F_c|| / \Sigma|F_o|$

[c] $wR_2 = \{\Sigma[w(F_o^2 - F_c^2)^2] / \Sigma[w(F_o^2)^2]\}^{1/2}$, $w = 1 / [\sigma^2(F_o^2) + (aP)^2 + bP]$, $P = [2F_c^2 + \text{Max}(F_o^2,0)]/3$. For **9**, a = 0.0617, b = 4.2708; for **10**, a = 0.0684, b = 0.

Table 12. Crystallographic data and structural refinement parameters for **(11)**•4CH_3OH and **(12)**•2CH_3OH.

	(11)•4CH_3OH	**(12)**•2CH_3OH
Formula	$Co_2Mn_2C_{98}H_{100}P_6N_4O_{12}B_4F_{16}$	$Co_2Ni_2C_{96}H_{104}P_6N_4O_{10}B_4F_{16}$
Space group	$C2/c$	$C2/c$
Unit cell	a = 27.2420(6) Å	a = 27.210(5) Å
	b = 14.560(3) Å	b = 14.180(3) Å
	c = 30.730(6) Å	c = 31.030(6) Å
	β = 105.08(3) °	β = 105.82(3) °
Unit cell volume, V	11846(4) $Å^3$	11808(4) $Å^3$
Z	4	4
Density, ρ_{calc}	1.282 g/cm^3	1.257 g/cm^3
Abs. coeff., μ	0.643 mm^{-1}	0.744 mm^{-1}
Crystal color and habit	Dark-red block	Dark-red block
Crystal size	0.21×0.18×0.17 mm	0.22×0.18×0.14 mm
Temperature	110(2) K	110(2) K
Radiation, λ	Mo-Kα, 0.71073 Å	Mo-Kα, 0.71073 Å
Min. and max. θ	1.37 to 28.38°	1.48 to 27.88°
Reflections collected	59124	59058
Independent reflections	14467	13492
Data/parameters/restraints	14467 / 713 / 10	13492 / 670 / 10
$R\ [F_o > 4\sigma(F_o)]$	R_1 = 0.0789	R_1 = 0.0886
	wR_2 = 0.2623	wR_2 = 0.3016

[a] $R_{int} = \Sigma|F_o^2 - F_o^2(\text{mean})| / \Sigma[F_o^2]$

[b] $R_1 = \Sigma||F_o| - |F_c|| / \Sigma|F_o|$

[c] $wR_2 = \{\Sigma[w(F_o^2 - F_c^2)^2] / \Sigma[w(F_o^2)^2]\}^{1/2}$, $w = 1 / [\sigma^2(F_o^2) + (aP)^2 + bP]$, $P = [2F_c^2 + \text{Max}(F_o^2,0)]/3$. For **11**, a = 0.0617, b = 4.2708; for **12**, a = 0.0684, b = 0.

metal-to-ligand bond distances appear in Tables 13-16, 18 and 19.

RESULTS AND DISCUSSION

Syntheses

The reaction of the mononuclear precursor Co(triphos)$(CN)_2$ with hydrated salts of 3d transition metal ions results in the formation of a series of trinuclear and tetranuclear cyanide-bridged clusters. The nuclearity of the resulting compound depends on the stoichiometric ratio of the reactants, the counter anion, and the temperature of the reaction medium. The reaction of Co(triphos)$(CN)_2$ and $M(ClO_4)_2 \cdot 6H_2O$ in the 2:1 ratio yields trinuclear clusters with the general formula $\{[Co(triphos)(CN)_2]_2[M(MeOH)_4]\}X_2$ (M= Mn, Fe, Co, Ni; X = ClO_4^-, BF_4^-). If the reaction is performed in a 1:1 ratio, the result is the same, namely a mixture of the trinuclear complex and a tetranuclear cluster $\{[Co(triphos)(CN)_2]_2[M(MeOH)_4]_2\}(BF_4)_4$. Efforts to isolate the tetranuclear cluster by using an excess of the transition metal ion M(II) also led to the mixture of aforementioned clusters, which can be explained by the higher solubility of the tetranuclear complexes in polar solvents. Consequently, the reactions were performed at low temperatures to decrease the solubility of the tetranuclear clusters. Slow mixing of methanolic solutions of Co(triphos)$(CN)_2$ and $M(BF_4)_2$ in the 1:1 ratio at –42°C resulted in crystals of the target tetranuclear compounds. Both tri- and tetranuclear complexes are soluble in common polar solvents such as CH_2Cl_2, CH_3OH, and CH_3CN.

In terms of previously reported related trinuclear clusters, there are known examples in which the central metal ion is surrounded by four solvent molecules.

Among them, the most studied class comprises compounds with the $Fe^{III}{}_2Mn^{II}$ metal core prepared by reacting $[(L_3)Fe^{III}(CN)_3]$ (L_3= hydrotris(pyrazolyl)borate (Tp^-)[143], 8-(pyridine-2-carboxamido)quinoline (pcq^-)[145], or bis(2-pyridylcarbonyl)amidate ($bpca^-$[146]) with the solvated Mn(II) ion.

Single Crystal X-ray Structures

The structures of the **7-10** (Figure 31) consist of a central octahedral M(II) ion that resides on the crystallographic inversion center and is surrounded by four methanol molecules in the equatorial plane. Two $Co(triphos)(CN)_2$ fragments are connected to the M(II) center in a trans fashion. The Co(II) sites retain their pentacoordinate square pyramidal geometry, in which one of the phosphorus atoms occupies the axial position while two carbon atoms of the cyanide and the two remaining phosphorus atoms occupy the equatorial positions of the square pyramid, similar to the $Co(triphos)(CN)_2$ molecule. The C–Co–C angles range from 80.8° to 84.1°, which are reduced from than that of the mononuclear precursor (87.6°) and the corresponding angles in the series of molecular squares, $\{[Co^{II}(triphos)(CN)_2][M^{II}Cl_2]\}$ (~85°). Such a dramatic decrease in the C–Co–C angle is due to the H-bonding interaction (H···N distance is ~1.98 Å) between the hydrogen atom of one of the methanol molecules connected to the M(II) center and the nitrogen of the dangling cyanide ligand, as confirmed by theoretical studies (Figure 32). This H-bonding interaction also causes the C–N–M angle to depart significantly from

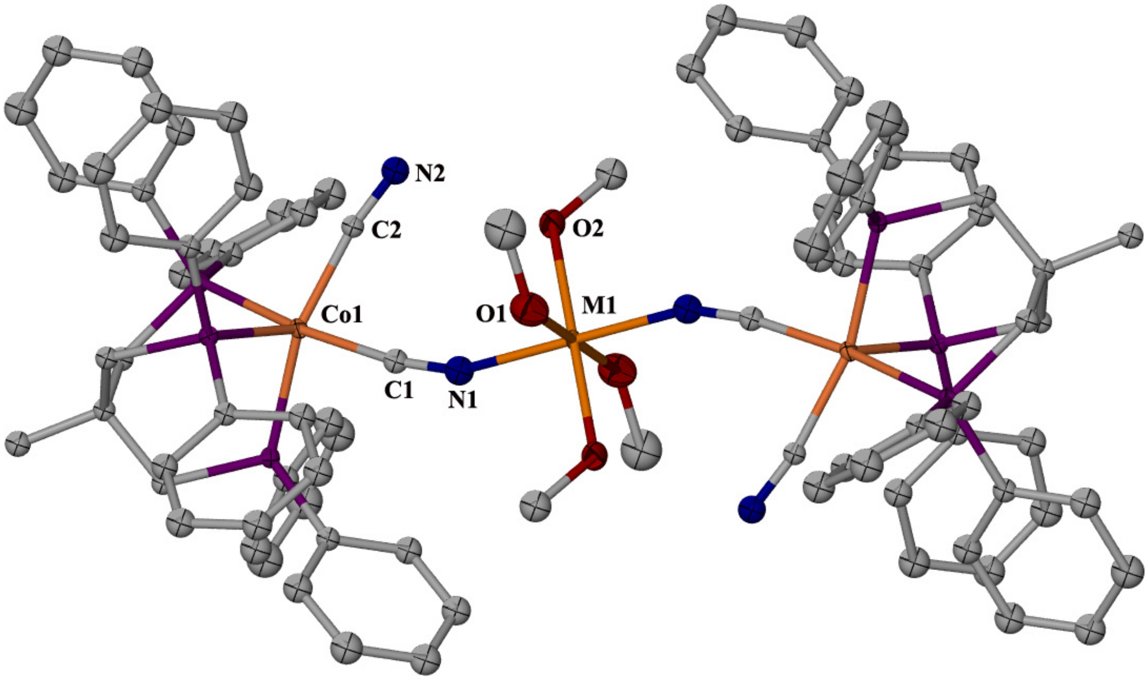

Figure 31. Basic structure of the trinuclear complexes **7-10** from X-ray coordinates. (Compound **10** is used to make the figure. H atoms are omitted for the sake of clarity.) Thermal ellipsoids are projected at the 50% probability level.

Table 13. Selected bond distances (Å) and angles (°) for compound **7**.

Atoms	**Distance (Å)**	**Atoms**	**Angle(°)**
Co1 – C1	1.886(3)	C1 – Co1 – C2	83.61(14)
Co1 – C2	1.908(3)	C1 – Co1 – P2	161.99(10)
Co1 – P1	2.2422(13)	C2 – Co1 – P2	88.19(10)
Co1 – P2	2.2154(13)	C1 – Co1 – P1	94.03(10)
Co1 – P3	2.2800(13)	C2 – Co1 – P1	164.49(10)
M1 – N1	2.107(3)	P2 – Co1 – P1	89.59(4)
M1 – O1	2.129(3)	C1 – Co1 – P3	101.95(10)
M1 – O2	2.144(3)	C2 – Co1 – P3	107.47(10)
O1M – C1M	1.441(5)	P2 – Co1 – P3	95.79(3)
		P1 – Co1 – P3	88.02(4)
		N1 – M1 – N1	180.00
		N1 – M1 – O2	88.67(11)
		N1 – M1 – O2	91.33(11)
		O2 – M1 – O2	180.00
		N1 – M1 – O1	88.29(11)
		N1 – M1 – O1	91.71(11)
		O2 – M1 – O1	89.59(11)
		O2 – M1 – O1	90.41(11)
		O1 – M1 – O1	180.00(12)
		C1 – N1 – M1	146.7(3)

Table 14. Selected bond distances (Å) and angles (^{o}) for compound **8**.

Atoms	**Distance (Å)**	**Atoms**	**Angle(^{o})**
Co1 – C1	1.877(6)	C1 – Co1 – C2	83.2(2)
Co1 – C2	1.906(6)	C1 – Co1 – P2	161.96(7)
Co1 – P1	2.227(3)	C2 – Co1 – P2	88.47(18)
Co1 – P2	2.219(2)	C1 – Co1 – P1	94.35(17)
Co1 – P3	2.285(3)	C2 – Co1 – P1	164.12(18)
M1 – N1	2.074(5)	P2 – Co1 – P1	89.26(6)
M1 – O1	2.119(4)	C1 – Co1 – P3	101.97(19)
M1 – O2	2.119(5)	C2 – Co1 – P3	107.46(19)
O1M – C1M	1.426(8)	P2 – Co1 – P3	95.78(10)
		P1 – Co1 – P3	88.41(8)
		N1 – M1 – N1	180.00(1)
		N1 – M1 – O2	88.34(18)
		N1 – M1 – O2	91.66(18)
		O2 – M1 – O2	180.0(2)
		N1 – M1 – O1	87.13(19)
		N1 – M1 – O1	92.87(19)
		O2 – M1 – O1	90.93(19)
		O2 – M1 – O1	89.07(19)
		O1 – M1 – O1	180.0(2)
		C1 – N1 – M1	148.4(4)

Table 15. Selected bond distances (Å) and angles (^{o}) for compound **9**.

Atoms	**Distance (Å)**	**Atoms**	**Angle(^{o})**
Co1 – C1	1.90(2)	C1 – Co1 – C2	84.1(7)
Co1 – C2	1.91(2)	C1 – Co1 – P2	161.2(5)
Co1 – P1	2.236(5)	C2 – Co1 – P2	88.0(6)
Co1 – P2	2.215(5)	C1 – Co1 – P1	93.8(5)
Co1 – P3	2.277(6)	C2 – Co1 – P1	164.9(6)
M1 – N1	2.023(14)	P2 – Co1 – P1	89.4(2)
M1 – O1	2.094(14)	C1 – Co1 – P3	102.8(5)
M1 – O2	2.089(10)	C2 – Co1 – P3	107.1(6)
O1M – C1M	1.42(2)	P2 – Co1 – P3	95.8(2)
		P1 – Co1 – P3	88.00(19)
		N1 – M1 – N1	180.000(1)
		N1 – M1 – O2	87.4(5)
		N1 – M1 – O2	92.6(5)
		O2 – M1 – O2	180.0(5)
		N1 – M1 – O1	88.6(6)
		N1 – M1 – O1	91.4(6)
		O2 – M1 – O1	92.3(5)
		O2 – M1 – O1	87.6(5)
		O1 – M1 – O1	180.0(9)
		C1 – N1 – M1	152.2(13)

Table 16. Selected bond distances (Å) and angles (^{o}) for compound **10**.

Atoms	**Distance (Å)**	**Atoms**	**Angle(^{o})**
Co1 – C1	1.877(3)	C1 – Co1 – C2	80.78(13)
Co1 – C2	1.900(3)	C1 – Co1 – P2	160.95(9)
Co1 – P1	2.2473(9)	C2 – Co1 – P2	90.39(9)
Co1 – P2	2.2277(10)	C1 – Co1 – P1	92.92(9)
Co1 – P3	2.2799(9)	C2 – Co1 – P1	167.94(12)
M1 – N1	2.020(3)	P2 – Co1 – P1	89.09(3)
M1 – O1	2.089(2)	C1 – Co1 – P3	101.59(10)
M1 – O2	2.090(3)	C2 – Co1 – P3	109.14(9)
O1M – C1M	1.412(6)	P2 – Co1 – P3	92.44(3)
		P1 – Co1 – P3	90.33(4)
		N1 – M1 – N1	180.00(17)
		N1 – M1 – O2	88.17(11)
		N1 – M1 – O2	91.83(11)
		O2 – M1 – O2	180.0(14)
		N1 – M1 – O1	89.59(12)
		N1 – M1 – O1	90.41(12)
		O2 – M1 – O1	86.14(12)
		O2 – M1 – O1	93.86(12)
		O1 – M1 – O1	180.000(1)
		C1 – N1 – M1	156.9(3)

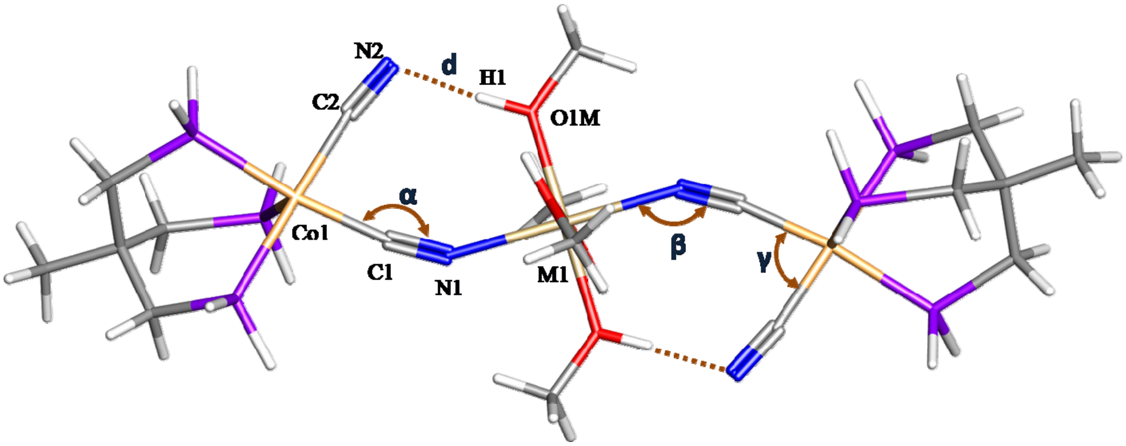

Figure 32. Molecular structure of the trinuclear complexes **7-10** indicating the presence of H-bonding between the atoms N2 and H1. (Compound **10** is used to make the figure.)

Table 17. Bond distances (Å) and angles (^{o}) displayed in Figure 32.

Compounds	**N2···H1** **d**	**Co1–C1–N1** **α**	**M1–N1–C1** **β**	**C1–Co1–C2** **γ**
7	1.992	169.6	146.7	83.6
8	1.982	169.6	148.4	83.2
9	2.091	165.9	152.2	84.0
10	2.052	170.2	156.8	80.8

180°; these vary between 146.7° and 156.9° and their magnitude directly affects the magnetic exchange across the cyanide bridge (Table 17).

The tetranuclear complexes **11-12** are composed of alternating Co(triphos)$(CN)_2$ and $[M(MeOH)_4]^{2+}$ fragments resulting in a cationic cluster with 4+ charge. The molecules crystallize on crystallographic inversion centers. The bridging cyanide ligands are connected to the M(II) centers in a *cis* fashion, in contrast to their *trans* arrangement in the trinuclear clusters described above (Figure 33). The C–Co–C angle is ~85° while the N–M–N angle is ~97° (Tables 18 and 19). Since all of the cyanide ligands are bridging in these products, there is no H-bonding interaction between cyanide and a methanol molecule. As a result, the C–N–M angle (~167°) does not deviate as much from 180° as compared to the angle in **7-10** (146.7–156.9°). Also the $Co^{II}\cdots M^{II}$ distance (~5.12 Å) is longer than the corresponding values in the clusters **7-10** (~4.81 Å).

IR Spectroscopy

Polycrystalline samples of **7-12** are characterized by distinctive stretching bands of the cyanide ligand in the frequency range of 2000–2200 cm^{-1}. The trinuclear compounds exhibit two $\nu_{C\equiv N}$ stretches located at 2121(s) and 2094(s) cm^{-1} for **7**, 2131(s) and 2094(s) cm^{-1} for **8**, 2134(s) and 2094(s) cm^{-1} for **9**, and 2138(s) and 2094(s) cm^{-1} for **10**. The band at 2094 cm^{-1}, which is common for all of these compounds, is assigned to the dangling cyanide ligands, whereas the band at higher frequencies is attributed to bridging cyanides.

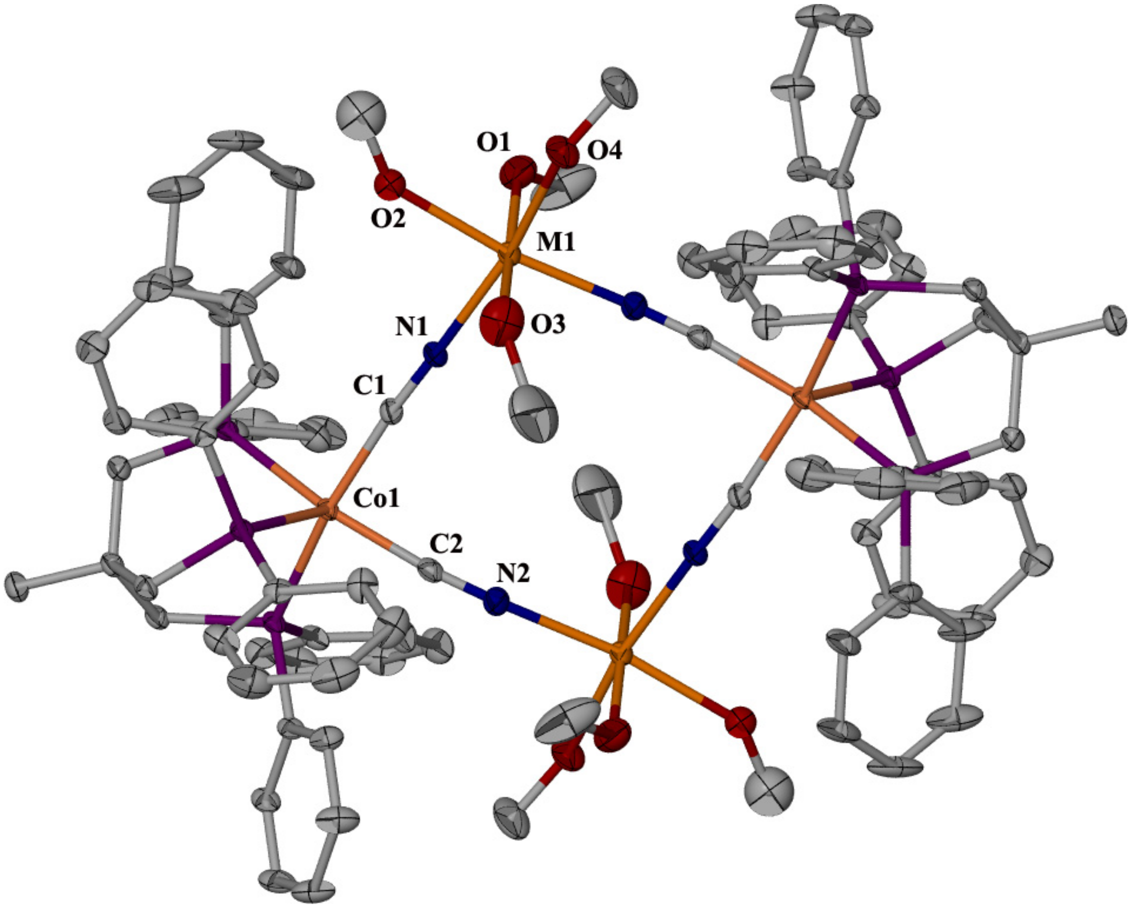

Figure 33. Molecular structure of the tetranuclear complexes **11** and **12**. (Compound **10** is used to make the figure. H atoms are omitted for the sake of clarity.) Thermal ellipsoids are projected at the 50% probability level.

Table 18. Selected bond distances (Å) and angles (°) for compound **11**.

Atoms	**Distance (Å)**	**Atoms**	**Angle(°)**
Co1 – C1	1.877(3)	C1 – Co1 – C2	80.78(13)
Co1 – C2	1.900(3)	C1 – Co1 – P3	160.95(9)
Co1 – P1	2.2473(9)	C2 – Co1 – P3	90.39(9)
Co1 – P2	2.2277(10)	C1 – Co1 – P1	92.92(9)
Co1 – P3	2.2799(9)	C2 – Co1 – P1	167.94(12)
M1 – O1	2.020(3)	P3 – Co1 – P1	89.09(3)
M1 – O2	2.089(2)	C1 – Co1 – P2	101.59(10)
M1 – O3	2.090(3)	C2 – Co1 – P2	109.14(9)
M1 – O4	1.412(6)	P2 – Co1 – P3	92.44(3)
M1 – N1	2.158(4)	P1 – Co1 – P2	90.33(4)
M1 – N2	2.156(4)	O1 – M1 – N2	180.00(17)
C1 – N1	1.158(6)	O1 – M1 – N1	88.17(11)
C2 – N2	1.148(6)	N2 – M1 – N1	91.83(11)
		O1 – M1 – O2	180.0(14)
		N2 – M1 – O2	89.59(12)
		N1 – M1 – O2	90.41(12)
		O2 – M1 – O3	86.14(12)
		N2 – M1 – O3	93.86(12)
		N1 – M1 – O3	180.000(1)
		O2 – M1 – O3	156.9(3)
		O2 – M1 – O4	83.1(4)
		O3 – M1 – O4	81.8(2)

Table 19. Selected bond distances (Å) and angles (^{o}) for compound **12**.

Atoms	**Distance (Å)**	**Atoms**	**Angle(^{o})**
Co1 – C1	1.914(5)	C1 – Co1 – C2	85.0(2)
Co1 – C2	1.907(8)	C1 – Co1 – P3	91.68(16)
Co1 – P1	2.2365(11)	C2 – Co1 – P3	164.52(17)
Co1 – P2	2.2919(14)	C1 – Co1 – P1	164.88(16)
Co1 – P3	2.2262(16)	C2 – Co1 – P1	90.40(15)
M1 – O1	2.098(6)	P3 – Co1 – P1	88.94(6)
M1 – O2	2.102(5)	C1 – Co1 – P2	102.64(16)
M1 – O3	2.086(5)	C2 – Co1 – P2	106.54(17)
M1 – O4	2.194(5)	P2 – Co1 – P3	88.94(5)
M1 – N1	2.104(4)	P1 – Co1 – P2	92.48(5)
M1 – N2	2.115(5)	O1 – M1 – N2	91.16(19)
C1 – N1	1.162(7)	O1 – M1 – N1	97.4(2)
C2 – N2	1.147(7)	N2 – M1 – N1	97.50(17)
		O1 – M1 – O2	81.7(4)
		N2 – M1 – O2	176.27(18)
		N1 – M1 – O2	85.98(17)
		O2 – M1 – O3	172.3(2)
		N2 – M1 – O3	91.4(2)
		N1 – M1 – O3	89.5(2)
		O2 – M1 – O3	92.44(19)
		O2 – M1 – O4	84.1(8)
		O3 – M1 – O4	81.7(2)

The tetranuclear compounds exhibit two bands located at 2132(s) and 2106(w) cm^{-1} for **11** and 2148(s) and 2106(w) cm^{-1} for **12**, which are similar to previously reported data for the tetranuclear complexes $\{[\mathrm{Co}^{\mathrm{II}}(\mathrm{triphos})(\mathrm{CN})_2][\mathrm{MCl}_2]\}$.[110] The $\nu_{\mathrm{C\equiv N}}$ stretches of the compounds **11-12** appear at higher frequencies as compared to the stretches observed for the trinuclear family due to stronger backbonding between the cyanide ligand and the octahedral metal center since the C–N–M angle in the tetranuclear clusters (167°) is much closer to 180° than the angles for the trinuclear family of compounds (~150°).

Magnetic Properties

Magnetic susceptibility measurements were performed on crushed polycrystalline samples in the temperature range of 2-300 K at an applied magnetic field of 1000 Oe. The DC magnetic susceptibility measurements performed on the parent complex, $\mathrm{Co(triphos)(CN)_2}$, have been discussed previously in Chapter II.[110] The χT value is 0.41 $\mathrm{emu{\cdot}mol^{-1}{\cdot}K}$ at 300 K and remains constant over the entire temperature range of 2-300 K. Such behavior is typical of a simple paramagnet with an $S = 1/2$ ground state and $g = 2.10$. This g-value was kept fixed for the low-spin Co(II) centers in modeling the behavior of the tri- and tetranuclear complexes discussed in the following sections.

$\{[\mathrm{Co(triphos)(CN)_2}]_2[\mathrm{M(MeOH)_4}]\}(\mathrm{ClO_4})_2$ (7-10). The room temperature χT value for **7** is 5.11 $\mathrm{emu{\cdot}mol^{-1}{\cdot}K}$ which is close to the value expected for two low-spin Co(II) ions

(S = 1/2, $\chi T = 0.41$) and one high spin Mn(II) ion in the absence of magnetic coupling. The χT value continuously decreases upon cooling and reaches a minimum of 1.85 emu·mol^{-1}·K at 4 K, indicating an antiferromagnetic interaction between the Co(II) and Mn(II) centers (Figure 34). An examination of the ground state spin for **7** was carried out by performing field dependent magnetization measurements at 1.8 K. The magnetization curve approaches a saturation value of 2.98 μ_B, in accord with the ground state spin value of $S = 3/2$ expected from antiferromagnetic coupling (Figure 35). A simulation of the magnetic data was carried out using MAGPACK, by applying Hamiltonian (4) in the limit of isotropic exchange interactions.

$$\boldsymbol{H} = \mu_B H_z(2g_{\mathrm{Co}}\boldsymbol{S}_{z,\mathbf{Co}} + g_{\mathrm{M}}\boldsymbol{S}_{z,\mathbf{M}}) - 2J(\boldsymbol{S}_{\mathbf{Co1}} + \boldsymbol{S}_{\mathbf{Co2}})\cdot(\boldsymbol{S}_{\mathbf{M}}) + D[\boldsymbol{S}^{\mathbf{2}}_{z,\mathbf{M}} - 1/3\boldsymbol{S}_{\mathbf{M}}(\boldsymbol{S}_{\mathbf{M}} + 1)] \qquad (4)$$

where g_{Co} was fixed at 2.10, as found for the mononuclear Co(triphos)(CN)$_2$ precursor. The best fit was obtained with $g_{\mathrm{Mn}} = 2.02$, $D = -0.13$ cm^{-1}, and J = –4.8 cm^{-1}. The field- and temperature-dependent magnetization data were satisfactorily simulated with ANISOFIT[121] for the $S = 3/2$ ground state with $D_{\mathrm{GS}} = -0.08$ cm^{-1} (Figure 35).

The room temperature χT value for compound **8** is 4.86 emu·mol^{-1}·K, which is higher than the expected spin-only value of 3.9 emu·mol^{-1}·K for two isolated low-spin Co(II) centers and high-spin Fe(II) center. The deviation is explained by an orbital contribution from the $S = 2$ Fe(II) ion (Figure 36a). The χT decreases slowly upon cooling down to 20 K and then more abruptly below 20 K due to zero field splitting (zfs)

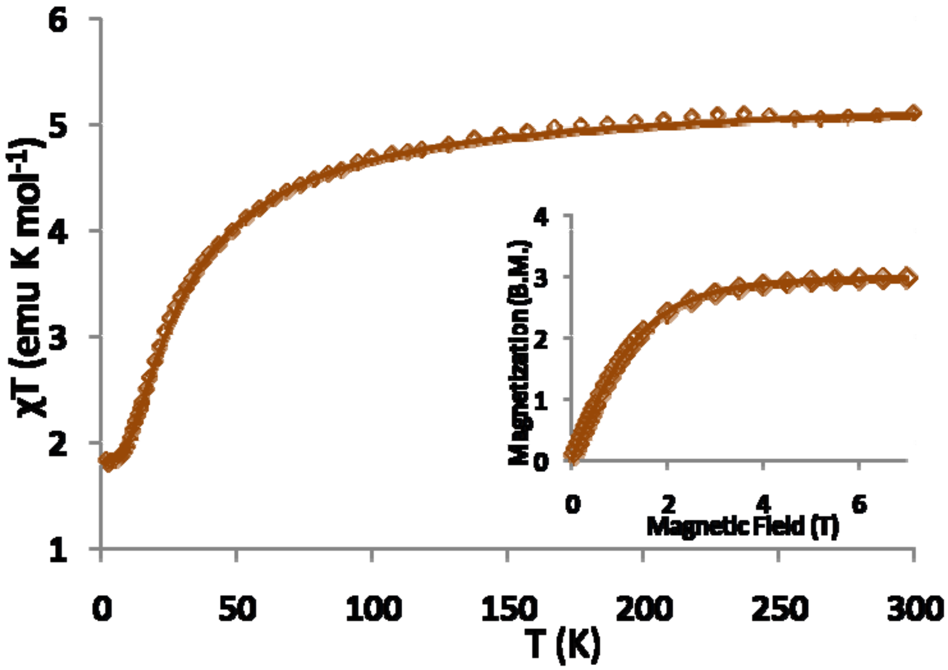

Figure 34. Temperature dependence of χT for **7** (see text). Inset: Magnetization measurement performed at 1.8 K. The solid lines correspond to the simulations by the Magpack program according to Eq. 4 (see text).

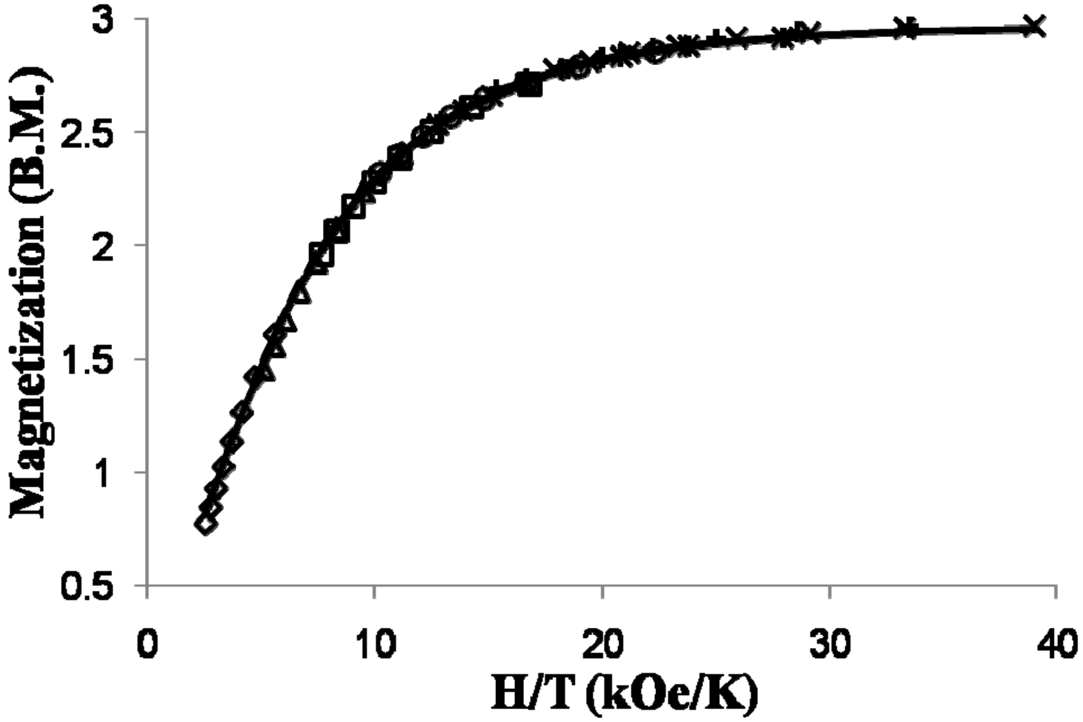

Figure 35. Plot of *M* vs *H*/*T* for **7** in the 1-7 T field range from 1.8 to 3.9 K. The solid lines represent the best fit to the parameters $g_{Mn^{II}}$ = 2.02, *D* = –0.13 cm^{-1}.

effects, reaching the minimum of 3.00 emu·mol^{-1}·K at 1.8 K. The magnetization value at 1.8 K and 7 kOe is 5.31 μ_B, which is higher than the expected ground state spin value (S = 1) from antiferromagnetic coupling. The magnetization curve recorded at 1.8 K shows gradual increase in the magnetization value that does not exhibit saturation and reaches the maximum of 5.31 μ_B at 7 T. Both temperature- and field-dependent behavior suggest that magnetic exchange between the Co(II) and Fe(II) ions is rather weak. Indeed, using Hamiltonian (4), the best fit to the experimental data was obtained with $g_{Fe} = 2.20$, $D_{Fe} = –2.7$ cm^{-1}, and $J = –0.6$ cm^{-1}.An examination of field dependent magnetization at different temperatures revealed that the **8** cluster is characterized by significant magnetic anisotropy (Figure 37).

For compound **9**, χT is 3.36 emu K mol^{-1} at 300 K and 2.18 emu·K·mol^{-1} at 1.8 K (Figure 36b). The high temperature value is higher than the spin-only value of 2.7 emu·K·mol^{-1} expected for two $S = 1/2$ Co(II) and one $S = 3/2$ Co(II) centers in the absence of magnetic interactions. This deviation is caused by the typical orbital contribution of the high-spin Co(II) ion. Similarly to the cluster **8**, the magnetization curve at 1.8 K does not exhibit saturation and reaches the maximum value of 5.53 μ_B at 7 T. Theoretical simulation according to Hamiltonian (4) resulted in the best-fit values of $g_{Co} = 2.21$, $D_{Co} = –1.3$ cm^{-1}, and $J = –0.4$ cm^{-1} (Figure 38, Table 20). Note that the latter value can be underestimated because spin-orbit coupling and crystal field splitting effects were not included in the model to avoid overparametrization. Nevertheless, the resulting magnetic behavior is reproduced reasonably well with the proposed model.

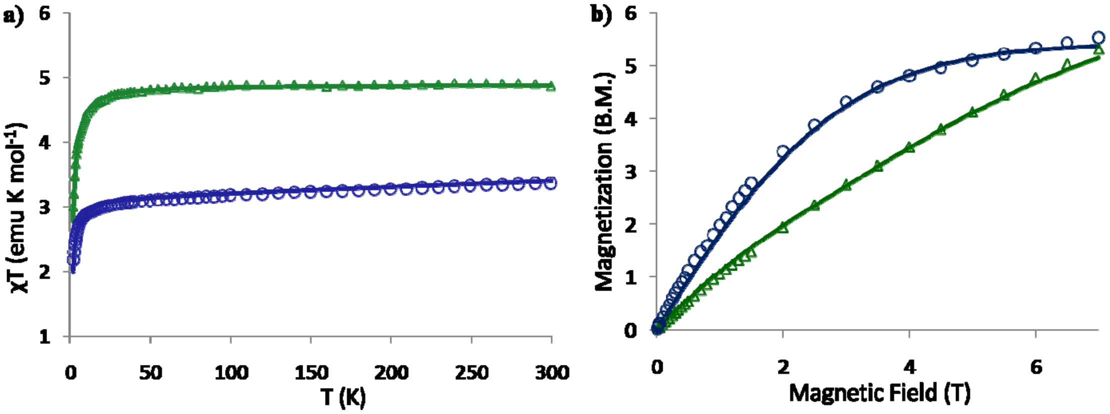

Figure 36. a) Temperature dependence of χT for **8** **(○)** and **9** **(Δ)**. b) Magnetization measurements performed at 1.8 K. The solid lines correspond to the simulations by Magpack program according to Eq. 4 (see text).

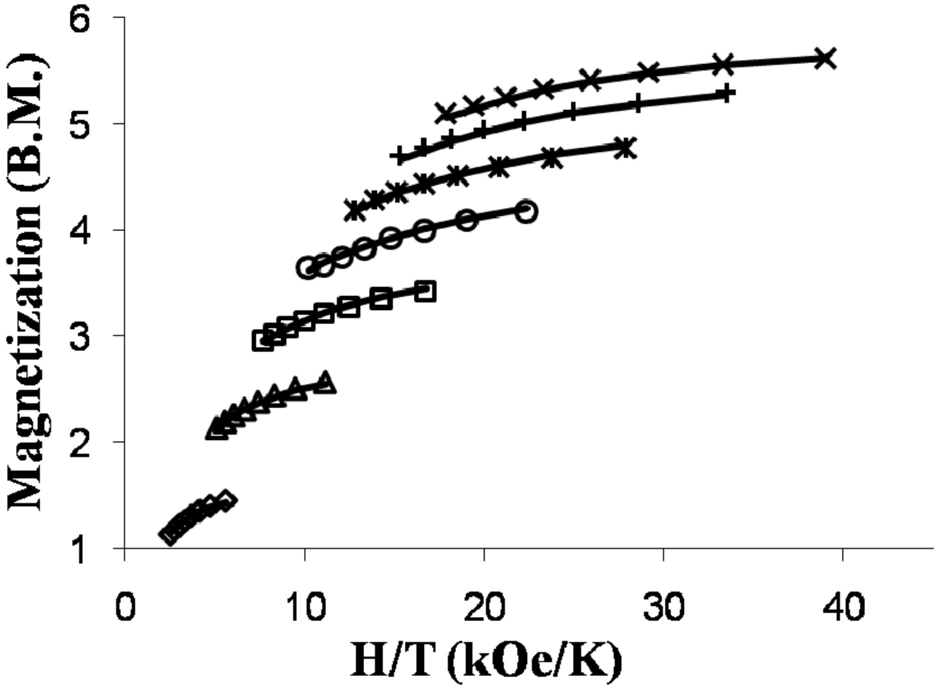

Figure 37. Plot of M vs H/T for **8** in the 1-7 T field range from 1.8 to 3.9 K. The solid lines represent the best fit to the parameters $g_{FeII} = 2.20$, $D = -2.7\ \mathrm{cm}^{-1}$.

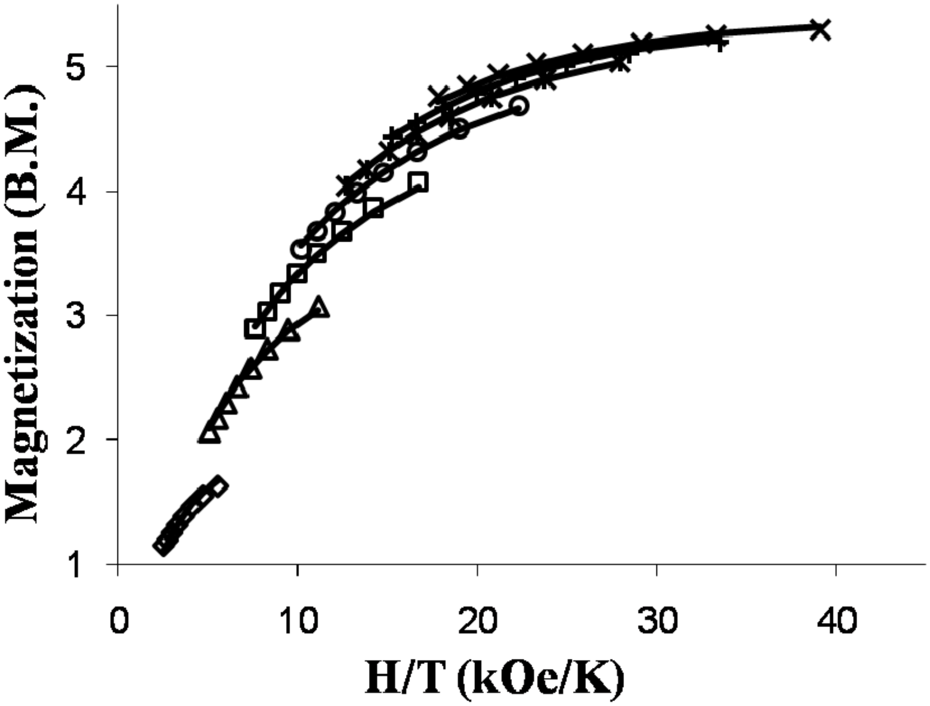

Figure 38. Plot of *M* vs *H*/*T* for **9** in the 1-7 T field range from 1.8 to 3.9 K. The solid lines represent the best fit to the parameters g_{CoII} = 2.21, *D* = –1.3 cm^{-1}.

Table 20. Magnetic properties of the trinuclear compounds, **7-10**.

Compound	g_{M}	D_{M} (cm^{-1})	J (cm^{-1})	Ground state	D_{GS} (cm^{-1})
7	2.02	–0.13	–4.8	$S = 3/2$	–0.08
8	2.20	–2.7	–0.6	$S = 1$	–1.4
9[a]	2.21	–1.3	–0.4	$S = 1/2$	–0.9
10	2.22	–6	+3.0	$S = 2$	–3.4

a) Temperature independent paramagnetic contribution (TIP) ($\chi_{\mathrm{TIP}} = 8.95 \times 10^{-4}$) is applied to fit the χT vs T plot of **9**.

For **10**, the χT product is 2.08 emu·K·mol^{-1} at 300 K, which is slightly higher than the sum of spin-only values for two Co(II) and one Ni(II) ions. The χT value increases with lowering temperature and reaches the maximum of 2.71 emu·K·mol^{-1} at 6 K, indicating ferromagnetic interactions between the Co(II) and Ni(II) centers and stabilization of the S = 2 ground state at low temperatures (Figure 39). The abrupt decrease of χT below 6 K could be attributed to zero-field splitting effects and/or intermolecular interactions. The field dependent magnetization curve attains the maximum value of 4.06 μ_B, which confirms the S = 2 ground state. The magnetic data were simulated with MAGPACK according to (4), resulting in the best-fit values of g_{Ni} = 2.22, D = –6 cm^{-1}, and J = 3.0 cm^{-1} (Table 20). An accurate measurement of the ground-state zfs parameter was obtained by fitting the field-dependent magnetization data at different temperatures using the ANISOFIT program,[121] which yielded D = –6 cm^{-1} with g = 2.22 (Figure 40). The poor fit of the field- and temperature-dependent magnetization data could be due to the presence of low-lying excited states which arise due to the relatively low vaule of the magnetic exchange constant. It must be added that an unusually high D value of –8 cm^{-1} was also observed in the previously reported Co_2Ni_2 square, $\{[Ni^{II}Cl_2]_2[Co^{II}(triphos)(CN)_2]_2\}$[110] that contains the same metal ions as **10**.

$\{[Co(triphos)(CN)_2]_2[M(MeOH)_4]_2\}(BF_4)_4$ (11, 12; M= Mn, Ni). The magnetic behavior for **11** is virtually identical to that of the tetranuclear cluster, $\{[Co(triphos)(CN)_2]_2[MnCl_2]_2\}$ previously reported by our group.[110] The χT *vs. T* plot

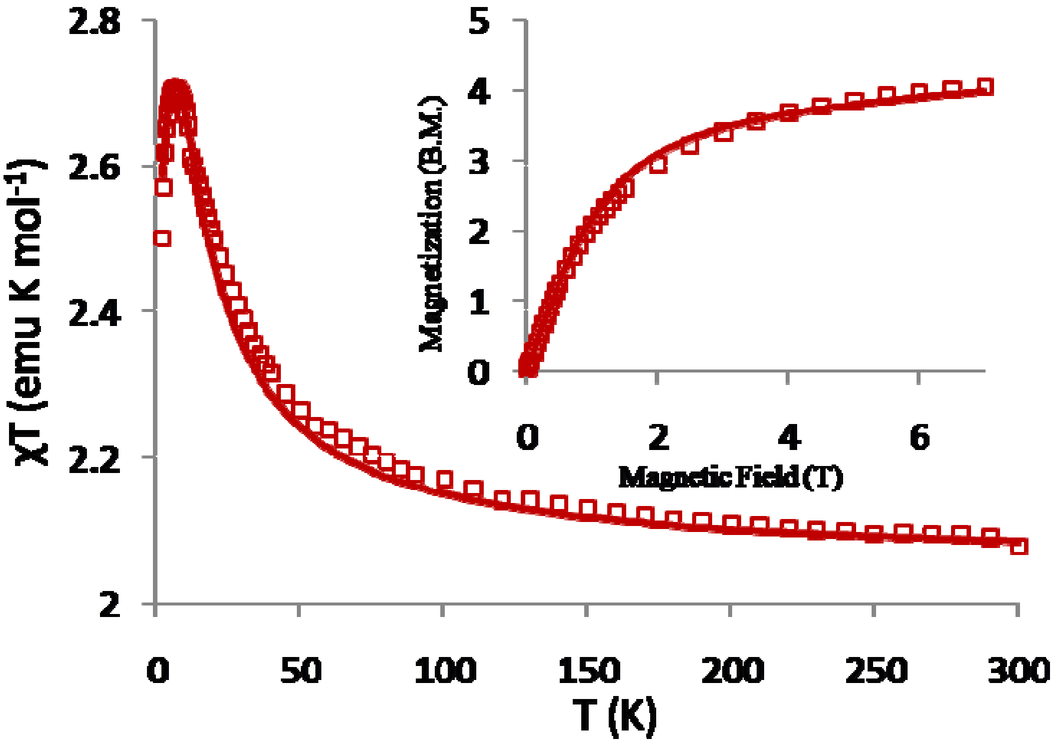

Figure 39. Temperature dependence of the χT product for **10**. Inset: Magnetization measurement performed at 1.8 K. The solid lines correspond to the simulations with the Magpack program according to Eq. 4 (see text).

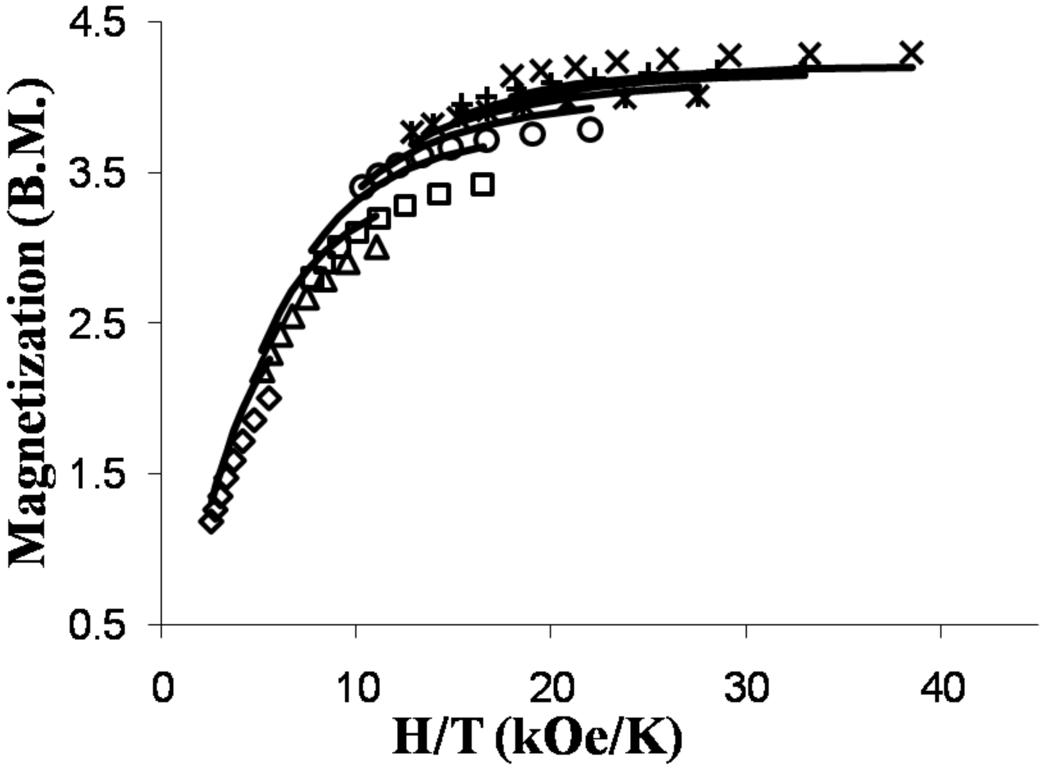

Figure 40. Plot of *M* vs *H*/*T* for **10** in the 1-7 T field range from 1.8 to 4 K. The solid lines represent the best fit to the parameters $g_{Ni^{II}}$ = 2.22, *D* = –6 cm^{-1}.

exhibits a room temperature value of 9.41 emu·K·mol^{-1}, which is in good agreement with the expected value (9.56 emu·K·mol^{-1}) for two Co(II) (S = 1/2) and two Mn(II) ions (S = 5/2) in the absence of magnetic coupling (Figure 41). The χT value decreases with cooling until ~ 45 K due to antiferromagnetic interactions between the metal spins. Below 45 K, χT increases to reach a maximum of 10.36 at 3 K, which is consistent with stabilization of an S = 4 ground state. The field-dependent magnetization curve measured at 1.8 K reaches a saturation value of 8.16 μ_B, which is also in support of an S = 4 ground state as a result of antiferromagnetic coupling. A fitting of magnetic data was performed using MAGPACK by treating all the interactions between Mn(II) and Co(II) spins as isotropic and identical:

$$\boldsymbol{H} = 2\mu_B H_z(g_{\mathrm{Co}}\boldsymbol{S}_{z,\mathbf{Co}} + g_{\mathrm{M}}\boldsymbol{S}_{z,\mathbf{M}}) - 2J(\boldsymbol{S}_{\mathbf{Co1}} + \boldsymbol{S}_{\mathbf{Co2}})\cdot(\boldsymbol{S}_{\mathbf{M1}} + \boldsymbol{S}_{\mathbf{M2}}) + 2D[\boldsymbol{S}^{\mathbf{2}}_{z,\mathbf{M}} - 1/3\boldsymbol{S}_{\mathbf{M}}(\boldsymbol{S}_{\mathbf{M}} + 1)] \qquad (5)$$

The resulting best-fit values are g_{Mn} = 2.05, D_{Mn} = –0.3 cm^{-1}, and J = –6.8 cm^{-1} (Figure 42, Table 21). The higher magnetic exchange constant as compared to that found for **7** is explained by the lower degree of distortion of the Co–CN–Mn bridge in **11** and, consequently, stronger interaction between the magnetic orbitals of the Co(II) and Mn(II) centers.

The χT value of 3.42 emu·K·mol^{-1} observed for **12** at 300 K is slightly higher than the expected value of 2.82 emu·K·mol^{-1} for two low-spin Co(II) (S = 1/2) and two high-spin Ni(II) non-interacting ions (S = 1); the deviation is explained by the orbital

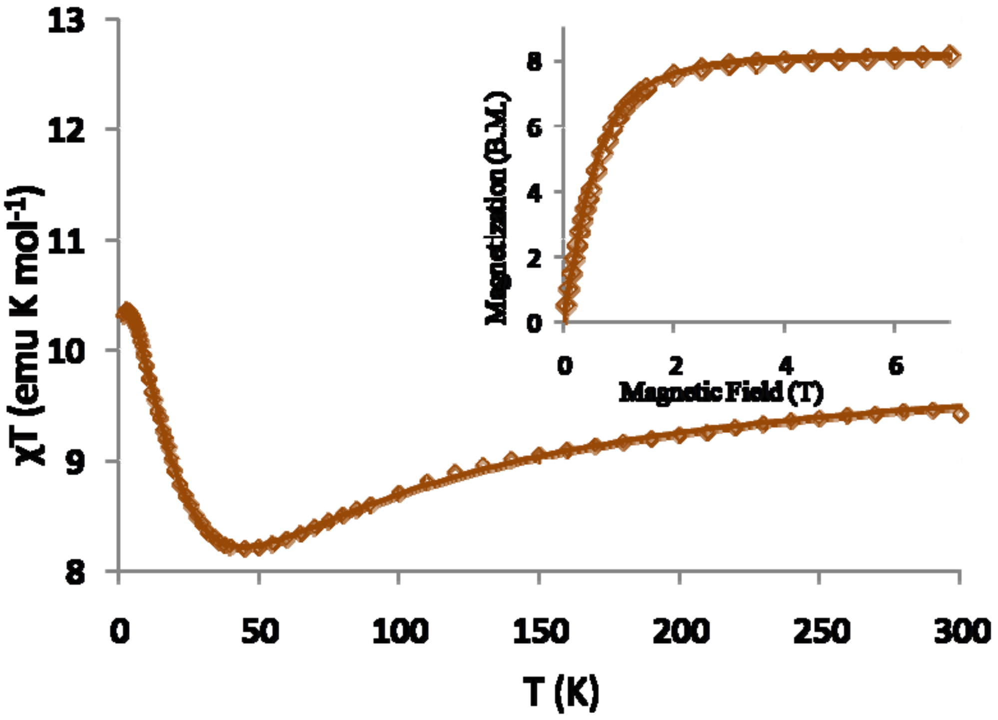

Figure 41. Temperature dependence of χT for **11**. Inset: Magnetization measurements performed at 1.8 K. The solid lines correspond to the simulations by the Magpack program according to Eq. 5 (see text).

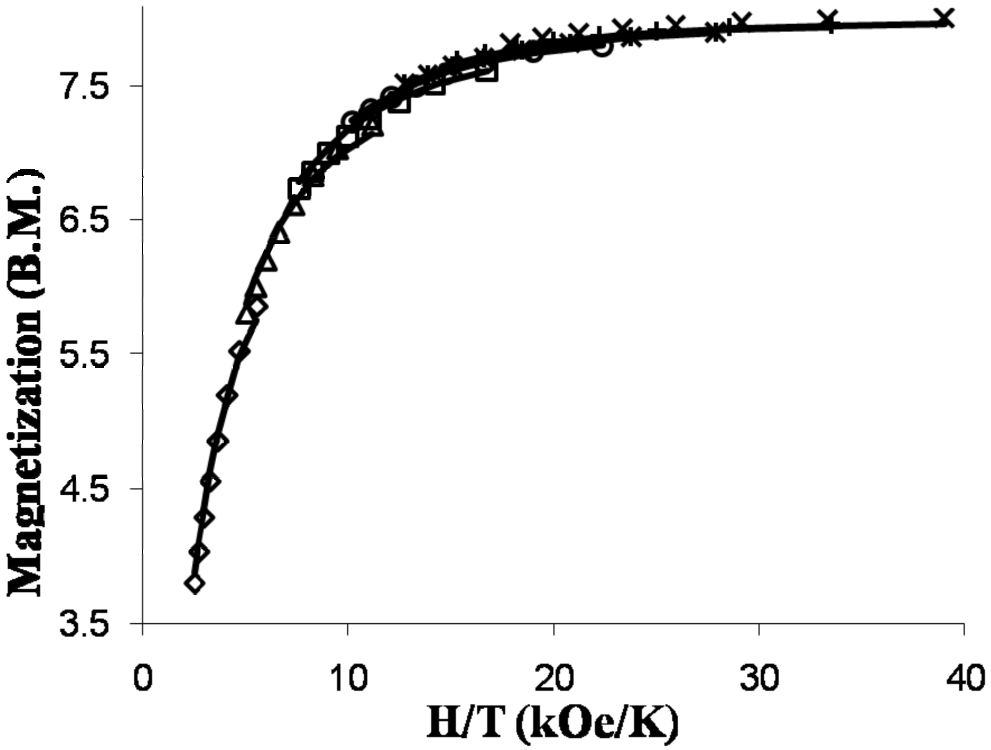

Figure 42. Plot of *M* vs *H*/*T* for **11** in the 1-7 T field range from 1.8 to 4 K. The solid lines represent the best fit to the parameters g_{MnII} = 2.05, D = –0.30 cm^{-1}.

Table 21. Magnetic properties of the tetranuclear compounds, **11** and **12**.

Compound	g_M	D_M (cm^{-1})	J (cm^{-1})	Ground state	D_{GS} (cm^{-1})
11	2.05	–0.3	–6.8	$S = 3/2$	–0.18
12	2.28	–1.4	–0.8	$S = 1$	–0.8

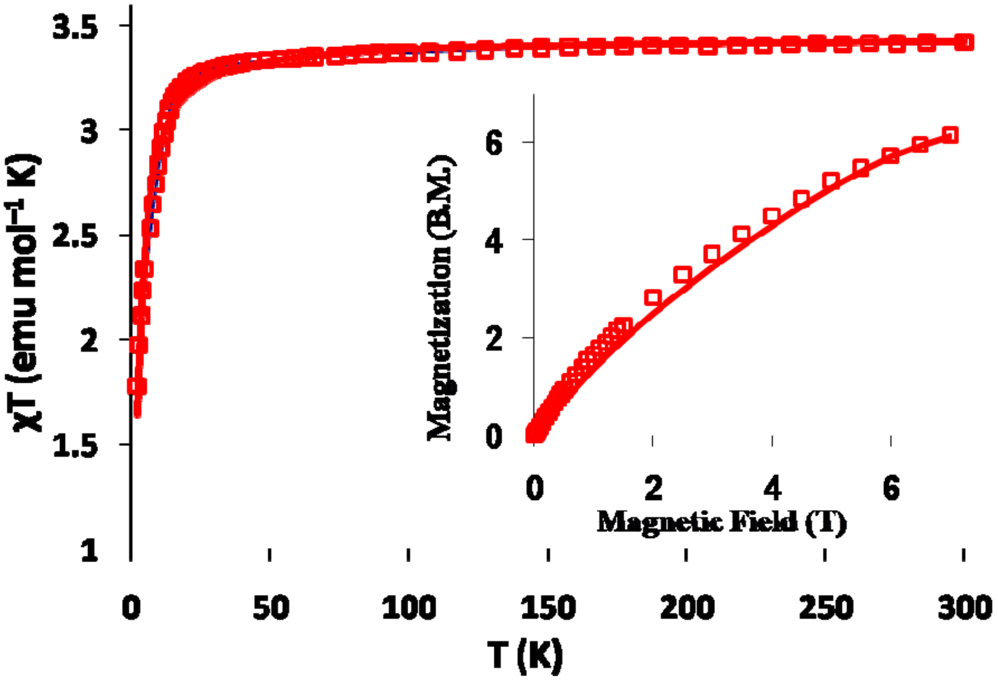

Figure 43. Temperature dependence of χT for **12**. Inset: Magnetization measurement performed at 1.8 K. The solid lines correspond to simulations by the Magpack program according to Eq. 5 (see text).

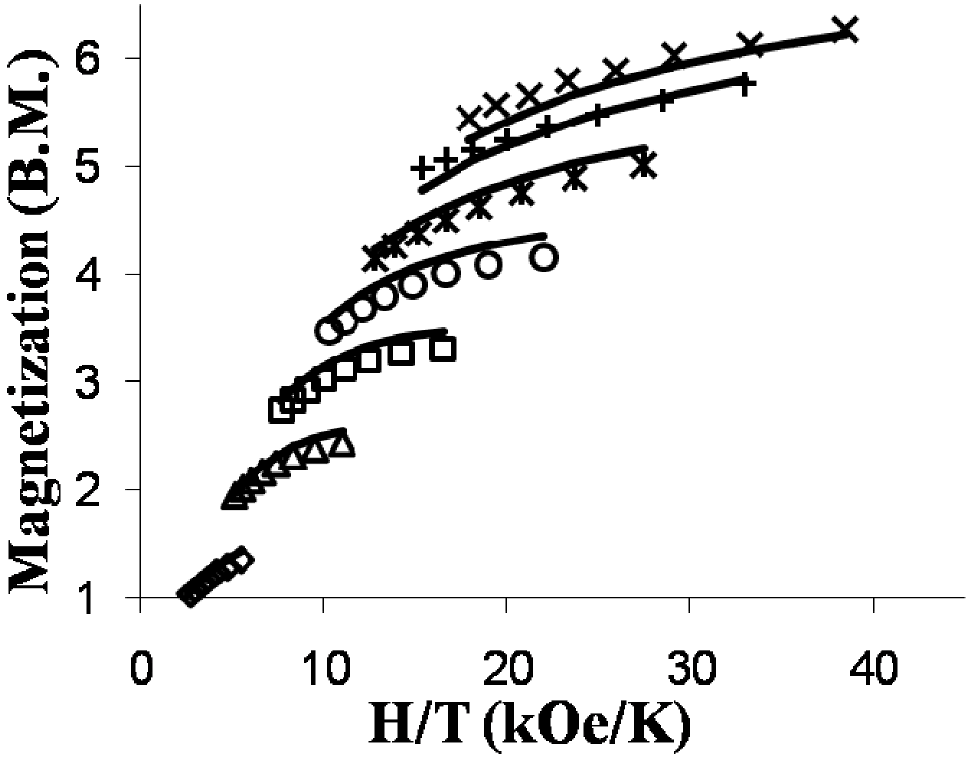

Figure 44. Plot of *M* vs *H*/*T* for **12** in the 1-7 T field range from 1.8 to 4 K. The solid lines represent the best fit to the parameters $g_{NiII} = 2.28$, $D = -1.4$ cm^{-1}.

contributions of the Ni(II) ions. Overall, the temperature dependence of χT is similar to that of the Co_2Ni_2 square, $\{[M^{II}Cl_2]_2[Co^{II}(triphos)(CN)_2]_2\}^{110}$, in which the χT value gradually decreases with lowering temperature indicating the presence of an antiferromagnetic interaction between the Co(II) and Ni(II) ions (Figure 43). The best fit to the theoretical model described with Hamiltonian (2) was obtained with parameters $g_{Ni} = 2.28$, $D_{Ni} = -1.4$ cm^{-1}, and $J = -0.8$ cm^{-1} (Table 21). Temperature- and field-dependent magnetization data were simulated with ANISOFIT[121] to yield best-fit parameters of $g = 2.28$ and $D_{GS} = -1.4$ cm^{-1} for the $S = 1$ ground state (Figure 44).

Interestingly, the change in the topology of magnetic centers results in the dramatic change in the type of magnetic superexchange, from ferromagnetic in the trimer **10** to antiferromagnetic in the square **12**. Obviously, the origin of such a change should be sought in the overlaps between magnetic orbitals in these clusters. To understand the difference in magnetic behavior of **10** and **12**, we carried out a theoretical study of magnetic superexchange in the tri- and tetranuclear complexes described herein.

Density Functional Theory Studies

Singly occupied molecular orbitals, the magnetic orbitals for the highest spin state of the considered systems, can be obtained by DFT calculations. For simplicity, the phenyl groups of the triphos ligands were replaced with H atoms. Calculations performed on the mononuclear precursor (Figure 45) and on the family of trinuclear and tetranuclear clusters have shown that the spin density of the pentacoordinate Co(II) ion is located predominantly on the d_{z^2} orbital, which is oriented toward the axial P atom

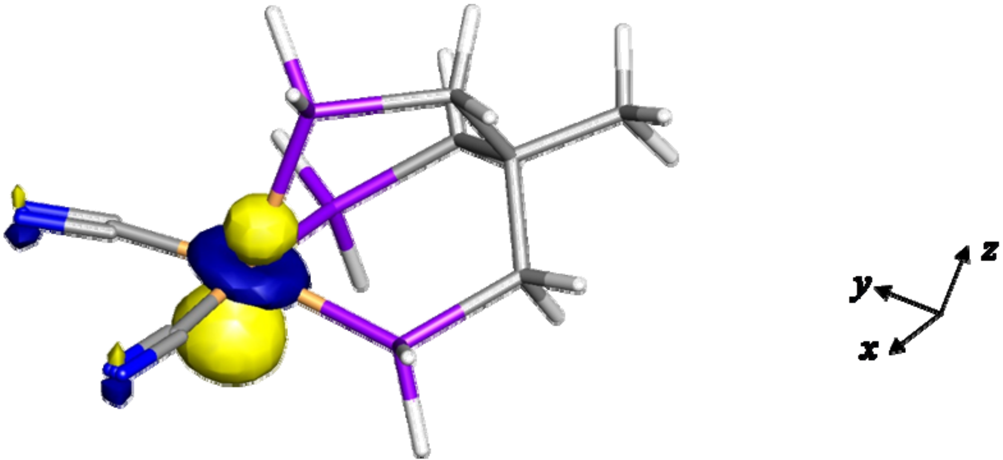

Figure 45. Magnetic molecular orbital of the Co^{II}(triphos)(CN)$_2$ precursor.

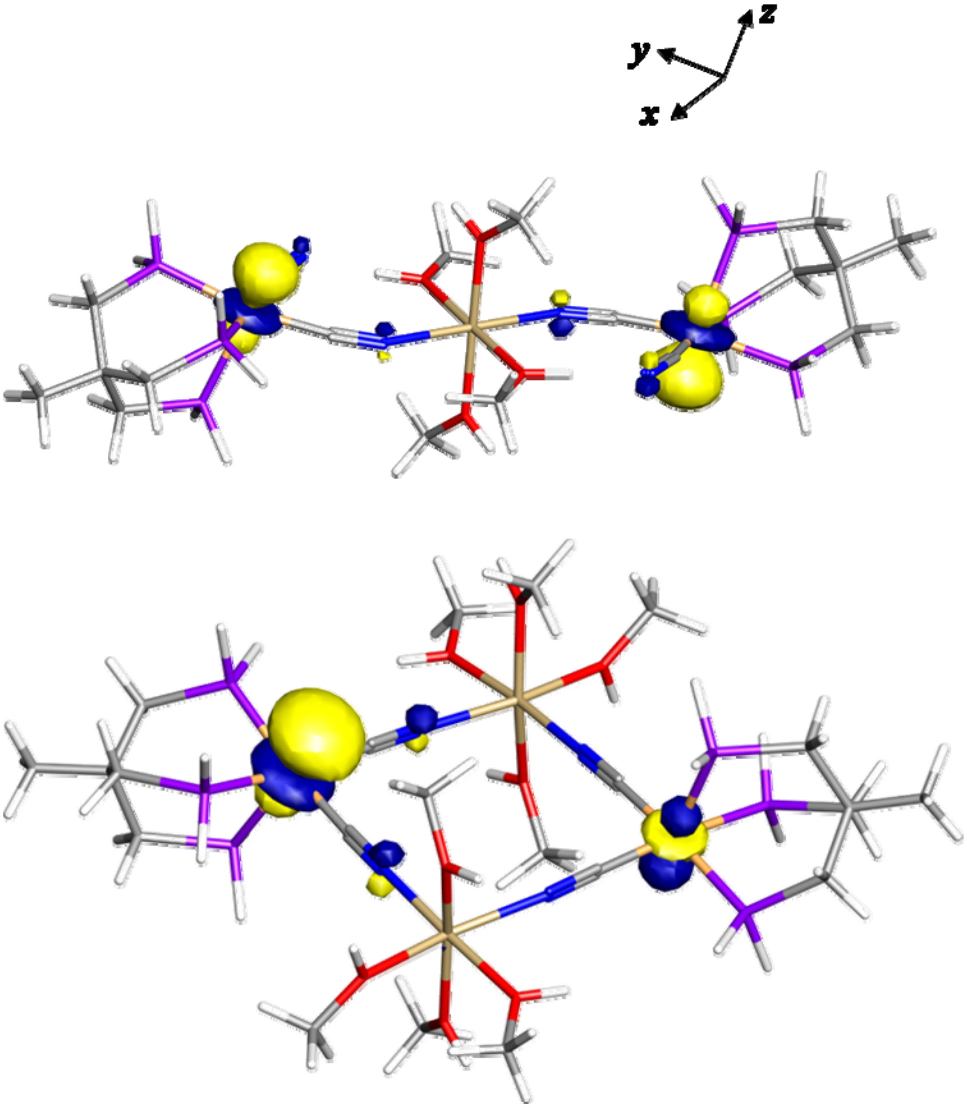

Figure 46. Magnetic molecular orbitals of the trinuclear (**7**) and tetranuclear (**11**) complexes on the Co(II) site.

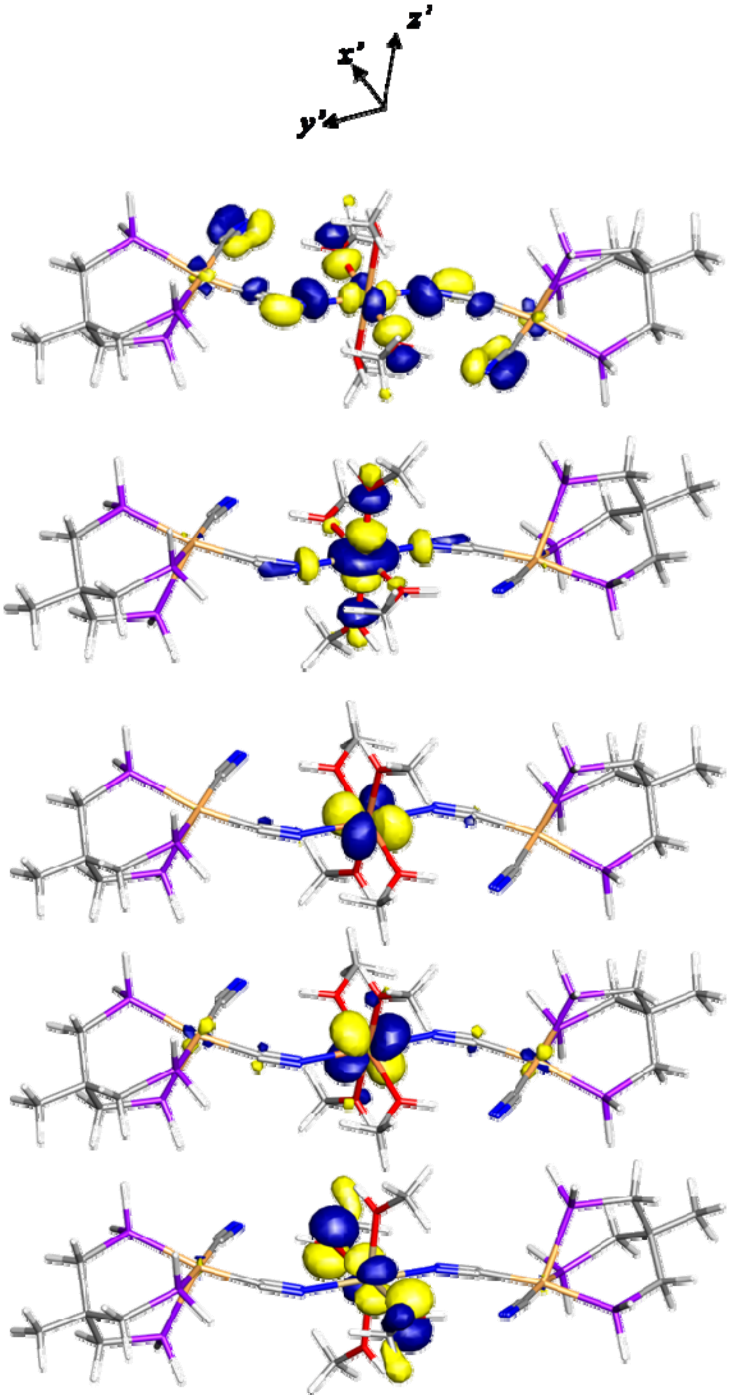

Figure 47. Magnetic molecular orbitals of **7** located on the internal octahedral M(II) site.

(Figure 46). Figure 47 shows magnetic molecular orbitals of the trinuclear clusters located on the M(II) site. In contrast to previously reported clusters containing e_g type magnetic orbitals that delocalize onto the σ orbital ($3a_1$) of the cyanide ligand, the "e_g-like" d_{z^2} orbital of the Co(II) ion delocalizes onto the π* orbital (2*e*) of the cyanide ligand. This conclusion is valid for both trinuclear and tetranuclear clusters. It is the orientation of the d_{z^2} orbital, which is not perpendicular to the σ orbital of the cyanide ligand (the P_{axial}–Co–C angle is ~105°), that is responsible for this unusual interaction. On the other hand, the e_g and t_{2g} type orbitals located on the central octahedral metal site of trinuclear clusters interact with the σ and π* orbitals of the cyanide ligand, respectively. Let us consider the orbital overlaps along the *x* axis of the trimers **7-10** that coincides with the direction of the Co–CN–M bridge. Since the d_{xz} orbital of the central metal atom and the d_{z^2} orbitals of the Co(II) sites delocalize into the π* orbital of CN^-, antiferromagnetic coupling is predicted between these orbitals. Nevertheless, ferromagnetic contribution is also present since the remaining orbitals of the central M atom delocalize into the other type of cyanide orbitals that do not overlap with the magnetic d_{z^2} orbital of the Co(II) site. Note that the bending of the bridging cyanide ligand increases the overlap of σ and π systems resulting in a weaker ferromagnetic coupling between orthogonal orbitals of adjacent metal ions. Therefore, a competition between the two opposing couplings is operative for the trinuclear systems, **7**, **8**, and **9**, in which the central atom has unpaired spin density in both e_g and t_{2g} type orbitals. The antiferromagnetic contribution dominates, as typically observed in such cases,[140] reaching the most negative value of *J* for **7**. On the other hand, the superexchange interaction between Co(II) and Ni(II) ions in **10** should be ferromagnetic due to the lack of unpaired spins in the t_{2g} type orbitals of the central Ni(II) ion. This conclusion agrees with the experimentally observed behavior of the complexes **7-10** (Table 20).

Compound **11** behaves similarly to **7** since the same symmetry considerations are also valid for tetranuclear clusters (Figure 48). The larger exchange coupling value can be attributed to less bending in the bridging cyanide ligands. For **12**, the magnetic orbitals delocalize on different orbitals of cyanide molecule suggesting ferromagnetic interactions, while the magnetic data indicate the presence of antiferromagnetic interactions. An examination of the calculated isosurfaces of difference density (Figure 49) allows rationalization of not only the magnetic orbitals but also spin polarization by comparing the excess α and β spin densities. As expected, the excess α spin density is localized on the metal centers and the bridging cyanide ligands. Furthermore, the presence of *excess* β spin density suggests spin polarization onto the σ orbital of cyanide ligands as well as the $d_{x^2-y^2}$ orbital of Co(II) sites due to additional spin densities on these orbitals. Such delocalization is not observed for the trinuclear complexes, most probably due to the stronger distortion of the Co–CN–M bridge that restricts the orbital overlap. A possible reason for spin polarization in the tetranuclear complex **12** is the interaction of e_g orbitals of Ni(II) ion with the $d_{x^2-y^2}$ orbital of Co(II) sites through the σ orbital of cyanide ligand due to nonorthogonality of these orbitals, which could result in lowering the energy of $d_{x^2-y^2}$ orbital of Co(II) site and therefore the mixing of the $d_{x^2-y^2}$

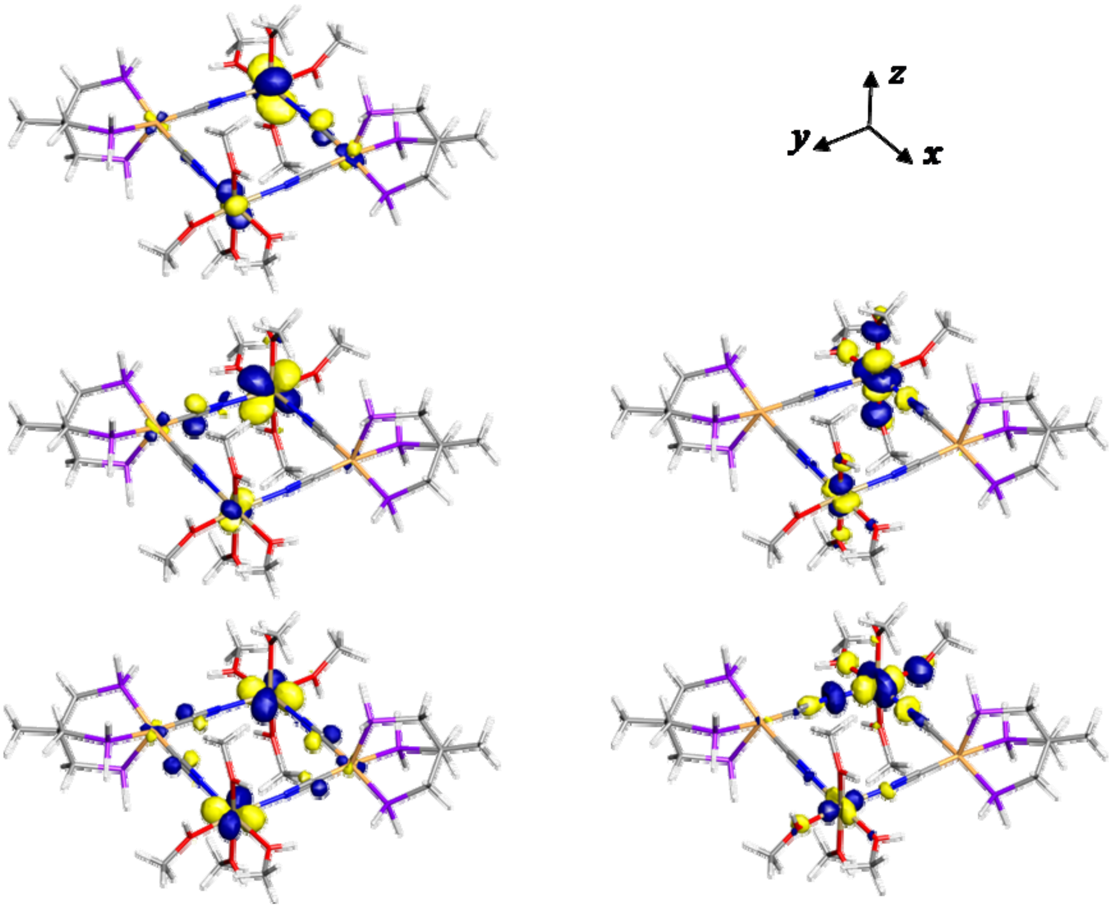

Figure 48. Magnetic molecular orbitals of **11** located at the octahedral M(II) sites.

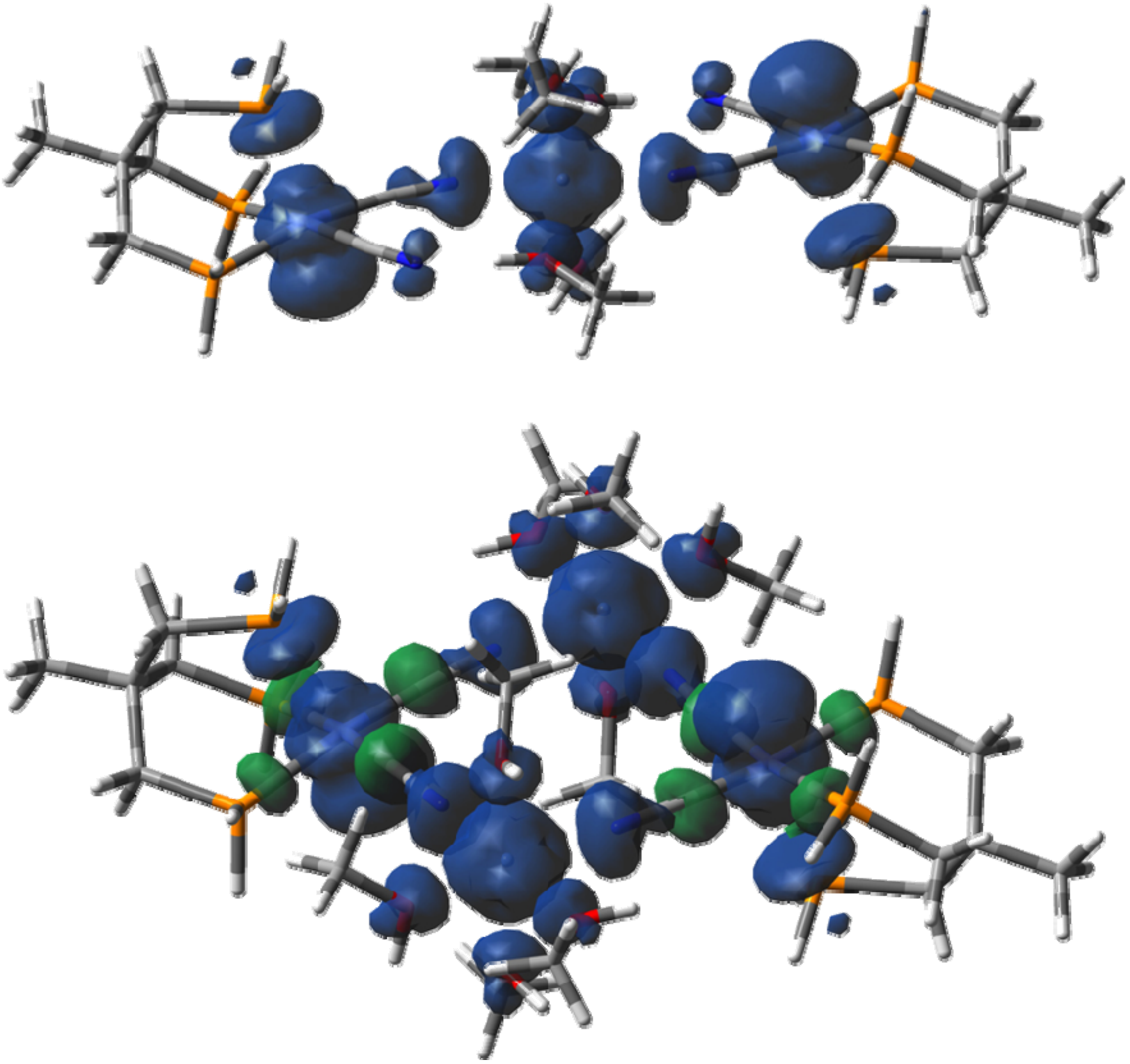

Figure 49. Isosurfaces of difference densities of **10** (top) and **12** (bottom). Spin densities of excess *α* orbitals are represented by blue and those of *β* orbitals are represented in green. Spin densities are displayed at an isosurface value of ±0.0015.

orbital with the e_g orbitals of Co(II) site. The aforementioned spin polarization could be the origin of antiferromagnetic contribution to superexchange in **12**. Thus, the weak antiferromagnetic coupling ($J = -0.8$ cm^{-1}) observed in this complex is a result of the competing antiferromagnetic and ferromagnetic interactions between the Ni(II) and Co(II) ions caused by the e_g-$d_{x^2-y^2}$ and e_g-d_{z^2} orbital combinations, respectively.

CONCLUSIONS

The reactions of $Co^{II}(triphos)(CN)_2$ with solvated 3*d* metal ions yielded a family of cationic trinuclear and tetranuclear complexes. Three trimers of the general formula $\{[Co^{II}(triphos)(CN)_2]_2[M^{II}(CH_3OH)_4]\}^{2+}$ (**7-10**) exhibit antiferromagnetic coupling between the Co(II) and M(II) centers while $\{[Co^{II}(triphos)(CN)_2]_2[M^{II}(CH_3OH)_4]\}(BF_4)_2$ (**10**) exhibits ferromagnetic coupling. The results of computational studies, which were undertaken to understand the nature of magnetic interactions in these complexes, are also in reasonable accord with magnetic data. Since the interaction of the d_{xz} orbital of the M(II) ion with the magnetic d_{z^2} orbital of the Co(II) ion through the π* orbital of the cyanide ligand is responsible for antiferromagnetic coupling, the complex **10** is the only cluster that exhibits ferromagnetic superexchange due to the lack of unpaired electrons in the t_{2g} type orbitals of the Ni(II) center.

Tetranuclear complex, $\{[Co^{II}(triphos)(CN)_2]_2[Mn(CH_3OH)_4]_2\}^{4+}$ (**11**) exhibits antiferromagnetic interactions between the metal centers, which is also supported by theoretical studies. Contrary to the behavior of **10**, **12** exhibits antiferromagnetic interactions between the Co(II) and Ni(II) ions. The difference in the nature of the magnetic superexchange in these Co^{II}-CN-Ni^{II} containing products is explained by the spin density maps, which suggest spin polarization onto the cyanide ligand for **12** but not for **10** due to the unusual bending of the M'–N–C angle (~145^{o}) in the latter case.

In addition to their interesting magnetic properties, the reported complexes hold significant promise as precursors for systematic preparation of higher nuclearity clusters or extended networks. The high solubility in common polar solvents and availability of labile coordinated solvent molecules render these tri- and tetranuclear species excellent building blocks for the assembly of more complex magnetic clusters.

CHAPTER IV

DERIVATIZATION OF SINGLE MOLECULE MAGNETS TO ENHANCE THEIR PHYSICAL AND MAGNETIC PROPERTIES

INTRODUCTION

The identification of $[Mn_{12}O_{12}(O_2CMe)_{16}(H_2O)_4]$ (Mn_{12}-acetate) compound in 1993 as a molecular nanomagnet initiated a new concept, so-called single-molecule magnetism, in the field of molecular magnetism.[44,45,147] Single molecule magnets (SMMs) have received much attention due to their possible applications in quantum computing and data information storage since they exhibit slow paramagnetic relaxation and hysteresis suggesting a bistable magnetic behavior.[47] The studies performed on the Mn_{12}-acetate compound indicated that the origin of the bistability is the combination of a large ground state spin value (S) and a negative uniaxial magnetic anisotropy (–D). Many examples of SMMs, with different S and D values, have been prepared by incorporating other paramagnetic metal ions and suitable bridging ligands and have led to increased understanding of this phenomenon.[52,54-56,91,95,147-156]

A different approach to designing entirely new SMMs is the modification of known SMMs in a controlled fashion. This method has been successfully used to prepare derivatives of the Mn_{12}-acetate SMM with essentially the same $[Mn_{12}(\mu_3\text{-}O)_{12}]$ core by substituting the periphery ligands of the complex (Table 22).[57-62,65,66,157-160] It was found that small structural modifications of these complexes yields remarkable changes in the

Table 22. The reported structures[a] and energy barriers[b] of some selected Mn_{12}-acetate SMM derivatives.

Compound	**R**	**n**	**Solvent**	**Space group**	**U_{eff}(K)**[a]
1[43]	$(MeCO_2)_{16}$	4	$4H_2O$	*I4*	62[45]
2	$(EtCO_2)_{16}$	3	$4H_2O$	*P1m*	–
3	$(PhCO_2)_{16}$	4	$2C_6H_5COOH$	*Fdd2*	–
4[62]	$(O_2CCH_2Bu^t)_{16}$	4	$CH_2Cl_2.MeNO_2$	$P1^{-}$	42
5[62]	$(O_2CCH_2Bu^t)_{16}$	4	$CH_2Cl_2.MeCN$	$P1^{-}$	61
6[161]	$(O_2C\text{-}C_6H_4\text{-p-Me})_{16}$	4	$HO_2CC_6H_4\text{-p-Me}$	*C2/c*	38
7[161]	$(O_2C\text{-}C_6H_4\text{-p-Me})_{16}$	4	$3H_2O$	*I2/a*	64
8[159]	$(CF_3CO_2)_{16}$	4	$2.5H_2O$	$P1^{-}$	62
9[158]	$(CH_2BrCO_2)_{16}$	4	$4CH_2Cl_2$	$I4_1/a$	13.7
10[60]	$(CO_2Me)_8(SO_3Ph)_8$	4	$4CH_2Cl_2$	$P1^{-}$	65.5
11[61]	$(CO_2Ph)_7(O_2PPh_2)_9$	4	$3CH_2Cl_2$	*C2/c*	41

a) General formula $[Mn_{12}O_{12}(R)_{16}(H_2O)_n]$•S.

b) $U_{eff} = |D|S^2$.

physical and magnetic properties of these clusters including solubility, redox chemistry and quantum tunneling properties.[58,62,65,66,157-159,162,163] For example, Christou *et al.*, have observed different magnetic properties in two Mn_{12}-acetate isomers that crystallize in the same space group and differ only in the identity of one solvent molecule of crystallization at one position.[66] The authors successfully isolated two forms of Mn_{12}-acetate complexes where one of them is characterized by frequency-dependent out-of-phase ac magnetic susceptibility signals in the 6-8 K range (U_{eff} = 62 K) and the latter with ac magnetic susceptibility signals in the 2-4 K range and an effective barrier to relaxation value of 42 K. They also concluded that the origin for such difference in two isomers is the abnormally oriented Jahn-Teller elongation axis at one high-spin Mn(III) centre.

Research in our group is focused on using metal cyanide chemistry to contribute to molecular magnetism research by preparing m6agnetic clusters with the cyanide linker, some of which exhibit SMM behavior.[51,52,54-56,91,95,96,148,150,152-155,164] As part of our research, the $[Re(triphos)(CN)_3]^-$ ligand has been employed to prepare a family of cubic clusters with four octahedral Re(II) ions and four tetrahedral Mn(II) sites bridged through cyanide ligands.[52,101] Magnetic studies revealed that a member of this family of clusters, namely $\{[Re(triphos)(CN)_3]_4[MnCl]_4\}$ (Re_4Mn_4), shows characteristics of SMM behavior (Figure 50).[101,165] This unique cluster represents an important molecule for gaining more knowledge about the SMM concept since it is the first example of a "cubic" SMM cluster and the first one with 5d metal ion. The compound exhibits hysteretic behavior at low temperatures, with strongly temperature and sweep-rate

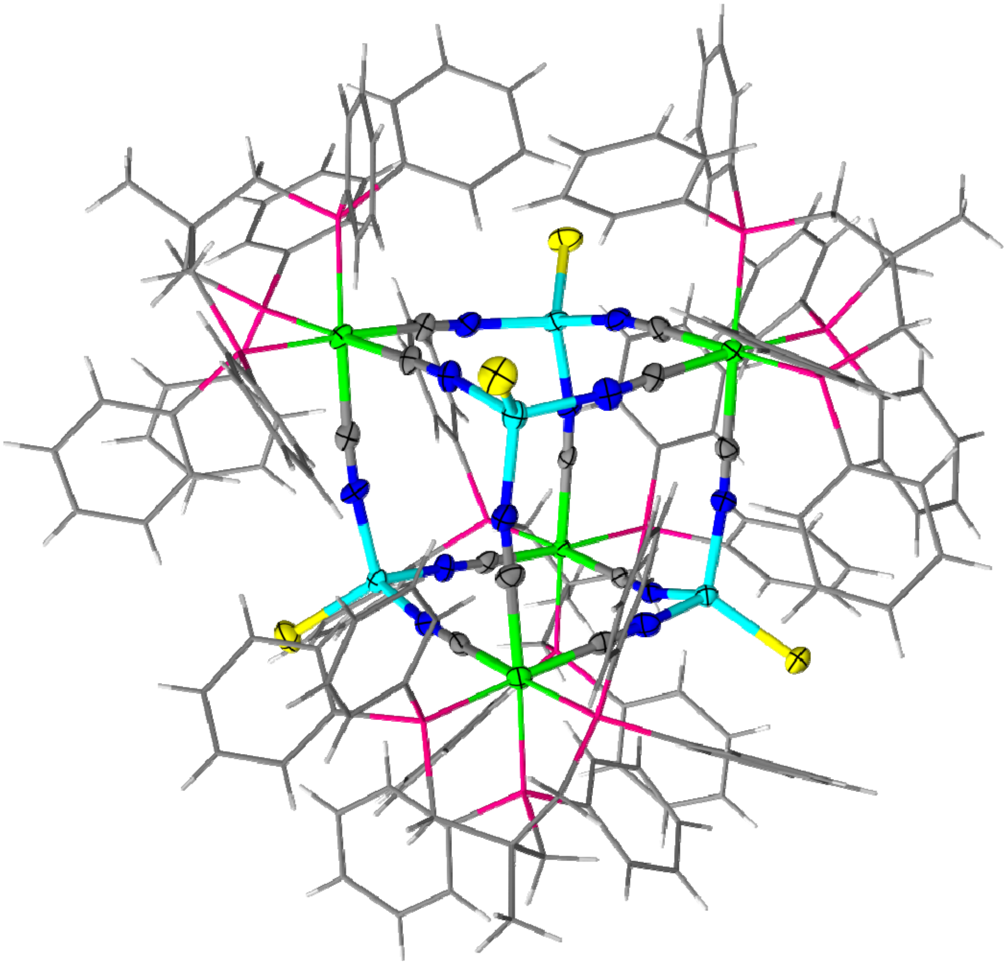

Figure 50. Structure of {[Re(triphos)(CN)$_3$]$_4$[MnCl]$_4$} (Re$_4$Mn$_4$) (Thermal ellipsoids are projected at the 50% probability level).[52]

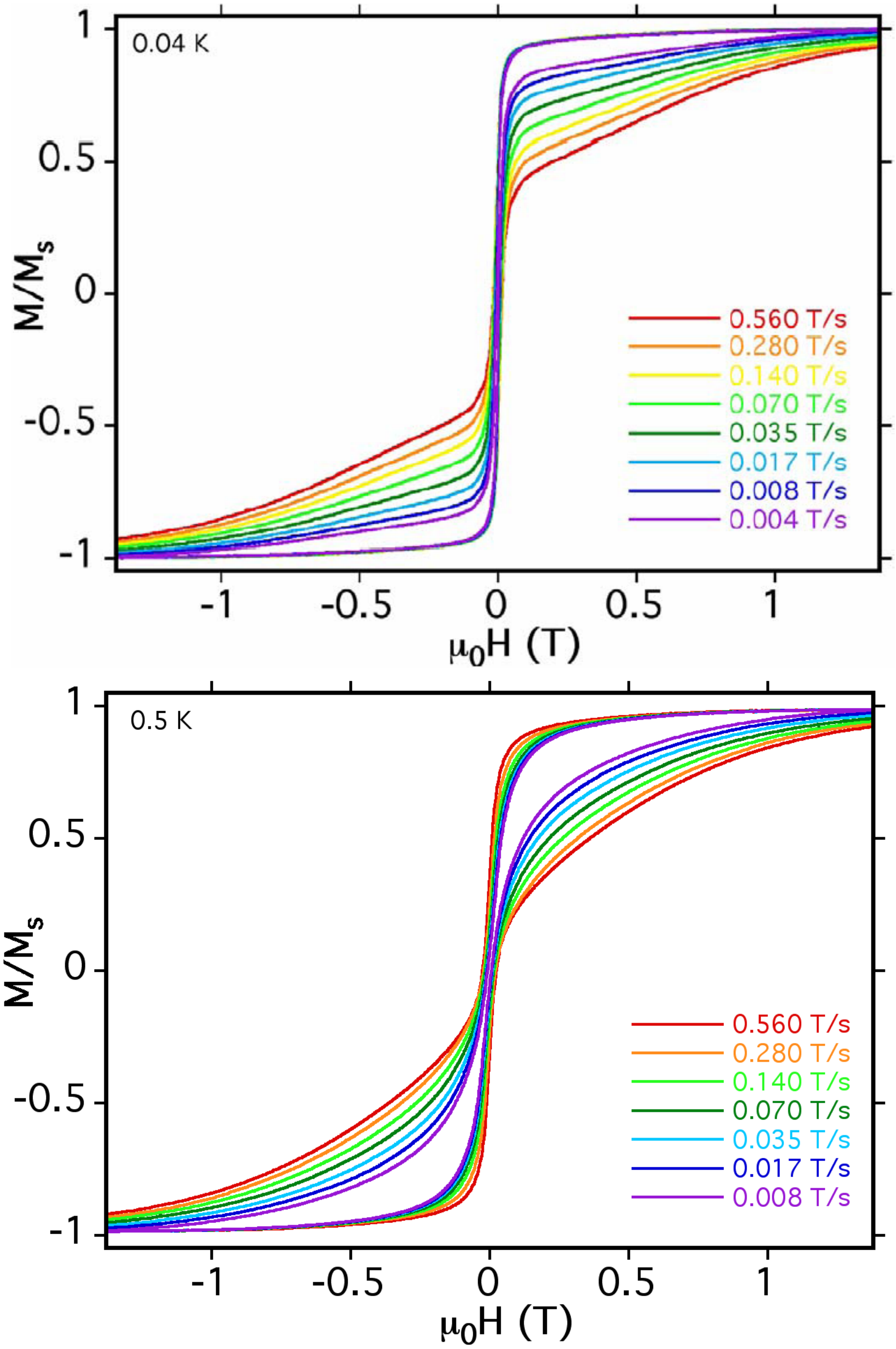

Figure 51. Scan rate dependences to the magnetization of Re_4Mn_4 cube obtained using a micro-SQUID apparatus on easy-axis oriented single crystals. Magnetization values are normalized to the magnetization value at 1.4 T.[101]

dependent coercivity; specifically the coercivity increases with decreasing temperatures and increasing field sweep rates (Figure 51). The magnetic measurements also show a significant step at zero field, which is the result of fast tunneling relaxation of the magnetization.

The aforementioned finding led to the development of a theoretical model, which describes the existence of many closely spaced low-lying energy levels; this situation is due to the weak magnetic coupling (small J value), resulting in closely spaced levels and fast relaxation by mixing of the ground state into excited states. The model explains the SMM behavior of the compound successfully because it takes into account the unquenched orbital angular momentum of Re(II) ion and treats the compound as having J rather than the S quantum numbers (Figure 52). The complexity of the problem, however, requires access to similar examples of cubic clusters to lend more insight into SMM properties for molecules with 5d metal ions.

In addition to discrete molecules, we are also interested in the design and preparation of magnetic networks using derivatives of Re_4Mn_4 cubes as building blocks. Such a bottom-up approach can provide a new strategy for constructing 1, 2, and 3-D networks incorporating SMM units. In this manner, trinuclear clusters with excellent superexchange pathways, such as $[M_3(\mu_3\text{–O})]$ clusters where M is Mn(III), Fe(III), Fe(II), Co(II), Ni(II), Cu(II), V(II), or Cr(III) have been used by several research groups to prepare frustrated lattices, single-chain magnets and 2D magnetic networks.[166-172] For example, Sato *et al.*, reported the preparation of a single-chain magnet from the reaction

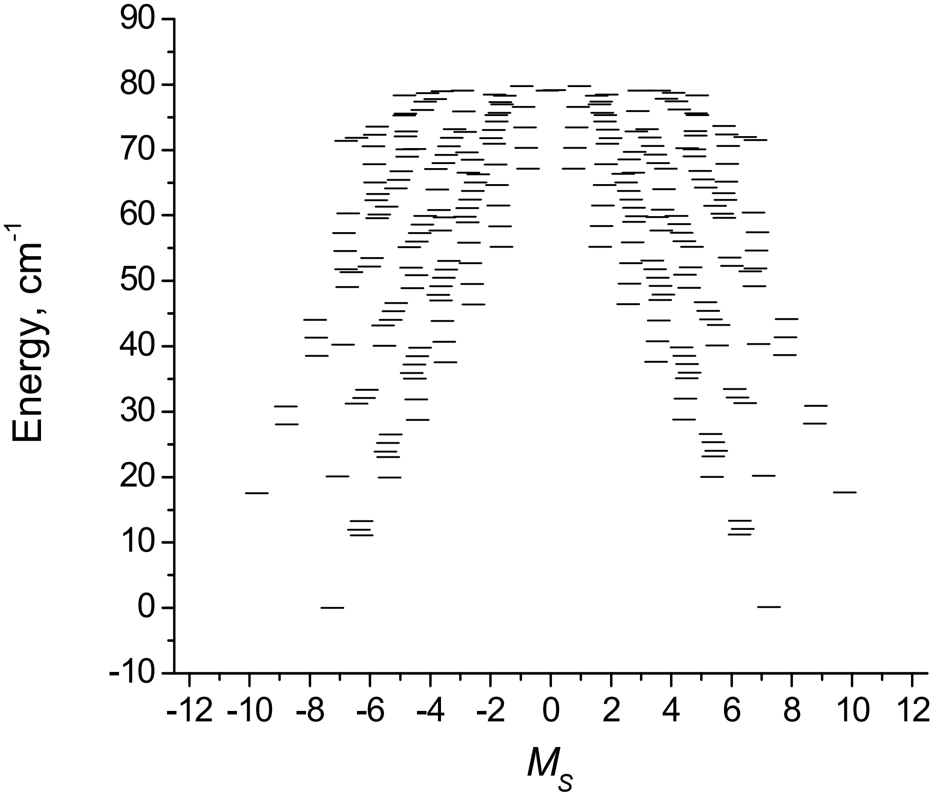

Figure 52. Distribution of energy levels for $\{[Re(triphos)(CN)_3]_4[MnCl]_4\}$.[165]

of the [Mn_3O] building block ($Mn^{III}_3O(Meppz)_3(EtOH)_5Cl$, Meppz = 3-(5-methyl-2-phenolate)pyrazolate) with sodium acetate. The product consists of [Mn_3O] units connected through bridging acetate units.[172] Additionally, Dunbar and co-workers have used metal-metal bonded dinuclear complexes based on Re_2, Mo_2, Ru_2, and Rh_2 cores as building-blocks to form extended networks with the use of π-acceptor polynitrile ligands.[173-181] A similar approach was taken recently with SMM building blocks especially after Wernsdorfer and co-workers discovered that the weak antiferromagnetic interactions in a dimer of single molecular magnets lead to a tuning of the quantum properties of the original SMM unit.[182] Christou *et al.*, later reported that a supramolecular dimer of SMMs ([Fe_9]$_2$) exist in the *OFF* and *ON* exchange-coupled states mediated solely by a single hydrogen-bond.[183] These breakthroughs have opened up new perspectives for the successful use of SMMs in networks with specific interactions. In fact, double-cuboidal [Mn_4] SMMs have been reacted with cyanometallates and the dicyanamide (dca$^-$) ligand for this purpose, the results of which are the formation of extended networks consisting of SMM building blocks.[184-186]

In this chapter, we report the reactions of the [$Re(triphos)(CN)_3$]$^-$ precursor with MnI_2 and solvated Mn(II) ions to prepare derivatives of the Re_4Mn_4 cube with different groups such as iodide, acetonitrile, and perchlorate ligands attached to the Mn center other than the chloride atom. Our efforts on linking these cubes to form extended networks are also discussed in this chapter.

EXPERIMENTAL

Materials

Unless otherwise stated, all experiments were performed using standard anaerobic, Schlenk-line techniques. The starting materials $Mn(ClO_4)_2{\cdot}6H_2O$ and $Na(C_2N_3)$ were purchased from Aldrich and used as received. All solvents were dried by standard methods.

Syntheses

$[Et_4N][Re(triphos)(CN)_3]$ (13). Compound **13** was prepared by a slightly modified procedure of the previously reported method.[187] Samples of $[(triphos)Re(\mu\text{–}Cl)_3Re(triphos)]Cl$[188] (0.656 g, 0.301 mmol) and $[Et_4N]CN$ (0.283 g, 1.81 mmol) were stirred in 25 mL of CH_3CN. The solution was then reacted with a solution of $TlPF_6$ in 25 mL of CH_3CN (0.421 g, 1.2 mmol) to give a dark-green solution with a white precipitate. The white solid was removed by filtration and the dark green filtrate was concentrated to 10 mL. At this stage, a bright yellow-green solid was collected by filtration and washed with 5 mL of acetonitrile and 20 mL of acetone followed by 15 mL of a 2/1 mixture of THF/CH_3CN. Yield: 0.203 g (0.199 mmol, 33%). Anal. Calcd for 1**3,** $C_{52}H_{59}N_4P_3Re$: C, 61.22; H, 6.41; N, 5.59. Found: C, 61.10; H, 6.63; N, 5.76. IR(Nujol): ν = 2060, 2070 cm^{-1} ($C{\equiv}N$).

$\{[Re(triphos)(CN)_3]_4[MnI]_4\}$ (14). A sample of $[Et_4N][Re(triphos)(CN)_3]$ (0.200 g, 0.196 mmol) was dissolved in a mixture of 20 mL acetonitrile to yield a red-brown solution. A mixture of 5 mL acetonitrile was added to MnI_2 (anhydrous) (0.061 g, 0.196 mmol) with stirring in a separate flask to give a white suspension. The red solution was then transferred via cannula to the white suspension which resulted in an immediate color change to dark red-orange. The reaction mixture was stirred for 12 h, with an orange-red microcrystalline product becoming evident after 1 h. The microcrystalline product was collected by filtration after 12 h and washed with acetone (3 − 5 mL), followed by copious amounts of acetonitrile and diethyl ether (3 − 5 mL), and finally dried in air. Yield = 0.156 g (0.036 mmol), 42%. Anal. Calc'd for **14**, $C_{176}H_{156}N_{12}I_4P_{12}Fe_4Re_4$: C, 49.41; H, 3.83; N, 3.87. Found: C, 49.35; H, 3.67; N, 3.92. IR(Nujol): ν(C≡N), cm^{-1}: 2096, 2081; ES^+–MS(CH_3CN/CH_2Cl_2, 1:1 mixture) *m*/*z* = 2078 ($[M - I]^{2+}$), 2014 ($[M - 2I]^{2+}$), 1301 ($[M - 3I]^{3+}$). UV–vis(CH_2Cl_2): λ_{max}, nm (ϵ in M^{-1} cm^{-1}) = 481 (8500).

{[Re(triphos)(CN)$_3$]$_4$[Mn(CH$_3$CN)]$_4$}(ClO$_4$)$_4$ (15). A colorless solution of $Mn(ClO_4)_2.6H_2O$ (0.070 g, 0.195 mmol) in 10 mL of acetonitrile was slowly added to a dark green-yellow solution of $[Et_4N][Re(triphos)(CN)_3]$ (0.200 g, 0.196 mmol) in 25 mL of acetonitrile. The mixture was left to stand undisturbed for 2 days under nitrogen. The solution was then concentrated to approximately 10 mL and the red powder obtained after the filtrate was washed with copious amounts of diethyl ether. Yield = 0.050 g (0.012 mmol), 24%. Elemental analysis calcd. for **15**, $C_{184}H_{168}N_{16}P_{12}Cl_4O_{16}Re_4Mn_4$: C 50.92, H 3.90, N 5.17, O 5.90, Cl 3.23; found: C 50.62, H 3.69, N 3.24, O 5.52, Cl 3.02. IR(Nujol), ν(C≡N), cm^{-1}: 2296(s), 2089(s), and 2070(w). Single crystals of compound **15** were grown over a 1 week period in a 3 mm diameter sealed thin tube by slow diffusion of a CH_2Cl_2 solution of the compound into diethyl ether.

{[Re(triphos)(CN)$_3$]$_4$[Mn(ClO$_4$)]$_3$[Mn(CH$_3$OH)(CH$_3$O)]} (16). A colorless solution of Mn(ClO$_4$)$_2$.6H$_2$O (0.070 g, 0.195 mmol) in 10 mL of methanol was slowly added to a dark green-yellow solution of [Et$_4$N][Re(triphos)(CN)$_3$] (0.200 g, 0.196 mmol) in 25 mL of methanol. The mixture was left to stand undisturbed for 2 days under nitrogen. The solution was then concentrated to ~10 mL and the red powder obtained after the solution was filtered was washed with copious amount of diethyl ether. Yield = 0.076 g (0.019 mmol), 38%. Elemental analysis calcd. for **16**, $C_{178}H_{163}P_{12}N_{12}Cl_3O_{14}Re_4Mn_4$: C 51.64, H 3.97, N 4.06, Cl 2.54, O 5.41; found: C 51.07, H 3.64, N 3.92, Cl 2.27, O 5.12. IR(Nujol), ν(C≡N), cm^{-1}: 2088(s), 2076(w). Single crystals of compound **16** were grown over a 1 week period in a 3 mm diameter sealed thin tube by slow diffusion of a CH_2Cl_2 solution of the compound into diethyl ether.

{[Re(triphos)(CN)$_3$]$_4$[Mn(N(CN)$_2$)]$_4$} (17). A colorless solution of Na(N(CN)$_2$) (0.018 g, 0.186 mmol) in 15 mL of ethanol was slowly added to a red solution of compound **3** (0.200 g, 0.046 mmol) in 25 mL of dichloromethane. The mixture was stirred for 3 days under nitrogen. An orange powder was isolated by filtration and washed with copious amount of diethyl ether. Yield= 0.118 g (0.029 mmol), 64%. Elemental analysis calcd. for **17**, $C_{184}H_{156}N_{24}P_{12}Re_4Mn_4$: C 54.65, H 3.89, N 8.32; found: C 54.52, H 3.68, N 8.15. IR(Nujol), ν(C≡N), cm^{-1}: 2262(s), 2206(s), 2156(s), 2095(s), 2077(w). Single crystals of compound **17** were obtained after 1 week by slow diffusion of a CH_2Cl_2 solution of the compound **15** into an ethanol solution of Na(N(CN)$_2$) in a 3 mm diameter sealed thin tube.

{[Re(triphos)(CN)$_3$]$_4$[(Mn(C$_{12}$H$_4$N$_4$))$_3$(Mn(C$_{12}$H$_5$N$_4$)(CH$_3$O))]} (18). A dark blue solution of LiTCNQ (0.051 g, 0.244 mmol) in 15 mL of methanol was slowly added to a red solution of compound **16** (0.250 g, 0.061 mmol) in 25 mL of dichloromethane. The mixture was stirred for 4 days under nitrogen. A red-brown powder removed by filtration was washed with copious amount of diethyl ether. Yield = 0.062 g (0.013 mmol), 22%. Elemental analysis calcd. for **16**, $C_{225}H_{173}N_{28}P_{12}O_1Re_4Mn_4$: C 58.42, H 3.77, N 8.48; found: C 57.95, H 3.59, N 3.42. IR(Nujol), ν(C≡N), cm^{-1}: 2195(s), 2171(s), 2130(s), 2113(s), 2087(s), 2074(w). Single crystals of compound **18** grew after 1 month in a 3 mm diameter sealed thin tube by slow diffusion of a CH_2Cl_2 solution of the compound **16** into a methanol solution of LiTCNQ.

Single Crystal X-ray Structures

In a typical experiment, a crystal selected for study was suspended in polybutene oil (Aldrich) and mounted on a cryoloop which was placed in an N_2 cold stream. Single crystal X-ray data for all the compounds were collected on a Bruker APEX diffractometer at 110 K. The data sets were recorded as three ω-scans of 606 frames each, at 0.3° stepwidth, and integrated with the Bruker SAINT[29] software package. For compound **14**, the data set was indexed in a monoclinic unit cell and systematic extinctions indicated the space group to be P21. For compounds **15**, **16**, and **17**, the diffraction patterns were each indexed using a monoclinic unit cell and were solved in the space group $P2_1/n$ (No. 14) based on the systematic absences. The diffraction patterns for compound **18** were indexed using a triclinic unit cell and were solved in the space group P-1. The absorption correction (SADABS[30]) was based on fitting a function to the empirical transmission surface as sampled by multiple equivalent measurements. Solution and refinement of the crystal structures was carried out using the SHELX[31] suite of programs and X-SEED[32], a graphical interface. Structure solution by direct methods resolved positions of all metal atoms and most of the lighter atoms. The remaining non-hydrogen atoms were located by alternating cycles of least squares refinements and difference Fourier maps. The option SQUEEZE in PLATON[33] was used to eliminate the contribution of the electron density in the solvent region from the intensity data. The use of SQUEEZE produced better refinement results, and the solvent-free model was employed for the final refinement. Hydrogen atoms were placed at calculated positions and refined with displacement parameters 1.2 or 1.5 times that of the heavy atoms to which they were bonded. The final refinement was carried out with anisotropic thermal parameters for all non-hydrogen atoms. A summary of pertinent information relating to unit cell parameters, data collection, and refinement is provided in Tables 23-25. Selected metal-to-ligand bond distances appear in Tables 26-30.

RESULTS AND DISCUSSION

Syntheses

The building-block approach has proven to be an effective method for systematic preparation of families of magnetic molecular complexes. Prior to this dissertation work, a family of cyanide-bridged molecular cubes was prepared by introducing various

Table 23. Crystallographic data and structural refinement parameters for compound **14**.

	(14)
Formula	$Re_{2.67}Mn_{2.67}C_{117.33}H_{104}P_8N_8I_{2.67}$
Space group	P21 (No. 14)
Unit cell	a = 22.893(4) Å b = 25.225(4) Å c = 22.902(4) Å β = 119.930(2) °
Unit cell volume, V	11462(3) Å^3
Z	3
Density, ρ_{calc}	1.241 g/cm^3
Abs. coeff., μ	2.978 mm^{-1}
Crystal color and habit	red block
Crystal size	0.32×0.22×0.19 mm
Temperature	110(2) K
Radiation, λ	Mo-Kα, 0.71073 Å
Min. and max. θ	1.03 to 28.26°
Reflections collected	69558 [R_{int} = 0.0389][a]
Independent reflections	47483
Data/parameters/restraints	47483 / 973 / 1
R [$F_o > 4\sigma(F_o)$]	R_1 = 0.0988[b] wR_2 = 0.2888[c]

[a] $R_{int} = \Sigma | F_o^2 - F_o^2(\text{mean}) | / \Sigma[F_o^2]$

[b] $R_1 = \Sigma \| F_o | - | F_c \| / \Sigma | F_o |$

[c] $wR_2 = \{\Sigma[w(F_o^2 - F_c^2)^2] / \Sigma[w(F_o^2)^2]\}^{1/2}$, $w = 1 / [\sigma^2(F_o^2) + (aP)^2 + bP]$, $P = [F_o^2 + 2F_c^2]/3$, a = 0.1660, b = 112.1631.

Table 24. Crystallographic data and structural refinement parameters for compounds **15** and **16**.

	(15)	**(16)**
Formula	$Re_4Mn_4C_{184}H_{xx}P_{12}N_{16}Cl_4O_{16}$	$Re_{3.2}Mn_{3.2}C_{145.6}H_{135.2}P_{9.6}N_{9.6}Cl_{2.4}O_{12}$
Space group	$P2_1/n$ (No. 14)	$P2_1/n$ (No. 14)
Unit cell	$a = 24.5782(8)$ Å	$a = 18.088(2)$ Å
	$b = 25.4175(8)$ Å	$b = 34.418(4)$ Å
	$c = 31.9582(9)$ Å	$c = 33.490(4)$ Å
	$\beta = 105.908(2)$ °	$\beta = 95.824(2)$ °
Unit cell volume, V	19200.2(10) Å^3	20742(4) Å^3
Z	4	5
Density, ρ_{calc}	1.304 g/cm^3	1.347 g/cm^3
Abs. coeff., μ	2.913 mm^{-1}	2.745 mm^{-1}
Crystal color and habit	Dark red plate	Dark red plate
Crystal size	0.30×0.22×0.08 mm	0.34×0.32×0.06 mm
Temperature	110(2) K	110(2) K
Radiation, λ	Mo-Kα, 0.71073 Å	Mo-Kα, 0.71073 Å
Min. and max. θ	0.93 to 27.05°	1.28 to 26.45°
Reflections collected	221692 [$R_{int} = 0.2514$]^a	218950 [$R_{int} = 0.0860$]
Independent reflections	11213	42507
Data/parameters/restraints	11213 / 982 / 0	42507 / 1204 / 0
R [$F_o > 4\sigma(F_o)$]	$R_1 = 0.0978^b$	$R_1 = 0.1105$
	$wR_2 = 0.2020^c$	$wR_2 = 0.3565$

[a] $R_{int} = \Sigma|F_o^2 - F_o^2(\text{mean})| / \Sigma[F_o^2]$

[b] $R_1 = \Sigma||F_o| - |F_c|| / \Sigma|F_o|$

[c] $wR_2 = \{\Sigma[w(F_o^2 - F_c^2)^2] / \Sigma[w(F_o^2)^2]\}^{1/2}$, $w = 1 / [\sigma^2(F_o^2) + (aP)^2 + bP]$, $P = [F_o^2 + 2F_c^2]/3$. For **15**, a = 0.1566, b = 1064.5675; for **16**, a = 0.1840, b = 811.8245.

Table 25. Crystallographic data and structural refinement parameters for compounds **17** and **18**.

	(17)	**$(18)\cdot 2CH_2Cl_2$**
Formula	$Re_4Mn_4C_{184}H_{156}P_{12}N_{23}$	$Re_{2.67}Mn_{2.67}C_{151.33}H_{120}P_8N_{18.67}Cl_{2.67}O_{0.67}$
Space group	$P2_1/n$ (No. 14)	$P2_1/n$ (No. 14)
Unit cell	$a = 25.262(8)$ Å	$a = 17.514(3)$ Å
	$b = 24.985(8)$ Å	$b = 18.087(3)$ Å
	$c = 32.556(11)$ Å	$c = 38.106(7)$ Å
	$\beta = 108.033(4)$ °	$\alpha = 90.764(5)$ °,
		$\beta = 97.408(5)$ °,
		$\gamma = 102.736(5)$ °
Unit cell volume, V	19539(11) Å^3	11605(3) Å^3
Z	4	3
Density, ρ_{calc}	1.372 g/cm^3	1.365 g/cm^3
Abs. coeff., μ	2.868 mm^{-1}	2.459 mm^{-1}
Crystal color and habit	Red plate	Red plate
Crystal size	0.19×0.12×0.06 mm	0.17×0.11×0.06 mm
Temperature	110(2) K	110(2) K
Radiation, λ	Mo-Kα, 0.71073 Å	Mo-Kα, 0.71073 Å
Min. and max. θ	1.47 to 26.95°	1.20 to 23.59°
Reflections collected	198.684 [$R_{int} = 0.2308$]^a	133941 [$R_{int} = 0.0945$]
Independent reflections	40874	32306
Data/parameters/restraints	40874 / 1034 / 0	32306 / 1230 / 0
R [$F_o > 4\sigma(F_o)$]	$R_1 = 0.1879$^{b}	$R_1 = 0.1156$
	$wR_2 = 0.4639$^{c}	$wR_2 = 0.3545$

[a] $R_{int} = \Sigma|F_o^2 - F_o^2(\mathrm{mean})| / \Sigma[F_o^2]$

[b] $R_1 = \Sigma||F_o| - |F_c|| / \Sigma|F_o|$

[c] $wR_2 = \{\Sigma[w(F_o^2 - F_c^2)^2] / \Sigma[w(F_o^2)^2]\}^{1/2}$, $w = 1 / [\sigma^2(F_o^2) + (aP)^2 + bP]$, $P = [F_o^2 + 2F_c^2]/3$. For **17**, a = 0.2, b = 0; for **18**, a = 0.1724, b = 561.6464.

3d metal ions in the form of metal chlorides into reaction with the mononuclear cyanide precursor, TEA[Re(triphos)$(CN)_3$][187]. Of particular interest, the Re_4Mn_4 cube, required a more detailed investigation than the other members of the family due to its promising magnetic properties. Our efforts to substitute the chloride ligands with other groups such as CN^- and dicyanamide (dca^-) anions to remove the chloride anions with $TlPF_6$ failed. We suspect that the inherent stability of the neutral cluster together with the steric effects caused by the bulky triphos ligands is responsible for these failed attempts. As a means around these problems, we sought to prepare molecular cubes by reacting the rhenium precursor with different Mn(II) salts in order to obtain cube derivatives wherein chloride atoms are replaced with other dangling ligands. Preliminary reactions of $[Et_4N]$[Re(triphos)$(CN)_3$] (**13**) (Figure 53), with Mn(II) salts yielded derivatives of the Re_4Mn_4 cube with chloride contamination of the sites occupied by the new ligand. For example, molecular cubes with the formula, {[Re(triphos)$(CN)_3]_4$[Mn$(CH_3CN)]_3$ $[MnCl]_1\}(ClO_4)_3$ (25% chloride contamination), and {[Re(triphos)$(CN)_3]_4$ [Mn$(CH_3CN)]_2[MnCl]_2\}(ClO_4)_2$ (50% chloride contamination) were obtained separately by reacting different samples of $[Et_4N]$[Re(triphos)$(CN)_3$] (**13**) with $Mn(ClO_4)_2 \cdot 6H_2O$ in acetonitrile as confirmed by elemental analysis and X-ray single crystal studied. Therefore, the samples of **13** were reacted with $TlPF_6$ to remove any chloride contamination present in the starting material that is carried along from previous steps in the synthesis (*Scheme 1*). The reactions of the pure rhenium precursor **13** with MnI_2 and $Mn^{II}(ClO_4)_2 \cdot 6H_2O$ yield compounds **14-16** with an approximate cubic geometry. The yields of compounds **14-16** vary depending on their differences in solubilities. For

Scheme 1. Synthesis of $[\mathrm{Re}^{\mathrm{II}}(\mathrm{triphos})(\mathrm{CN})_3]^-$ starting from $[\mathrm{Re}^{\mathrm{VII}}\mathrm{O}_4]^-$ anion (Phenyl groups of the triphos ligand were omitted for the sake of clarity).

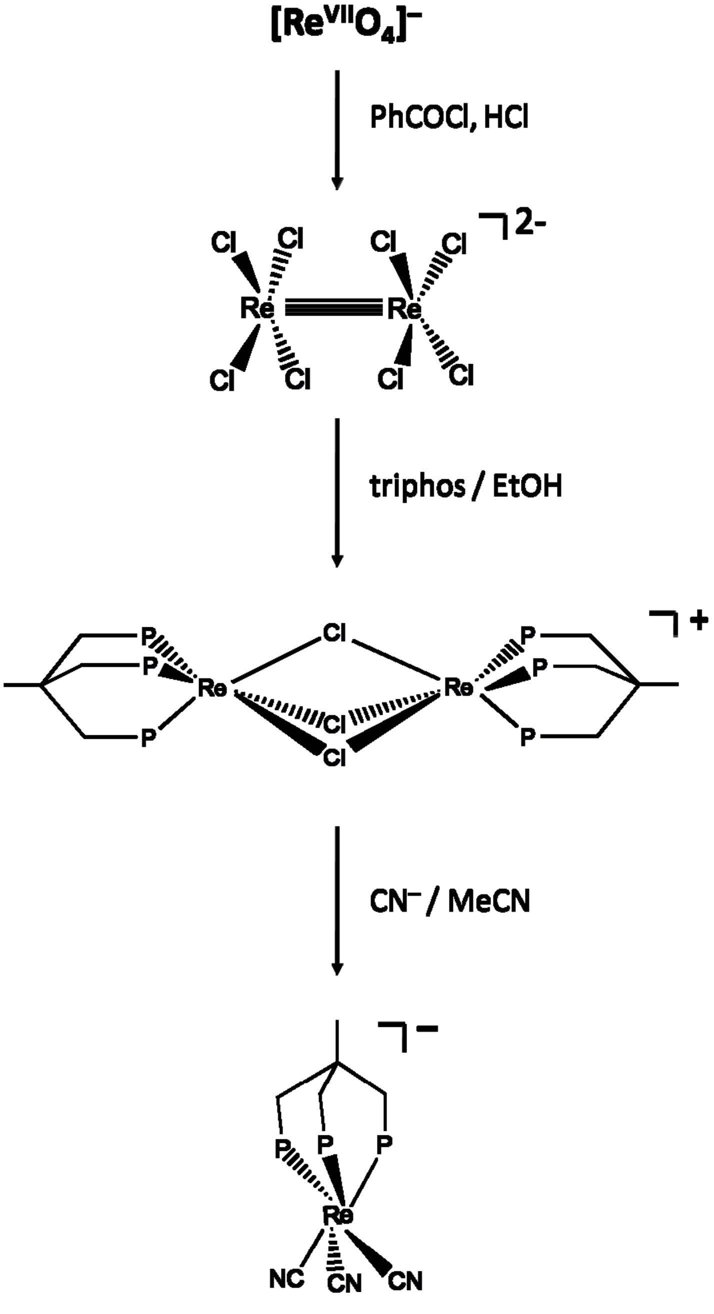

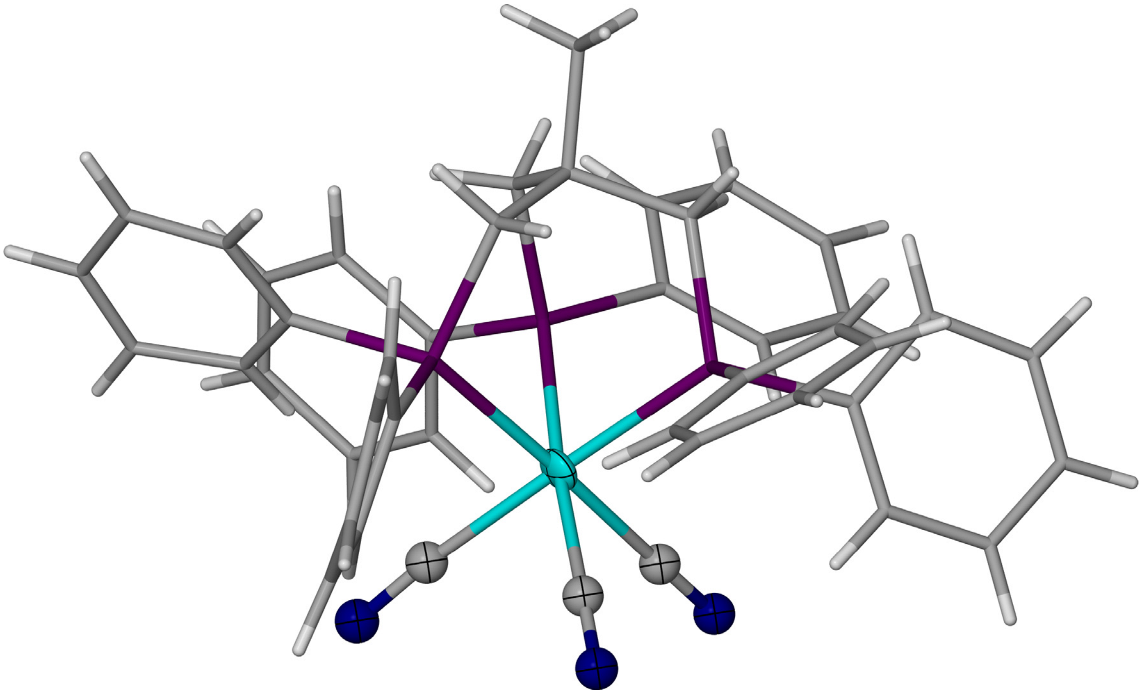

Figure 53. Structure of compound **1**.[187] Thermal ellipsoids are projected at the 50% probability level.

example, compound **15** with a 4+ charge has the highest solubility in common polar solvents, which translates to a lower isolable yield among the cube derivatives. The introduction of methanol into the reaction solution used to prepare compound **16** yielded an unexpected result. Compound **16** contains four Mn(II) ions for which three of the sites are occupied with perchlorate anion with the fourth one being connected to one methanol ligand and one methoxy anion that resides inside the cubic cavity. The result is a neutrally charged compound with one five-coordinate Mn(II) center.

Compounds **15** and **16** were reacted with dca^{-} and $TCNQ^{-}$ ligands. They are more soluble than the halide-containing Re_4Mn_4 cubes in polar solvents such as CH_2Cl_2, MeOH, and MeCN and they also contain labile ligands on the Mn(II) centers. When sodium dicyanamide was added to a red solution of compound **15** in CH_2Cl_2 the rapid formation of pale-brown precipitate was observed. The result is the product **17**, in which Mn(II) site is connected to one dicyanamide ligand. A substitution reaction between the dangling acetonitrile ligands connected to the Mn sites of the cube with the dca^{-} ligand is favored most likely due to the formation of a neutral compound, which is easily removed from the reaction media by precipitation. A similar reaction of compound **16** with LiTCNQ in CH_2Cl_2/MeOH solution led to the formation of **18**. This latter product is best described as a single chain of dimers of Re_4Mn_4 cubes bridged through σ-bonded $TCNQ_2^{2-}$ linkers.

Single Crystal X-ray Diffraction Studies

Single-crystal X-ray diffraction experiments performed on **14-16** revealed that the products consist of distorted molecular cubes with four altering Re(II) and Mn(II) ions. The edges of the neutral clusters are spanned by 12 bridging cyanide ligands that link the metal ions. The Re(II) sites retain their distorted octahedral geometry with the triphos ligands acting as a facially capping ligand and the carbon end of three cyanide ligands completing the coordination sphere. The Mn(II) ions in the clusters adopt four-coordinate distorted tetrahedral environments with three coordinated nitrogen atoms from bridging cyanide ligands and a fourth ligand extending out of the cube along a pseudo-C_3-axis. The asymmetric unit in these studies consists of one entire cube and its accompanying solvent molecules.

The unit cell determination for **14** (a = 22.893(4) Å, b = 25.225(4) Å, c = 22.902(4) Å, β = 119.930(2) ^{o}) and elemental analysis revealed **14** to be isomorphous to the Re_4Mn_4 cube (Figure 54). Selected metal ligand bond distances and angles are listed in Table 26. All of the Re(II) sites are in an octahedral geometry with Re–C and Re–P bond distances of ~2.10 Å and ~2.42 Å, respectively. The C–Re–C angles are slightly less than 90^o, ranging from 84.8^o to 89^o with an average of 87.2^o, which is slightly larger than those of the precursor **13** (an average of 85.1^o). The four Mn(II) sites are surrounded by three nitrogen atoms belonging to the cyanide ligands and one iodide ion to yield a distorted tetrahedral geometry with an average value of ~105^o for the N–Mn–N angles. The Mn–N distances range from 2.026 Å to 2.081 Å, which is in reasonable accord with the Mn–N distances reported for the Re_4Mn_4 cube (~2.070 Å) and the Co_2Mn_2 square (~2.080 Å). The Mn–I bond distances range from 2.678 Å to 2.683 Å with an average value of 2.680 Å. The most severe distortions of the structure are observed in Mn–N=C angles as in case of the Re_4Mn_4 cube, where the angles range from

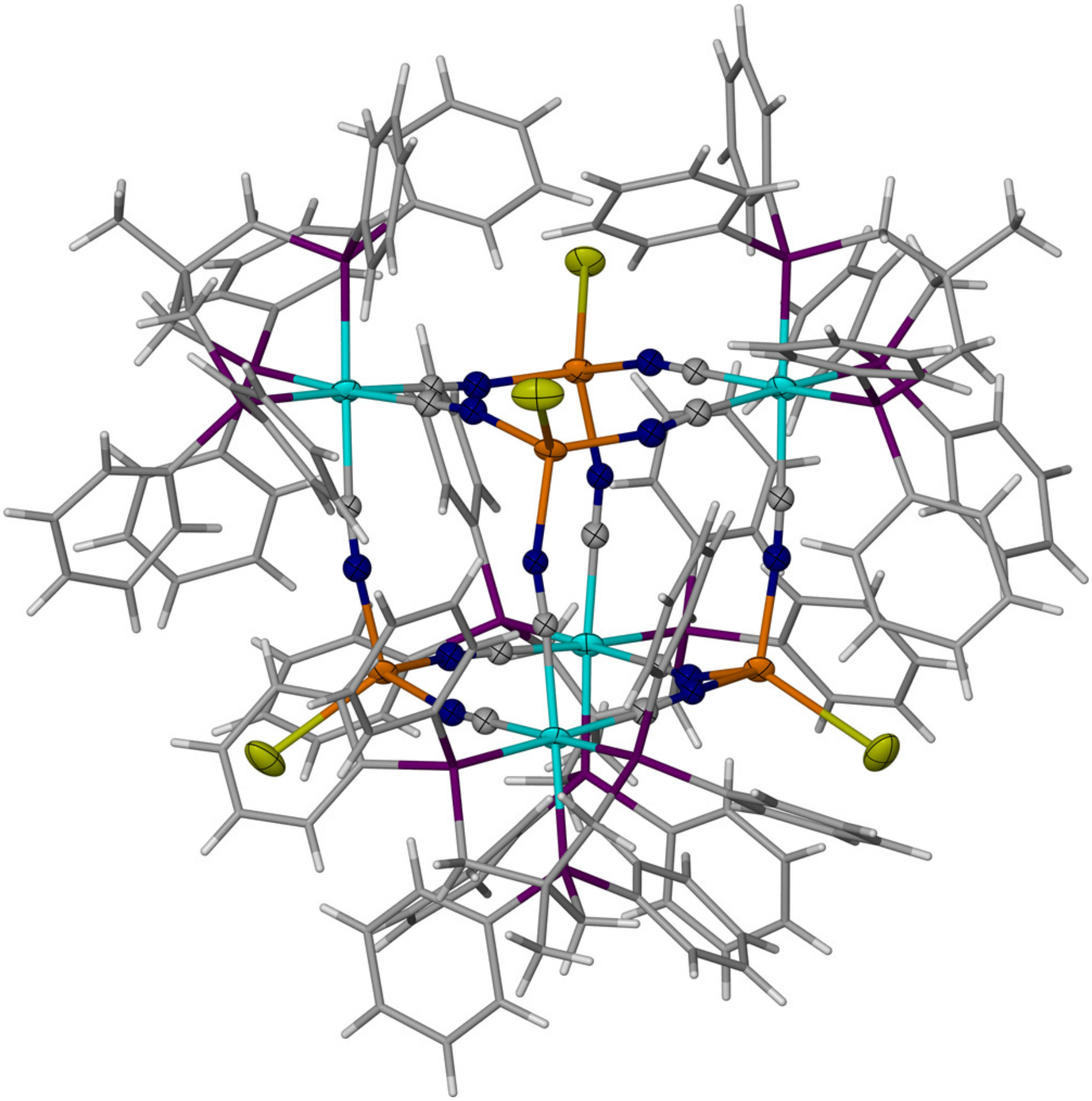

Figure 54. The molecular structure of {[Re(triphos)(CN)$_3$]$_4$[MnI]$_4$} **(14)**. Thermal ellipsoids are projected at the 50% probability level (only the thermal ellipsoids of the atoms that make up the cubic core were shown for the sake of clarity).

Table 26. Selected bond distances (Å) and angles (°) for compound **14**.

Atoms	**Distance (Å)**	**Atoms**	**Distance (Å)**
Re1 – C1	2.100(18)	Mn1 – N1	2.026(16)
Re1 – C2	2.109(18)	Mn1 – N4	2.066(17)
Re1 – C3	2.086(17)	Mn1 – N7	2.053(17)
Re1 – P1	2.405(4)	Mn1 – I1	2.678(3)
Re1 – P2	2.407(4)	Mn2 – N2	2.029(17)
Re1 – P3	2.405(4)	Mn2 – N5	2.048(18)
Re2 – C4	2.115(16)	Mn2 – N10	2.053(17)
Re2 – C5	2.051(17)	Mn2 – I2	2.683(3)
Re2 – C6	2.083(18)	Mn3 – N3	2.042(16)
Re2 – P4	2.409(5)	Mn3 – N8	2.045(18)
Re2 – P5	2.430(5)	Mn3 – N11	2.076(17)
Re2 – P6	2.423(5)	Mn3 – I3	2.680(3)
Re3 – C7	2.079(17)	Mn4 – N6	2.078(16)
Re3 – C8	2.091(18)	Mn4 – N9	2.062(17)
Re3 – C9	2.102(17)	Mn4 – N12	2.081(17)
Re3 – P7	2.413(5)	Mn4 – I4	2.682(3)
Re3 – P8	2.421(5)	C1 – N1	1.15(2)
Re3 – P9	2.423(5)	C2 – N2	1.14(2)
Re4 – C10	2.113(17)	C3 – N3	1.15(2)
Re4 – C11	2.095(17)	C4 – N4	1.11(2)
Re4 – C12	2.084(16)	C5 – N5	1.16(2)
Re4 – P10	2.417(5)	C6 – N6	1.12(2)
Re4 – P11	2.421(5)	C7 – N7	1.13(2)
Re4 – P12	2.418(5)	C8 – N8	1.15(2)
		C9 – N9	1.12(2)
		C10 – N10	1.12(2)
		C11 – N11	1.10(2)
		C12 – N12	1.11(2)

Table 26. Continued.

Atoms	**Angle(^{o})**	**Atoms**	**Angle(^{o})**
C3 – Re1 – C1	86.9(7)	N9 – Mn4 – N6	102.8(6)
C3 – Re1 – C2	86.9(7)	N9 – Mn4 – N12	102.4(7)
C1 – Re1 – C2	87.3(7)	N6 – Mn4 – N12	102.2(7)
C5 – Re2 – C6	86.2(7)	N9 – Mn4 – I4	115.8(5)
C5 – Re2 – C4	89.0(6)	N6 – Mn4 – I4	115.5(5)
C6 – Re2 – C4	85.0(7)	N12 – Mn4 – I4	116.1(5)
C7 – Re3 – C8	88.7(7)	C1 – N1 – Mn1	163.8(15)
C7 – Re3 – C9	86.5(7)	C4 – N4 – Mn1	161.9(16)
C8 – Re3 – C9	84.8(7)	C7 – N7 – Mn1	167.5(16)
C12 – Re4 – C11	86.0(7)	C2 – N2 – Mn2	163.8(16)
C12 – Re4 – C10	85.1(6)	C5 – N5 – Mn2	166.6(16)
C11 – Re4 – C10	89.0(7)	C10 – N10 – Mn2	163.2(16)
N1 – Mn1 – N7	101.9(6)	C3 – N3 – Mn3	163.0(14)
N1 – Mn1 – N4	103.5(6)	C8 – N8 – Mn3	163.3(17)
N7 – Mn1 – N4	104.9(7)	C11 – N11 – Mn3	166.9(17)
N1 – Mn1 – I1	114.3(4)	C6 – N6 – Mn4	164.0(15)
N7 – Mn1 – I1	115.3(5)	C9 – N9 – Mn4	164.5(16)
N4 – Mn1 – I1	115.4(5)	C12 – N12 – Mn4	163.3(16)
N2 – Mn2 – N5	103.1(7)	N1 – C1 – Re1	175.0(16)
N2 – Mn2 – N10	103.6(7)	N2 – C2 – Re1	175.4(16)
N5 – Mn2 – N10	105.9(7)	N3 – C3 – Re1	174.4(15)
N2 – Mn2 – I2	114.0(5)	N4 – C4 – Re2	170.7(15)
N5 – Mn2 – I2	114.1(5)	N5 – C5 – Re2	178.8(16)
N10 – Mn2 – I2	114.9(5)	N6 – C6 – Re2	178.6(17)
N3 – Mn3 – N8	104.2(7)	N7 – C7 – Re3	177.0(16)
N3 – Mn3 – N11	102.3(6)	N8 – C8 – Re3	173.3(17)
N8 – Mn3 – N11	105.3(7)	N9 – C9 – Re3	179.4(18)
N3 – Mn3 – I3	114.1(5)	N10 – C10 – Re4	172.2(15)
N8 – Mn3 – I3	114.8(5)	N11 – C11 – Re4	178.4(16)
N11 – Mn3 – I3	114.7(5)	N12 – C12 – Re4	178.8(16)

161.9^{o} to 167.5^{o}. As observed in the structure of **14**, the internal void present in the cube does not appear to be occupied by any solvent molecules or ligands.

Inspection of the structure of **15** revealed that it has a cubic core similar to **14** and the Re_4Mn_4 cube (Figure 55). The cluster **15** possesses a 4+ charge in contrast to the previously reported neutral cubes since negatively charged halogen atoms have been replaced with neutral acetonitrile ligands. Relevant metal-ligand bond distances for structure **15** are listed in Table 27. The cluster **15** exhibits less deviation from an idealized cubic geometry as compared to **14**, which is probably due to the fact that Mn sites are coordinated to four smaller nitrogen atoms as compared to iodide anions. An average value of 168^{o} was observed for the M–N=C angle whereas it is ~165^{o} for **14**.

The molecular structure of **16** revealed that perchlorate anions are used to complete the coordination sphere of three Mn(II) sites whereas a methanol ligand is connected to the other manganese center, a situation that results in drastic differences in the coordination geometry of this Mn(II) site as compared to the other three (Figure 56). The atom labeled as Mn(1) is compressed towards the center of the cube as evidenced by the fact that the Mn(1)–N=C angles are significantly reduced from linearity as a result of one dangling methanol ligand attached to the manganese site in addition to a methoxy ligand bound to the same center that points to the inside of the internal cavity of the cube. Such an occupancy inside the internal void of the cube had been previously noted for the Re_4Mn_4 cube, in which a methanol ligand is present inside the cavity and for a derivative of a Re_4Fe_4 cube, namely $\{[FeCl]_{3.5}[Fe(OCH_3)(THF)]_{0.5}[Re(triphos)(CN)_3]_4\}$[101], in which the cavity is occupied by a methoxy ligand. The methoxy group

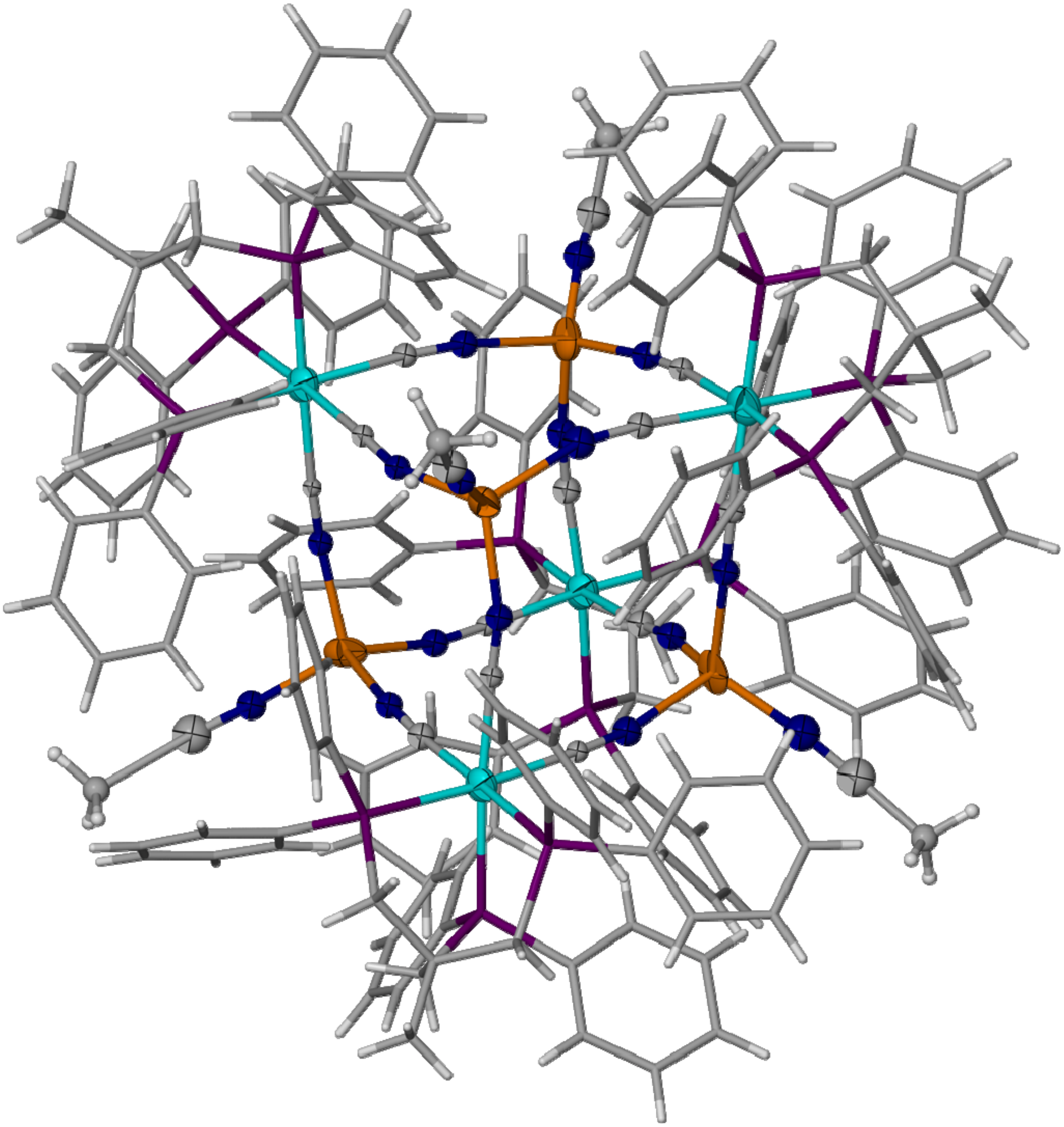

Figure 55. The molecular structure of $\{[\mathrm{Re(triphos)(CN)_3}]_4[\mathrm{Mn(CH_3CN)}]_4\}(\mathrm{ClO_4})_4$ (**15**). Thermal ellipsoids are projected at the 50% probability level (only the thermal ellipsoids of the atoms that make up the cubic core were shown for the sake of clarity).

Table 27. Selected bond distances (Å) and angles (°) for compound **15**.

Atoms	**Distance (Å)**	**Atoms**	**Distance (Å)**
Re1 – C1	2.04(4)	Mn1 – N1	2.04(3)
Re1 – C2	2.07(3)	Mn1 – N4	2.06(3)
Re1 – C3	2.07(4)	Mn1 – N7	2.06(3)
Re1 – P1	2.415(11)	Mn1 – N13	1.68(4)
Re1 – P2	2.419(10)	Mn2 – N2	2.07(3)
Re1 – P3	2.427(12)	Mn2 – N5	2.10(3)
Re2 – C4	2.03(4)	Mn2 – N10	2.07(3)
Re2 – C5	2.04(4)	Mn2 – N14	1.68(3)
Re2 – C6	2.08(4)	Mn3 – N3	2.03(3)
Re2 – P4	2.412(10)	Mn3 – N8	2.10(3)
Re2 – P5	2.421(11)	Mn3 – N11	2.13(3)
Re2 – P6	2.424(11)	Mn3 – N15	1.87(5)
Re3 – C7	2.07(3)	Mn4 – N6	2.03(4)
Re3 – C8	2.05(4)	Mn4 – N9	2.05(3)
Re3 – C9	2.09(4)	Mn4 – N12	2.08(3)
Re3 – P7	2.421(10)	Mn4 – N16	2.13(3)
Re3 – P8	2.427(10)	C1 – N1	1.19(4)
Re3 – P9	2.427(10)	C2 – N2	1.13(3)
Re4 – C10	1.99(4)	C3 – N3	1.12(4)
Re4 – C11	2.03(4)	C4 – N4	1.13(4)
Re4 – C12	2.14(4)	C5 – N5	1.14(4)
Re4 – P10	2.410(11)	C6 – N6	1.21(4)
Re4 – P11	2.423(10)	C7 – N7	1.19(4)
Re4 – P12	2.432(12)	C8 – N8	1.10(4)
		C9 – N9	1.14(4)
		C10 – N10	1.13(4)
		C11 – N11	1.14(3)
		C12 – N12	1.11(4)

Table 27. Continued.

Atoms	**Angle(^{o})**	**Atoms**	**Angle(^{o})**
C3 – Re1 – C1	85.8(12)	N9 – Mn4 – N6	110.6(12)
C3 – Re1 – C2	88.5(13)	N9 – Mn4 – N12	106.0(11)
C1 – Re1 – C2	86.7(12)	N6 – Mn4 – N12	115.8(12)
C5 – Re2 – C6	85.8(15)	N9 – Mn4 – N16	105.0(10)
C5 – Re2 – C4	85.1(14)	N6 – Mn4 – N16	111.5(12)
C6 – Re2 – C4	84.8(13)	N12 – Mn4 – N16	107.1(11)
C7 – Re3 – C8	86.3(13)	C1 – N1 – Mn1	170(3)
C7 – Re3 – C9	82.8(12)	C4 – N4 – Mn1	162(3)
C8 – Re3 – C9	84.5(13)	C7 – N7 – Mn1	173(3)
C12 – Re4 – C11	83.7(13)	C2 – N2 – Mn2	164(3)
C12 – Re4 – C10	85.7(13)	C5 – N5 – Mn2	171(3)
C11 – Re4 – C10	85.0(13)	C10 – N10 – Mn2	171(3)
N1 – Mn1 – N7	102.4(11)	C3 – N3 – Mn3	169(3)
N1 – Mn1 – N4	108.9(12)	C8 – N8 – Mn3	163(3)
N7 – Mn1 – N4	105.5(11)	C11 – N11 – Mn3	175(4)
N1 – Mn1 – N13	117.6(15)	C6 – N6 – Mn4	166(3)
N7 – Mn1 – N13	111.1(16)	C9 – N9 – Mn4	168(3)
N4 – Mn1 – N13	110.5(14)	C12 – N12 – Mn4	170(3)
N2 – Mn2 – N5	105.2(11)	N1 – C1 – Re1	176(3)
N2 – Mn2 – N10	110.5(11)	N2 – C2 – Re1	177(3)
N5 – Mn2 – N10	105.1(10)	N3 – C3 – Re1	180(3)
N2 – Mn2 – N14	110.0(14)	N4 – C4 – Re2	179(3)
N5 – Mn2 – N14	110.3(14)	N5 – C5 – Re2	174(3)
N10 – Mn2 – N14	115.2(14)	N6 – C6 – Re2	178(3)
N3 – Mn3 – N8	105.2(10)	N7 – C7 – Re3	174(3)
N3 – Mn3 – N11	105.1(11)	N8 – C8 – Re3	179(3)
N8 – Mn3 – N11	106.2(11)	N9 – C9 – Re3	174(3)
N3 – Mn3 – N15	114.6(14)	N10 – C10 – Re4	176(3)
N8 – Mn3 – N15	111.1(15)	N11 – C11 – Re4	177(3)
N11 – Mn3 – N15	113.9(14)	N12 – C12 – Re4	174(3)

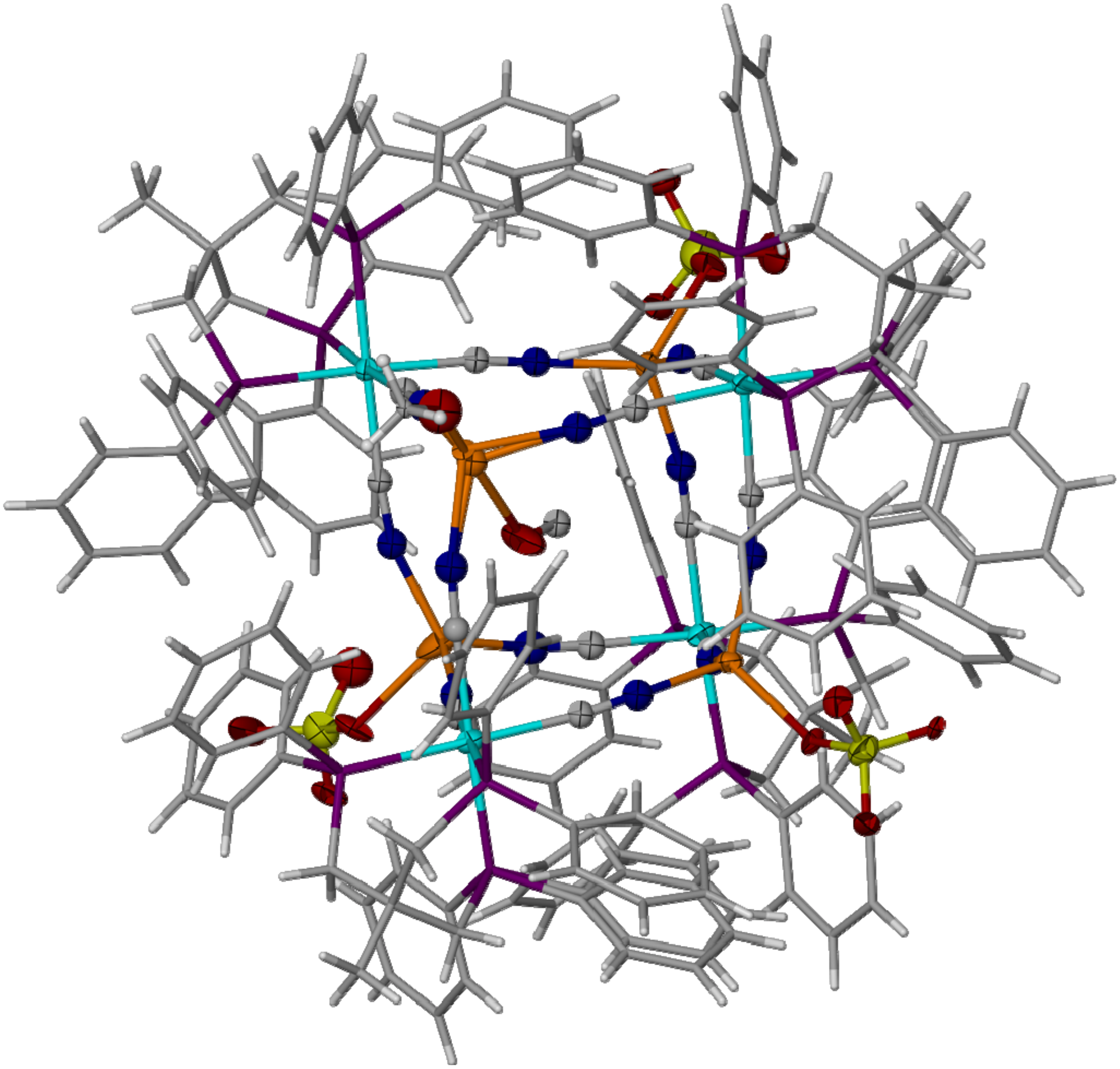

Figure 56. The molecular structure of the compound $\{[Re(triphos)(CN)_3]_4[Mn(ClO_4)]_3[Mn(CH_3OH)(CH_3O)]\}$ (**16**). Thermal ellipsoids are projected at the 50% probability level (only the thermal ellipsoids of the atoms that make up the cubic core were shown for the sake of clarity).

Table 28. Selected bond distances (Å) and angles (^{o}) for compound **16**.

Atoms	**Distance (Å)**	**Atoms**	**Distance (Å)**
Re1 – C1	2.075(14)	Mn1 – N1	2.011(15)
Re1 – C2	2.088(16)	Mn1 – N4	2.053(16)
Re1 – C3	2.076(15)	Mn1 – N7	2.049(16)
Re1 – P1	2.411(4)	Mn1 – O3	2.33(4)
Re1 – P2	2.409(4)	Mn2 – N2	2.099(16)
Re1 – P3	2.426(4)	Mn2 – N5	2.142(17)
Re2 – C4	2.041(17)	Mn2 – N10	2.109(15)
Re2 – C5	2.075(16)	Mn2 – O4	2.15(10)
Re2 – C6	2.088(15)	Mn3 – N3	2.036(13)
Re2 – P4	2.421(5)	Mn3 – N8	2.059(14)
Re2 – P5	2.416(5)	Mn3 – N11	2.054(14)
Re2 – P6	2.421(5)	Mn3 – O7	2.17(2)
Re3 – C7	2.062(16)	Mn4 – N6	2.051(14)
Re3 – C8	2.089(16)	Mn4 – N9	2.068(14)
Re3 – C9	2.058(16)	Mn4 – N12	2.035(14)
Re3 – P7	2.433(4)	Mn4 – O11	2.097(15)
Re3 – P8	2.435(4)	C1 – N1	1.17(2)
Re3 – P9	2.426(4)	C2 – N2	1.12(2)
Re4 – C10	2.079(15)	C3 – N3	1.148(19)
Re4 – C11	2.057(15)	C4 – N4	1.14(2)
Re4 – C12	2.083(14)	C5 – N5	1.14(2)
Re4 – P10	2.431(4)	C6 – N6	1.12(2)
Re4 – P11	2.419(4)	C7 – N7	1.14(2)
Re4 – P12	2.428(4)	C8 – N8	1.13(2)
		C9 – N9	1.15(2)
		C10 – N10	1.14(2)
		C11 – N11	1.14(2)
		C12 – N12	1.137(19)

Table 28. Continued.

Atoms	**Angle(°)**	**Atoms**	**Angle(°)**
C3 – Re1 – C1	85.6(6)	N9 – Mn4 – N6	112.1(6)
C3 – Re1 – C2	87.7(6)	N9 – Mn4 – N12	106.4(6)
C1 – Re1 – C2	84.9(6)	N6 – Mn4 – N12	108.1(6)
C5 – Re2 – C6	85.5(6)	N9 – Mn4 – O11	96.7(6)
C5 – Re2 – C4	86.3(6)	N6 – Mn4 – O11	112.6(7)
C6 – Re2 – C4	82.7(6)	N12 – Mn4 – O11	120.2(6)
C7 – Re3 – C8	85.5(6)	C1 – N1 – Mn1	163.8(13)
C7 – Re3 – C9	82.0(6)	C4 – N4 – Mn1	167.3(15)
C8 – Re3 – C9	84.1(6)	C7 – N7 – Mn1	157.4(15)
C12 – Re4 – C11	86.5(6)	C2 – N2 – Mn2	169.1(14)
C12 – Re4 – C10	85.0(6)	C5 – N5 – Mn2	168.7(14)
C11 – Re4 – C10	86.2(6)	C10 – N10 – Mn2	170.5(14)
N1 – Mn1 – N7	120.7(6)	C3 – N3 – Mn3	167.1(13)
N1 – Mn1 – N4	109.4(6)	C8 – N8 – Mn3	169.2(14)
N7 – Mn1 – N4	114.1(6)	C11 – N11 – Mn3	168.6(13)
N1 – Mn1 – O3	108.9(15)	C6 – N6 – Mn4	162.9(14)
N7 – Mn1 – O3	109.8(14)	C9 – N9 – Mn4	168.1(14)
N4 – Mn1 – O3	89.3(14)	C12 – N12 – Mn4	166.6(13)
N2 – Mn2 – N5	106.2(6)	N1 – C1 – Re1	174.4(13)
N2 – Mn2 – N10	99.2(6)	N2 – C2 – Re1	178.7(16)
N5 – Mn2 – N10	106.6(6)	N3 – C3 – Re1	173.2(13)
N2 – Mn2 – O3A	93.6(16)	N4 – C4 – Re2	174.9(15)
N5 – Mn2 – O3A	104(3)	N5 – C5 – Re2	176.4(15)
N10 – Mn2 – O3A	141(4)	N6 – C6 – Re2	174.0(14)
N3 – Mn3 – N8	110.9(5)	N7 – C7 – Re3	174.8(15)
N3 – Mn3 – N11	101.6(5)	N8 – C8 – Re3	174.8(14)
N8 – Mn3 – N11	107.1(6)	N9 – C9 – Re3	174.1(14)
N3 – Mn3 – O7	120.7(8)	N10 – C10 – Re4	174.3(14)
N8 – Mn3 – O7	119.3(9)	N11 – C11 – Re4	178.4(14)
N11 – Mn3 – O7	92.4(9)	N12 – C12 – Re4	177.3(14)

not only leads to flattening of one of the corners of the cube but also serves to compensate for the loss of one negative charge from the molecule resulting in a neutral cluster. The Mn–N distances for Mn(2), Mn(3), and Mn(4) are similar to **14** and **15**, whose ranges are from 2.036 Å to 2.142 Å (Table 28). Although the Mn(1) atom adopts a 5-coordinate distorted trigonal bipyramidal geometry, the Mn(1)–N distances fall within the range of those for the Mn(2), Mn(3), and Mn(4) atoms. The Mn(1)–O(ClO_3) distance, however, is 2.33 Å, which is much longer than the Mn–O distances observed for the other three manganese sites (2.097, 2.150, and 2.170 Å). The origin of the increase in bond length is obviously due to the flattening of the corner of the cube, thereby resulting in unfavorable steric effects from the neighbouring triphos ligands to prevent the perchlorate anion from binding more tightly to the metal center. The interaction of an oxygen atom of the perchlorate anion to Mn(1), which is in such a sterically hindered position, also causes distortions in the O–Cl–O angles of the perchlorate anion as evidenced by variations from 89° to 130°.

Figure 57 depicts the molecular structure of **17** and Table 29 lists the selected metal-ligand bond distances and angles. Compound **17** exhibits a similar molecular structure to that of **15**. The Re–C distances in **17** adopt values in the range from 2.01 to 2.14 Å, distances that are in reasonable accord with those observed for **15**. The Mn–N distances are also comparable to those for **15** and range from 2.00 to 2.09 Å.

The molecular structure of **18** reveals the presence of a single chain of cubes connected via σ-$[TCNQ_2]^{2-}$ ligands. The asymmetric unit of **6** consists of one cubic

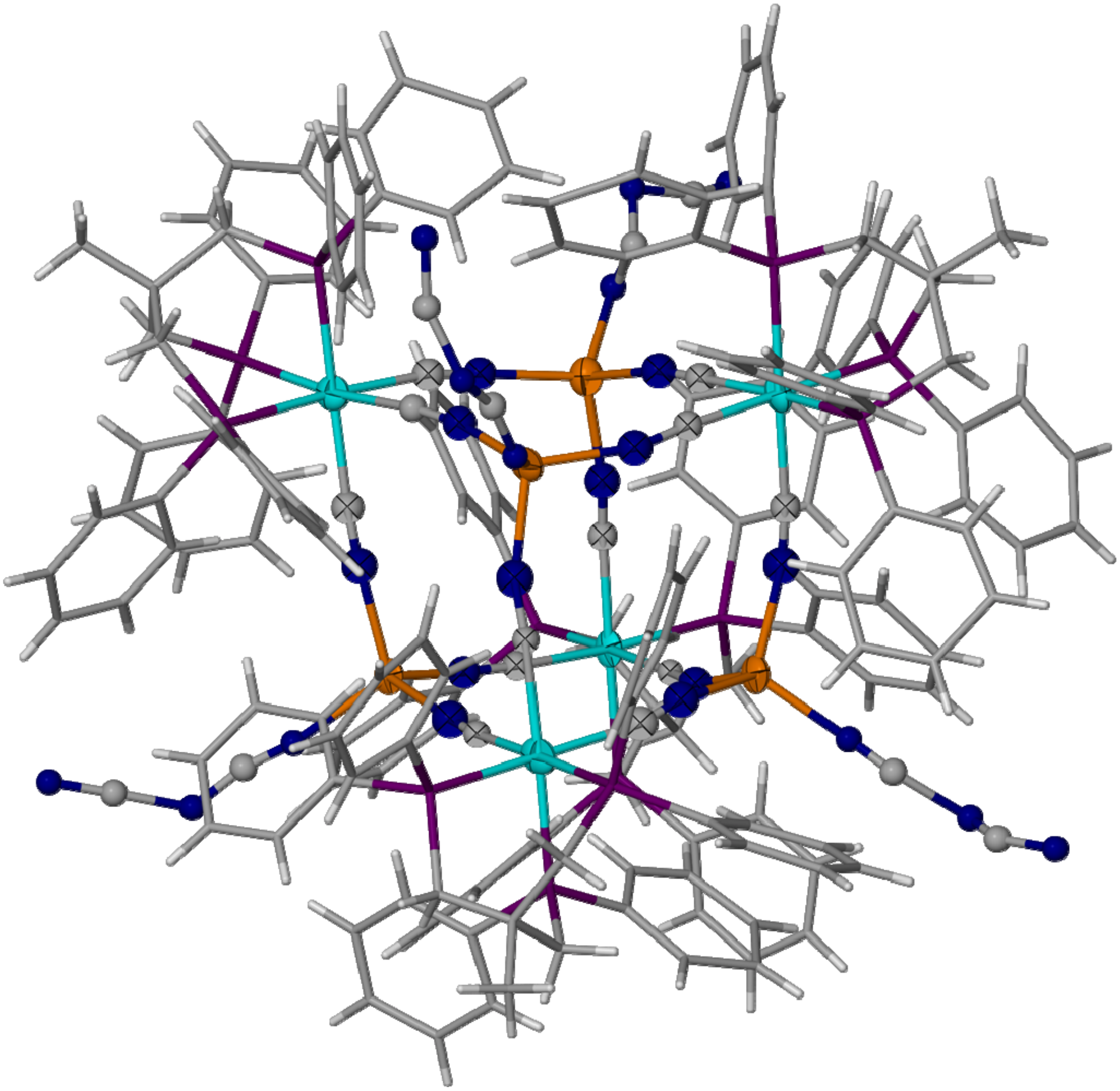

Figure 57. The molecular structure of {[Re(triphos)$(CN)_3]_4[Mn(N(CN)_2)]_4$} (**17**). Thermal ellipsoids are projected at the 50% probability level (only the thermal ellipsoids of the atoms that make up the cubic core were shown for the sake of clarity).

Table 29. Selected bond distances (Å) and angles (^{o}) for compound **17.**

Atoms	Distance (Å)	Atoms	Distance (Å)
Re1 – C1	2.10(3)	Mn1 – N1	2.07(3)
Re1 – C2	2.13(3)	Mn1 – N4	2.00(3)
Re1 – C3	2.05(3)	Mn1 – N7	2.04(3)
Re1 – P1	2.420(8)	Mn1 – N13	2.01(4)
Re1 – P2	2.420(9)	Mn2 – N2	2.05(3)
Re1 – P3	2.423(7)	Mn2 – N5	2.05(3)
Re2 – C4	2.14(3)	Mn2 – N10	2.01(3)
Re2 – C5	2.09(3)	Mn2 – N16	2.13(4)
Re2 – C6	2.01(3)	Mn3 – N3	2.05(3)
Re2 – P4	2.421(5)	Mn3 – N8	2.08(3)
Re2 – P5	2.419(8)	Mn3 – N11	2.09(3)
Re2 – P6	2.426(9)	Mn3 – N19	2.10(3)
Re3 – C7	2.21(4)	Mn4 – N6	2.03(3)
Re3 – C8	2.11(3)	Mn4 – N9	2.03(3)
Re3 – C9	2.13(3)	Mn4 – N12	2.03(3)
Re3 – P7	2.420(10)	Mn4 – N22	2.08(6)
Re3 – P8	2.409(9)	C1 – N1	1.09(3)
Re3 – P9	2.413(8)	C2 – N2	1.09(3)
Re4 – C10	2.10(3)	C3 – N3	1.15(4)
Re4 – C11	2.09(3)	C4 – N4	1.12(4)
Re4 – C12	2.07(3)	C5 – N5	1.10(3)
Re4 – P10	2.418(8)	C6 – N6	1.21(4)
Re4 – P11	2.421(9)	C7 – N7	1.00(4)
Re4 – P12	2.418(9)	C8 – N8	1.05(3)
		C9 – N9	1.10(3)
		C10 – N10	1.15(4)
		C11 – N11	1.09(3)
		C12 – N12	1.14(3)

Table 29. Continued.

Atoms	**Angle(^{o})**	**Atoms**	**Angle(^{o})**
C3 – Re1 – C1	84.2(10)	N9 – Mn4 – N6	103.5(11)
C3 – Re1 – C2	84.3(11)	N9 – Mn4 – N12	106.0(11)
C1 – Re1 – C2	86.3(10)	N6 – Mn4 – N12	105.7(11)
C5 – Re2 – C6	84.1(11)	N9 – Mn4 – N22	112(2)
C5 – Re2 – C4	84.6(11)	N6 – Mn4 – N22	113.4(16)
C6 – Re2 – C4	88.3(11)	N12 – Mn4 – N22	115.6(19)
C7 – Re3 – C8	86.9(11)	C1 – N1 – Mn1	163(2)
C7 – Re3 – C9	87.6(11)	C4 – N4 – Mn1	163(3)
C8 – Re3 – C9	87.7(10)	C7 – N7 – Mn1	164(3)
C12 – Re4 – C11	87.1(11)	C2 – N2 – Mn2	172(3)
C12 – Re4 – C10	83.1(11)	C5 – N5 – Mn2	170(3)
C11 – Re4 – C10	85.8(12)	C10 – N10 – Mn2	163(2)
N1 – Mn1 – N7	105.7(11)	C3 – N3 – Mn3	165(2)
N1 – Mn1 – N4	108.7(11)	C8 – N8 – Mn3	171(3)
N7 – Mn1 – N4	104.7(11)	C11 – N11 – Mn3	177(3)
N1 – Mn1 – N13	110.9(12)	C6 – N6 – Mn4	161(2)
N7 – Mn1 – N13	115.1(13)	C9 – N9 – Mn4	163(3)
N4 – Mn1 – N13	111.3(13)	C12 – N12 – Mn4	168(2)
N2 – Mn2 – N5	105.8(11)	N1 – C1 – Re1	174(3)
N2 – Mn2 – N10	107.3(11)	N2 – C2 – Re1	172(3)
N5 – Mn2 – N10	108.7(10)	N3 – C3 – Re1	177(3)
N2 – Mn2 – N16	112.7(12)	N4 – C4 – Re2	173(3)
N5 – Mn2 – N16	107.9(12)	N5 – C5 – Re2	179(3)
N10 – Mn2 – N16	114.0(12)	N6 – C6 – Re2	177(3)
N3 – Mn3 – N8	105.0(11)	N7 – C7 – Re3	169(3)
N3 – Mn3 – N11	108.1(10)	N8 – C8 – Re3	175(3)
N8 – Mn3 – N11	106.7(11)	N9 – C9 – Re3	171(3)
N3 – Mn3 – N19	113.1(11)	N10 – C10 – Re4	171(3)
N8 – Mn3 – N19	111.6(11)	N11 – C11 – Re4	176(3)
N11 – Mn3 – N19	111.9(11)	N12 – C12 – Re4	172(2)

molecule, wherein each manganese site is connected to one TCNQ moiety. Each TCNQ ligand is composed of two N–$(CN)_2$ units, one of which is planar to the phenyl ring is used to connect to the manganese site and one that is twisted with respect to the phenyl ring of TCNQ ligand in order to form a σ-bonded TCNQ dimer. Once the crystal structure of **18** was revived in the extended mode, it was observed that only three of the TCNQ ligands participate in the formation of σ-bonded TCNQ dimer, which is used to connect the cubes into a chain (Figure 58). One of the TCNQ ligands, however, does not have a centrosymmetric counterpart indicating the presence of H–TCNQ, which is also supported by the observations that; (i) the dangling C(23)–(CN)2 unit is twisted with respect to phenyl ring of TCNQ ligand suggesting the presence of an atom bonded to C(23) and (ii) the particular TCNQ unit must not bear a charge since each electroneutral cube already consists of one methoxy anion and three $TCNQ^{-}$ ligands (half of a σ-$[TCNQ_2]^{2-}$ ligand). Further inspection of the σ-bond present in the $[TCNQ_2]^{2-}$ unit by X-ray single crystal studies confirms that two of the σ-$[TCNQ_2]^{2-}$ ligands are identical. Both of these identical σ-$[TCNQ_2]^{2-}$ bridges are used to connect identical, the overall result of which is a dimer of cubes linked through two sets of σ-$[TCNQ_2]^{2-}$ ligands (Figure 58). The third σ-$[TCNQ_2]^{2-}$ ligand connects these dimers of cubes to form a single chain of cubes (Figures 59-60). The σ-bond present in the former σ-$[TCNQ_2]^{2-}$ ligand (C(47)–C(59) is 1.553 Å) is shorter than the one in the latter unit (C(35)–C(35') is 1.605 Å) (Table 30). Both values are in reasonable accord with the distances reported for $[Cu(DMP)_2]_2(TCNQ)_2$ (1.630 Å) prepared by Hatfield *et al.*, which consists of σ-$[TCNQ_2]^{2-}$ stacks.[189] Moreover, the $Mn(TCNQ)_2(MeOH)_2$ polymer prepared by Dunbar

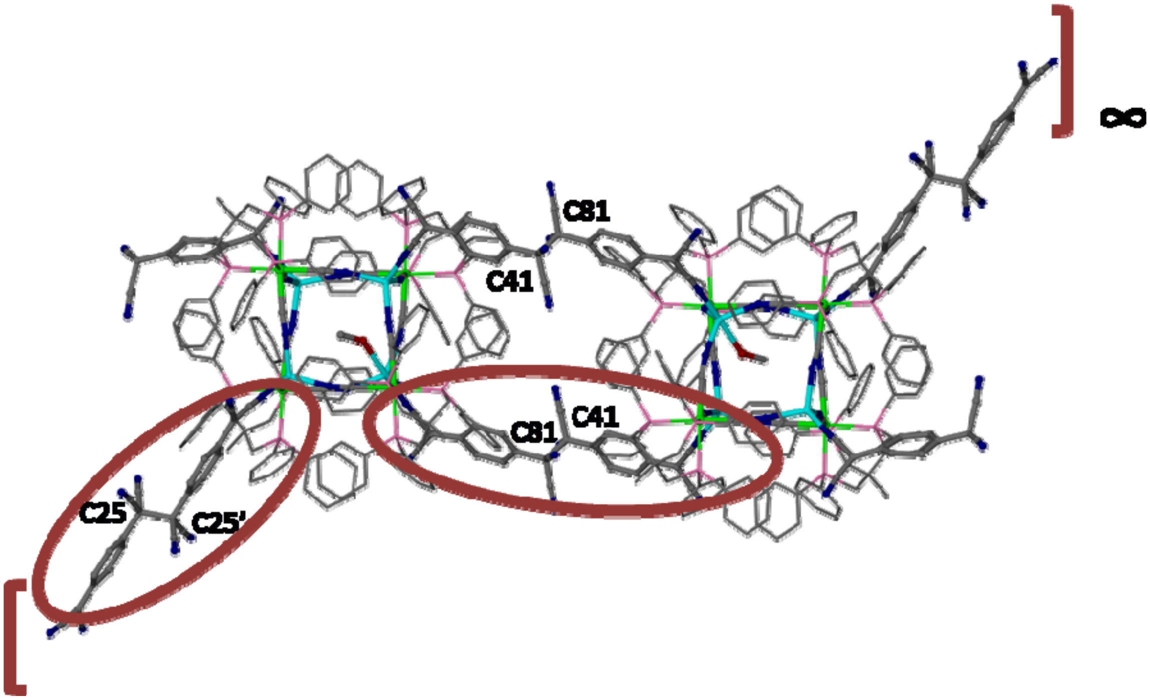

Figure 58. Structure of a segment of the chain in **18** emphasizing the σ-$[TCNQ_2]^{2-}$ units that are linking the Re_4Mn_4-cubes.

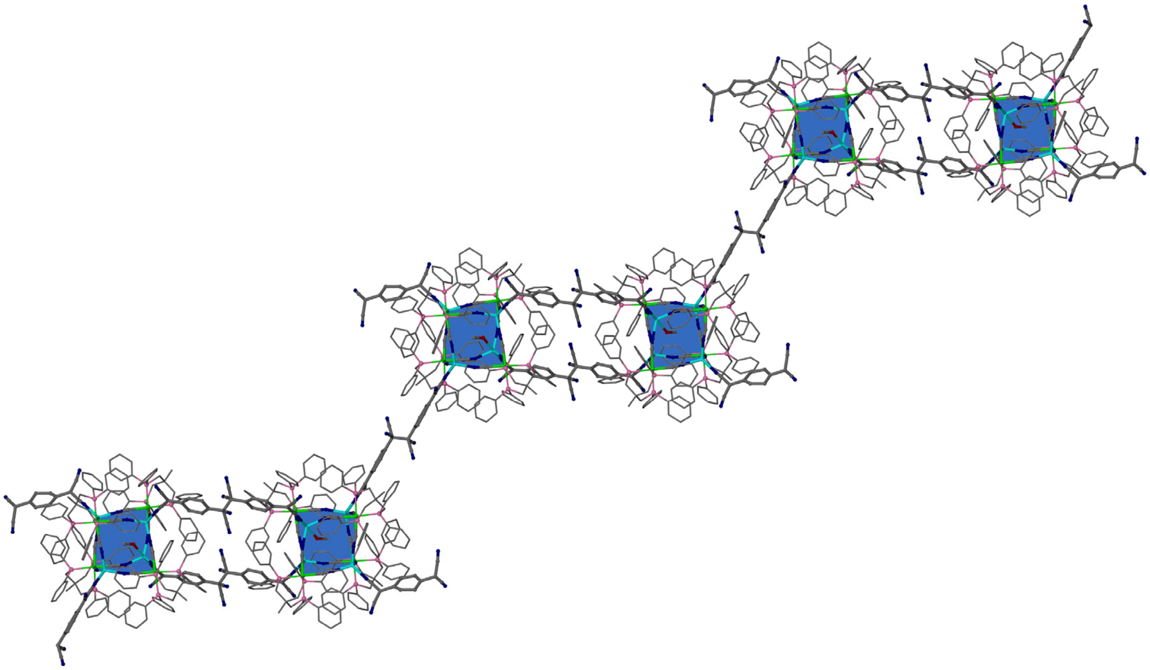

Figure 59. Structure of a chain of the linked cubes in **6**.

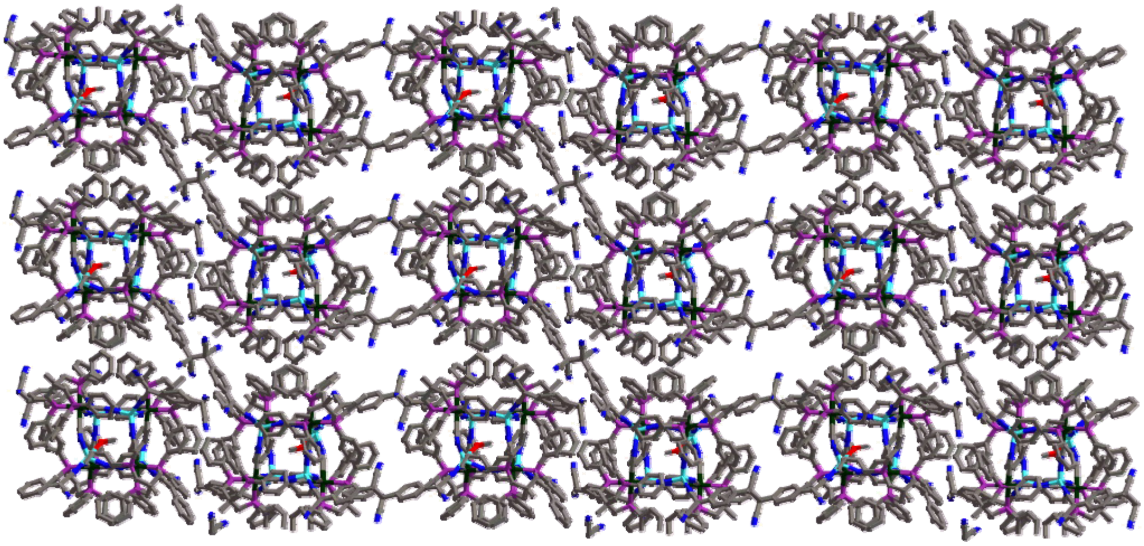

Figure 60. Packing diagram of compound **6** depicted along the *c* axis.

Table 30. Selected bond distances (Å) and angles (^{o}) for compound **18**.

Atoms	**Distance (Å)**	**Atoms**	**Distance (Å)**
Re1 – C1	2.095(19)	Mn1 – N1	2.057(18)
Re1 – C2	2.111(17)	Mn1 – N4	2.052(17)
Re1 – C3	2.084(19)	Mn1 – N7	2.063(19)
Re1 – P1	2.415(6)	Mn1 – N13	2.190(16)
Re1 – P2	2.421(5)	Mn2 – N2	2.062(17)
Re1 – P3	2.425(5)	Mn2 – N5	2.081(17)
Re2 – C4	2.127(17)	Mn2 – N10	2.068(17)
Re2 – C5	2.094(18)	Mn2 – N17	2.124(19)
Re2 – C6	2.064(17)	Mn3 – N3	2.021(18)
Re2 – P4	2.411(5)	Mn3 – N8	2.066(19)
Re2 – P5	2.414(6)	Mn3 – N11	2.057(19)
Re2 – P6	2.406(5)	Mn3 – N21	2.094(18)
Re3 – C7	2.10(2)	Mn4 – N6	2.055(19)
Re3 – C8	2.07(2)	Mn4 – N9	2.08(2)
Re3 – C9	2.13(2)	Mn4 – N12	2.066(18)
Re3 – P7	2.411(6)	Mn4 – N25	2.16(2)
Re3 – P8	2.421(6)	C1 – N1	1.11(2)
Re3 – P9	2.415(6)	C2 – N2	1.09(2)
Re4 – C10	2.077(17)	C3 – N3	1.14(2)
Re4 – C11	2.102(18)	C4 – N4	1.09(2)
Re4 – C12	2.097(18)	C5 – N5	1.08(2)
Re4 – P10	2.415(6)	C6 – N6	1.14(2)
Re4 – P11	2.409(5)	C7 – N7	1.12(3)
Re4 – P12	2.422(5)	C8 – N8	1.11(2)
		C9 – N9	1.06(2)
		C10 – N10	1.11(2)
		C11 – N11	1.11(2)
		C12 – N12	1.11(2)

Table 30. Continued.

Atoms	**Angle(^{o})**	**Atoms**	**Angle(^{o})**
C3 – Re1 – C1	85.1(7)	N9 – Mn4 – N6	121.5(7)
C3 – Re1 – C2	84.9(7)	N9 – Mn4 – N12	118.5(8)
C1 – Re1 – C2	87.3(7)	N6 – Mn4 – N12	111.6(7)
C5 – Re2 – C6	85.6(7)	N9 – Mn4 – N25	97.9(8)
C5 – Re2 – C4	88.0(7)	N6 – Mn4 – N25	96.7(8)
C6 – Re2 – C4	84.7(6)	N12 – Mn4 – N25	104.7(7)
C7 – Re3 – C8	85.7(8)	C1 – N1 – Mn1	167.8(17)
C7 – Re3 – C9	87.2(8)	C4 – N4 – Mn1	165.9(16)
C8 – Re3 – C9	86.6(8)	C7 – N7 – Mn1	169.7(18)
C12 – Re4 – C11	85.8(7)	C2 – N2 – Mn2	164.6(15)
C12 – Re4 – C10	86.3(7)	C5 – N5 – Mn2	165.7(17)
C11 – Re4 – C10	86.7(7)	C10 – N10 – Mn2	167.1(16)
N1 – Mn1 – N7	104.6(7)	C3 – N3 – Mn3	167.4(17)
N1 – Mn1 – N4	100.4(7)	C8 – N8 – Mn3	164.4(18)
N7 – Mn1 – N4	107.9(7)	C11 – N11 – Mn3	168.3(17)
N1 – Mn1 – N13	113.3(6)	C6 – N6 – Mn4	160.3(16)
N7 – Mn1 – N13	115.1(6)	C9 – N9 – Mn4	154.6(19)
N4 – Mn1 – N13	114.1(6)	C12 – N12 – Mn4	153.1(17)
N2 – Mn2 – N5	108.1(6)	N1 – C1 – Re1	174.5(18)
N2 – Mn2 – N10	107.6(7)	N2 – C2 – Re1	174.7(16)
N5 – Mn2 – N10	107.3(7)	N3 – C3 – Re1	172.1(17)
N2 – Mn2 – N17	108.1(7)	N4 – C4 – Re2	169.2(16)
N5 – Mn2 – N17	112.3(7)	N5 – C5 – Re2	173.9(18)
N10 – Mn2 – N17	113.2(7)	N6 – C6 – Re2	176.8(16)
N3 – Mn3 – N8	108.1(7)	N7 – C7 – Re3	170.8(19)
N3 – Mn3 – N11	107.6(7)	N8 – C8 – Re3	176.2(19)
N8 – Mn3 – N11	106.8(7)	N9 – C9 – Re3	172.7(19)
N3 – Mn3 – N21	107.5(7)	N10 – C10 – Re4	176.1(16)
N8 – Mn3 – N21	114.0(7)	N11 – C11 – Re4	174.6(17)
N11 – Mn3 – N21	112.6(7)	N12 – C12 – Re4	176.1(18)

et al., is composed of a 2D network of six-coordinate Mn(II) ions equatorially bound to the four outer nitrile groups of σ-$[TCNQ_2]^{2-}$ ligands that exhibit a σ-bond of 1.635 Å between $TCNQ^-$ anions.[190]

Infrared Spectroscopy

Infrared spectroscopy performed on polycrystalline samples of **2** reveals two $\nu_{C\equiv N}$ stretches located at 2096 and 2081 cm^{-1}. These band are shifted by +26 and +21 cm^{-1} from the starting material **13** and are in good agreement with the Re_4Mn_4 cube that exhibits $\nu_{C\equiv N}$ stretches at 2100 and 2085 cm^{-1}.

An infrared (IR) spectrum of compound **15** contains three absorptions in the $\nu_{C\equiv N}$ region. The assignment of these modes was carried out by a comparison to the stretching frequencies of **14** as well as the complex $[Mn(MeCN)_4](BF_4)_2$ (2282, 2307 cm^{-1}) reported by Hathaway *et al.*,[144] since **15** also contains acetonitrile ligands on the Mn(II) centers. With the help of these data, the two energy modes at 2089 and 2070 cm^{-1} were assigned to the bridging cyanides that make up the cubic core, and the higher energy mode at 2296 cm^{-1} is attributed to the dangling acetonitrile ligands. The shift of the $\nu_{C\equiv N}$ stretches of the bridging cyanide ligands to lower frequencies as compared to the Re_4Mn_4 cube is attributed to weaker Mn–N bonds.

Infrared (IR) spectroscopy performed on polycrystalline samples of **16** revealed the presence of two intense $\nu_{C\equiv N}$ stretches located at 2088 and 2076 cm^{-1}, which are assigned to the bridging cyanides similar to cluster **15**.

The infrared spectra in the $\nu_{C\equiv N}$ region for **17** reveals three stretches at 2262, 2206, and 2156 cm^{-1}, which are assigned to the dangling dicyanamide ligands in addition to the ones at 2077 and 2095 cm^{-1} that belong to the bridging cyanide ligands. The three former absorptions are indicative of terminal monodentate coordination of dicyanamide ligands, which is also consistent with the X-ray crystal structure of **17**. An IR spectrum of $Na[N(CN)_2]$, in which the dicyanamide anions are not coordinated exhibits three $\nu_{C\equiv N}$ stretches. The peak located at 2179 cm^{-1} is assigned to the symmetric $\nu_{C\equiv N}$ mode, the one at 2232 cm^{-1} to asymmetric $\nu_{C\equiv N}$ mode and the one at 2286 cm^{-1} to a combination of asymmetric and symmetric $\nu_{C\equiv N}$ modes. Coordination of the dicyanamide anion to a metal center results in a shift of these bands to higher frequencies similar to what happens to $\nu_{C\equiv N}$ stretches of bridging cyanide ligands. For example, $\nu_{C\equiv N}$ stretches at 2194, 2261, and 2293 cm^{-1} are observed for a 3D framework compound, $Mn(dca)_2$, consisting of dicyanamide ligands using both of its cyano groups for binding.[191] The stretches observed for **17** are in good agreement with other clusters that contain monodentate dicyanamide ligands attached to Mn(II) centers such as $[Mn_4(hmp)_6(NO_3)_2(dca)_2]\cdot 2MeCN$ (hmp= 2–hydroxymethylpyridine), which exhibit $\nu_{C\equiv N}$ stretches at 2264, 2210, and 2154 cm^{-1}.[184]

Clearly the shift of $\nu_{C\equiv N}$ modes with respect to reference data is useful for assigning the coordination mode of cyano groups since coordination of the N-atom to a metal center usually leads to a shift to higher frequencies due to σ-donation from the cyanide ligand to the metal ion, but there are complications with this argument for

TCNQ molecule. The $\nu_{C\equiv N}$ stretching modes of TCNQ molecule can shift to higher energies if TCNQ acts primarily as a σ-donor or to lower energies if there is significant metal to TCNQ π-backbonding. As an illustration, we note that three distinct absorptions ranging from 2168 to 2226 cm^{-1} were observed in the infrared spectra of a series of materials of general formula $M(TCNQ)_2(H_2O)_2$ (M= Mn, Fe, Co, and Ni).[192] But it was also discovered that δ(C–H) bend of TCNQ is more informative for detecting the presence of the σ-dimer $[TCNQ–TCNQ]^{2-}$ unit. The series of extended networks exhibit a δ(C–H) mode at around 825 cm^{-1} indicative of $[TCNQ]^{-\bullet}$ being present as well as for $[Mn(TCNQ–TCNQ)(MeOH)_4]_\infty$ a bending mode at 806 cm^{-1}, which is assigned to the presence of σ-$[TCNQ–TCNQ]^{2-}$. Compound **18** exhibits features at 804 and 812 cm^{-1} data that support the finding of the X-ray crystal structure of **18** that points to both σ-$[TCNQ–TCNQ]^{2-}$ and [H–TCNQ] units being present. Additional features at $\nu_{C\equiv N}$ region (2050–2300 cm^{-1}) are observed at 2113, 2130, 2171, and 2195 cm^{-1}, which are assigned to cyanide stretches of TCNQ ligands present in **18**.

Magnetic Properties

The magnetic behavior of compounds **14-18** is similar to that of the Re_4Mn_4 cube. The temperature-dependent magnetic behavior of compound **14** (Figure 61) exhibits similar features to that of the Re_4Mn_4 cube. The χT value is 16.02 $emu\cdot mol^{-1}\cdot K$ at 300 K, which corresponds to a value of 3.38 $emu\cdot mol^{-1}\cdot K$ per Mn(II) ion, using the value of 0.63 $emu\cdot mol^{-1}\cdot K$ obtained for the parent Re(II) complex. The high temperature moment of the complex is in accord with the expected value per Mn(II) ion (4.38

emu·mol^{-1}·K) for isolated magnetic ions. With decreasing temperatures, the χT product decreases until 70 K at which temperature it exhibits a broad minimum, which is followed by an abrupt increase in χT at 5.5 K to a value of 22.42 emu·mol^{-1}·K. As in the case of **14**, this behavior is consistent with an antiferromagnetic interaction between the Re(II) and Mn(II) ions. Field dependent magnetization data for $[\{MnI\}_4\{Re(triphos)(CN)_3\}_4]$ (**14**) is collected at 1.8 K (Figure 62). The high field value of 11.26 μB obtained from this experiment is significantly less than the expected value for an S = 8 fround state (16 μB), and the high field response of the complex does not saturate. These observations can be rationalized on the basis of the orbital contribution of the Re(II) ion, which results in the cluster having g < 2. Complete sweep of the field in the positive and negative directions in this experiment reveals the compound does not exhibit coercivity at 1.8 K. AC susceptometry revealed a signal in χ'' with frequency dependence, indicating that **14** also behaves as a single molecule magnet. The effective barrier height (U_{eff}) could not be determined, since the blocking temperatures lie below 1.8 K (Figure 63).

The magnetic properties of **15** in the temperature range of 2-300 K reveal the existence of antiferromagnetic coupling between the metal ions. The χT value at 300 K is 17.57 emu·mol^{-1}·K for this cluster, which corresponds to four non-interacting Re(II) centers (based on the reference value from the starting material of 0.63 emu·mol^{-1}·K per metal ion) and four high-spin S = 5/2 Mn(II) ions with a moment of 4.11 emu·mol^{-1}·K

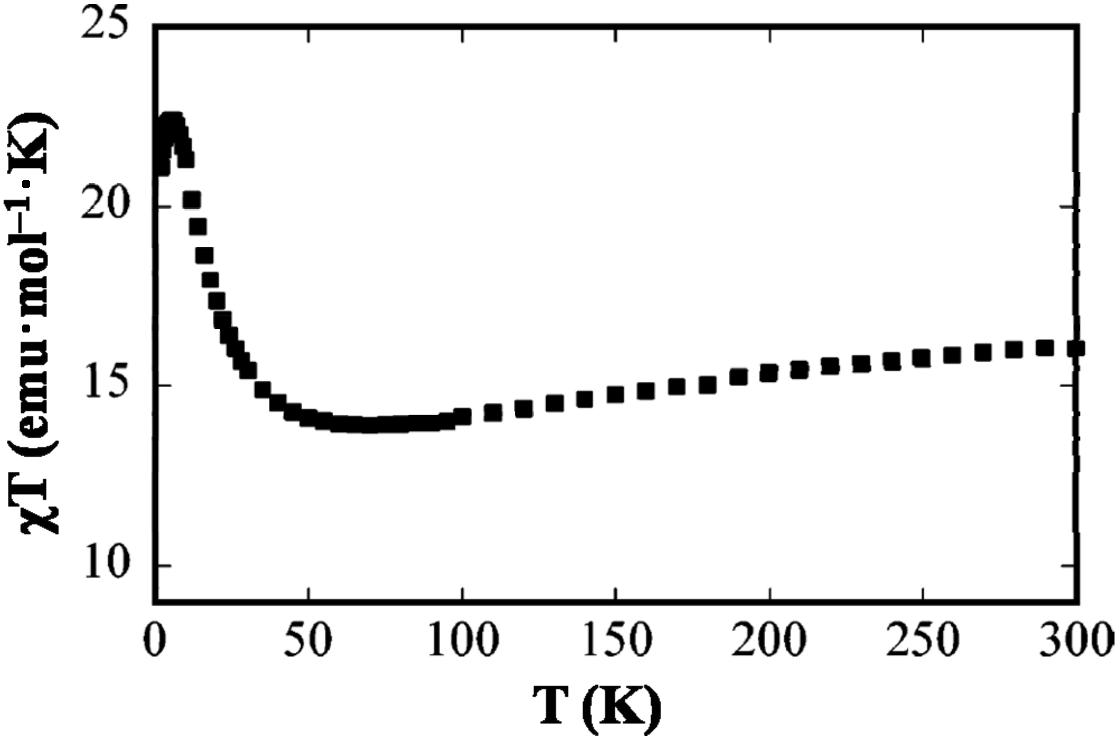

Figure 61. Temperature-dependent magnetic susceptibility data for **14** recorded in the range of 1.8 – 300 K.

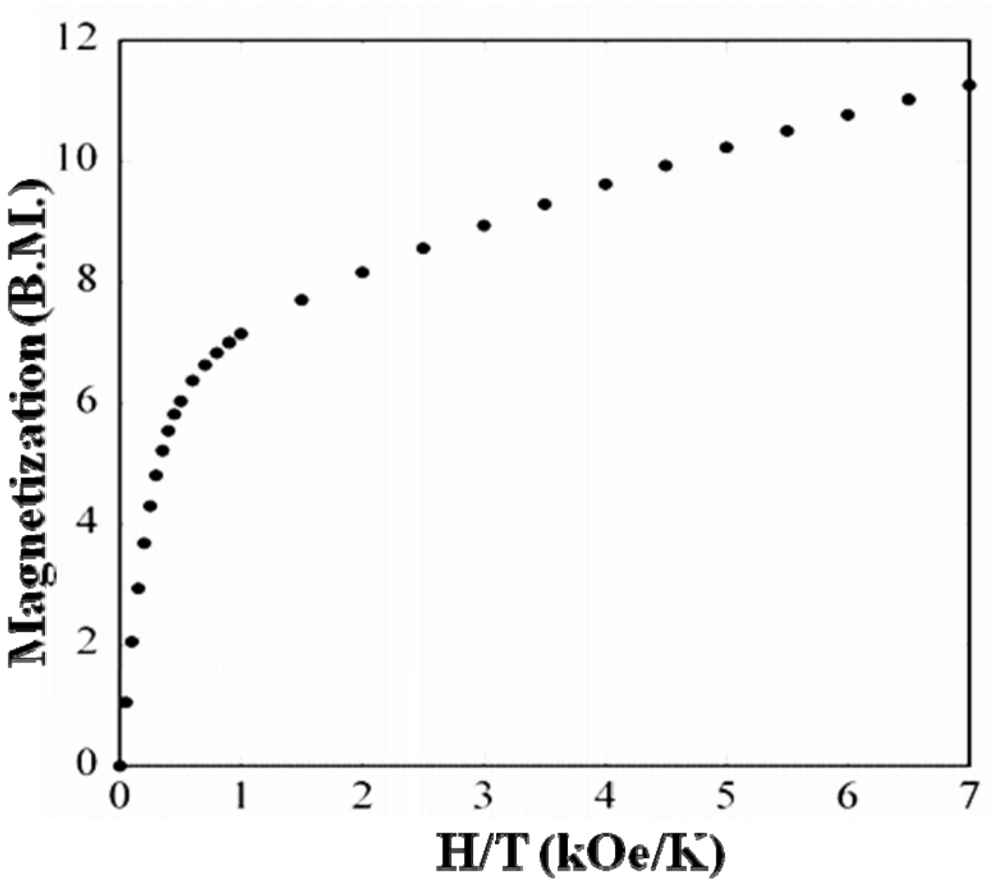

Figure 62. Field dependent magnetization data for **14** collected at 1.8 K.

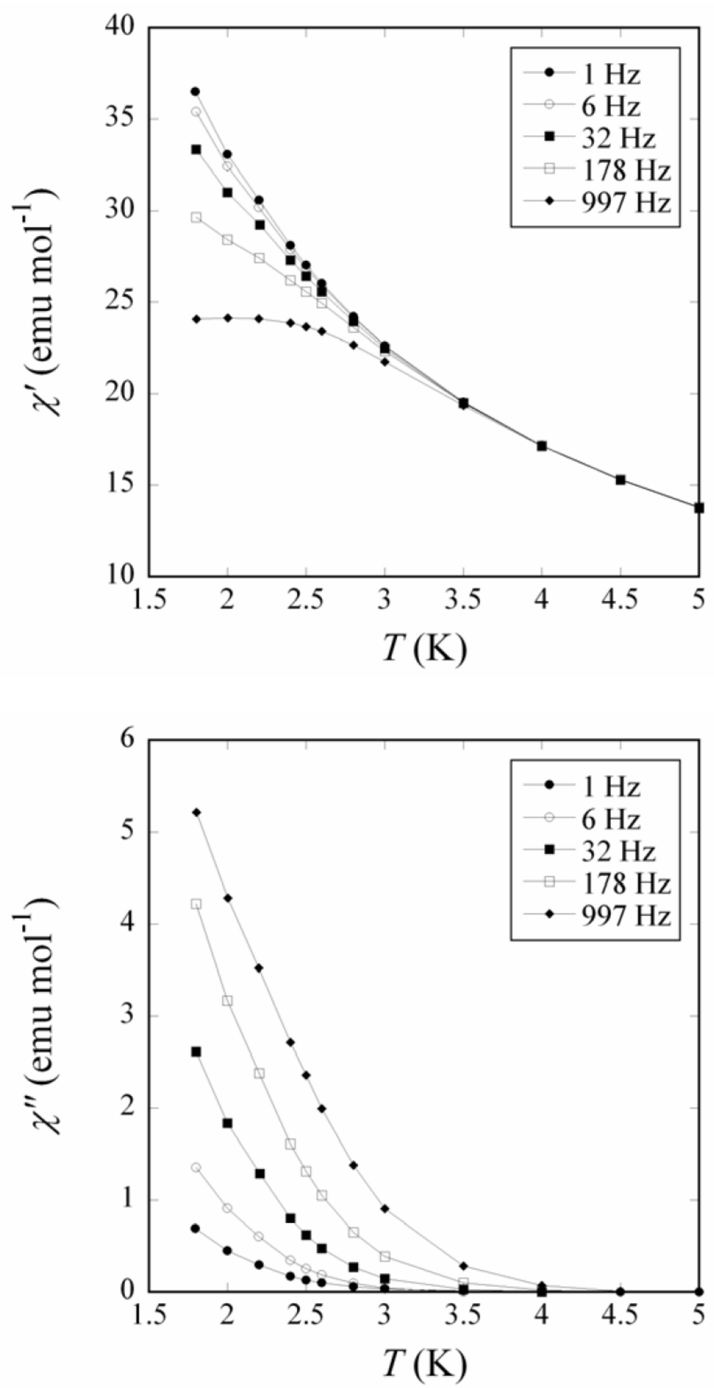

Figure 63. AC susceptibility studies of **14** from 1.8 – 5 K with H_{DC} = 0 Oe and H_{AC} = 3 Oe.

per Mn center (Figure 64). This value is slightly lower than the expected value of 4.38 emu·mol^{-1}·K per Mn(II). The χT vs T curve decreases over the low temperature range until it reaches a minimum at 56 K after which temperature it begins to increase until it reaches a low temperature maximum of 23.05 emu·mol^{-1}·K at ~3.8 K. The low temperature χT product maximum achieved by the compound is very low based on the expected value for antiferromagnetic coupling (S = 8, 36 emu·mol^{-1}·K) between isotropic metal ions, which is clearly a consequence of the anisotropic behavior of the Re(II) ion (Figure 65). The g value of this cluster is lower than the isotropic value of 2.0 in which accounts for the low temperature maximum value found. AC susceptibility experiments were performed in order to probe whether the cluster exhibits slow paramagnetic relaxation. Measurements performed at 1.8 K using four frequencies from 1-1000 Hz (MPMS SQUID) exhibit a signal with both an in-phase (χ) and out-of phase (χ”) component which is an indication the molecule exhibits slow paramagnetic relaxation (Figure 66). The effective height of the energy barrier for magnetization reversal is rather small for this compound, as evidenced by the lack of a maximum in the χ” vs T data in this temperature range at these frequencies.

The room temperature χT value of 16.77 emu·mol^{-1}·K was observed for **16**, which is lower than the expected spin-only value of four Re(II) and four Mn(II) centers. The χT value decreases to 13.87 emu·mol^{-1}·K at ~50 K as the temperature is lowered, after which temperature χT increases to a maximum of 16.64 emu·mol^{-1}·K at 6.60 K (Figure 67). The magnetic behavior below 50 K is indicative of antiferromagnetic

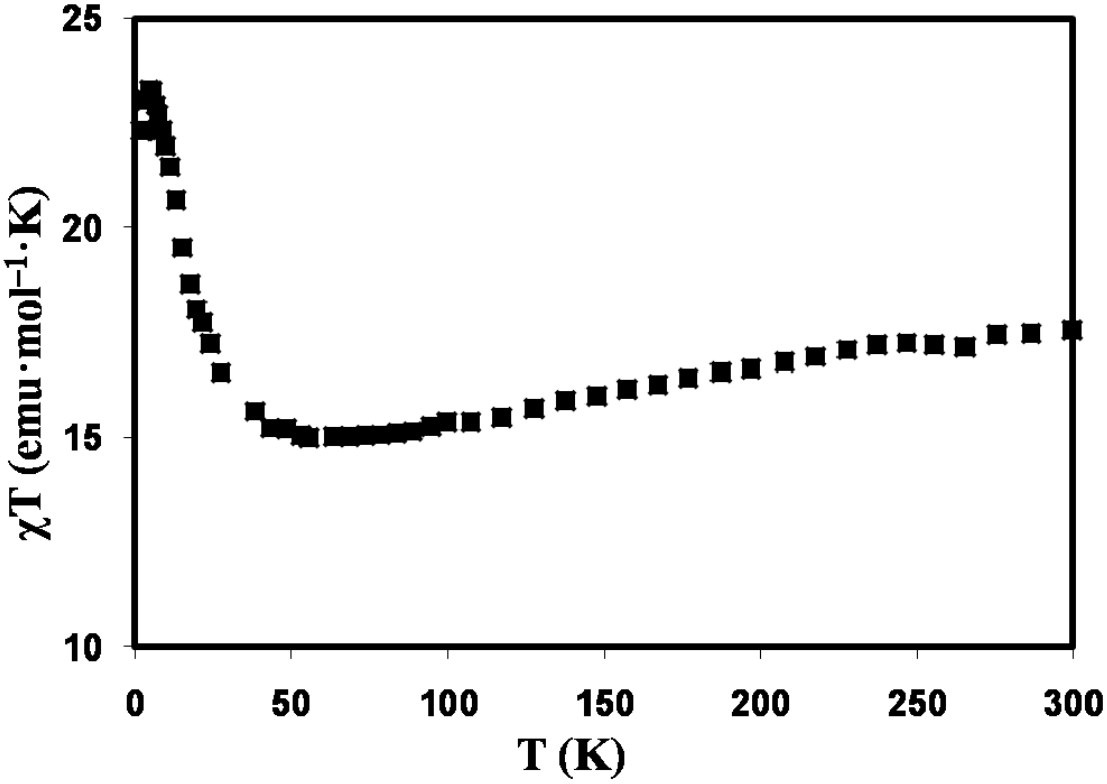

Figure 64. Temperature-dependent magnetic susceptibility data for **15** recorded in the range of 1.8 – 300 K.

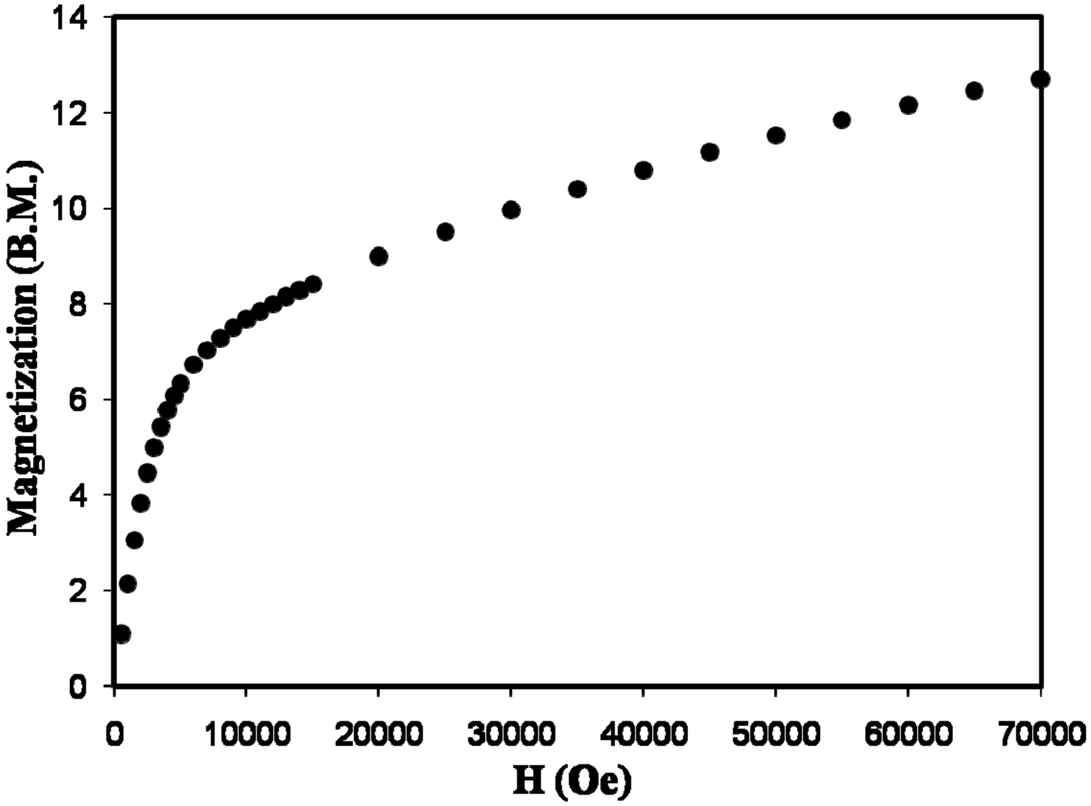

Figure 65. Field dependent magnetization data for **15** collected at 1.8 K.

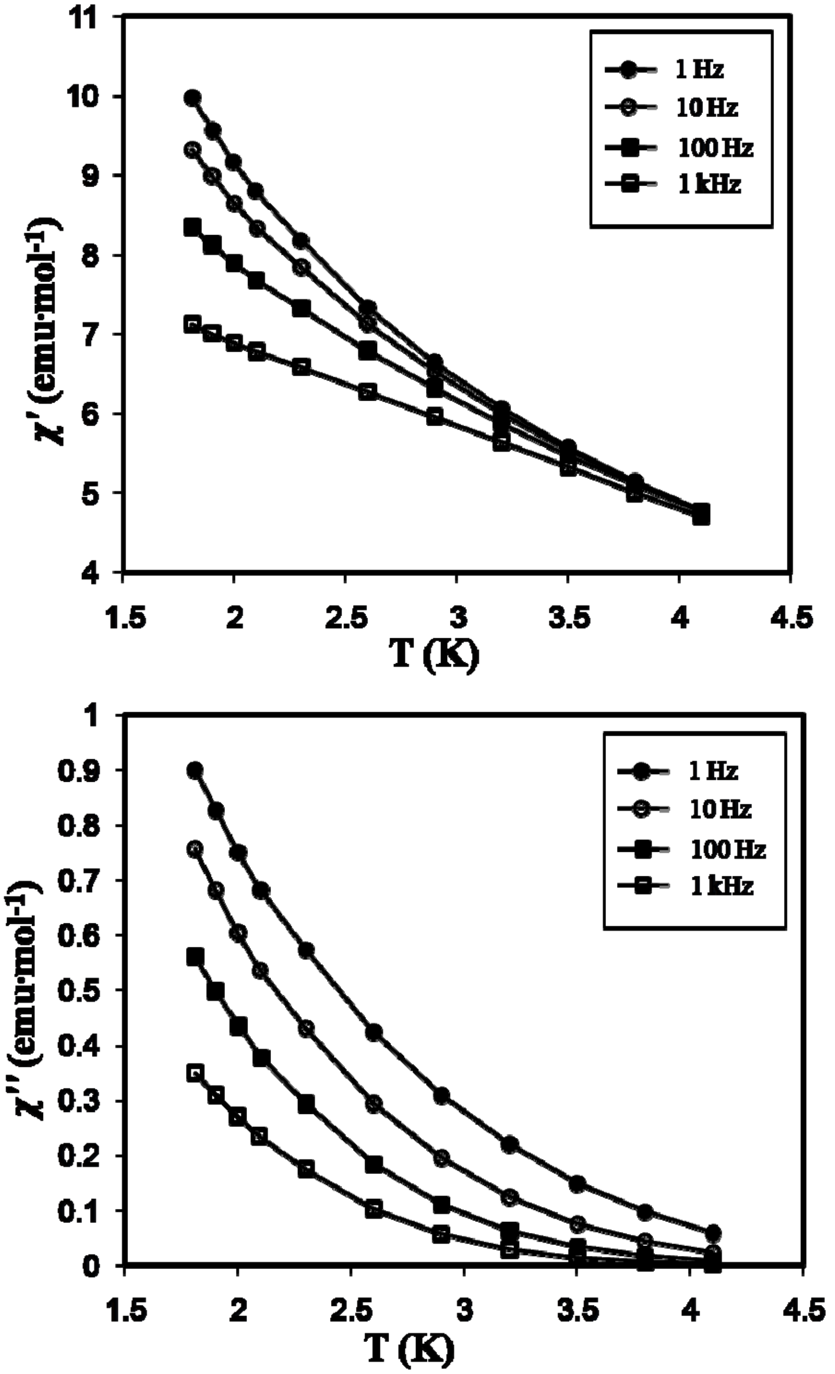

Figure 66. AC susceptibility studies of **15** from 1.8 – 5 K with H_{DC} = 0 Oe and H_{AC} = 3 Oe.

(Figure 67). The magnetic behavior below 50 K is indicative of antiferromagnetic coupling between the paramagnetic centers that stabilize a high-spin ground state. The magnetization data that reaches to a value of 13.80 μB also suggests the stabilization of a high-spin ground state (Figure 68). To probe the dynamics of the magnetization relaxation of compound **16**, AC susceptibility measurements were performed in a 3 G AC field oscillating at 1–1000 Hz in the temperature range of 1.8 – 4.5 K on the same sample of crystals that was used for the DC studies. The in-phase magnetic susceptibility signal (χ') follows the expected behavior for a paramagnetic system. In addition to the χ' signal, the compound exhibits an out-of-phase (χ'') signal below 4 K (Figure 69). Although no maximum was observed down to 1.8 K, there is an obvious frequency dependence of the χ'' signal consistent with SMM behavior.

DC magnetic susceptibility measurements were performed on a sample of **17** to probe the nature of the magnetic exchange coupling within the Re_4Mn_4 core. The variation of χT product with temperature is plotted in Figure 70. The χT value is 16.27 $emu \cdot mol^{-1} \cdot K$ at 300 K, somewhat below the spin-only value of 20.02 $emu \cdot mol^{-1} \cdot K$ expected for four Re(II) and four Mn(II) ions in the absence of any exchange coupling. The χT value decreases as the temperature is lowered and reached a minimum of 13.95 $emu \cdot mol^{-1} \cdot K$ at approximately 50 K before rising steeply to a maximum of 16.81 $emu \cdot mol^{-1} \cdot K$ at 6.5 K. This behavior is consistent with antiferromagnetic coupling between the Mn(II) and Re(II) ions, giving rise to a ferrimagnetic $S = 8$ ground state. This conclusion is in accord with the magnetization data measured at 1.8 K which

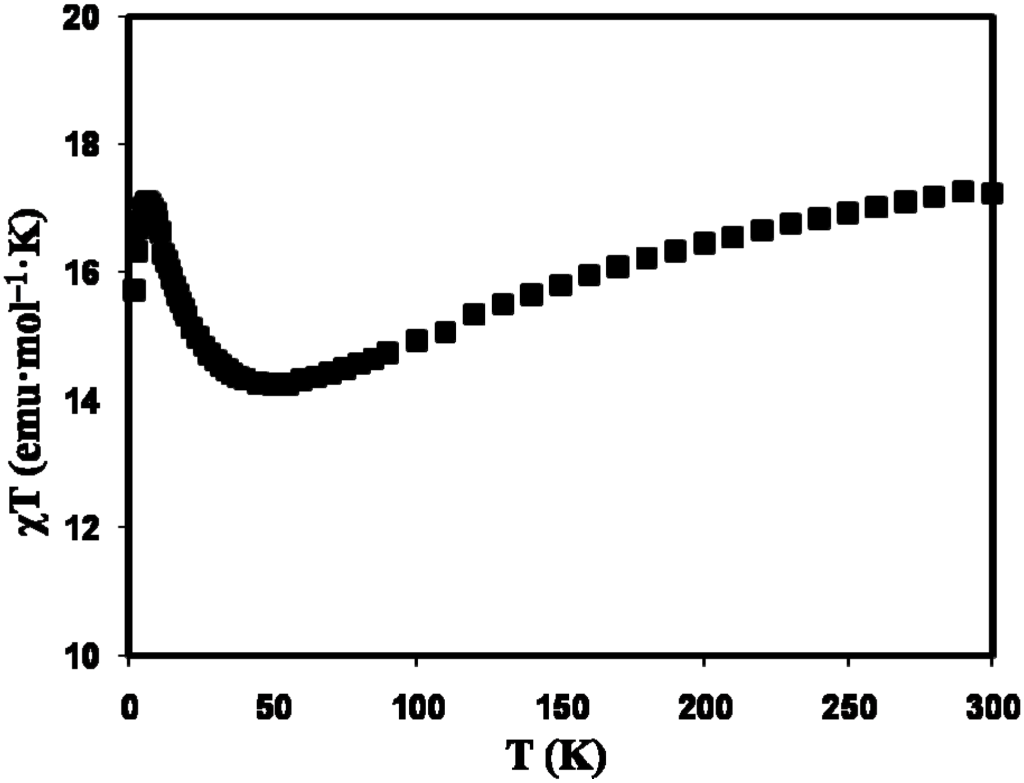

Figure 67. Temperature-dependent magnetic susceptibility data for **16** recorded in the range of 1.8 – 300 K.

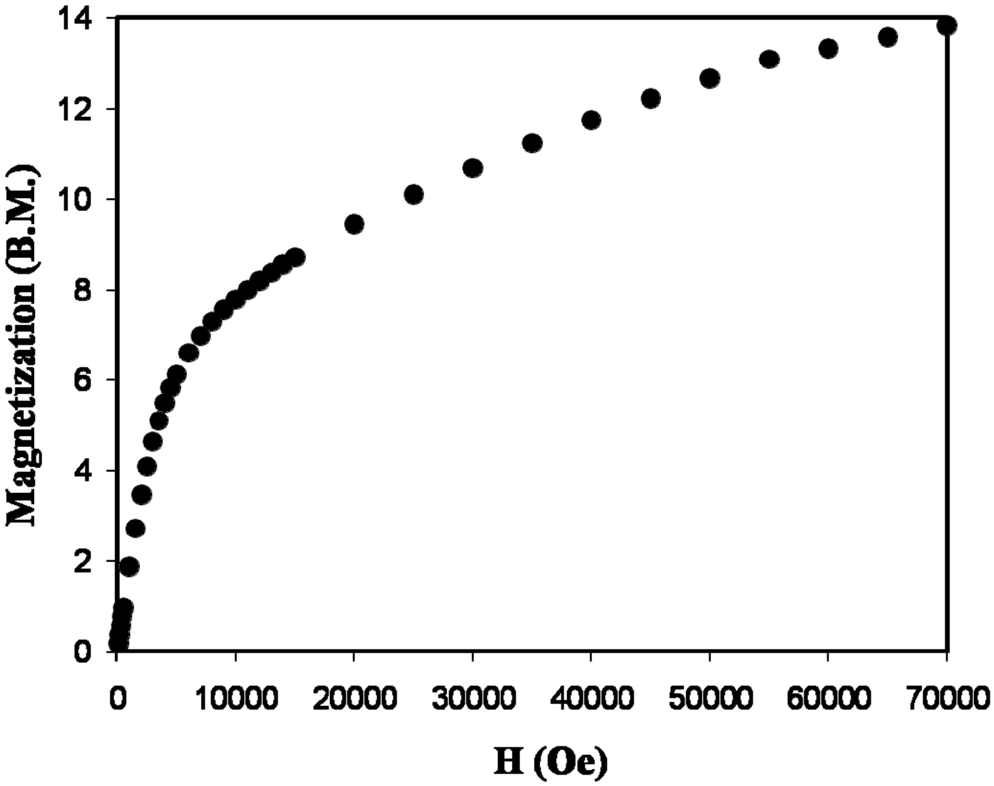

Figure 68. Field dependent magnetization data for **16** collected at 1.8 K.

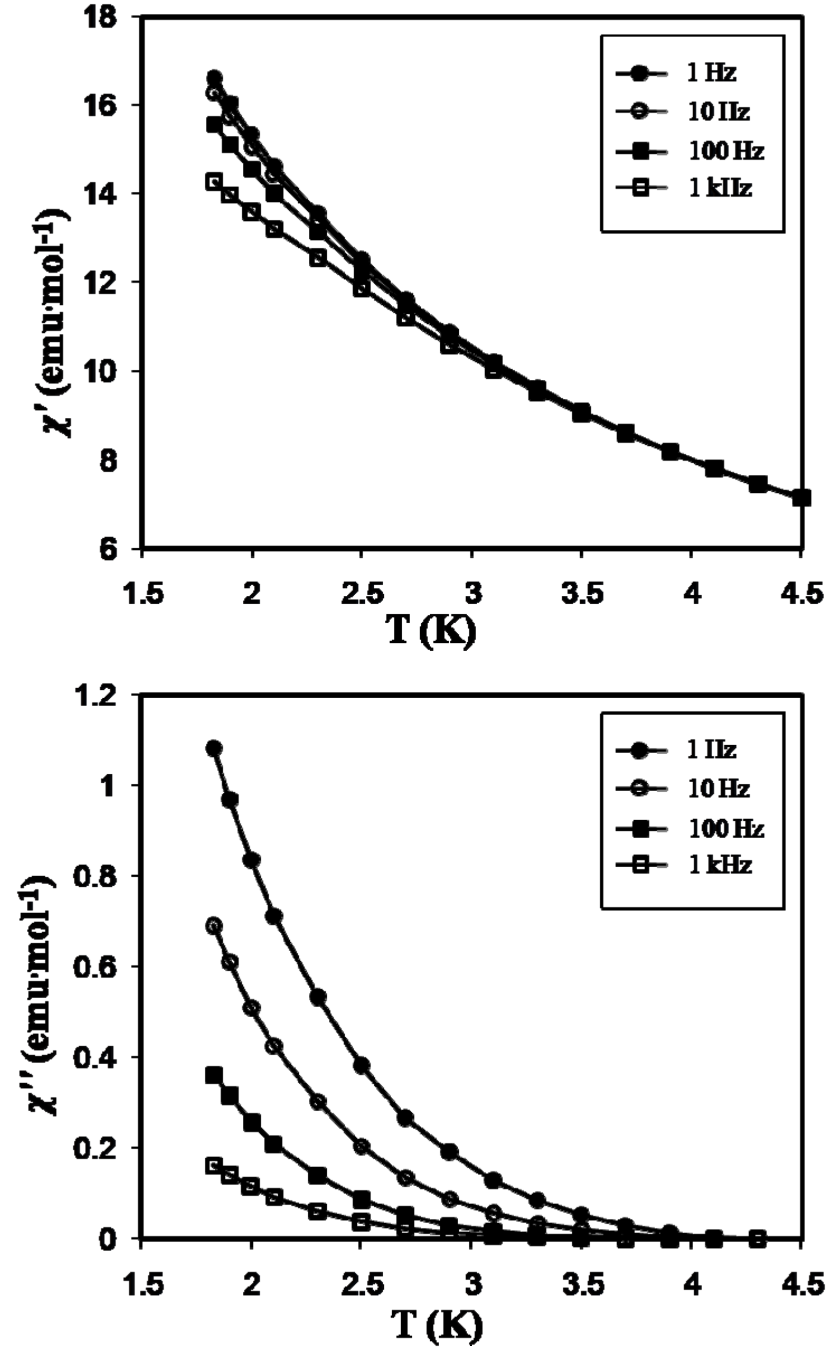

Figure 69. AC susceptibility studies of **16** from 1.8 – 5 K with H_{DC} = 0 Oe and H_{AC} = 3 Oe.

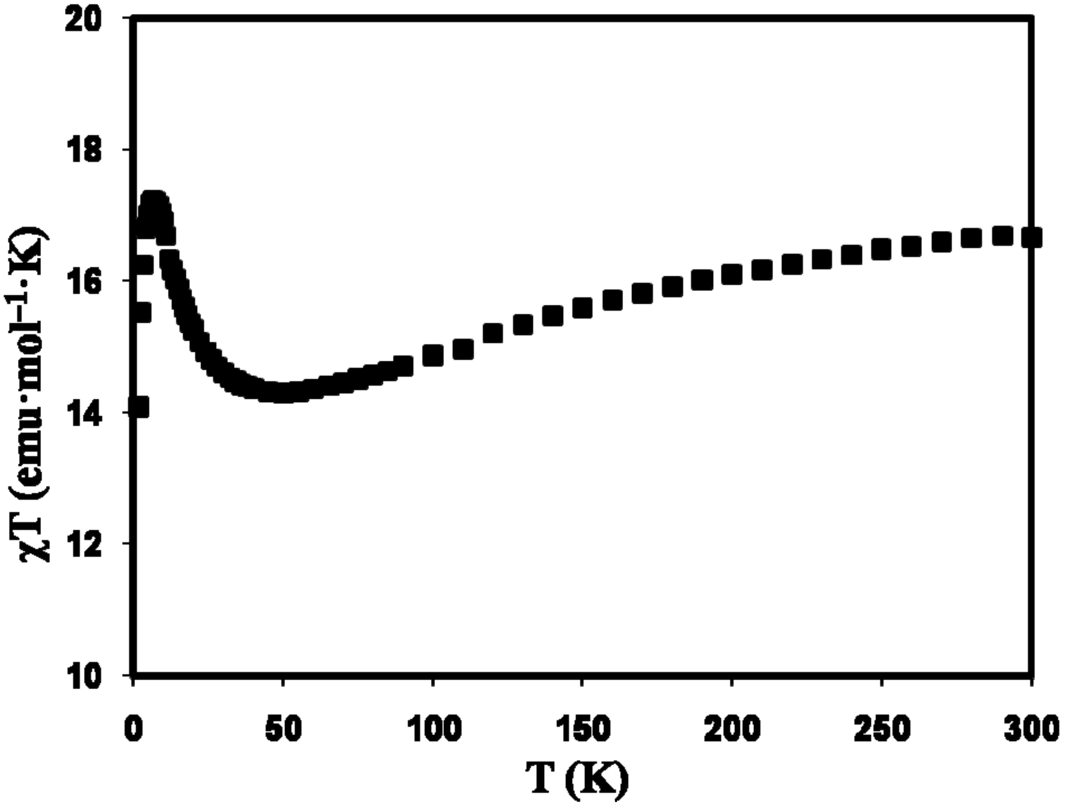

Figure 70. Temperature-dependent magnetic susceptibility data for **17** recorded in the range of 1.8 – 300 K.

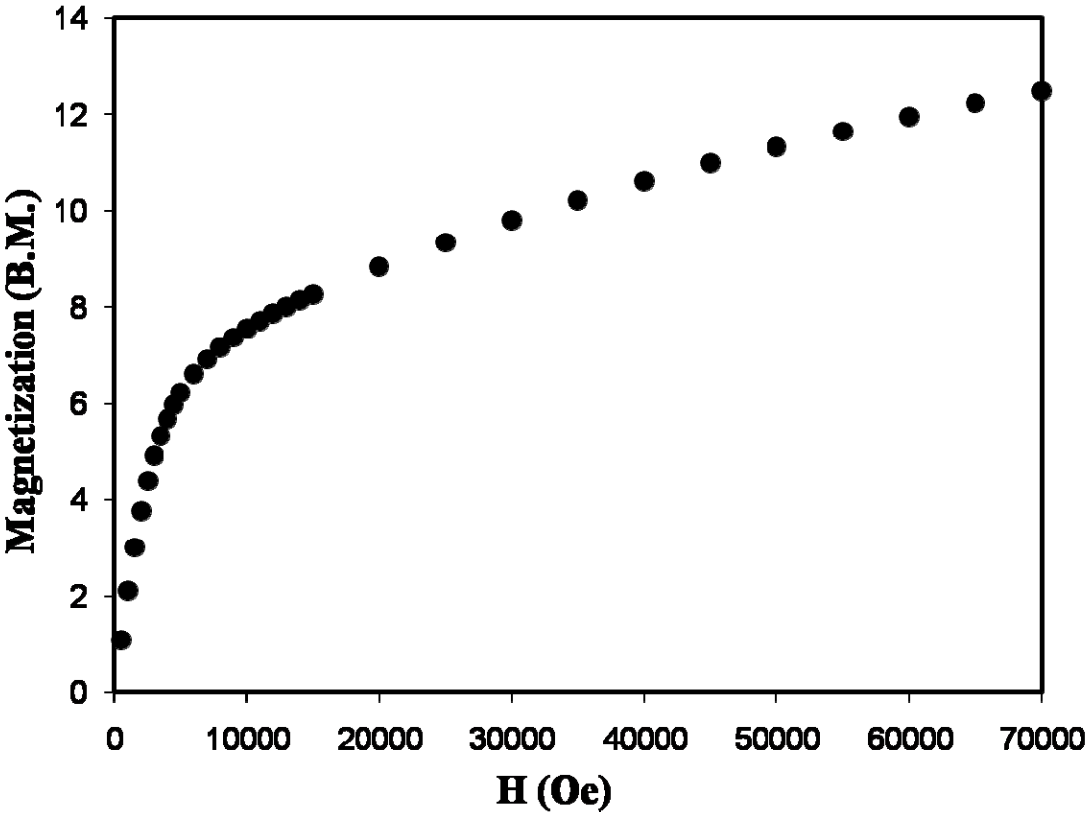

Figure 71. Field dependent magnetization data for **17** collected at 1.8 K.

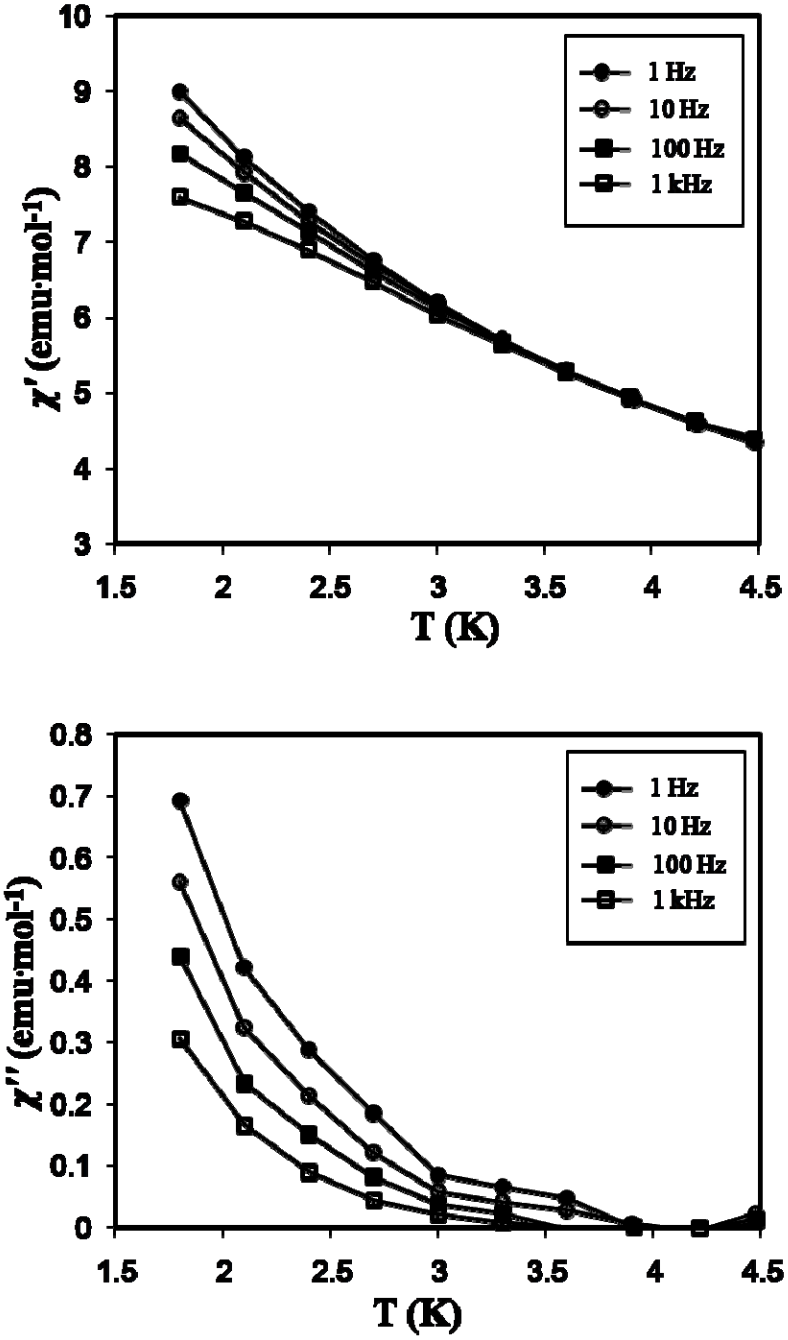

Figure 72. AC susceptibility studies of **17** from 1.8 – 5 K with H_{DC} = 0 Oe and H_{AC} = 3 Oe.

reaches a maximum of 12.48 μB (Figure 71). AC magnetic susceptibility measurements performed in the range of 1 – 1000 Hz revealed a frequency dependency of the χ'' signal similar to the aforementioned clusters (Figure 72).

Temperature-dependent magnetic susceptibility studies were performed on **18** at 1000 Oe over the temperature range 1.8 – 300 K. The observed χT value at room temperature is 16.73 emu·mol^{-1}·K which decreases to 13.97 emu·mol^{-1}·K as the temperature is lowered to 50 K, an indication of weak antiferromagnetic coupling between the Re(II) and Mn(II) ions (Figure 73). The χT product then increases to a maximum of 18.70 emu·mol^{-1}·K at 6 K. Field dependent magnetization data collected at 1.8 K in the range of 0–7 T reaches a value of 12.72 μB revealing the stabilization of an S = 8 high-spin ground state as a result of antiferromagnetic coupling between the Re(II) and Mn(II) ions (Figure 74). AC susceptometry performed in a 3 G AC field oscillating at 1–1000 Hz in the temperature range of 1.8 – 4.5 K shows a frequency dependent out-of-phase signal (Figure 75). Similar magnetic behavior for **18** with the mentioned discrete Re_4Mn_4 derivatives under dc and ac fields suggests that the cubes that form the single chain are well isolated from each other which precludes any significant magnetic interactions resulting in the single chain behaving like a single molecule magnet.

CONCLUSIONS

The syntheses of the distorted cubic cyanide cluster, $\{[Re^{II}(triphos)(CN)_3]_4[Mn^{II}Cl]_4\}$ (Re_4Mn_4), by reacting $Mn^{II}Cl_2$ with $[Re^{II}(triphos)(CN)_3]^-$ (triphos: 1,1,1-tris(diphenylphosphinomethyl)ethane), which was found to exhibit single molecule

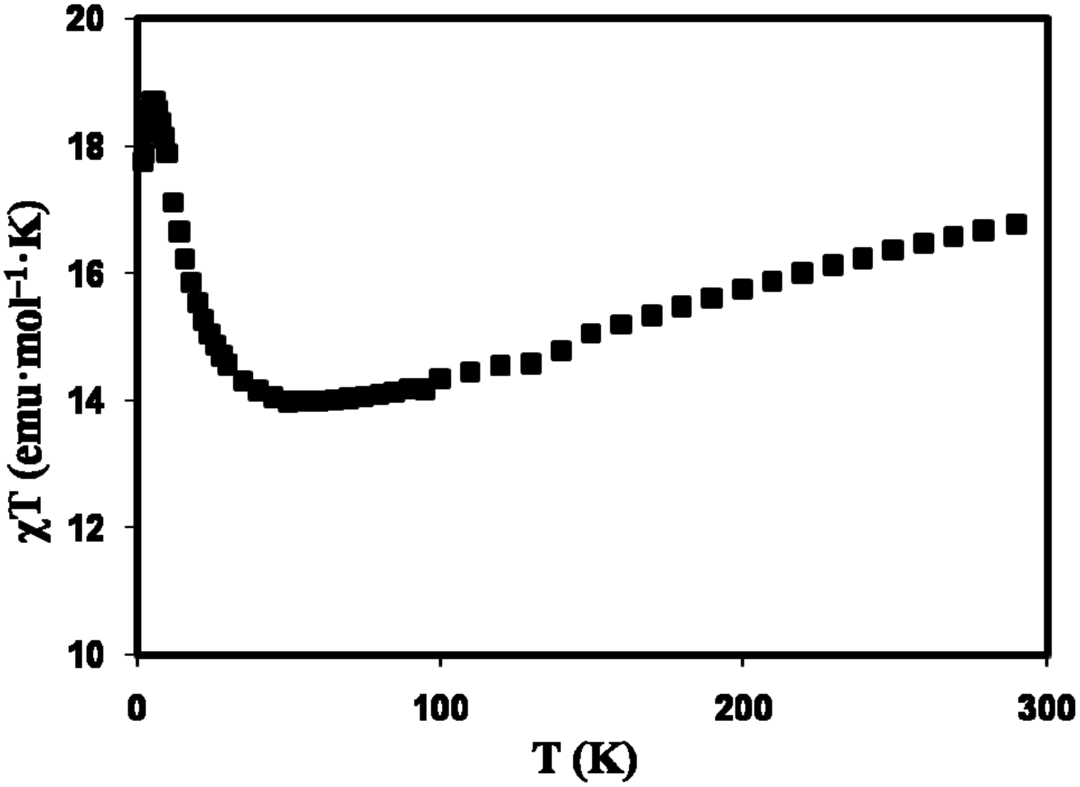

Figure 73. Temperature-dependent magnetic susceptibility data for **18** recorded in the range of 1.8 – 300 K.

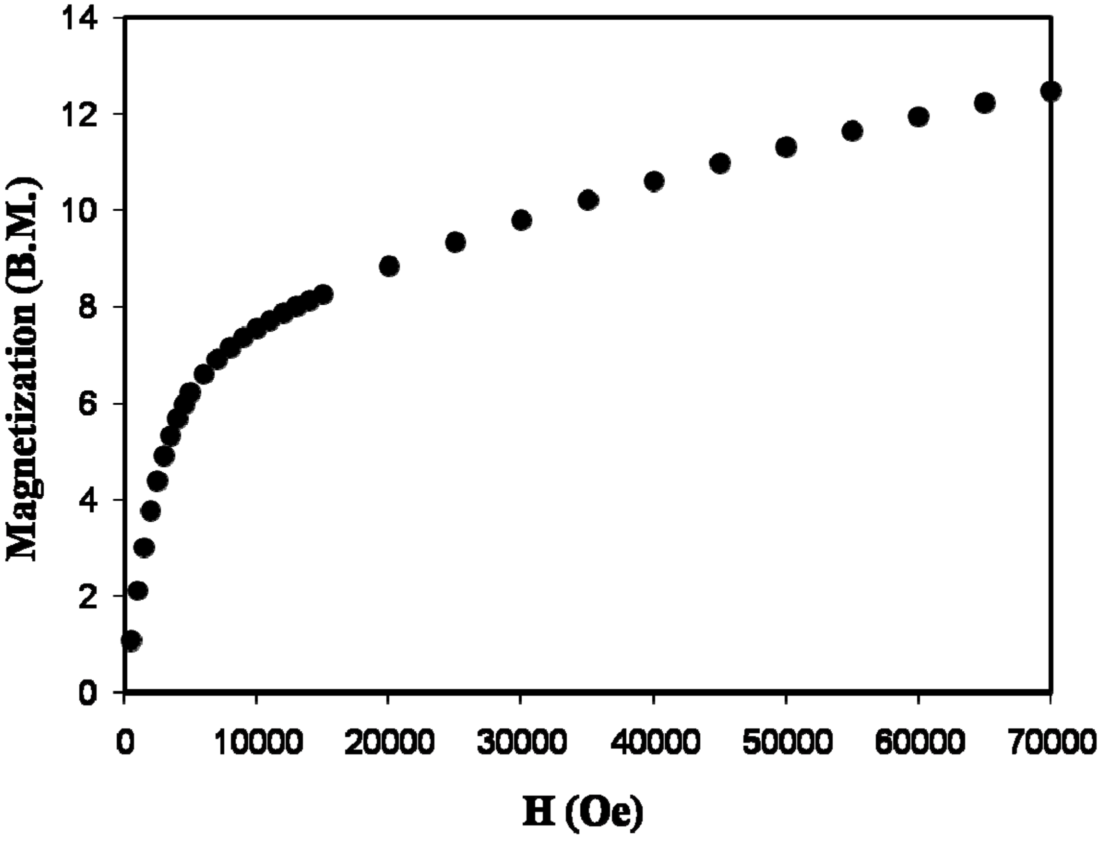

Figure 74. Field dependent magnetization data for **18** collected at 1.8 K.

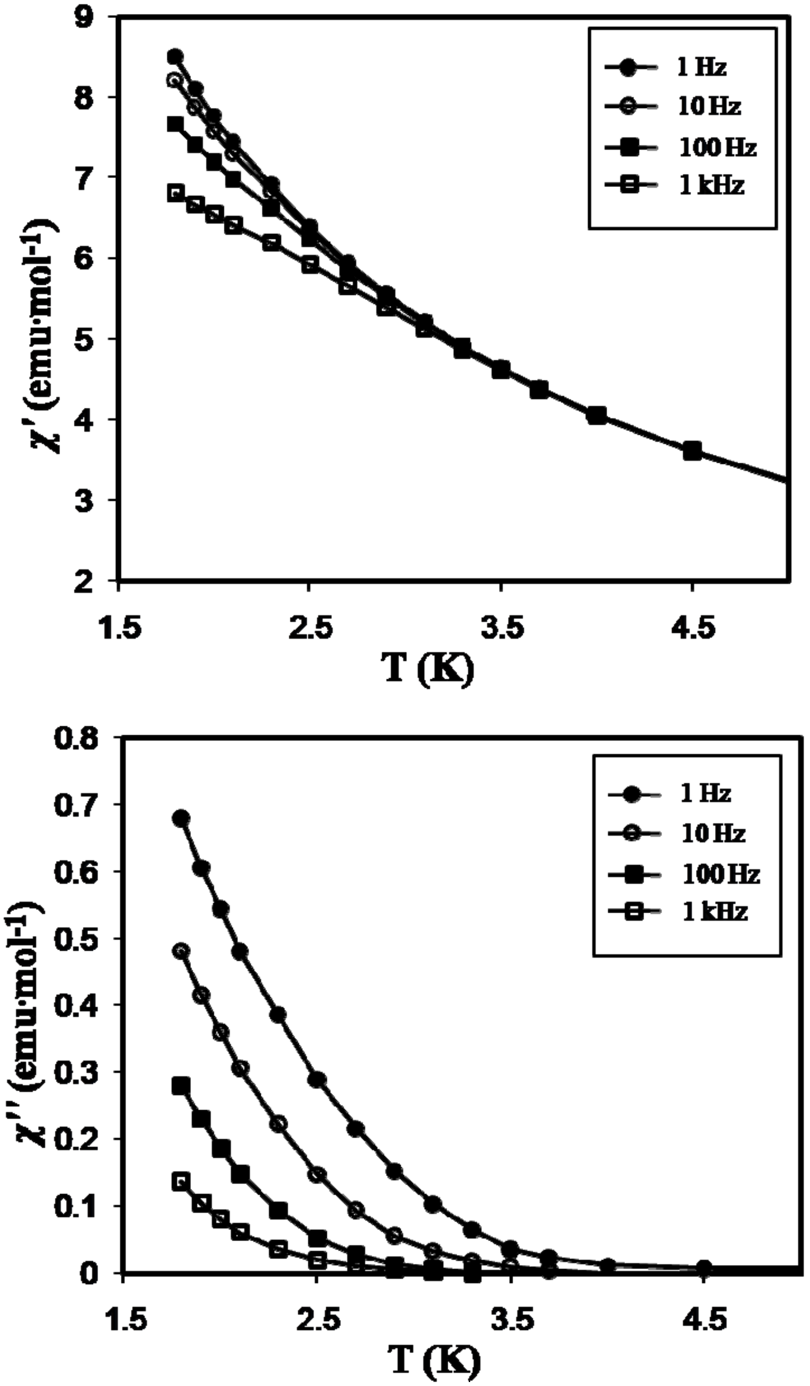

Figure 75. AC susceptibility studies of **18** from 1.8 – 5 K with H_{DC} = 0 Oe and H_{AC} = 3 Oe.

magnetic (SMM) behavior had been previously reported but no new compounds of this type have been available until this work. Derivatives of the Re_4Mn_4 SMM clusters have been prepared by using other Mn(II) salts, *e.g*, $[Mn(H_2O)_6]^{2+}$ and MnI_2 in order to extend the range of accessible precursors. Derivative **14**, which is isomorphous to the Re_4Mn_4 cube, has four dangling iodide atoms attached to the Mn(II) sites. The cluster **15** possesses a 4+ charge in contrast to the Re_4Mn_4 cube and derivative **14** since negatively charged halogen atoms have been replaced with neutral acetonitrile ligands. For compound **16** perchlorate anions are used to complete the coordination sphere of three Mn(II) sites and a methanol ligand is connected to the other Mn(II) center. The crystal structure also revealed the presence of a methoxy ligand that points to the inside of the internal cavity of the cube. This methoxy ligand is bound to the Mn(II) centre with the methanol ligand resulting in a penta-coordinate Mn(II) site. AC susceptometry revealed that a frequency dependency of the χ'' signal was observed for all of the reported derivatives similar to the Re_4Mn_4 cube.

The successful use of the new clusters to prepare additional compounds from reactions with organocyanide molecules including dicyanamide anion (dca^-) and TCNQ (7,7,8,8–tetracyanoquinodimethane) were presented in this chapter. The reaction of the derivative **15** with dca^- ligand yielded a discrete cluster with dangling dicyanamide ligands (**17**). Furthermore, such a reaction with LiTCNQ produces a single chain of dimers of Re_4Mn_4 cubes bridged through σ-bonded $TCNQ_2^{2-}$ molecule (**18**). Magnetic measurements revealed that both of these compounds exhibit SMM behavior similar to Re_4Mn_4 cube.

Given that derivatives of the Re_4Mn_4 cube have been successfully synthesized and characterized, and that they can be used as a building block for the preparation of extended networks, these derivatives could be used in further reactions to incorporate such molecules into extended networks or higher nuclearity clusters to improve their properties and functionality.

CHAPTER V

CONCLUDING REMARKS AND OUTLOOK FOR FUTURE WORK

In the last decades, transition metal chemistry has led to polynuclear clusters that exhibit a variety of intriguing and exciting physical and chemical properties. In recent decades particularly high interest has been placed on cyanide bridged clusters due to the ability of the bridging cyanide linker to promote relatively strong and predictable magnetic coupling.[68,193] The obvious conventional wisdom of using short tethers to connect metal spin centers notwithstanding, coordination compounds bridged by polynitrile ligands such as TCNQ, DCNQI or their derivatives present fascinating alternatives for engendering magnetic and electronic coupling.

Cyanide bridged clusters are good candidates for reactions with nitrile acceptor ligands because of the fact they can have open sites on the metal ions available for further coordination. The presence of π-stacked columns of the organocyanide ligand is an important component of the conducting pathway, but interactions through the metal-organic framework are essential for the high metallic conductivities exhibited by some of these coordination polymers.[193-195] The synthetic challenge of preparing suitable precursor molecules that are both reasonably stable yet poised to react further has led us to design and prepare the derivatives of previously prepared clusters with promising magnetic properties, which could be used further as a building block to prepare extended networks.

The triphos ligand (triphos: 1,1,1-tris(diphenylphosphinomethyl)ethane) has successfully been used in this project to prepare a family of trinuclear, tetranuclear and octanuclear clusters based on the $[Co^{II}(triphos)(CN)_2]$ or $[Re^{II}(triphos)(CN)_3]^-$ building blocks. The numbers of coordinated cyanide ligands as well as the bond angles between these cyanide ligands make them remarkable complexes for preparing magnetic clusters. The triphos ligand serves as a bulky ligand that effectively isolates the molecules in the solid state, thereby resulting in fascinating magnetic properties such as single molecular magnetism. Furthermore, metal complex coordinated to the aforementioned ligand can possess unique coordination geometries due to electronic effects. The quest for introducing metal ions with different geometries is one of the main themes in this field since orientation of magnetic orbitals is an essential parameter in defining magnetic coupling. For example, the penta-coordinate geometry of Co(II) center in $[Co^{II}(triphos)(CN)_2]$ complex is an important factor that leads to unusual superexchange behavior in the family of trinuclear complexes (**7-10**) as discussed in Chapter III.

The family of cyanide-bridged molecular squares, $[Co(triphos)(CN)_2]_2[MCl_2]_2$ (M= Mn, Fe, Co, Ni, and Zn), has been prepared by reacting the $Co(triphos)(CN)_2$ precursor with the chloride salts of 3d metal ions.[109,110] The efforts to substitute the chloride ion with bridging ligands, such as oxalate, $N(CN)_2^-$, and N_3^- anion, has failed due to the electroneutrality and hence the solubility of these clusters. Therefore, the precursor $Co(triphos)(CN)_2$ has been reacted with perchlorate salts of 3d metal ions resulting in a similar family of molecular squares where the octahedral 3d metal center is occupied with 4 solvent ligands instead of 2 chloride anions, which results in a charged cluster with higher solubility in organic solvents. A family of molecular trinuclear clusters has also been prepared by changing the stoichiometric ratio of the precursors.

This progress has inspired us to prepare derivatives of other magnetic clusters particularly those that exhibit interesting physical properties such as single molecule magnetism (SMM) or interesting electrochemical behavior.

The $[Re(triphos)(CN)_3]_4[MnCl]_4$ (Re_4Mn_4) cube, which is studied by our collaborators extensively due to its SMM behavior,[101,106,165] resembles the family of squares since both clusters have cyanide-bridged metal cores surrounded by triphos ligands and chloride atoms available for further chemistry. Similar to the approach discussed above, the precursor $[Re(triphos)(CN)_3]^-$ has been reacted with $Mn(ClO_4)_2.6H_2O$ in MeCN, forming a similar molecular cube where each Mn(II) site is coordinated to one MeCN ligand resulting in the charged complex, $\{[Re(triphos)(CN)_3]_4[Mn(MeCN)]_4\}^{4+}$ (**15**). The same reaction in methanol yields another molecular cube where the central void of the cubic core is occupied by a methoxide anion in addition to three perchlorate and one methanol ligands connected to Mn(II) sites resulting in $\{[Re(triphos)(CN)_3]_4[Mn_4(ClO_4)_3(MeOH)(MeO)\}$ (**16**). These derivatives not only are good models to study the SMM behavior of the Re_4Mn_4 core, but could also be used as building blocks for further chemistry due to the accessible sites on the Mn(II) ion. This approach has been verified by reacting $[Re_4Mn_4(MeCN)_4]^{4+}$ and $N(CN)_2^-$ in a 1:4 ratio. The result is a neutral cluster, $[Re(triphos)(CN)_3]_4[Mn(C(CN)_2)]_4$ (**17**), where each of the MeCN ligands are replaced by $N(CN)_2^-$. More importantly, the reaction of **16** with LiTCNQ led to single crystals of an extended network of cubes. The compound **18** is a chain magnet where the cubes are connected through sigma dimerized TCNQ molecules, σ-$[TCNQ]_2^{2-}$. The resulting compound can be described as a 1D chain of dimers of cubes. The compound consists of cubes, which assemble into a chain forming dimers using two of its σ-$[TCNQ_2]^{2-}$ ligands and the dimers of cubes connect to each other by another σ-$[TCNQ_2]^{2-}$, with the last available coordination site of the cube being occupied by a one H-TCNQ resulting in a neutral extended network.

Given that derivatives of the $[Co(triphos)(CN)_2]_2[MCl_2]_2$ (M= Mn, Fe, Co, Ni, and Zn) molecular squares and the Re_4Mn_4 cube have been successfully synthesized and characterized, and in the case of the Re_4Mn_4 cube it has been demonstrated that it can be used as a building block for the preparation of extended networks, our efforts can be extended into the synthesis of derivatives of previously reported clusters, such as the Re_4Fe_4 cube,[101] which have accessible sites for further chemistry, not only to investigate but also to take advantage of their unique intrinsic properties in various environments. These derivatives will further be used to incorporate the clusters into extended networks or higher nuclearity clusters to improve their properties and functionality.

The aforementioned trinuclear and square clusters with labile solvent ligands could be reacted with common bridging ligands such as oxalate, azide, and dicyanamide, aiming to introduce these clusters into extended networks. Given that aforementioned derivatives of cube molecules are stable in solution, have accessible sites, and exhibit interesting physical properties, they could also be used as building-blocks to design and synthesize various extended networks, which could result in multifunctional materials.

The reaction of **16** with $TCNQ^-$ which resulted in a chain of molecular cubes will also be performed with **15**, which could result in a 2D network of molecular cubes since the electron neutrality of the cube allows for all the Mn sites to be available for further chemistry. Furthermore, since the sigma bond of the dimerized TCNQ molecule can be perturbed at high temperatures due to the weakness of the bond[189,190] the possibility to systematically lower the dimensionality of the chain by breaking the two different sigma bonds present will be studied. Reactions that lead to other chains and networks obtained from the use of different organocyanide ligands (TCNQ, DCNQI, and their derivatives) will also be undertaken. This group of compounds will not only help to study the behavior of the sigma-bond of the TCNQ dimer but also yield a family of chains, which will be the first example of such a study.

Compound **17** has available coordination sites on the dicyanamide ligand for bridging to other metal centers. This derivative could be reacted with capped metal precursors to prepare discrete clusters with higher nuclearity. We are proposing to introduce metal ions with appreciable anisotropy into this chemistry in order to improve the SMM behavior of the cubes as well as to obtain higher nuclearity clusters. Metal complexes capped by triphos or Tp ligands (Tp= tris(pyrazolylborate)), such as (triphos)$Mo^{III}Cl_3$, (Tp)$Mo^{III}Br_2$(THF), (Tp)$V^{III}Cl_2$(THF), (Tp)$Ti^{III}Cl_2$(THF) are good candidates for this purpose since these metal ions are rarely studied in molecular magnetism due to their synthetic challenge. Moreover, compound **17** could be reacted with solvated 3d metal ions systematically to form extended networks with a possibility of a high degree of porosity.

The preliminary reactions of the mentioned derivatives with cyano ligands, showing the availability of the Mn(II) site of the cubic core towards the nitrogen end of bridging cyanide ligands, encourages us to introduce other convenient organocyanide ligands into this chemistry. One remarkable aim of this research is to incorporate SMMs in variable networks to investigate this unique magnetic behavior extensively, as well as to prepare multifunctional materials deliberately. The use of long linear organocyanide ligands could be used to prepare magnetic porous frameworks. Dicyanopolyphenylene (NC-Ph$_n$-CN, n=1-5) molecules will particularly be used to connect cubes to form a porous network. Porous networks with SMM behavior could be potentially used to separate magnetic particles with different sizes from a non-magnetic bulk media. We are also proposing to introduce polyalkylene dicyanamide molecules, which are convenient ligands to serve the purpose of linking the cubes via long ligands since they are longer bridging ligands than the dicyanamide ligand and they have 2– charges similar to the TCNQ dimer. Another approach we are pursuing is the use of long aliphatic molecules with nitrile groups which are commonly used to make liquid crystals. Such commercially available molecules will mainly be used for this purpose to make discrete cube molecules with long tails.

This general synthetic approach will also be exploited in order to study the electronic properties of interesting building blocks since the use of individual molecules as functional electronic devices has various applications in molecule-based electronics. Single molecule measurements can be performed by connecting the derivatized cluster between two surfaces. Organocyanide ligands that have protected thiol groups on the other end will be coordinated to the cubic SMM [Re_4Mn_4], in which the thiol group will further be used to connect the SMM to gold electrodes. This unique method could be a key measurement to understand the intrinsic properties of SMMs. Research is also in progress to prepare the Re_4Fe_4 cube with dangling solvent molecules in order to functionalize it by attaching the thiol protected organocyanide ligands and perform single molecule measurements to study its rich electrochemical properties as judged by its cyclic voltammogram.

REFERENCES

(1) Aubin, S. M. J.; Dilley, N. R.; Pardi, L.; Krzystek, J.; Wemple, M. W.; Brunel, L. C.; Maple, M. B.; Christou, G.; Hendrickson, D. N. *J. Am. Chem. Soc.* **1998,** *120*, 4991-5004.

(2) Friedman, J. R.; Sarachik, M. P.; Tejada, J.; Maciejewski, J.; Ziolo, R. *J. Appl. Phys.* **1996,** *79*, 6031-6033.

(3) Friedman, J. R.; Sarachik, M. P.; Tejada, J.; Ziolo, R. *Phys. Rev. Lett.* **1996,** *76*, 3830-3833.

(4) Hernandez, J. M.; Zhang, X. X.; Luis, F.; Tejada, J.; Friedman, J. R.; Sarachik, M. P.; Ziolo, R. *Phys. Rev. B: Condens. Matter Mater. Phys.* **1997,** *55*, 5858-5865.

(5) Sangregorio, C.; Ohm, T.; Paulsen, C.; Sessoli, R.; Gatteschi, D. *Phys. Rev. Lett.* **1997,** *78*, 4645-4648.

(6) Thiaville, A.; Miltat, J. *Science* **1999,** *284*, 1939-1940.

(7) Thomas, L.; Lionti, F.; Ballou, R.; Gatteschi, D.; Sessoli, R.; Barbara, R. *Nature* **1996,** *383*, 145-147.

(8) Mannini, M.; Sainctavit, P.; Sessoli, R.; Moulin, C. C. d.; Pineider, F.; Arrio, M.-A.; Cornia, A.; Gatteschi, D. *Chem. Eur. J.* **2008,** *14*, 7530-7535.

(9) Gatteschi, D.; Sessoli, R.; Villain, J. *Molecular Nanomagnets;* Oxford University Press: London, 2006.

(10) Jo, M.-H.; Grose, J. E.; Baheti, K.; Deshmukh, M. M.; Sokol, J. J.; Rumberger, E. M.; Hendrickson, D. N.; Long, G. J.; Park, H.; Ralph, D. C. *Nano Letters* **2006,** *6*, 2014-2020.

(11) Heersche, H. B.; de Groot, Z.; Folk, J. A.; van der Zant, H. S. J. *Phys. Rev. Lett.* **2006,** *96*, 2068011-4).

(12) Bogani, L.; Wernsdorfer, W. *Nature Materials* **2008,** *7*, 179-186.

(13) Wolf, S. A.; Awschalom, D. D.; Buhrman, R. A.; Daughton, J. M.; von Molnar, S.; Roukes, M. L.; Chtchelkanova, A. Y.; Treger, D. M. *Science* **2001,** *294*, 1488-1495.

(14) Rocha, A. R.; Garcia-Suarez, V. M.; Bailey, S. M.; Lambert, C. J.; Ferrer, J.; Sanvito, S. *Nature Materials* **2005,** *4*, 335-339.

(15) Bleaney, B.; Bowers, K. D. *Proc. Roy. Soc. London Ser A* **1952,** *214*, 451-465.

(16) Guha, B. C. *Proc. Roy. Soc. London Ser A* **1951,** *206*, 353-373.

(17) Abragam, A.; Bleaney, B. *Electron Paramagnetic Resonance of Transition Ions*; Oxford University Press: Oxford 1970.

(18) Van Niekerk, J. N.; Schoening, F. R. L. *Acta Cryst.* **1953,** *6*, 227-232.

(19) Barclay, G. A.; Kennard, C. H. L. *J. Chem. Soc.* **1961**, 3289-3294.

(20) Kokot, E.; Martin, R. L. *Inorg. Chem.* **1964,** *3*, 1306-1312.

(21) Dubicki, L.; Harris, C. M.; Kokot, E.; Martin, R. L. *Inorg. Chem.* **1966,** *5*, 93-100.

(22) Porter, L. C.; Doedens, R. J. *Inorg. Chem.* **1984,** *23*, 997-999.

(23) Moreland, J. A.; Doedens, R. J. *Inorg. Chem.* **1978,** *17*, 674-679.

(24) Curely, J.; Barbara, B. *Struct. Bond.* **2006,** *122*, 207-250.

(25) Curely, J. *Monatshefte für Chemie* **2005,** *136*, 1013-1036.

(26) Hay, P. J.; Thibeault, J. C.; Hoffmann, R. *J. Am. Chem. Soc.* **1975,** *97*, 4884-4899.

(27) Summerville, R. H.; Hoffmann, R. *J. Am. Chem. Soc.* **1976,** *98*, 7240-7254.

(28) Julve, M.; Verdaguer, M.; Kahn, O.; Gleizes, A.; Philoche-Levisalles, M. *Inorg. Chem.* **1983,** *22*, 368-370.

(29) Charlot, M. F.; Kahn, O.; Jeannin, S.; Jeannin, Y. *Inorg. Chem.* **1980,** *19*, 1411-1413.

(30) Julve, M.; Verdaguer, M.; Gleizes, A.; Philoche-Levisalles, M.; Kahn, O. *Inorg. Chem.* **1984,** *23*, 3808-3818.

(31) Carlin, R. L.; Kopinga, K.; Kahn, O.; Verdaguer, M. *Inorg. Chem.* **1986,** *25*, 1786-1789.

(32) Julve, M.; Kahn, O. *Inorg. Chimica Acta* **1983,** *76*, L39-L41.

(33) Wrobleski, J. T.; Brown, D. B. *Inorg. Chimica Acta* **1979,** *35*, 109-118.

(34) Wickman, H. H.; Trozzolo, A. M.; Williams, H. J.; Hull, G. W.; Merritt, F. R. *Phys. Rev.* **1967,** *155*, 563-566.

(35) Barraclough, C. G.; Martin, R. L.; Mitra, S. *J. Chem. Phys.* **1970,** *53*, 1638-1642.

(36) Pei, Y.; Kahn, O.; Sletten, J. *J. Am. Chem. Soc.* **1986,** *108*, 3143-3145.

(37) Pei, Y.; Verdaguer, M.; Kahn, O. *J. Am. Chem. Soc.* **1986,** *108*, 7428-7430.

(38) Kahn, O.; Pei, Y.; Verdaguer, M.; Renard, J. P.; Sletten, J. *J. Am. Chem. Soc.* **1988,** *110*, 782-789.

(39) Manriquez, J. M.; Yee, G. T.; Mclean, R. S.; Epstein, A. J.; Miller, J. S. *Science* **1991,** *252*, 1415-1417.

(40) Holmes, S. M.; Girolami, S. G. *J. Am. Chem. Soc.* **1999,** *121*, 5593-5594.

(41) Ferlay, S.; Mallah, T.; Ouahes, R.; Veillet, P.; Verdaguer, M. *Inorg. Chem.* **1999,** *38*, 229-234.

(42) Coey, J. M. D. *J. Alloys Compd.* **2001,** 326, 2-6.

(43) Lis, T. *Acta Crystallogr., Sect. B: Struct. Sci.* **1980,** *B36*, 2042-2046.

(44) Sessoli, R.; Tsai, H. L.; Schake, A. R.; Wang, S.; Vincent, J. B.; Folting, K.; Gatteschi, D.; Christou, G.; Hendrickson, D. N. *J. Am. Chem. Soc.* **1993,** *115*, 1804-1816.

(45) Sessoli, R.; Gatteschi, D.; Caneschi, A.; Novak, M. A. *Nature* **1993,** *365*, 141-143.

(46) Aromi, G.; Aubin, S. M. J.; Bolcar, M. A.; Christou, G.; Eppley, H. J.; Folting, K.; Hendrickson, D. N.; Huffman, J. C.; Squire, R. C.; Tsai, H.-L.; Wang, S.; Wemple, M. W. *Polyhedron* **1998,** *17*, 3005-3020.

(47) Gatteschi, D.; Sessoli, R. *Angew. Chem. Int. Ed.* **2003,** *42*, 268-297.

(48) Gatteschi, D.; Sessoli, R. *J. Magn. Magn. Mater.* **2004,** *272-276*, 1030-1036.

(49) Tasiopoulos, A. J.; Vinslave, A.; Wernsdorfer, W.; Abboud, K. A.; Christou, G. *Angew. Chem. Int. Ed.* **2004,** *43*, 2117-2121.

(50) Soler, M.; Rumberger, E.; Folting, K.; Hendrickson, D. N.; Christou, G. *Polyhedron* **2001,** *20*, 1365.

(51) Sokol, J. J.; Hee, A. G.; Long, J. R. *J. Am. Chem. Soc.* **2002,** *124*, 7656-7657.

(52) Schelter, E. J.; Prosvirin, A. V.; Dunbar, K. R. *J. Am. Chem. Soc.* **2004,** *126*, 15004-15005.

(53) Freedman, D. E.; Jenkins, D. M.; Iavarone, A. T.; Long, J. R. *J. Am. Chem. Soc.* **2008,** *130*, 2884-2885.

(54) Yoon, J. H.; Lim, J.-H.; Kim, H.-C.; Hong, C. S. *Inorg. Chem.* **2006,** *45*, 9613-9615.

(55) Freedman, D. E.; Bennett, M. V.; Long, J. R. *Dalton Trans.* **2006**, 2829-2834.

(56) Song, Y.; Zhang, P.; Ren, X. M.; Shen, X. F.; Li, Y. Z.; You, X.-Z., *J. Am. Chem. Soc.* **2005,** *127*, 3708-3709.

(57) Artus, P.; Boskovic, C.; Yoo, J.; Streib, W. E.; Brunel, L.-C.; Hendrickson, D. N.; Christou, G. *Inorg. Chem.* **2001,** *40*, 4199-4210.

(58) Soler, M.; Artus, P.; Folting, K.; Huffman, J. C.; Hendrickson, D. N.; Christou, G. *Inorg. Chem.* **2001,** *40*, 4902-4912.

(59) Eppley, H. J.; Tsai, H.-L.; de Vries, N.; Folting, K.; Christou, G.; Hendrickson, D. N. *J. Am. Chem. Soc.* **1995,** *117*, 301-317.

(60) Chakov, N. E.; Abboud, K. A.; Zakharov, L. N.; Rheingold, A. L.; Hendrickson, D. N.; Christou, G. *Polyhedron* **2003,** *22*, 1759-1763.

(61) Brockman, J. T.; Abboud, K. A.; Hendrickson, D. N.; Christou, G. *Polyhedron* **2003,** *22*, 1765-1769.

(62) Soler, M.; Wernsdorfer, W.; Sun, Z.; Ruiz, D.; Huffman, J. C.; Hendrickson, D. N.; Christou, G. *Polyhedron* **2003,** *22*, 1783-1788.

(63) Murugesu, M.; Wernsdorfer, W.; Abboud, K. A.; Brechin, E. K.; Christou, G. *Dalton Trans.* **2006**, 2285-2287.

(64) Tasiopoulos, A. J.; Wernsdorfer, W.; Abboud, K. A.; Christou, G. *Inorg. Chem.* **2005,** *44*, 6324-6338.

(65) King, P.; Wernsdorfer, W.; Abboud, K. A.; Christou, G. *Inorg. Chem.* **2005,** *44*, 8659-8669.

(66) Soler, M.; Wernsdorfer, W.; Sun, Z.; Huffman, J. C.; Hendrickson, D. N.; Christou, G. *Chem. Commun.* **2003**, 2672-2673.

(67) Dunbar, K. R.; Heintz, R. A. *Prog. Inorg. Chem.* **1997,** *45*, 283-391.

(68) Shatruk, M.; Avendano, C.; Dunbar, K. R. *Prog. Inorg. Chem.* **2009,** *56*, 155-334.

(69) Buser, H. J.; Schwarzenbach, D.; Petter, W.; Ludi, A. *Inorg. Chem.* **1977,** *16*, 2704-2710.

(70) Herren, F.; Fischer, P.; Ludi, A.; Halg, W. *Inorg. Chem.* **1980,** *19*, 956-959.

(71) Buschmann, W. E.; Miller, J. S. *Inorg. Chem.* **2000,** *39*, 2411-2421.

(72) Juszczyk, S.; Johansson, C.; Hanson, M.; Ratuszna, A.; Malecki, G. *J. Phys. Condens. Matter* **1994,** *6*, 5697-5706.

(73) Entley, W. R.; Treadway, C. R.; Girolami, S. G. *Mol. Cryst. Liq. Cryst.* **1995,** *273*, 153-166.

(74) Gadet, V.; Mallah, T.; Castro, I.; Verdaguer, M. *J. Am. Chem. Soc.* **1992,** *114*, 9213-9214.

(75) Entley, W. R.; Girolami, S. G. *Inorg. Chem.* **1994,** *33*, 5165-5166.

(76) Marvaud, V.; Decroix, C.; Scuiller, A.; Guyard-Duhayon, C.; Vaissermann, J.; Gonnet, F.; Verdaguer, M. *Chem. Eur. J.* **2003,** *9*, 1677-1691.

(77) Rodriguez-Fortea, A.; Alemany, P.; Alvarez, S.; Ruiz, E.; Scuiller, A.; Decroix, C.; Marvaud, V.; Vaissermann, J.; Verdaguer, M. *Inorg. Chem.* **2001,** *40*, 5868-5877.

(78) Kim, J. I.; Yoon, J. H.; Kwak, H. Y.; Koh, E. K.; Hong, C. S. *Eur. J. Inorg. Chem.* **2008**, 2756-2763.

(79) Bieksza, D. S.; Hendrickson, D. N. *Inorg. Chem.* **1977,** *16*, 924-929.

(80) Steed, J. W.; Atwood, J. L., *Supramolecular Chemistry:* John Wiley & Sons, New York, NY, 2001.

(81) Berlinguette, C. P.; Smith, J. A.; Galan-Mascaros, J. R.; Dunbar, K. R. *C. R. Chimie* **2002**, 665-672.

(82) Oshio, H.; Onodera, H.; Tamada, O.; Mizutani, H.; Hikichi, T.; Ito, T. *Chem. Eur. J.* **2000,** *6*, 2523-2530.

(83) Oshio, H.; Tamada, O.; Onodera, H.; Ito, T.; Ikoma, T.; Tero-Kubota, S. *Inorg. Chem.* **1999,** *38*, 5686-5689.

(84) Kou, K.; Gao, S.; Li, C.; Liao, D.; Bei-Zhou, C.; Wang, R.; Li, Y. *Inorg. Chem.* **2002,** *41*, 4756-4762.

(85) Falvello, L. R.; Tomas, M. *Chem. Commun.* **1999**, 273-274.

(86) Klausmeyer, K. K.; Rauchfuss, T. B.; Wilson, S. R. *Angew. Chem. Int. Ed.* **1998,** *37*, 1694-1696.

(87) Darensbourg, D. J.; Lee, W.; Adams, M. J.; Yarbrough, J. C. *Eur. J. Inorg. Chem.* **2001**, 2811-2822.

(88) Oshio, H.; Yamamoto, M.; Ito, T. *Inorg. Chem.* **2002,** *41*, 5817-5820.

(89) Schinnerling, P.; Thewalt, U. *Organomet. Chem.* **1992,** *431*, 41-45.

(90) Flay, M.; Comte, V.; Vahrenkamp, H. Z. *Anorg. Allg. Chem.* **2003,** *629*, 1147-1152.

(91) Li, D.; Parkin, S.; Wang, G.; Yee, G. T.; Prosvirin, A. V.; Holmes, S. M. *Inorg. Chem.* **2005,** *44*, 4903-4905.

(92) Toma, L. M.; Lescouezec, R.; Cangussu, D.; Llusar, R.; Mata, J.; Spey, S.; Thomas, J. A.; Lloret, F.; Julve, M. *Inorg. Chem.* **2005,** *8*, 382-385.

(93) Yeung, W.-F.; Kwong, H.-K.; Lau, T.-C.; Gao, S.; Szeto, L.; Wong, W.-T. *Polyhedron* **2006,** *25*, 1256-1262.

(94) Kim, J.; Han, S.; Cho, I.-K.; Choi, K.-Y.; Heu, M.; Yoon, S.; Suh, B. J. *Polyhedron* **2004,** *23*, 1333-1339.

(95) Li, D.; Parkin, S.; Wang, G.; Yee, G. T.; Holmes, S. M. *Inorg. Chem.* **2006,** *45*, 2773-2775.

(96) Li, D.; Parkin, S.; Wang, G.; Yee, G. T.; Holmes, S. M. *Inorg. Chem.* **2006,** *45*, 1951-1959.

(97) Liu, W.; Wang, C.; Li, Y.; Zuo, J.; You, X. *Inorg. Chem.* **2006,** *45*, 10058-10065.

(98) Rodriguez-Diéguez, A.; Kivekás, R.; Sillanpáá, R.; Cano, J.; Lloret, F.; McKee, V.; Stoeckli-Evans, H.; Colacio, E. *Inorg. Chem.* **2006,** *45*, 10537-10551.

(99) Jiang, L.; Feng, X.; Lu, T.; Gao, S. *Inorg. Chem.* **2006,** *45*, 5018-5026.

(100) Rebilly, J.; Catala, L.; Charron, G.; Rogez, G.; Riviére, E.; Guillot, R.; Thuéry, P.; Barra, A.; Mallah, T. *Dalton Trans.* **2006**, 2818-2828.

(101) Schelter, E. J.; Karadas, F.; Avendano, C.; Prosvirin, A. V.; Wernsdorfer, W.; Dunbar, K. R. *J. Am. Chem. Soc.* **2007,** *129*, (26), 8139-8149.

(102) Ruiz, D.; Sun, Z.; Albela, B.; Folting, K.; Ribas, J.; Christou, G.; Hendrickson, D. N. *Angew. Chem. Int. Ed.* **1998,** *37*, 300-302.

(103) Campos-Fernandez, C. S.; Clerac, R.; Dunbar, K. R. *Angew. Chem. Int. Ed.* **1999,** *38*, 3477-3479.

(104) Youinou, M.; Rahmouni, N.; Fischer, J.; Osborn, J. A. *Angew. Chem. Int. Ed.* **1992,** *31*, 733-735.

(105) Campos-Fernandez, C. S.; Clerac, R.; Koomen, J. M.; Russell, D. H.; Dunbar, K. R. *J. Am. Chem. Soc.* **2001,** *123*, 773-774.

(106) Schelter, E. J.; Prosvirin, A. V.; Reiff, W. M.; Dunbar, K. R. *Angew. Chem. Int. Ed.* **2004,** *43*, 4912-4915.

(107) Jacob, V.; Mann, S.; Huttner, G.; Walter, O.; Zsolnai, L.; Kaifer, E.; Rutsch, P.; Kircher, P.; Bill, E. *Eur. J. Inorg. Chem.* **2001**, 2625-2640.

(108) Rupp, R.; Huttner, G.; Kircher, P.; Soltek, R.; Buchner, M. *Eur. J. Inorg. Chem.* **2000**, 1745-1757.

(109) Karadas, F.; Schelter, E. J.; Prosvirin, A. V.; Bacsa, J.; Dunbar, K. R. *Chem. Comm.* **2005**, 1414-1416.

(110) Karadas, F.; Schelter, E. J.; Shatruk, M.; Prosvirin, A. V.; Bacsa, J.; Smirnow, D.; Ozarowski, A.; Krzystek, J.; Telser, J.; Dunbar, K. R. *Inorg. Chem.* **2008,** *47*, 2074-2082.

(111) Cotton, F. A.; Luck, R. L.; Son, K. A. *Inorg. Chim. Acta* **1991,** *179*, 11-15.

(112) *SMART and SAINT; Siemens Analytical X-ray Instruments Inc.: Madison, WI* 1996.

(113) Sheldrick, G. M., *SADABS, University of Göttingen, Göttingen, Germany,* **1996**.

(114) Sheldrick, G. M., In *SHELXS-97 and SHELXL-97*, University of Göttingen, Göttingen, Germany: 1997.

(115) Barbour, L. J. *J. Supramol. Chem.* **2001,** *1*, 189-191.

(116) Van der Sluis, P.; Spek, A. L. *Acta Crystallogr. Sect. A* **1990,** *A46*, 194-201.

(117) Zvyagin, S. A.; Krzystek, J.; Sienkiewicz, A.; Goy, P.; Rohrer, M.; Brunel, L. C. *J. Magn. Reson.* **2000,** *142*, 300-312.

(118) Hassan, A. K.; Pardi, L. A.; Kryzstek, J.; Sienkiewicz, A.; Goy, P.; Rohrer, M.; Brunel, L. C. *J. Magn. Reson.* **2000,** *142*, 300-312.

(119) Rigo, P.; Turco, A. *Coord. Chem. Rev.* **1974,** *13*, 133-172.

(120) Brown, L. D.; Raymond, K. N. *Inorg. Chem.* **1975,** *14*, 2590-2594.

(121) Shores, M. P.; Sokol, J. J.; Long, J. R. *J. Am. Chem. Soc.* **2002,** *124*, 2279-2292.

(122) Borras-Almenar, J. J.; Clemente-Juan, J. M.; Kou, H.-Z.; Gao, S.; Jin, X. *Inorg. Chem.* **2001,** *40*, 6295-6303.

(123) Borras-Almenar, J. J.; Clemente-Juan, J. M.; Coronado, E.; Tsukerblat, B. S. *J. Comput. Chem.* **2001,** *22*, 985-991.

(124) Abragam, A.; Bleaney, B., *Electron Paramagnetic Resonance of Transition Ions;* Oxford University Press, Oxford 1986.

(125) Krzystek, J.; Zvyagin, S. A.; Ozarowski, A.; Trofimenko, S.; Telser, J. *J. Magn. Reson.* **2006,** *178*, 174-183.

(126) Krzystek, J.; Park, J.-H.; Meisel, M. W.; Hitchman, M. A.; Stratemeier, H.; Brunel, L. C.; Telser, J. *Inorg. Chem.* **2002,** *41*, 4478-4487.

(127) Drago, R. S., *Physical Methods in Chemistry:* Saunders, Chapter 13, 1992.

(128) Krzystek, J.; Zvyagin, S. A.; Ozarowski, A.; Fiedler, A. T.; Brunold, T. C.; Telser, J. *J. Am. Chem. Soc.* **2004,** *126*, 2148-2155.

(129) Weihe, H.; Gudel, H. U. *Comments Inorg. Chem.* **2000,** *22*, (1), 75-103.

(130) Atanasov, M.; Busche, C.; Comba, P.; Hallak, F.; Martin, B.; Rajaraman, G.; Slageren, J.; Wadepohl, H. *Inorg. Chem.* **2008,** *47*, 8112-8125.

(131) Marvaud, V.; Herrera, J. M.; Barilero, T.; Tuyeras, F.; Garde, R.; Scuiller, A.; Decroix, C.; Cantuel, M.; Desplanches, C. *Monatshefte fur Chemie* **2003,** *134*, 149-163.

(132) Atanasov, M.; Comba, P.; Daul, C. A. *J. Phys. Chem. A* **2006,** *110*, 13332-13340.

(133) Daul, C.; Atanasov, M. *Chimia* **2005,** *59*, 504-510.

(134) Eyert, V.; Siberchicot, B.; Verdaguer, M. *Phys. Rev. B* **1997,** *56*, (14), 8959-8969.

(135) Kahn, O.; Briat, B. *J. Chem. Soc. Faraday Trans. II* **1976,** *72*, 268-274.

(136) Kahn, O.; Briat, B. *J. Chem. Soc. Faraday Trans. II* **1976,** *72*, 1441-1444.

(137) Ferlay, S.; Mallah, T.; Ouahes, R.; Veillet, P.; Verdaguer, M. *Nature* **1995,** *378*, 701-706.

(138) Mallah, T.; Thiebaut, M.; Verdaguer, M.; Veillet, P. *Science* **1993,** *262*, 1554-1556.

(139) Herrera, J. M.; Bachschmidt, A.; Villain, F.; Bleuzen, A.; Marvaud, V.; Wernsdorfer, W.; Verdaguer, M. *Phil. Trans. R. Soc. A* **2008,** *366*, 127-138.

(140) Ruiz, E.; Rodriguez-Fortea, A.; Alvarez, S.; Verdaguer, M. *Chem. Eur. J.* **2005,** *11*, 2135-2144.

(141) Heinrich, J. L.; Berseth, P. A.; Long, J. R. *Chem. Commun.* **1998**, 1231-1232.

(142) Toma, L.; Lescouezec, R.; Vaissermann, J.; Delgado, F. S.; Ruiz-Perez, C.; Carrasco, R.; Cano, J.; Lloret, F.; Julve, M. *Chem. Eur. J.* **2004,** *10*, 6130-6145.

(143) Wang, S.; Zuo, J.-L.; Zhou, H.-C.; Song, Y.; Gao, S.; You, X.-Z. *Eur. J. Inorg. Chem.* **2004**, 3681-3687.

(144) Hathaway, B. J.; Holah, D. G.; Underhill, A. E. *J. Chem. Soc.* **1962,** 2444-2448.

(145) Ni, Z.-H.; Kou, H.-Z.; Zhang, L.-F.; Ni, W.-W.; Jiang, Y.-B.; Cui, A.-L.; Ribas, J.; Sato, O. *Inorg. Chem.* **2005,** *44*, 9631-9633.

(146) Wen, H.-R.; Wang, C.-F.; Zuo, J.-L.; Song, Y.; Zeng, X.-R.; You, X.-Z. *Inorg. Chem.* **2006,** *45*, 582-590.

(147) Mukhin, A. A.; Travkin, V. D.; Zvezdin, A. K.; Lebedev, S. P.; Caneschi, A.; Gatteschi, D. *Europhys. Lett.* **1998,** *44*, 778-780.

(148) Li, D.; Parkin, S.; Wang, G.; Yee, G. T.; Clerac, R.; Wernsdorfer, W.; Holmes, S. M. *J. Am. Chem. Soc.* **2006,** *128*, 4214-4219.

(149) Choi, H. J.; Sokol, J. J.; Long, J. R. *Inorg. Chem.* **2004,** *43*, 1606-1614.

(150) Berlinguette, C. P.; Vaughn, D.; Canada-Vilalta, C.; Galan-Mascaros, J. R.; Dunbar, K. R. *Angew. Chem. Int. Ed.* **2003,** *42*, 1523-1526.

(151) Raghu, C.; Rudra, I.; Sen, D.; Ramasesha, S. *Phys. Rev. B: Condens. Matter Mater. Phys.* **2001,** *64*, 64419-64432.

(152) Wang, C.-F.; Zuo, J.-L.; Bartlett, B. M.; Song, Y.; Long, J. R.; You, X.-Z. *J. Am. Chem. Soc.* **2006,** *128*, 7162-7167.

(153) Ferbinteanu, M.; Miyasaka, H.; Wernsdorfer, W.; Nakata, K.; Sugiura, K.; Yamashita, M.; Coulon, C.; Clerac, R. *J. Am. Chem. Soc.* **2005,** *127*, 3090-3097.

(154) Wang, S.; Zuo, J.-L.; Zhou, H.-C.; Choi, H. J.; Ke, Y.; Long, J. R.; You, X.-Z. *Angew. Chem. Int. Ed.* **2004,** *43*, 5940-5943.

(155) Miyasaka, H.; Takahashi, H.; Madanbashi, T.; Sugiura, K.; Clerac, R.; Nojiri, H. *Inorg. Chem.* **2005,** *44*, 5969-5980.

(156) Barra, A. L.; Debrunner, P.; Gatteschi, D.; Schulz, C. E.; Sessoli, R. *Europhys. Lett.* **1996,** *35*, 133-135.

(157) Bagai, R.; Christou, G. *Inorg. Chem.* **2007,** *46*, 10810-10818.

(158) Chakov, N. E.; Lee, S.-C.; Harter, A. G.; Kuhns, P. L.; Reyes, A. P.; Hill, S. O.; Dalal, N. S.; Wernsdorfer, W.; Abboud, K. A.; Christou, G. *J. Am. Chem. Soc.* **2006,** *128*, 6975-6989.

(159) Gomez-Segura, J.; Lhotel, E.; Paulsen, C.; Luneau, D.; Wurst, K.; Veciana, J.; Ruiz-Molina, D.; Gerbier, P. *New J. Chem.* **2005,** *29*, 499-503.

(160) Gomez-Segura, J.; Campo, J.; Imaz, I.; Wurst, K.; Veciana, J.; Gerbier, P.; Ruiz-Molina, D. *Dalton Trans.* **2007**, 2450-2456.

(161) Aubin, S. M. J.; Sun, Z. M.; Eppley, H. J.; Rumberger, E. M.; Guzei, I. A.; Folting, K.; Gantzel, P. K.; Rheingold, A. L.; Christou, G.; Hendrickson, D. N. *Inorg. Chem.* **2001,** *40*, 2127-2146.

(162) Hill, S.; Anderson, N.; Wilson, A.; Takahashi, S.; Chakov, N. E.; Murugesu, M.; North, J. M.; Dalal, N. S.; Christou, G. *J. Appl. Phys.* **2005,** *97*, 510-512.

(163) Wernsdorfer, W.; Murugesu, M.; Christou, G. *Phys. Rev. Lett.* **2006,** *96*, 0572081-4.

(164) Choi, H. J.; Sokol, J. J.; Long, J. R. *Inorg. Chem.* **2004,** *43*, 1606-1608.

(165) Palii, A. V.; Ostrovsky, S. M.; Klokishner, S. I.; Tsukerblat, B. S.; Schelter, E. J.; Prosvirin, A. V.; Dunbar, K. R. *Inorg. Chimica Acta* **2007,** *360*, 3915-3924.

(166) Kim, J.; Lim, J. M.; Do, Y. *Eur. J. Inorg. Chem.* **2003**, 2563-2566.

(167) Zheng, Y.-Z.; Tong, M.-L.; Xue, W.; Zhang, W.-X.; Chen, X.-M.; Grandjean, F.; Long, G. J. *Angew. Chem. Int. Ed.* **2007,** *46*, 6076-6080.

(168) Xu, H.-B.; Wang, B.-W.; Pan, F.; Wang, Z.-M.; Gao, S. *Angew. Chem. Int. Ed.* **2007,** *46*, 7388-7392.

(169) Viciano-Chumillas, M.; Tanase, S.; Mutikainen, I.; Turpeinen, U.; de Jongh, L. J.; Reedijk, J. *Inorg. Chem.* **2008,** *47*, 5919-5929.

(170) Albores, P.; Rentschler, E. *Inorg. Chem.* **2009,** ASAP.

(171) Bai, Y.-L.; Tao, J.; Wernsdorfer, W.; Sato, O.; Huang, R.-B.; Zheng, L.-S. *J. Am. Chem. Soc.* **2006,** *128*, 16428-16429.

(172) Tao, J.; Zhang, Y.-Z.; Bai, Y.-L.; Sato, O. *Inorg. Chem.* **2006,** *45*, 4877-4879.

(173) Bartley, S. L.; Dunbar, K. R. *Angew. Chem. Int. Ed.* **1991,** *30*, 448-450.

(174) Finniss, G. M.; Canadell, E.; Campana, C.; Dunbar, K. R. *Angew. Chem. Int. Ed.* **1996,** *108*, 2771-2774.

(175) Bartley, S. L.; Dunbar, K. R. *Angew. Chem.* **1991,** *103*, 447-450.

(176) Bartley, S. L.; Dunbar, K. R. *Angew. Chem. Int. Ed. Engl.* **1991,** *30*, 448-450.

(177) Campana, C.; Dunbar, K. R.; Ouyang, X. *Chem. Commun.* **1996**, 2427-2428.

(178) Bartley, S. L.; Bazile, M. J.; Clerac, R.; Zhao, H.; Ouyang, X.; Dunbar, K. R. *Dalton Trans.* **2003**, 2937-2944.

(179) Ouyang, X.; Campana, C.; Dunbar, K. R. *Inorg. Chem.* **1996,** *35*, 7188-7189.

(180) Uzelmeier, C. E.; Bartley, S. L.; Fourmigué, M.; Rogers, R.; Grandinetti, G.; Dunbar, K. R. *Inorg. Chem.* **1998,** *37*, 6706-6713.

(181) Bartley, S. L.; Bernstein, S. N.; Dunbar, K. R. *Inorg. Chim. Acta* **1993,** *213*, 213-231.

(182) Wernsdorfer, W.; Aliaga-Alcalde, N.; Hendrickson, D. N.; Christou, G. *Nature* **2002,** *416*, 406-409.

(183) Bagai, R.; Wernsdorfer, W.; Abboud, K. A.; Christou, G. *J. Am. Chem. Soc.* **2007,** *129*, 12918-12919.

(184) Miyasaka, H.; Nakata, K.; Lecren, L.; Coulon, C.; Nakazawa, Y.; Fujisaki, T.; Sugiura, K.; Yamashita, M.; Clerac, R. *J. Am. Chem. Soc.* **2006,** *128*, 3770-3783.

(185) Lin, Z.; Li, Z.; Zhang, H. *Crsytal Growth & Design* **2007,** *7*, 589-591.

(186) Miyasaka, H.; Nakata, K.; Sugiura, K.; Yamashita, M.; Clerac, R. *Angew. Chem. Int. Ed.* **2004,** *43*, 707-711.

(187) Schelter, E. J.; Bera, J. K.; Bacsa, J.; Galan-Mascaros, J. R.; Dunbar, K. R. *Inorg. Chem.* **2003,** *42*, 4256-4258.

(188) Costello, M. T.; Schrier, P. W.; Fanwick, P. E.; Walton, R. A. *Inorg. Chim. Acta* **1993,** *212*, 157-163.

(189) Hoffmann, S. K.; Corvan, P. J.; Singh, P.; Sethulekshmi, C. N.; Metzger, R. M.; Hatfield, W. E. *J. Am. Chem. Soc.* **1983,** *105*, 4608-4617.

(190) Zhao, H.; Heintz, R. A.; Dunbar, K. R. *J. Am. Chem. Soc.* **1996,** *118*, 12844-12845.

(191) Manson, J. L.; Kmety, C. R.; Epstein, A. J.; Miller, J. S. *Inorg. Chem.* **1999,** *38*, 2552-2553.

(192) Zhao, H.; Heintz, R. A.; Ouyang, X.; Dunbar, K. R. *Chem. Mater.* **1999,** *11*, 736-746.

(193) Heintz, R. A.; Zhao, H.; Ouyang, X.; Grandinetti, G.; Cowen, J.; Dunbar, K. R. *Inorg. Chem.* **1999,** *38*, 144-156.

(194) Naito, T.; Inabe, T.; Niimi, H.; Asakura, K. *Adv. Mater.* **2004,** *16*, (20), 1786-1790.

(195) Kato, R.; Kobayashi, H.; Kobayashi, A. *J. Am. Chem. Soc.* **1989,** *111*, 5224-5232.

APPENDIX

PHYSICAL MEASUREMENTS

Elemental Analysis

Elemental Analyses were performed by Atlantic Microlab Inc. (Norcross, GA). Infrared spectra were collected in the range of 400 - 4000 cm^{-1} using a Nicolet Nexus 470 FTIR spectrometer.

Electrospray Ionization Mass Spectra (ESI-MS)

Electrospray-ionization mass spectra were acquired using a PE Sciex (Concord, Ontario, Canada) API Qstar Pulsar using an Ionwerks time-to-digital converter, TDCx4, for data recording at 625 ps time resolution. MeOH solutions of the samples were electrosprayed and the data were acquired in the positive-ion mode. The ionspray (needle) voltage was held constant at –4.5 kV. The nozzle skimmer potential was set to –10 V to minimize fragmentation in that region. Time-of-flight (TOF) voltages were tuned to optimize the resolving power over the mass range observed, but usually the following parameters were used: grid +338 V, plate –360 V, mirror –960 V, and liner –4000 V. Acquisition and data analysis were performed with the Analyst QS software.

Infrared Spectroscopy

IR Samples were measured in the form of Nujol mulls that were prepared by grinding samples to a fine powder followed by addition of minimal amounts of mineral oil to generate a thick paste. The measurements were performed on samples suspended between polished plates of potassium bromide or cesium iodide.

Magnetic Studies

DC magnetic susceptibility measurements were collected in the range of 2 - 300 K using a Quantum Design Multi-Property Measurement System (MPMS) employing a Superconducting Quantum Interference Device (SQUID). DC magnetic measurements were performed with an applied field of 1000 Oe in the 2 - 300 K temperature range. AC magnetic susceptibility measurements were performed in a 3 Oe AC field at a operating frequencies in the 1 - 1000 Hz range. Magnetization data were collected in the 0 - 70000 Oe range starting at zero field at 2 K and were corrected for the diamagnetic contributions calculated from the Pascal constants. Unless otherwise noted, all magnetic data in this dissertation were collected on crushed single crystals, which were structurally confirmed by unit cell determination.

High-frequency and -field EPR (HFEPR)

All of the molecular square complexes **2-6** were investigated by HFEPR using either the Mm and sub-mm Wave Facility, or the EMR Facility at NHMFL. The former experimental setup employs tunable frequencies in the 150 – 700 GHz range generated by backward wave oscillators, and the resistive “Keck” magnet enabling 0 – 25 T field sweeps. The latter spectrometer is based on a 17 T superconducting magnet and uses a 13 ± 1 GHz base frequency source (Virginia Diodes Inc., Charlottesville, VA) followed by an amplifier and a series of frequency multipliers, thus providing EPR spectra at intermediate frequencies, e.g., V-band (48 – 56 GHz), as well as at high frequencies. Detection was effected with an InSb hot-electron bolometer (QMC Ltd., Cardiff, UK). Modulation for detection purposes was provided alternatively by chopping the sub-THz wave beam ("optical modulation") or by modulating the magnetic field. A Stanford Research Systems SR830 lock-in amplifier converted the modulated signal to DC voltage. Typically, 30 – 50 mg of polycrystalline sample was used in either experiment. Additional X-band measurements were performed on **6** using a commercial Bruker E680X spectrometer.

DFT Studies

The molecular and electronic structure calculations were performed with density functional theory (DFT) using the Gaussian03 (G03) program package. The B3LYP functional along with the 6–31G* basis set was used for H, C, N, P, and O, along with the Couty-Hall Modified LANL2DZ Basis Sets for transition metal ions. H atoms were used instead of phenyl groups for the triphos ligand in the computationally modeled complexes. All geometries were fully optimized under the conditions of the respective programs. Orbital analysis was completed with Molekel 4.3.

VITA

Ferdi Karadaş received his Bachelor of Sciences degree in chemistry from the Middle East Technical University (METU) in 2002 followed by a M.S. degree in chemistry from Bilkent University in 2003. He then entered the Ph D. program at Texas A&M University in 2003, where he joined the group directed by Prof. Kim R. Dunbar. His research interests include instrumental and physical chemistry as well as organometallic chemistry.

Ferdi Karadas may be reached at Fatih Mah. Okul Sok. No: 25, Karacasu, Bolu, Turkey. His email address is birileri@gmail.com.